Contribution to flight guidance in high density traffic

Héctor Escamilla Núñez

▶ To cite this version:

HAL Id: tel-01833564

https://theses.hal.science/tel-01833564v2

Submitted on 15 May 2019

THÈSE

En vue de l'obtention du

DOCTORAT DE L'UNIVERSITÉ DE TOULOUSE

Délivré par : *l'Université Toulouse 3 Paul Sabatier (UT3 Paul Sabatier)*

Présentée et soutenue le *19/06/2018* **par :**

Héctor ESCAMILLA NÚÑEZ

Contribution au guidage des avions en trafic à haute densité

JURY

DAVID ZAMMIT MANGION	Université de Malte	Rapporteur
JOSÉ RAUL CARREIRA AZINHEIRA	Université de Lisbonne	Rapporteur
BOUTAIB DAHHOU	Université Paul Sabatier	Président du Jury
FATIHA NEJJARI	Université Polytechnique de Catalogne	Examinateur
ANTOINE DROUIN	ENAC	Examinateur
FELIX MORA CAMINO	ENAC	Examinateur

École doctorale et spécialité :
> *MITT : Signal, Image, Acoustique et Optimisation*

Unité de Recherche :
> *École Nationale de l'Aviation Civile (ENAC), Laboratoire de Mathématiques Appliquées, Informatique, et Automatique pour l'Aérien (MAIAA).*

Directeur(s) de Thèse :
> *Felix MORA CAMINO* et *Antoine DROUIN*

Rapporteurs :
> *David ZAMMIT MANGION* et *José Raul CARREIRA AZINHEIRA*

Declaration of Authorship

I, Héctor ESCAMILLA NÚÑEZ, declare that this thesis titled, "Contribution to Flight Guidance in High Density Traffic" and the work presented in it are my own. I confirm that:

- This work was done wholly or mainly while in candidature for a research degree at this University.

- Where I have consulted the published work of others, this is always clearly attributed.

- I have acknowledged all main sources of help.

Signed:

_____

Date:

_____

"It matters not how strait the gate,
How charged with punishments the scroll,
I am the master of my fate,
I am the captain of my soul."

William Ernest Henley

Abstract

This work is developed with the perspective of SESAR and Next-Gen projects, where new applications of Air Traffic Management (ATM) such as the Full 4D Management concept, are centered on Trajectory-Based Operations (TBO), deeply related with the extension of the flexibility in separation between aircraft, and hence, with the augmentation of air traffic capacity.

Therefore, since a shift from fixed routes and Air Traffic Control (ATC) clearances to flexible trajectories is imminent, while relying on higher levels of onboard automation, the thesis hinges around topics that should enable or ease the transition from current systems to systems compliant with the new expectancies of Trajectory-Based Operations.

The main axes of the manuscript can be summarized in three topics: 4D trajectory generation, 4D guidance, and mass estimation for trajectory optimization.

Regarding the trajectory generation, the need of airspace users to plan their preferred route from an entry to an exit point of the airspace without being constrained by the existent configurations is considered. Thus, a particular solution for 4D smooth path generation from preexisting control points is explored.

The method is based on Bezier curves, and is able to control the Euclidian distance between the given control points and the proposed trajectory. This is done by reshaping the path to remain within load factor limits, taking into account a tradeoff between path curvature and aircraft intended speed, representing a milestone in the road towards Trajectory-Based Operations.

It is considered that accurate 4D guidance will improve safety by decreasing the occurrence of near mid-air collisions for planned conflict free 4D trajectories. In consequence, two autopilots and two guidance approaches are developed with the objective of diminishing the workload for air traffic controllers associated to a single flight. The backstepping and feedback linearization techniques are used for attitude control, while direct and indirect nonlinear inversion are adopted for guidance.

Furthermore, the impact of inaccurate mass knowledge in trajectory guidance, with consequences in optimization, fuel consumption, and aircraft performance, has led to the implementation of an on-board aircraft mass estimation. The created approach is based on least squares, providing an initial mass estimation, and online computations of the current mass, both with enough accuracy to meet the objectives related to TBO.

The methods proposed in this thesis are tested in a six degrees of freedom Matlab model with its parameters chosen similar to an aircraft type B737-200 or A320-200. The simulation is based on a full nonlinear modelling of transport aircraft dynamics under wind disturbances. Trained neural networks are used to obtain the aerodynamic coefficients corresponding the aircraft forces and moments.

   Keywords: *Trajectory Generation, Automatic control, Trajectory Tracking, Mass Estimation, Transport Aircraft Simulation*

Résumé

Ce travail est développé dans le contexte des projets SESAR et Next-Gen, où de nouvelles applications de la gestion du trafic aérien (ATM) comme le concept de gestion d'opérations en 4D, se sont focalisées sur les opérations basées sur la trajectoire (TBO - Trajectory Based Operations). Ces opérations sont en relation avec l'extension de la flexibilité de la séparation entre avions, et par conséquence, avec l'augmentation de la capacité du trafic aérien.

En sachant qu'une évolution des routes fixes et autorisations émises par le contrôle du trafic aérien (ATC - Air Traffic Control) vers des trajectoires flexibles est imminente, en s'appuyant en même temps aux niveaux les plus élevés de l'automatique embarquée, ce travail de recherche s'intéresse aux sujets qui aideront à la transition des systèmes actuels vers les systèmes compatibles avec les nouveaux besoins des TBO.

Les principaux axes de recherche de ce manuscrit s'articulent en trois points: La génération de trajectoires en 4D, le guidage en 4D, et l'estimation de la masse d'un avion pour l'optimisation des trajectoires.

Concernant la génération des trajectoires, le besoin des utilisateurs d'espaces aériens de planifier leurs routes préférées à partir d'un point d'entrée dans l'espace aérien sans être limités par les configurations existantes est considéré. Une solution particulière pour la génération de trajectoires lisses en 4D à partir de points de contrôle prédéfinis est alors explorée.

La méthode proposée s'appuie sur les courbes de Bézier, et elle permet de contrôler la distance euclidienne entre le point de contrôle donné et la trajectoire proposée. Ceci est fait en modifiant la trajectoire de telle façon qu'elle reste à l'intérieur des limites des facteurs de charge, en considérant un compromis entre la courbure de la trajectoire et la vitesse voulue de l'avion, ce qui représente une étape importante dans le chemin vers les TBO.

Le guidage précis en 4D améliorera la sûreté en diminuant l'occur- rence de quasi-collisions aériennes pour des trajectoires en 4D planifiées en avance. En conséquence, deux autopilotes et deux méthodes de guidage sont développées avec l'objectif de réduire la charge de travail des contrôleurs du trafic aérien associée à un vol. Les techniques de backstepping et feedback linearization sont utilisées pour le pilotage, alors que l'inversion non linéaire directe et indirecte sont adoptées pour le guidage.

De plus, l'impact de la connaissance inexacte de la masse de l'avion dans le suivi de trajectoires, ses conséquences dans l'optimisation, la consommation de carburant, et la performance de l'avion, a conduit à l'implémentation d'une estimation embarquée de la masse de l'avion. L'approche créée est basée sur les moindres carrées, en fournissant des estimations de la masse initiale et la masse courante, toutes les deux avec une précision suffisante pour atteindre les objectifs liées aux TBO.

Les méthodes proposées dans cette thèse sont examinées en utilisant un modèle à six degrés de liberté, dont les paramètres approchent un appareil du type B737-200 ou A320-200. La simulation est basée sur une modélisation complète et non linéaire de la dynamique des avions de transport incluant des perturbations liées au vent. Des réseaux de neurones sont utilisés pour obtenir les différents coefficients aérodynamiques correspondant aux forces et moments de l'avion.

Acknowledgements

I would like to thank first to my parents, for their limitless love and support throughout my life. Secondly, I give my gratitude to my brother and my friends, for their love and sincere advice full of rawness and truth. They are all pillars of my life.
To E., for encouraging me in every possible way, and for being an outstanding person since the day we met.

To my thesis supervisors F. Mora and A. Drouin, for accepting me in their research environment and show me the different facets and commitments of a researcher.
To CONACYT, for its support program to Ph.D. students, knowing that without it, this professional and personal growth would have been impossible.

Contents

List of Figures

xviii

List of Tables

List of Abbreviations

ABAS	Aircraft Based Augmentation System
a.c.	Aerodynamic Center
ACAS	Airborne Collision Avoidance Systems
ACC	Area Control Centre
ADS-B	Automatic Dependent Surveillance – Broadcast
AGL	Above Ground Level
AIS/AIM	Aeronautical Information Services/Management
ANSP	Air Navigation Service Provider
AoA	Angle of Attack
ARTCC	Air Route Traffic Control Center
ASAS	Airborne Separation Assistance System
ASM	Air Space Management
ATC	Air Traffic Control
ATFCM	Air Traffic Flow and Capacity Management
ATM	Air Traffic Management
ATS	Air Traffic Services
ATSAW	Airborne Traffic Situational AWareness
BADA	Base of Aircraft DAta
CANSO	Civil Air Navigation Services Organisation
CAS	Calibrated Air Speed
CDM	Collaborative Decision Making
CDO/CCO	Continuous Descent/Climb Operations
c.g.	Center of Gravity
CNS	Communications, Navigation and Surveillance Systems
DCAC	Direction Générale de l'Aviation Civile
DOF	Degrees Of Freedom
DME	Distance Measuring Equipment
DSNA	Direction des Services de la Navigation Aérienne
EOW	Empty Operating Weight
FAB	Functional Airspace Block
FANS	Future Air Navigation Systems
FCU	Flight Control Unit
FDR	Flight Data Recorder
FGS	Flight Guidance Systems
FIR	Flight Information Region
FIS/-B	Flight Information Service / - Broadcast
FL	Flight Level
FMS	Flight Management System
FPA	Flight Path Angle
FRA	Free Route Airspace
GBAS	Ground Based Augmentation Systems
GNSS	Global Navigation Satellite Systems
GTOW	Gross Take-Off Weight

IAS	**I**ndicated **A**ir **S**peed
ICAO	**I**nternational **C**ivil **A**viation **O**rganization
IFR	**I**nstrument **F**light **R**ules
ILS	**I**nstrument **L**anding **S**ystem
INS	**I**nertial **N**avigation **S**ystem
IRU	**I**nertial **R**eference **U**nit
MCDU	**M**ultipurpose **C**ontrol **D**isplay **U**nit
MET	Aeronautical **MET**eorology Service for Air Navigation
MLS	**M**icrowave **L**anding **S**ystem
NLI	**N**on **L**inear **I**nversion
NDB	**N**on **D**irectional **B**eacon
NN	**N**eural **N**etowrk
PBN	**P**erformance **B**ased **N**avigation
PFD	**P**rimary **F**light **D**isplay
RBT	**R**eference **B**usiness **T**rajectory
RNP	**R**equired **N**avigation **P**erformance
RVR	**R**unway **V**isual **R**ange
SAR	**S**earch **A**nd **R**escue
SBAS	**S**atellite - **B**ased **A**ugmentation **S**ystems
SSR	**S**econdary **S**urveillance **R**adar
SVFR	**S**pecial **V**isual **F**light **R**ules
TAS	**T**rue **A**ir **S**peed
TCAS	**T**raffic **C**ollision **A**voidance **S**ystem
TIS-B	**T**raffic **I**nformation **S**ervice - **B**roadcast
TBO	**T**rajectory **B**ased **O**perations
TMA	**T**erminal **M**anoeuvring **A**rea
TOW	**T**ake-**O**ff **W**eight
TRACON	**T**erminal **R**adar Approach **CON**trol
VFR	**V**isual **F**light **R**ules
VHF	**V**ery **H**igh **F**requency
VOR	**V**ery **H**igh **F**requency **O**mnidirectional **R**ange
VoP	**V**olume **o**f **P**rotection
w.r.t.	**w**ith **r**espect **t**o
ZFW	**Z**ero **F**uel **W**eight

List of Constants

Aircraft c.g. position	$X_{cg} = 15.3$ m
Aircraft c.g. position	$Y_{cg} = 0$ m
Aircraft c.g. position	$Z_{cg} = -1.016$ m
Control surfaces time-constants	$\xi_{ail,ele,rud} = .05$ s
Inertia matrix component	$A = 1,278,369.56$ kg· m^2
Inertia matrix component	$B = 3,781,267.79$ kg·m^2
Inertia matrix component	$C = 4,877,649.98$ kg·m^2
Inertia matrix component	$E = 135,588.17$ kg·m^2
Maximum speed	$V_{max} = 0.85$ Mach
Mean chord	$\bar{c} = 4.35$ m
Pitching due to aircraft c.g. offset w.r.t. the a.c. coefficient	$C_{m_0} = -0.094$
Pitching due to elevator deflection coefficient	$C_{m_{\delta_{ele}}} = -0.003$ rad^{-1}
Rolling due to ailerons deflection coefficient	$C_{l_{\delta_{ail}}} = -0.02$ rad^{-1}
Rolling due to ruder deflection coefficient	$C_{l_{\delta_{rud}}} = 0$ rad^{-1}
Service ceiling	$h_{max} = 10,700$ m
Thrust time-constant	$\xi_T = 2.5$ s
Wing area	$S = 123.55$ m^2
Wingspan	$b = 28.34$ m
Yawing due to ailerons deflection coefficient	$C_{n_{\delta_{ail}}} = 0.002$ rad^{-1}
Yawing due to ruder deflection coefficient	$C_{n_{\delta_{rud}}} = -0.07$ rad^{-1}

List of Symbols

C_L, C_D, C_Y	Lift/Drag/Sideforce aerodynamic coefficients	
C_l, C_m, C_n	Rolling/Pitching/Yawing aerodynamic coefficients	
f_E	Resultant force in the earth frame acting on the aircraft	N
F_{thr}, L, D, Y	Thrust/Lift/Drag/Sideforce	N
$F_{x_a}, F_{y_a}, F_{z_a}$	Aerodynamic Forces in the body frame	N
g	Gravity	m/s^2
h_E	Angular momentum in the earth frame	kg $\cdot$ m^2/s
I	Inertia Matrix	kg$\cdot$ m^2
L_{EB}	Rotation matrix from the body to earth frame	
L_{BW}	Rotation matrix from the wind to body frame	
$M_{ext} = [L', M, N]^T$	Rolling/Pitching/Yawing moments	N$\cdot$m
m	Aircraft mass	kg
$n_{cg} = [n_x, n_y, n_z]^T$	Load Factor in the body frame	g
$\bar{q}$	Free-stream dynamic pressure	kg/(m$\cdot$s^2)
u, v, w	Groundspeed in the body frame	m/s
V_a	Airspeed in the wind frame	m/s
V_{ab}	Airspeed in the body frame	m/s
$V_W = \left[V_{W_x}, V_{W_y}, V_{W_z}\right]^T$	Wind in the body frame	m/s
W	Aircraft weight	N
W_{app}	Apparent weight of the aircraft	N
X_E, Y_E, Z_E	Aircraft position in the earth frame	m
α	Angle of Attack	°
α_m	AoA required to fly at minimum Thrust	°
β	Sideslip Angle	°
$\delta = [\delta_{ail}, \delta_{ele}, \delta_{rud}]^T$	Deflection of aileron/elevator/rudder	°
$\eta = [\phi, \theta, \psi]^T$	Euler angles (roll, pitch, yaw)	°
γ	Flight Path Angle	°
μ	Thrust specific fuel consumption	kg/(N$\cdot$s)
$\Omega = [p, q, r]^T$	Angular velocities	°/s
ω_d	Damped natural frequency	rad/s
ω_n	Undamped natural frequency	rad/s
ρ	Air density	kg/m^3
σ	Standard deviation	
ζ	Damping ratio of second order systems	

A mis padres . . .
A México, mi tierra natal con amor . . .

Chapter 1

General Introduction

Air traffic is experiencing a sustained growth since the last decades, provoking the saturation of the main air spaces in large areas of many countries. Moreover, air traffic is expected to increase even more in the upcoming years. In 2012, 9.5 million flights and 0.7 billion passengers were processed, but for 2035, 14.4 million flights with 1.4 billion passengers are expected (Eurocontrol, 2016). In general terms, twice of today's flight demand is expected over the next 20 years.

Therefore, it is a fact that current Air Traffic Management (ATM) infrastructure will not be able to support the growing demand unless refinements and enhancements are addressed towards an improved ATM service.

In consequence, research projects such as SESAR JU (Single European Sky ATM Research Joint Undertaking) and Next-Gen (Next Generation Air Transportation System) are in charge of the development and deployment of the necessary items to build the world's future air transportation system.

Among all the objectives encompassed within these projects, two main items seem pertinent:

1. Strategic datalink services for information sharing.

2. Negotiation between Air Traffic Control (ATC) constraints and aircraft preferences in order to ensure an optimal use of airspace, while allowing aircraft to fly their preferred trajectories under the 4D guidance paradigm.

For this research work, the second point is of great interest.

Current Flight Guidance Systems (FGS) for transport aircraft operate in a mode-based logic, where the Flight Management System (FMS) switches different control strategies (modes) to achieve specific control objectives. These control strategies are currently based on linear control theory, using either PID controllers, or State-Feedback linear approaches. However, since wind disturbances remain as one of the main causes of guidance errors, these guidance techniques need to be improved. Therefore, the first objective of this research is to develop a nonlinear control strategy including both guidance and piloting loops, capable of taking into account wind disturbances, such that an enhanced tracking performance is achieved. Furthermore, considering that the approaches used to develop these guidance strategies rely on a numerical inversion of the aircraft model, better knowledge of the aircraft parameters is tough to improve the numerical inversion accuracy, and therefore, lead to a better guidance performance. In this work, the aircraft mass is considered a game-changer in terms of performance, such that a method to estimate this parameter is developed.

In addition to this, worldwide stakeholders are interested in flying their preferred routes. However, current ATC structure seems too rigid to support such action, and the unpredictability of aircraft operations eliminates the possibility of planning an

intended trajectory free of conflicts. In this way, with the view of increasing traffic safety and airspace capacity, the second objective of this manuscript is to provide a trajectory generation device able to better manage air traffic flows while meeting a set of flight profile constraints, which vary in general from flight to flight. The method proposed, should be able to address potential conflict resolution, allow aircraft to fly closer, and display the same functionalities of current flight planing devices.

Since the numerical feasibility of the presented approaches needs to be analyzed, the numerical simulation of a transport aircraft is needed. Thus, an important action of this thesis dissertation arises.

Stated this, the principal objectives of the thesis can be summarized in two items ($\mathcal{O}$.1 and $\mathcal{O}$.2), along with two needed actions ($\mathcal{A}$.1 and $\mathcal{A}$.2):

- $\mathcal{O}$.1 Development of a Trajectory Generation Algorithm valid for 4D Guidance.

- $\mathcal{O}$.2 Development of an Autopilot and a 4D Guidance Strategy for Transport Aircraft.

  $\mathcal{A}$.1 Numerical Simulation of a 6DOF Transport Aircraft.

  $\mathcal{A}$.2 Aircraft Mass Estimation.

In order to better present the efforts and findings towards the principal objectives of this research, the manuscript is organized as follows:

Chapter 2 provides a panoramic vision of the current organization of Air traffic and its evolution towards the Trajectory-Based Operations paradigm, motivated by the expected growth of air traffic in the upcoming years and its related issues. This is crucial to understand the context that drives the contributions tackled in this research. Moreover, fundamental concepts such as the Performed-Based Navigation, Freeflight, and 4D operations are provided, all converging in the frame of SESAR and Next-Gen projects.

Chapter 3 introduces the flight dynamics of transport aircraft using the principal notation and reference frames. The rotational and translational motions are described by a set of nonlinear equations, which are presented in both a complete, and reduced form, taking into account wind contributions. Furthermore, notions of aerodynamics and load factor are given due to its relevance in other chapters. The equations presented throughout the chapter establish the basis of flight analysis, since they represent the behavior of an aircraft during flight.

Chapter 4 describes a numerical simulation of the presented flight dynamics using Matlab, such that any theoretical proposition with regards to the aircraft motion is tested. Considering that many aerodynamic parameters are obtained via machine learning techniques, a background on this subject is presented, along with their particular application in this work.

Chapter 5 formulates a new method to generate trajectories valid for transport aircraft equipped with 4D guidance capabilities. These trajectories are meant to help in the transition from current ATC routes to Business trajectories, fulfilling safety constraints and helping to ease capacity issues and performance of guidance systems. The smoothness and feasibility of the proposed trajectories is analyzed for different scenarios, where current FMS functions of modern aircraft are reproduced

and optimized.

Chapter 6 discusses the relevance of an accurate aircraft mass estimation for airborne and ground systems performance, pointing out the lack of information and possible benefits regarding the knowledge of the aircraft mass. In consequence, a mass estimation method based on fuel consumption models is presented. The approach considered is only analyzed during the climb phase, but its extension to a complete flight is straightforward. The algorithm also enables the computation of initial mass estimates, which increases its accuracy as more data becomes available. In general terms, the aircraft mass estimation is conceived to complete the simulation of a transport aircraft, in order to ease the guidance efforts to follow a desired trajectory, considering that a better knowledge of the aircraft parameters leads to a better guidance performance.

Chapter 7 delivers a sound background on linear and nonlinear systems, as well as linear and nonlinear control techniques. This serves as a basis for the proposition of guidance and autopilot methods. Moreover, the structure and operating principle of flight control systems of modern transport aircraft is covered, where special attention is put on the lateral/vertical guidance modes, since they are encouraged to be substituted by up-to-date approaches.

Chapter 8 presents two autopilots and two 4D guidance methods based on nonlinear control theory. In this manner, having a time-parameterized trajectory to be followed, full 4D trajectory tracking is enabled by the use of any of the guidance algorithms along with any of the autopilots. This automation level is a milestone towards Trajectory-Based Operations. Furthermore, each autopilot controls different piloting variables, such that compatibility issues are addressed. In the same way, each guidance approach use different control inputs, such that compatibility issues with current guidance systems are also avoided. The advantages and drawbacks of each method are pointed out.

Chapter 9 is the final chapter of this research, such that a general conclusion and the potential improvements are provided. This chapter summarizes the efforts developed towards the transition from current organization of air traffic towards the future air transportation system, compliant with the new expectancies of Trajectory-Based Operations.

Chapter 2

General view of Air Traffic Organization

In this Chapter, with the aim of providing a general view of transport aircraft in the aviation world, a general description of the major components for traffic organization are described. Moreover, since air travel is the fastest and one of the safest methods of transport for long distances, a dramatic increase of air traffic is foreseen, such that twice of current flight demand is expected over the next 20 years.

In Section 2.1, the current traffic organization is covered, encompassing relevant enablers and topics regarding Air Traffic Management, Air Traffic Services and Air Traffic Control, Air Traffic Flow and Capacity Management, Airspace Management, Aeronautical meteorology, among others. Then, under the new requirements which are going to be needed to face the air traffic growth expected in the upcoming years, a modern traffic organization based on emerging technologies is provided in Section 2.2. This section covers topics related to Performance-Based Navigation, Global Navigation Satellite Systems, the Freeflight concept, and the SESAR and Next-Gen projects along with Trajectory-Based Operations.

Finally, conclusions of the chapter are given in Section 2.3.

The upgrade of current systems towards new air traffic organizations is being performed gradually. In this manner, a shift from sensor-based to performance-based navigation is expected first, reducing aviation congestion and establishing flexible routes with new procedures. Moreover, safety and accessibility to challenging airports will be improved, increasing airspace capacity and reducing the impact of aircraft noise, working towards the next ATM evolution and reducing dramatically ATC intervention.

Therefore, flight-crews will be eventually expected to ensure aircraft separation, performed without excluding the key role that the expansion of Global Navigation Satellite Systems plays at the enhancement an efficient use of airspace. Hence, air traffic conflicts in the modern air traffic organization will be handled by self-separation on-board systems, and airspace users will be able to freely plan their preferred route from an entry to an exit point of the airspace, using published or unpublished waypoints for their routes. This represents a milestone towards Trajectory-Based Operations and 4D trajectories usage in a defined airspace. Besides, airspace definition will depend on traffic flows demands instead of national borders. In other words, aircraft will be flying their preferred trajectories without being constrained by airspace configurations, implying a shift from fixed routes and ATC clearances to flexible trajectories, while relying on higher levels of on-board automation.

2.1   Current Organization of Air Traffic

The main goal of air navigation is to guide an aircraft from an initial geographic position to a final destination. The use of operational, juridic, and technical frameworks, as well as Air Navigation Service Providers (ANSPs), are pillars to achieve this goal.

Regarding the ANSPs (also known as aids to navigation), they refer to a public or a private legal entity in charge of providing Air Navigation Services to airspace users during all phases of operations.

A non-exhaustive scheme of the current air traffic organization and the principal navigation service providers are:

- Air Navigation Service Providers (ANSPs)

    - Communications, Navigation and Surveillance Systems - Air Traffic Management (CNS-ATM).

        a Air Traffic Services (ATS)
            · Flight Information Service (FIS)
            · Alerting Service
            · Air Traffic Control (ATC)
        b Air Traffic Flow and Capacity Management (ATFCM)
        c Air Space Management (ASM)

    - Aeronautical Meteorology Service for Air Navigation (MET)

    - Aeronautical Information Services/Management (AIS/AIM).

    - Search and Rescue (SAR).

ANSPs can be private organisations, government departments or state companies. An extensive number of the world's ANSPs are members of the Civil Air Navigation Services Organisation (CANSO), located at the airport Amsterdam Schiphol. CANSO supports over 85% of world's air traffic. According to (EC, 2017), the five biggest ANSPs in Europe (DFS for Germany, DSNA for France, ENAIRE for Spain, ENAV for Italy and NATS for the UK), deal with 60% of the European gate-to-gate service provision costs, and handle around 54% of European traffic. The 40% of remaining gate-to-gate costs are taken by 32 other ANSPs.

In the case of France, the General Directorate of Civil Aviation (Direction Générale de l'Aviation Civile, DCAC) governs and supervises the civil aviation activities, while the DSNA (Direction des Services de la Navigation Aérienne), acts as the civil ANSP. The DSNA has three regional centers for overseas territories (Antilles-French Guiana, Indian Ocean and Saint-Pierre-et-Miquelon), five en-route control centers (Brest, Paris, Reims, Aix-en-Provence and Bordeaux), and nine regional approach and control centers (Nantes, Lille, Paris, Strasburg, Lyon, Nice, Marseille, Toulouse and Bordeaux).

One of the main enablers is the International Civil Aviation Organization (ICAO), a specialized agency created in 1947 that reaches consensus and develops international Standards, Recommended Practices and Procedures (SARPs), as well as policies in support of sectors of the air transportation systems such as:

- Safety

- Air Navigation Capacity and Efficiency

- Security

- Air Transport Policy and Regulation

- Environmental Protection

Furthermore, ICAO is committed to provide optimal responses to problems in aviation systems originated by natural disasters or other causes. Moreover, it supports regional security initiatives towards the strengthening of global aviation security. Regarding ICAO's involvement in the environment, limitation or reduction of greenhouse gas emissions and the number of people affected by significant aircraft noise are important. ICAO is in charge of monitoring and report of numerous air transport performance metrics and auditation of States' civil aviation capabilities.

In close relation to ICAO, Eurocontrol is an intergovernmental organisation in charge of building a Single European Sky committed to deliver the required ATM performance of the future.

In this chapter, only the CNS-ATM and MET services are described. However, more information about AIS/AIM and SAR can be found in (*ICAO* July 2010) and (*ICAO* July 2004), respectively.

2.1.1 Air Traffic Management (ATM)

The Communications, Navigation and Surveillance - Air Traffic Management (CNS-ATM) refer to all the procedures, technology and human resources which make possible the safe guidance of aircraft, by respecting separation constraints with respect to other aircraft. Moreover, it refers to the management of aircraft traffic at the airports where they take-off and land, considering the evolving needs of air transit over time. In other words, CNS-ATM encompasses all the systems that enable an aircraft to depart from an airport, transit their respective trajectories, and land at their destination.

Further information about CNS sytems is available on (*ICAO* July 2006).

2.1.1.1 Air Traffic Services (ATS)

According to (*ICAO* July 2001[a]), ATS is a generic term encompassing flight information service, alerting service, air traffic advisory service and air traffic control service. Each item is described briefly based on the Chapter 9 of (*ICAO* July 2016).

- Flight Information Service (FIS):
  It is provided with the aim of giving advice and useful information for the safe and efficient conduct of flights. This service is available to any aircraft within a Flight Information Region (FIR). Some of the data provided are:

  a Meteorological information which may affect the safety of aircraft operations (SIGMET and AIRMET).

  b Volcanic activity (volcanic ash clouds and volcanic eruptions).

  c Release of radioactive materials or toxic chemicals into the atmosphere .

  d Navigation aids availability.

  e Aerodromes and associated facilities condition (state of areas affected by water, ice, or snow).

  f Unmanned free balloons.

  g Collision hazards.

- Alerting service:
  It is provided to notify the concerned organizations of aircraft in need of search and rescue, as well as assistance. This service is given to all aircraft subject to air traffic control, to aircraft that have filed a flight plan, aircraft known to ATS units, and aircraft in threat or subject of illicit interference. This is a 24/7 service provided by competent ATC units.

- Air traffic advisory service:
  It is provided within advisory airspace to ensure separation between aircraft operating on Instrument Flight Rules (IFR) flight plans. Since this service may provide incomplete information about the traffic in the area, the safety degree to replace an air traffic control service is not reached. Thus, it is only implemented temporarily and provides only *advisory information* and not *clearances* when actions are proposed to an aircraft regarding collision avoidance.

- Air traffic control service:
  It is provided in order to maintain safe separation between aircraft in general (in line with (*ICAO* 2016)) and on the aerodrome manoeuvring areas (areas used for take-off, landing and taxiing, excluding aprons[1]) between aircraft and obstructions. Another purpose is to dispatch and maintain an orderly flow of air traffic.
  Air traffic control service is provided to all IFR flights in airspace Classes A, B, C, D and E, to all Visual Flight Rules (VFR) flights in airspace Classes B, C and D, to all special VFR flights, and to all aerodrome traffic at controlled aerodromes. Airspace classes are explained later.
  Clearances issued by ATC units provide separation between all flights in airspace Classes A and B, between IFR flights in airspace Classes C, D and E, between IFR flights and VFR flights in airspace Class C, between IFR flights and special VFR flights, and between special VFR flights when they are issued by the corresponding ATS authority.
  In order to accomplish its purposes, the air traffic control service is divided in three parts:

  a Aerodrome control service.
  Concerned to the provision of air traffic control service for aerodrome traffic.

  b Approach/Terminal control service.
  Concerned to the provision of air traffic control service for those parts of controlled fights associated with arrival or departure.

  c Area control service.
  Concerned to the provision of air traffic control service for controlled flights, except for those parts of arrival, departure, and aerodrome traffic.

2.1.1.1.1　Air Traffic Control (ATC)

ATC is a service which has the objective to provide a safe and expeditious control of air traffic. This service is supplied by ground-based air traffic controllers in charge of guiding an aircraft on the ground and through the sky in controlled airspace. In

---

[1]Areas of an airport intended to accommodate aircraft for loading/unloading of mail or cargo, passengers, fuelling, parking or maintenance.

addition to this, it can address advisory services in non-controlled airspace.

Depending on the type of flight and the class of airspace, ATC may provide instructions that pilots are required to follow. On the other hand, ATC advisories (or flight information) can be neglected at the pilot's discretion. Thus, even if the responsibility for the safe operation of the aircraft is shared between ATC and the pilots, the final authority is the pilot in command, being able to deviate from ATC instructions in an emergency to assure the safe operation of their aircraft.

Concerning the separation between aircraft, mandatory rules are imposed for collision prevention, assuring a minimum empty space around each aircraft at all times. In this manner, when a trajectory is planned for an aircraft, the uncertainty in the computation of future position of the aircraft is expressed in a "Volume of Protection" (VoP) around the estimated position of the aircraft, along with a level of confidence that the aircraft will be within this VoP. Then, if no transgression between VoPs of different aircraft is found in the specified look-ahead time, it is considered that there is no conflict for the planned trajectory (Suchkov, Swierstra, and Nuic, June 2003).

The minimum size of this VoP is a circle of 2.5NM around the aircraft position, and then, due to different longitudinal/lateral errors, an oval-shape bubble representing uncertainties is considered (Suchkov, Swierstra, and Nuic, June 2003). Also, it is often considered that the longitudinal-track uncertainty increases with respect to the look-ahead time.

Current aircraft are equipped with collision avoidance systems that alert the pilots when other aircraft get too close. This is the case of the Traffic Alert and Collision Avoidance Systems (TCAS), which is a specific implementation of the Airborne Collision Avoidance Systems (ACAS) concept developed by ICAO (*ICAO* 2006a). However, not all TCAS systems can be considered as accepted ACAS.

The TCAS II concept, for example, operates such that, when there is a reasonable confidence that minimum separation standard (time-based) might become violated in the near future, pilots are advised with tactical resolutions in order to avoid potential collisions (mid-air collisions and near mid air collisions). This is achieved through Resolution Advisories (RAs), which recommend actions (including manoeuvres), and through Traffic Advisories (TAs), which are intended to prompt visual acquisition and to act as a precursor to RAs.

An RA is generated nominally 15 to 35 seconds before the closest point of approach of the aircraft, and a TA from 48 to 20 seconds in advance of a RA. In Figure 2.1 is shown an example of the TCAS Protection Volume. Note that warning times depend on sensitivity levels of RAs.

Consequently, it can be said that ACAS has been designed to provide a safety-net collision avoidance service for the existing conventional air traffic control systems, while minimizing unwanted alarms in encounters where the collision risk does not need escape manoeuvres. This system is based on Secondary Surveillance Radar (SSR) transponders, where three types of operation modes are available:

- Mode A: Transmission of 4 digit code on request.

- Mode C: Transmission of the standard barometric altitude on request.

- Mode S: Transmission of various parameters upon selective request. Coverage up to 120NM.

Since 1995, all Airbus aircraft are equipped with Mode S transponder, transmitting flight ID, altitude, and mode A code, and since 2001, all IFR aircraft in Europe are required to be equiped with mode S transponder.

ACAS equipment in the aircraft interrogates Mode A/C and Mode S transponders
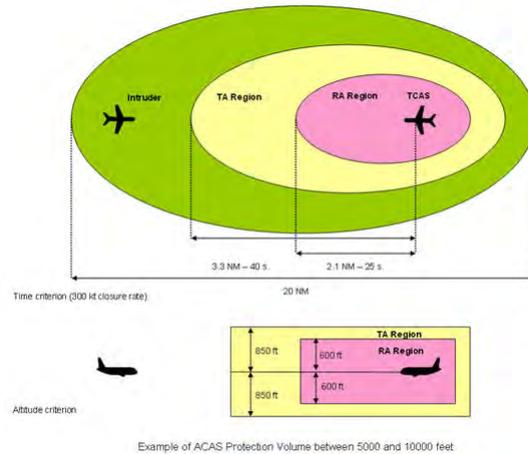
FIGURE 2.1: Example of an TCAS time/altitude Volume of Protection
(Wikipedia, 2017).

on other aircraft in its vicinity and listen for their replies. By processing these replies,
ACAS determines which aircraft represents potential collision threats and provides
appropriate display indications (or advisories) to the flight crew.

Different ACAS levels have been defined: 1. ACAS I, which gives TAs but does not
recommend any manoeuvres. The only implementation of the ACAS I concept is
TCAS I, still valid today on small aircraft; 2. ACAS II, gives TAs and RAs in the
vertical sense. The only implementations fully compliant with the ACAS II concept
are TCAS II Version 7.0 and Version 7.1, mandated on large transport aircraft; 3.
ACAS III, planned to give TAs and RAs in vertical and/or horizontal directions.
This version was abandoned and no SARPs have been issued.

The TCAS II can be operated in the following modes:

- Standby: The system does not issue any interrogations and the transponder
  only replies to discrete interrogations. This mode is used on ground, outside
  the runway.

- Transponder: The transponder replies to all appropriate ground and TCAS
  interrogations. TCAS remains in stand-by. This is a passive mode, considered
  as the minimum mandatory mode to be set by any airborne aircraft.

- Traffic Advisory (TA): TCAS issues the appropriate interrogations and perform
  all tracking functions. In this mode, TCAS will only provide TAs. RAs are
  inhibited.

- Automatic (TA/RA): TCAS provides TAs and RAs when appropriate. This
  mode is mandated according to number of seats for all transport aircraft.

Nevertheless, even if only 1 in 10 TA provided by TCAS II results in a RA, serious
consequences of human error and lack of homogeneity in TCAS have been experi-
enced:

- Germany, July 2002, two transport-category aircraft collided after TCAS in-
  structed one pilot to climb, but the pilot descended in compliance to ATC in-
  structions.

- Japan, January 2001, a Boeing 747 followed the ATC instruction to descend instead of the TCAS RA to climb, intersecting course with a McDonnell Douglas DC-10. The collision was avoided when the 747 was put into a steep descent after visual contact with the other aircraft. About 100 crew and passengers on the B747 sustained injuries due the emergency maneuver.

- Switzerland, June 2011, the crew from a Raytheon 390 followed an ATC descent clearance during their TCAS climb RA, creating a conflict with an Airbus 319. Both aircraft passed in very close proximity (0.6 nm horizontally and 50 feet vertically) without either seeing the other.

- Switzerland, May 2012, an Airbus 320 departing Zurich in a climbing turn received a TCAS RA to climb caused by an AW 139 only equipped with TCAS I, also departing from Zurich. The conflict in Class C airspace was attributed to inappropriate clearance by the TWR controller and inappropriate separation monitoring.

- May 2013, an Airbus 319 in Swiss Class C airspace received a TCAS RA to level off. This was due to a Boeing 737 located above, after being inadvertently given an incorrect climb clearance by ATC.

The standardisation of ADS-B (Automatic Dependent Surveillance – Broadcast), TIS-B (Traffic Information Service - Broadcast), FIS-B (Flight Information Services - Broadcast) messages, and their use on new Airborne Traffic Situational Awareness Applications (ATSAW) (explained in Section 2.2.1), could lead to the replacement of the radar as a primary surveillance method. These broadcasts do not depend on any ground-based systems, but on transponders installed on the aircraft. This is a surveillance technique that relies on aircraft or airport vehicles broadcasting their identity, position, speed, altitude, heading and other information (ADS-B Out) derived from on board systems (e.g. GNSS). The transmitted signal can be captured for surveillance purposes on the ground, or on board other aircraft (ADS-B In) in order to facilitate airborne traffic situational awareness, and self-separation.

The ADS-B is automatic because no external stimulus is needed. Therefore, the emitter has no knowledge of who receives the message due to the lack of interrogation or two-way contract. Also, the ADS-B is dependent because it relies on on-board systems. Moreover, wind estimations based on ADS-B data have been the subject of recent research (Leege, Mulder, and Paassen, 2012), (Leege, Paassen, and Mulder, 2013).

2.1.1.1.2 ATC units

The controlled airspace is divided into three ATC units in order to provide alerting service and flight information service.

- Aerodrome control unit or Tower Control Unit (TWR): This unit controls flights in the vicinity of aerodromes as well as traffic on the runway and taxiway. In other words, it is in charge of the aircraft during landing and take-off phases. Visual contact with traffic is made from the TWR cab (see Fig. 2.2).

- Approach/Terminal Control Unit (APP)
  This unit controls arriving and departing aircaft in the Terminal Manoeuvring Areas (TMAs) and sometimes beyond (see Fig. 2.3). The area of responsibility

(a) TWR outside view.

(b) TWR cab inside view.

FIGURE 2.2: Tower Control Unit (KLM, 2017).

of the APP is larger than that of the TWR. Approach controllers are responsible for sequencing arriving traffic for landing, and for providing separation between departing and arriving aircraft. The main tool of APP controllers is radar. In the United States of America, the APP is referred to as a Terminal Radar Approach Control (TRACON).
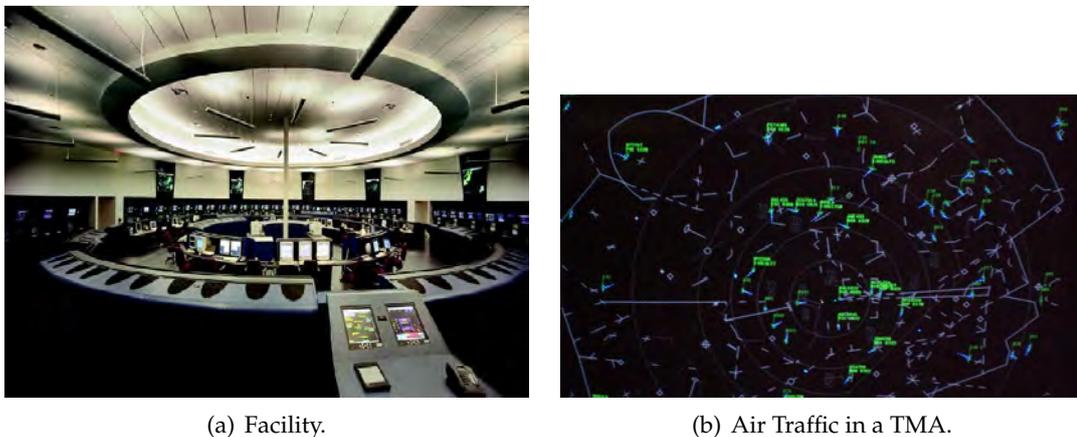
(a) Facility.

(b) Air Traffic in a TMA.

FIGURE 2.3:   Approach/Terminal Control Unit (StackExchange, 2017a).

- Area Control Centre (ACC)
  Defined as a facility responsible for controlling en-route traffic in a defined volume of airspace or FIR at high altitudes between airport approaches and departures. In USA, the ACC is referred to as an Air Route Traffic Control Center (ARTCC).

The APP (or TRACON) unit works between ACC (or ARTCC) and TWR (see Fig. 2.4).

2.1.1.2   Air Traffic Flow and Capacity Management (ATFCM)

According to (*ICAO* July 2001[a]), ATFCM is a service in charge of managing a safe, orderly and expeditious flow of air traffic in order to avoid exceeding airport or air traffic control capacity, but ensuring that the maximum available capacity declared by the appropriate ATS authority is used efficiently. In other words, it aims to meet traffic demand without overflowing airspace and/or aerodrome capacity, and if capacity is exhausted, rejects excess demand to maintain the maximum available capacity.

FIGURE 2.4: Handling of Air Traffic (StackExchange, 2017b).

Since all aircraft using ATC need to file a flight plan and send it to a central repository, air traffic flow and capacity computations are performed before flights. According to (Eurocontrol, 2017a), the ATFCM activities are divided into three phases:

- Strategic Phase (1 year before flight - 1 week before time operations).
  The Network Operations Centre (NMOC), which manages one single flow management system over Europe, helps the ANSPs to predict the capacity demand for each ATC center. Then, a routing scheme is prepared such that capacity is maximized and air traffic is balanced. A Network Operations Plan (NOP) is issued.

- Pre-tactical Phase (6 days before time operations).
  The NMOC provides a daily plan optimising the ATM network performance by minimising delays and costs. This plan is the result of Collaborative Decision Making (CDM) processes, designed to ensure that affected stakeholders, service providers, and airspace users, can discuss capacity demands, flight efficiency issues, and formulate plans considering all pertinent aspects. The output of this phase is an ATFCM daily plan (ADP), which can anticipate capacity shortfalls for certain ACCs/airports due to specific events such as large-scale military exercises, sporting events, holidays, etc.

- Tactical Phase (the day of operations).
  The tactical phase consists of the monitoring and update of the Daily Plan made the day before, continuing to optimise capacity in order to minimise delays. Also, the flights of that day receive an individual departure time (slots). According to (Eurocontrol, 2017b), in order to avoid too many aircraft in the air at the same time and place, the NMOC calculates take-off times (CTOTs), also known as slots. One slot is a period of time within which take-off has to take place (in Europe, 5 minutes before and 10 minutes after the CTOT). If, for some reason a slot is missed, the NMOC assigns a new one. Also, slot improvements can be made to make use of the newly available capacity.

Both ATC sectors and airports have finite capacities and both are highly computerized for its regulation.
Regarding airports, only one aircraft can land or take-off from a given runway at one moment. In this manner, due to minimum separation distance or time to avoid collisions between planes, hourly capacities and aircraft delay computation are needed to evaluate the airport performance. Moreover, airport capacity varies throughout the day since it depends on several factors such as the number of runways, availability of ATC, layout of taxiways, weather, etc. In (*FAA* September 1983), computation

of airport capacity and aircraft delay for airport planning and design is stated, defining properly the capacity as a measure of the maximum number of aircraft operations which can be accommodated on the airport or airport component in one hour. On the other hand, capacity in an ATC sector is determined by the number of air traffic controllers and complexity of the airspace under their control, such that one aircraft may be subject to many restrictions such as changing routes instead of late departure, so no overflow of capacity in the departing airport, nor in the airspace sector is ensured. Nevertheless, time-critical flights (e.g. flights carrying human organs for organ transplantation) are exempted from such restrictions.

Detailed information about the procedures and roles of the involved participants in the ATFCM can be found in (*Eurocontrol* 2017g).

2.1.1.3 Air Space Management (ASM)

An airspace is defined as a portion of the atmosphere controlled by a country above its territory, including its territorial waters. Then, a controlled airspace is an airspace where air traffic control service is provided in accordance with the airspace classification.

In Table 2.1, the airspace classification is described according to the Chapter 2, Appendix 4 of (*ICAO* July 2001[a]). It is important to note that ICAO is a regulatory body and not a direct ATC service. Thus, international air traffic control is delegated to those nations who accept the responsibility for providing ATC services.

The airspace classification assigns letters to each class. Classes from A to E are considered as controlled airspace by an ACC, and F and G are uncontrolled airspace. However, since each national aviation authority determines how it uses the ICAO classifications in its airspace design, the rules in some countries are modified so that they can fit the airspace rules and air traffic services that existed before the ICAO standardisation. For example, class F is designed as an special airspace depending on the country or region, which may not be always available.

Figure 2.5 depicts these airspace classes at different altitudes Above Ground Level (AGL).

In terms of normativity, (*ICAO* July 2005) is the guiding document when flying in
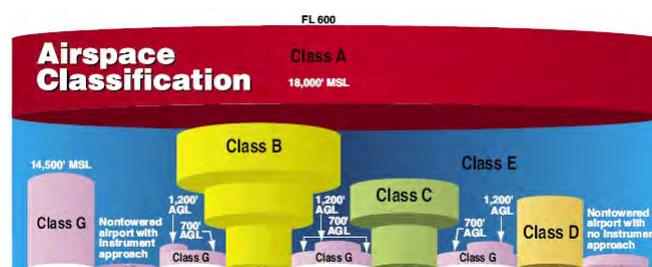
FIGURE 2.5: Classification of Airspace (FAA, 2017).

international airspace.

In order to identify which country controls which airspace and determines which procedures needs to be used, ICAO divided the airspace of the world into Flight Information Regions (FIRs), where one major ATC authority is identified with each FIR.

The FIRs may be subdivided into smaller Areas which can comprise from two to nine sectors. Each Area has enough controllers trained on all sectors in that Area.

In sectors, they use distinct radio frequencies for communication with aircraft, and

TABLE 2.1: Airspace Classification

Class	Type of flight	Separation provided	Service provided	Speed limitation[a]	Radio communication requirement	Subject to ATC clearance
A	IFR only	All aircraft	ATC service	N/A	Continuous two-way	Yes
B	IFR	All aircraft	ATC service	N/A	Continuous two-way	Yes
	VFR	All aircraft	ATC service	N/A	Continuous two-way	Yes
C	IFR	IFR from IFR IFR from VFR	ATC service	N/A	Continuous two-way	Yes
	VFR	VFR from IFR	1. ATC service for separation from IFR. 2. VFR/VFR traffic information (and traffic avoidance advice on request)	Yes	Continuous two-way	Yes
D	IFR	IFR from IFR	ATC service, traffic information about VFR flights (and traffic avoidance advice on request)	Yes	Continuous two-way	Yes
	VFR	Nil	IFR/VFR and VFR/VFR traffic information (and traffic avoidance advice on request)	Yes	Continuous two-way	Yes
E	IFR	IFR from IFR	ATC service and, as far as practical, traffic information about VFR flight	Yes	Continuous two-way	Yes
	VFR	Nil	Traffic information as far as practical	Yes	No	No
F	IFR	IFR from IFR as far as practical	Ait traffic advisory service; Flight information service	Yes	Continuous two-way	No
	VFR	Nil	Flight information service	Yes	No	No
G	IFR	Nil	Flight information service	Yes	Continuous two-way	No
	VFR	Nil	Flight information service	Yes	No	No

[a]250knot IAS below 10,000ft AMSL (or FL100 when height of the transition altitude is lower).

each sector has a secure landline communication with adjacent sectors, approach controls, areas, ACCs, flight service centers, and military aviation control facilities. These landline communications are shared among all sectors that need them and are available on a first-come / first-served basis. Aircraft passing from one sector to another are handed off and requested to change frequencies to contact the next sector controller.

Concerning the sector boundaries, these are specified by aeronautical charts. The usage of aeronautical charts allow pilots to know their location, topographic features, hazards and obstructions, navigation aids, navigation routes, landing areas, and other information such as radio frequencies and airspace boundaries.

Moreover, specific types of charts are used depending on the phases of a flight. According to (*ICAO* July 2001[b]), a rough and non extensive classification of chart types is:

- World aeronautical

- Airport

- Terrain

- En-route

- Area/Sectional

- Standard Instrument Departure (SID)

- Standard Terminal Arrival Routes (STARS)

- Visual Approach

Examples of the aeronautical charts corresponding to the Toulouse area are shown in Figure 2.6. The charts used for IFR flights contain all relevant information about locations of waypoints, or fixes. This is due to the lack of visual reference to the ground, and therefore the need of pilots to rely on internal (GPS) or external (VOR) navigation aids. Moreover, the Victor airways defined as straight-line segments can be appreciated in the figure.

Special Areas of Operations (SAOs) can also be included in the aeronautical charts, defined as permanent or temporary designated airspaces in which certain activities are confined, or areas where limitations are imposed to aircraft which are not part of those activities. These SAOs consist usually of:

- Prohibited areas (e.g. location of the White House)

- Military Operation Areas (MOAs)

- Military Training Route (MTR)

- Restricted areas (artillery firing, aerial gunnery, or guided missiles)

- Parachute jump aircraft operations

- Warning areas

- Alert areas

The traffic organization within airspaces can be split into en-route/oceanic and airport/TMA.

Concerning the en-route/oceanic airspaces, aircraft are expected to fly through the center line of airways or in a direct course between navaids. Each airway is based on a straight line at a certain Flight Level between fixed geographic coordinates of satellite navigation systems (GNSS), between two navigational aids (navaids), or at the intersection of two navaids. Commonly used navaids are the Very High Frequency (VHF) Omnidirectional Range (VOR) stations, Non Directional Beacons (NDBs) and Distance Measuring Equipment (DME). Airways possess a limited width used to define the permitted navigation errors for each airway.

On the other hand, en-route flights controlled by the ACCs, or arriving and departing traffic in the TMAs, need to ensure a minimum separation distance between aircraft. According to the Chapter 5 of (*ICAO* July 2016), this separation distance varies depending on the use of navaids, flight level, flight phase, etc.
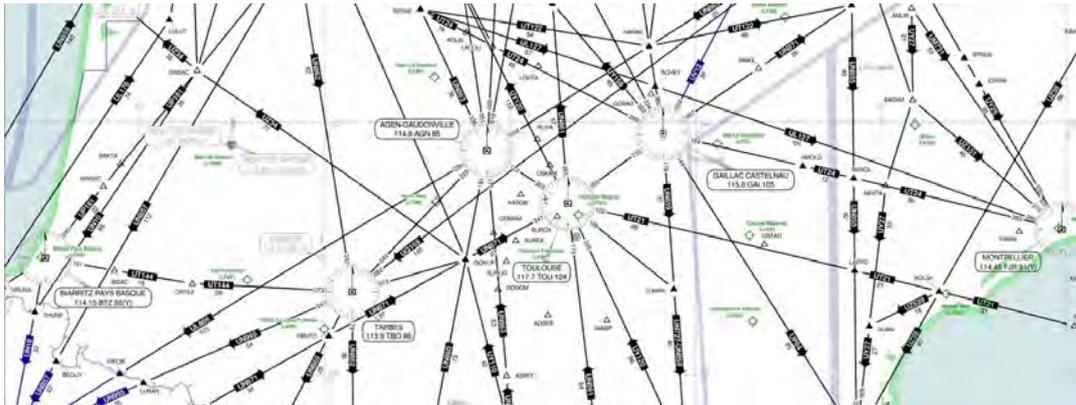
(a) High-altitude IFR en-route chart.

(b) Low-altitude IFR en-route chart.

(c) Sectional VFR chart for low levels.

FIGURE 2.6: Aeronautical charts (SkyVector, 2017).

2.1.2 Aeronautical Meteorology

A forecast is defined as the expected meteorological conditions for a specified area within a period of time. The organizations providing global weather forecasts are the European Centre for Medium-Range Weather Forecasts (ECMWF) (ECMWF, 2017) and the USA National Center for Environmental Prediction (NCEP) (NOAA, 2017). The ECMWF's forecasts cover time frames ranging from medium-range, to monthly and seasonal, and up to a year ahead. The predictions describe the range of possible scenarios and their likelihood of occurrence using their own atmospheric model and data assimilation system, the Integrated Forecast System (IFS).

In parallel, the NCEP delivers weather, water, climate and space weather guidance, forecasts, warnings and analyses to its partners and external user communities. The NCEP is divided in nine centers: Climate Prediction, Environmental Modeling, National Hurricane, NCEP Central Operations, Ocean Prediction, Space Weather Prediction, Storm Prediction, Weather Prediction, and the most relevant to this work, the Aviation Weather Center (AWC, 2017), which delivers consistent, timely and accurate weather information like aviation warnings and forecasts of hazardous flight conditions at all levels for the world airspace system. The model used for the NCEP is the Global Forecast System (GFS).

According to Eurocontrol (Eurocontrol, 2017e), the meteorological service is provided unlike any other within ATM systems. This is due to the division of responsibilities. Either a member state can provide MET services as an element in a portfolio of weather services, or it can have a service dedicated only to aviation meteorology. Thus, the MET service provider may be the meteorological service of a member state, a part of the national ANSP, military services, or a commercial provider of weather services.

In the international field, the World Meteorological Organisation (WMO) is responsible to meet the operational requirements stated by ICAO in (*ICAO* July 2007), which is the annex describing the meteorological services that shall be provided by all designated MET providers around the globe.

Common information given by MET providers are the METAR/TAF, SIGMET and AIRMET. The METAR (METeorological Airport Report) is an observation report (not a forecast) containing data such as temperature, dew point, wind direction and speed, precipitation, cloud cover and heights, visibility, and barometric pressure. It can also include precipitation amounts, lightning, Runway Visual Range (RVR) and other information.

The complement to METARs are called TAF (Terminal Aerodrome Forecast), and they report forecasted weather rather than current weather.

The SIGMET (SIGnificant METeorologic information), advises of weather that is potentially hazardous to all aircraft: Severe Icing, Extreme Turbulence, Dust storms, low visibility to less than three miles and Volcanic Ash.

Concerning AIRMET (AIRmen's METeorological information), they advise of potentially hazardous weather that does not meet SIGMET criteria, for example:

- IFR or Mountain Obscuration

    a Visibility less than three miles affecting more than 50% of the given area.

    b Extensive mountain obscuration.

- Turbulence

    a Continuous surface winds greater than 30 knots at the surface.

    b Moderate Turbulence.

- Icing

    a Freezing levels

    b Moderate icing

In Figure 2.7, weather stations and SIGMET areas in Europe, as well as AIRMET areas in USA are shown.
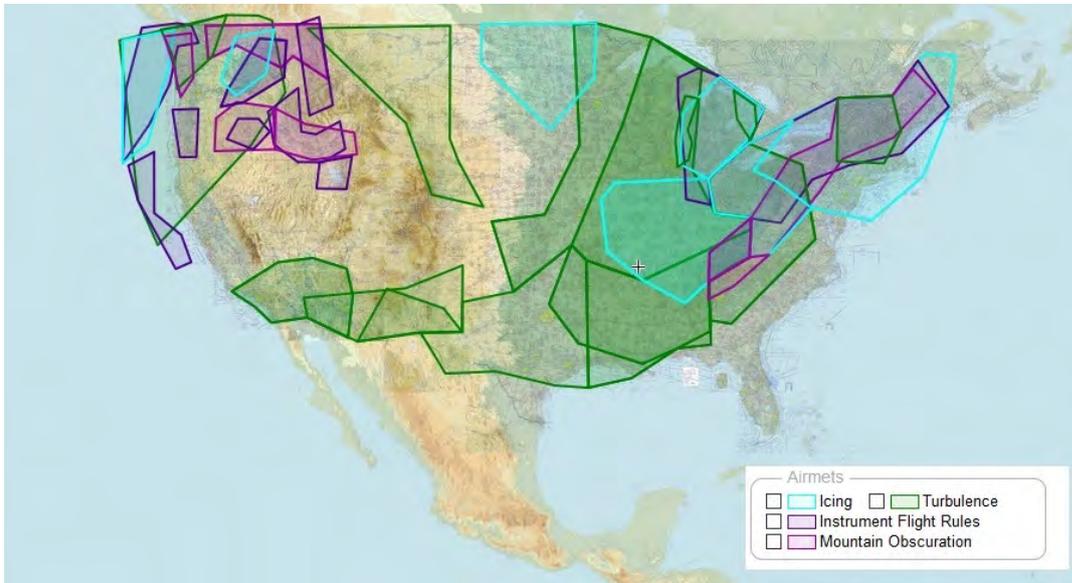
(a) AIRMETS in the US. 12 Dec 2017, 13hrs UTC
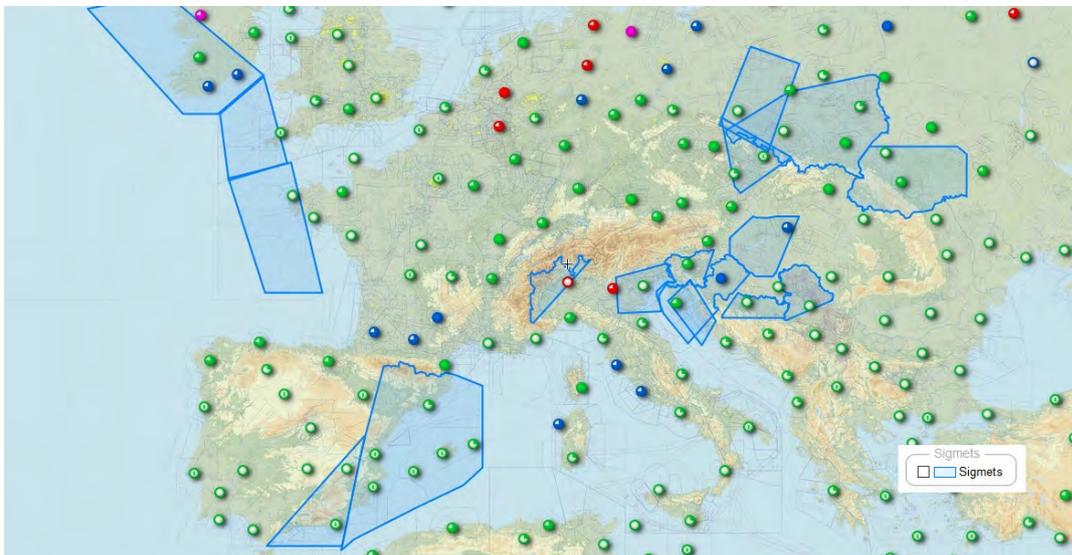
(b) SIGMETS and weather stations in Europe. 12 Dec 2017, 13hrs UTC

FIGURE 2.7: Common MET information (SkyVector, 2017).

2.2 Modern Air Traffic Organization

The expected growth of air traffic in the upcoming years has led to the need of airspace optimization. An approach to this optimization is through the improvement of Area Navigation (RNAV) systems, such that flight crew and air traffic controllers need to know the on-board RNAV system performance capabilities of each aircraft to determine if they fit into the new airspace requirements.

RNAV is a method of navigation that allows aircraft to fly on a desired path within the coverage of ground navaids, and/or within the capability limits of self-contained aids. This navigation system may involve VORs and DMEs (Distance Measurement Equipments), INS/IRU (Inertial Navigation System / Inertial Reference Unit), or satellite systems (GNSS positioning) to determine the position of aircraft.

However, since area navigation is based on the performance of available equipment, an alternative concept was introduced by ICAO in 2008, the Performance-Based Navigation (PBN). PBN is based on the specification of performance requirements for aircraft navigating on an ATS route, on a terminal or approach procedure (*ICAO 2008*). In other words, a shift from sensor-based to performance-based navigation is carried on.

The Performance-Based Navigation concept identifies 3 main components to respond to airspace requirements:

- Navigation Application: It refers to the application of the NAVAID infrastructure with its associated Navigation Specification in ATS routes and instrument flight procedures for an airspace concept. Considering an airspace concept as a general plan (in terms of safety, capacity, efficiency, environment and access objectives) for a particular airspace.

- NAVAID infrastructure: It refers to the ground (VOR and DME) and space (GNSS) navaids. The use of NDBs is excluded from PBN.

- Navigation Specification: It is a set of aircraft and air-crew requirements needed to support a navigation application within a defined airspace concept. There are two navigation specifications, the Area Navigation (RNAV) and the Required Navigation Performance (RNP). The RNP specification requires on-board performance monitoring and alerting, and RNAV does not. Then, an RNAV system with an on-board performance monitoring and alerting capability, capable of achieving the performance requirement of RNP specifications, it is referred to it as a RNP system.

As stated before, modern aircraft equipped with RNAV capabilities allow aircraft to fly a chosen route within the navaids coverage, rather than flying from one navaid to another, like conventional navigation systems. However, the use of RNP systems allows to monitor the navigation performance that is being achieved while informing the crew about it. This on-board monitoring and alerting enhances the pilot's situational awareness, such that closer spacing from aircraft to aircraft without ATC intervention and reduced distances for obstacle clearance are achieved.

The constraints associated to conventional, ground-based sensor specific routes / procedures, and the flexibility and benefits of performance-based, non-sensor specific navigation, are shown in Figure 2.8.

Each RNP and RNAV specification is designated in the form of RNP-X/RNAV-X, where X denotes the lateral navigation accuracy in nautical miles. This means that an aircraft following the specification must have the capability of remaining within X nautical miles to the right or left side of the centerline with an accuracy of at least

Conventional Routes   RNAV Routes   RNP Routes

Navaids   Waypoints   Curved Paths

Limited flexibility   Increased airspace efficiency   Highly optimized use of airspace

Possible flight plan - Aircraft must stay within this limits
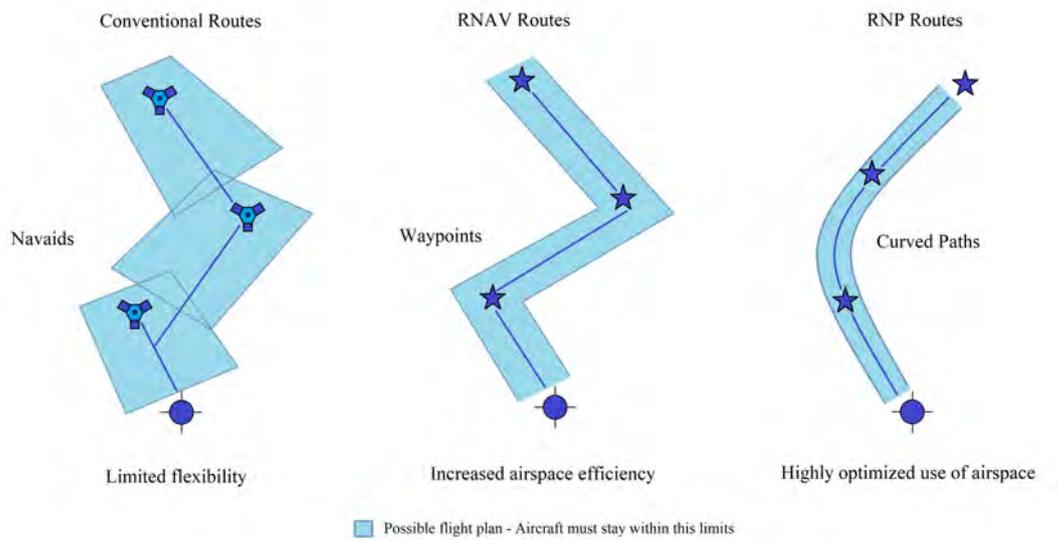
FIGURE 2.8: Comparison between Conventional, RNAV, and RNP
routes.

the 95% (within 2σ in a normal distribution) of the flight time. The performance of
RNP systems is quantified by the Total System Error (TSE), which is given by

$$TSE = \sqrt{NSE^2 + FTE^2 + PDE^2} \tag{2.1}$$

where the Path Definition Error (PDE), Navigation System Error (NSE), and the
Flight Technical Error (FTE), can be seen in Figure 2.9.

In terms of integrity, the probability that the TSE of each aircraft operating in RNP
stays within the specified cross-track containment limit (expressed by $\pm$2xRNP) shall
be at least the 99.999% (within 4.4σ in a normal distribution) per flight hour for RNP,
and 99.99999% (5.3σ) for RNP AR (RNP Authorization Required) (*ICAO* 2008).

The navigation specifications for different flight phases is given by the tree in Fig-
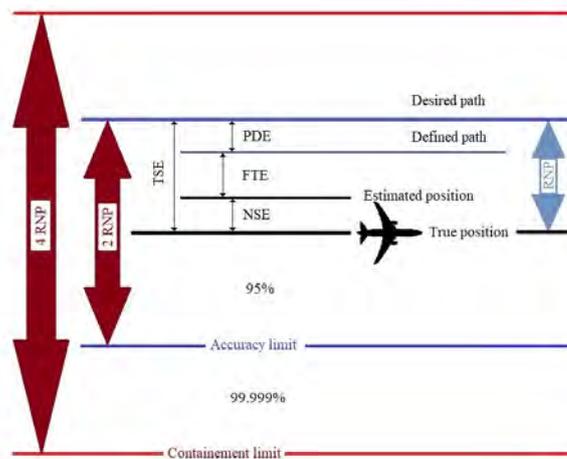
FIGURE 2.9: Error definition in RNP.

ure 2.10. For arrival and departure trajectories on an aerodrome, RNP 1 or RNAV
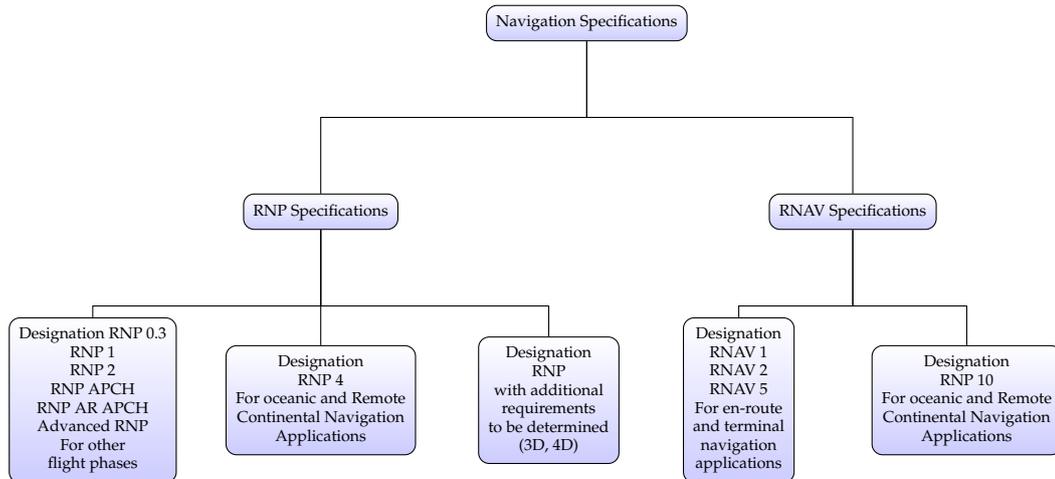
FIGURE 2.10: Navigation specifications for different flight phases.

1 or 2 is planned according to traffic density, radar equipment and communication resources, but the approach operations are divided in two specifications, the RNP APCH and RNP AR APCH. According to (*ICAO* 2009), the RNP APCH is intended for general RNP requirements without operational authorization (up to RNP 0.3), and the RNP AR APCH demands a higher level of navigation performance (from RNP 0.3 to RNP 0.1) in order to overcome issues of airport access in obstacle-rich environments, facilitating ATM evolution. RNP AR APCH approach requires operational authorization from the state regulatory authority.

In the same way, it is important to include the key role that the expansion of Global Navigation Satellite Systems (GNSS) such as GPS (USA), BeiDou (China), Galileo (Europe), and Glonass (Russia), plays at the enhancement of the diversity of RNP and RNAV systems, as well as allowing an efficient use of airspace (route placement, fuel efficiency and noise abatement).

According to (GSA, 2017), the performance of European GNSS is assessed by:

- Accuracy: Difference between the measured and real position, speed or time of the receiver.

- Integrity: Capacity to provide confidence thresholds and alarms during anomalies in the positioning data.

- Continuity: Navigation system's ability to function uninterruptedly.

- Availability: Time percentage where the signal is accurate, integral and continuous.

Furthermore, current expansions of GNSS can be categorized as:

- Satellite-Based Augmentation Systems (SBAS): Errors from GNSS are corrected in ground stations. Then, correction/information messages are broadcasted using geostationary satellites to final users (aircraft), covering large areas and improving performance of regular GNSS.

    - Wide Area Augmentation System (WAAS) for North America.

- – Multi-functional Transport Satellite (MTSAT) and Multi-functional Satellite-based Augmentation System (MSAS) from Japan.
  - – European Geostationary Navigation Overlay Service (EGNOS) from Europe.
  - – Global Positioning System (GPS) and Geostationary Earth Orbit (GEO) Augmented Navigation (GAGAN) from India.
  - – Systems under development:
    * System of Differential Correction and Monitoring (SDCM) from Russia
    * Beidou SBAS from China
    * KASS from South Korea
    * SBAS ASECNA from 17 African states

- Ground Based Augmentation Systems (GBAS): They provide augmentation to regular GNSS constellations at airport level, enhancing approach, landing, departure and surface operations. Position errors below $1\mathrm{m}$ (1σ) in both horizontal and vertical axis are achieved. These systems broadcast correction messages using VHF radio datalink from ground transmitters, as an evolution of ILS (Instrument Landing System) and MLS (Microwave Landing System). In terms of landing performance[2], primary GNSS with SBAS augmentation are limited to CAT I approaches. On the other hand, GBAS allows CAT I, II and III approaches. Global standards for GBAS CAT III validation were agreed in 2010 and are expected to be ready in the 2015-17 timeframe.

- Aircraft Based Augmentation System (ABAS): They augment and/or integrate information obtained from other GNSS elements with available on-board information.

In France, a schedule for the implementation of PBN operations is developed in (*DGAC* March 2012), where short, medium and long term goals are established.
The short term goals (2012/2014) involve the following milestones: RNP 4 or RNAV10 for oceanic operations and RNAV 5 for continental; Gradual implementations of RNAV 1 for terminal operations; Gradual implementations of RNP APCH[3] (foreseeing to RNP AR APCH) for approach operations.

---

[2]Instrument approach operations are classified based on a designed lower operating minima. Below this minima, an approach operation shall only be continued with the required visual reference as follows:

- – Type A: A minimum descent height or decision height at or above $75\mathrm{m}$ (250ft).
- – Type B: A decision height below $75\mathrm{m}$. Type B approaches are categorize as:
  * CAT I: A decision height not lower than 60m and with either a visibility not less than 800m or a RVR not less than 550m.
  * CAT II: A decision height lower than 60m but no lower than 30m and RVR not less than 300m.
  * CAT IIIA: A decision height lower than 30m or no decision height and RVR not less than 175m.
  * CAT IIIB: A decision height lower than 15m or no no decision height and RVR less than 175m but not less than 50m.
  * CAT IIIC:no decision height and no runway visual range limitations.

  CAT II and III instrument approach operations shall not be authorized unless RVR information is provided.

[3]The RNP APCH, also called RNAV (GNSS), is associated to 4 type of approaches:

As medium term goals (2015/2019), the widescale deployment of RNAV1 for terminal operations, and the widescale deployment of RNP APCH and RNP AR APCH for approach operations is planned, along with the initiation of advanced RNP.

Finally, the long term objectives planned for the 2020 and after are: RNP 2 specification for continental en-route operations and RNP 0.3 applicable to departure, en-route, and approach operations (developed mainly for helicopter operations); Definition of the Advanced RNP specification, whose objective is to enable various requirements (variable navigation details, capacity to make fixed radius turns, 4D management) for en-route, arrival, departure and approach requirements under a single navigation specification; Introduction of new functionalities for RNP specifications such as fixed radius turns (RF or Radius to Fix) in Terminal Areas, and FRT (Fixed Radius Transition) for the en-route phase.

Currently, the French territory has RNAV 1 trajectories (PRNAV in Europe) available in more than 75% of terminal zones of the DSNA.

The expected benefits of the PBN concept through the navigation application are to provide flexible routes and terminal procedures, reduce aviation congestion, conserve fuel, reduce the impact of aircraft noise, improve safety and accessibility to challenging airports, and increase airspace capacity, all of this while reducing or avoiding sensor-specific operations, routes and procedures and their associated costs. Moreover, the use of RNAV and RNP systems is clarified, such that the need of tactical ATC intervention is reduced dramatically, as the aircraft-to-aircraft separation is within the airspace design (*Eurocontrol* January 2013).

All these benefits pointed out converge into the Freeflight concept, where the flight-crew is supposed to assure the separation from all known aircraft in accordance with applicable airborne separation minima.

2.2.1   Freeflight

After the establishment of a Committee regarding the Future Air Navigation Systems (FANS) in the early nineties, a new ATC method with no centralized control was proposed. This proposal, known as Freeflight, aimed to reduce the human factor dependance, transferring more responsabilities to the growing technology, such that computers will ensure the required separation between aircraft.

The main objective of the Freeflight concept is to allow aircraft flying under IFR to follow their optimal route, while moving the responsibility of self-separation to the flight-crew, such that new procedures and rules of the air will be necessary, and ground ATM components will be assigned a different role.

This infers that the Freeflight concept requires a very high performance of aircraft navigation systems in order to achieve a required level of safety, back-up procedures might be necessary for noncompliance scenarios.

- Non Precision Approach (NPA) with LNAV (Lateral Navigation) minima: Lateral guidance based on ABAS reinforced GNSS signal is provided for final approach.

- Non Precision Approach (NPA) with LP (Localiser Performance) minima: Lateral guidance based on SBAS reinforced GNSS signal is provided for final approach.

- Approach with vertical guidance of barometric type in final (APV Baro-VNAV) with LNAV/VNAV minima: Lateral guidance based on ABAS reinforced GNSS signal.

- Approach with SBAS type vertical guidance in final (APV SBAS) with LPV (Localiser Performance with Vertical guidance) minima: Lateral guidance based on SBAS reinforced GNSS signal.

By the end of 2016, the DGAC expects to publish RNAV(GNSS) approaches over all controlled IFR aerodrome runway ends, including a certain number with vertical guidance (APV SBAS or APV Baro-VNAV).

Concerning modern systems in charge of providing flight information of surrounding traffic, and enabling the flight-crew to maintain separation of their aircraft from one or more aircraft, ACAS versions like TCAS III and IV were abandoned. In spite of the fact that these versions were capable to give Vertical and/or Horizontal direction as RAs, TCAS in its current form is not compatible with new operational concepts where spacing between aircraft is reduced, since superior technology has made TCAS approaches obsolete. Thus, the Airborne Separation Assistance System (ASAS) was proposed instead. The different ASAS application categories are:

- Airborne Traffic Situational AWareness applications (ATSAW): They only help the pilot to understand surrounding traffic.

- Airborne SPAcing applications (ASPA): Air Traffic Controllers are responsible of separation between aircraft while demanding pilots to perform tasks to ensure separation.

- Airborne SEParation applications (ASEP): Air Traffic Controller gives the separation responsibility to the pilot for a limited time and only to one aircraft.

- Airborne Own-separation applications (AO): All pilots are responsible of their own separation with respect to other aircraft. Air Traffic Controllers have no responsibility, and indeed, they are not required. This is a highest autonomous level, corresponding to the Freeflight concept.

Therefore, the suggested strategy to avoid traffic conflicts in the modern air traffic organization is to maintain the self-separation trough the ASAS systems, and if needed, ACAS systems would provide a last-minute alert. In other words, the ASAS assumes the responsibility of maintaining separation but the ACAS will remain as the final conflict resolution resource.

In this way, aircraft would operate with more and more autonomy when changing from one airspace to another, flying closer and assuring a safe distance with respect to other aircraft, provoking an enhancement of airspace capacity, safety and flexibility of air routes. It must be considered that the evolution from current controlled airspace to the airspaces where airborne self-separation is implemented will be gradually, hereby, special attention to transition areas is required. The expected evolution of ATM after the Freeflight implementation in low density areas is focused in the dynamic use of airspace, and then, in the implementation of the Freeflight concept in all domains.

Currently, the Free Flight concept is implemented at Europe as a Free Route Airspace (FRA), where according to (Eurocontrol, 2017h), is a defined airspace where users can freely plan a route from an entry to an exit point of the airspace, using published or unpublished waypoints for their routes (with no relation to ATS route networks). These routes are subjected to availability, and flights are subjected to air traffic control. Besides, it is stated that flying distances caused by moving from routes to free airspace can be reduced by 7.5 million NM, equivalent to 45,000 tons of fuel saved, or 37 million euros. Moreover, a FRA environment provides more stable trajectories and enhancement of conflict detection tools usage.

Since the free routing across the European airspace represents a milestone on the road to SESAR business trajectories and 4D profiles, a major part of the European airspace is expected to have implemented FRA by the end of 2019 as a result of cooperation between the ANSPs, airspace users, network managers, and military partners. In Figure 2.11 is shown the planned implementation of FRA in Europe, from a start in the summer of 2017 up to 2021/2022.

(a) Free Flight implementation in 2017.

(b) Free Flight implementation at the end of 2021.

FIGURE 2.11: Free Flight implementation (Eurocontrol, 2017i).

2.2.2 SESAR and NextGen

According to (Eurocontrol, 2016), in 2012, 9.5 million flight were processed (0.7 billion passengers), and for 2035, 14.4 million flights with 1.4 billion passengers are expected. Furthermore, according to (Eurocontrol, 2017j), ATM in Europe handles around 26,000 flights daily, and by 2020, the traffic is expected to be doubled. In addition to this, the operating costs of ATM are rising at 2-3 billion euros per year. Therefore, the issue of improving the ATM performance while reducing operative costs needs to be addressed.

When this dramatic air traffic growth was detected, two projects were launched, one by the U.S.A., and the other by the European Comission.

In 2003, the Joint Planning and Development Office (JPDO) was established in order to provide a vision of the future U.S.A. air transportation system. The result was the Integrated National Plan for the Next Generation Air Transportation System (better known as Next-Gen) in 2004, which defined the needed objectives and requirements to improve the air transportation system (FAA, 2016). This project involves several government agencies such as the FAA, NASA, Department of Defense, National Weather Service, and the Transportation Security Administration, which released in 2007 the Next-Gen Concept of Operations, providing an overview of the project goals for 2025.

On the european side, a solution was launched by the European Commission in 1999, under the idea to organize the airspace considering traffic flows instead of national borders (FAB - Functional Airspace Block), giving birth to the Single European Sky (SES).

The current proposal of 9 FABs for the optimization of the European airspace is given by (Eurocontrol, 2017k) as:

- FAB Europe Central (FABEC): France, Germany, Belgium, Netherlands, Luxembourg and Switzerland (55% of flights through Europe pass over this airspace).

- FAB Central Europe (FABCE): Czech Republic, Slovak Republic, Austria, Hungary, Croatia, Slovenia, Bosnia and Herzegovina;

- North European FAB (NEFAB): Estonia, Finland, Latvia and Norway.

- South West FAB (SW FAB): Portugal and Spain.

- Baltic FAB: Poland and Lithuania.

- Danube FAB: Bulgaria and Romania;

- Denmark-Sweden FAB.

- UK- Ireland FAB.

- Blue Med FAB: Italy, Malta, Greece, Cyprus, as well as Egypt, Tunisia, Albania and Jordan as observers;

The primary goal of the SES was to provide the legislative framework required to cope with the capacity, environmental impact, and safety needs of future air traffic, foreseeing the improvement of current systems in the mentioned areas.

Regarding the technological side of the SES, the Single European Sky ATM Research (SESAR) project was launched in 2004, in charge of the development and deploy of the necessary items to build the Europe's future air transportation system. Three years later, a private-public partnership in the research and development sector of

ATM was founded by the European Union and Eurocontrol, named SESAR Joint Undertaking (SESAR JU), encompassing 19 members representing over 100 companies working towards the innovation of the ATM community.

Some updated goals to be achieved by SESAR JU in the middle term (2009-2016) were to start the improvements concerning Continuous Descents and Climbs, taxiing, and CDM processes, and by the 2020 and further, depending on the availability of on-board equipment in aircraft, to introduce an optimized management of 4D trajectories (3D+T), autonomous self-separation of aircraft, and consequently, the redistribution of pilots/air traffic controllers/ machines roles. Yielding to a more efficient air traffic management and reductions of CO2 emiisions (SESAR, 2017).

These objectives are based on the Trajectory-Based Operations, which relies on the provision of air navigation services (ANS) for business trajectories, and consists of several ATM functions such as demand and capacity balancing, flexible use of airspace, solution to air traffic conflicts, and tactical separation of aircraft, just to mention a few. In other words, the TBO concept allows aircraft to fly their preferred trajectories without being constraint by airspace configurations.

According to (ICAO, March 2014), a Business Trajectory is the preferred (optimal) profile for a flight determined by the aircraft operator. This trajectory is defined in a three dimensional flight profile with timestamps in specific points (4D), such that ATM constraints are meet. Prior to departure, a Shared Business Trajectory (SBT) is submitted to ATM, and if agreed, it will become the Reference Business Trajectory (RBT). This RBT is updated and shared as required during the flight with every new manoeuver resulting from the trajectory management loop between all ATM stakeholders. In other words, ideal TBO operates gate-to-gate using 4D trajectories for manage and control of airborne/ground operations. However, in (ICAO, July 2014), a not so radical 4D end-to-end trajectory is suggested, assuring that this would create a rigid non in-flight optimizable structure, incapable to respond to unpredictable elements such as capacity or weather. Alternatively, it is suggested the definition of "how to" and "how much" to optimize a trajectory depending on the type of constraint.

In the same tenor, since 4D trajectories are negotiated and updated between flight crews and ATC, a shift from fixed routes and ATC clearances to flexible trajectories is inherent. Thus, higher levels of onboard automation are mandatory, while the lack of detailed aircraft parameters (usually known only on-board) become a reason for the SESAR TBO concept to support the use of ADS-C EPP (Extended Projected Profile). This is an improved version of ADS-C messages[4]. The EPP extends the trajectory prediction beyond ANSP boundaries by reflecting the future trajectory predicted by the FMS. Also, the EPP confirms that the aircraft's FMS is consistent with any issued lateral or vertical constraints and/or target time. In this manner, one reference trajectory and the corresponding flight information is shared between all ATM actors. More information regarding the sharing of trajectory predictions and time adherence in TBO, is available in (ICAO, October 2014[a]), (ICAO, October 2014[b]). Summarising, the general benefits of TBO can be stated as:

- Aircraft separation is reduced due to the decrease of uncertainty in the trajectories, thanks to higher guidance accuracy.

---

[4]ADS-C (Automatic Dependent Surveillance-Contract) operates similarly to ADS-B, but the data is transmitted based on an explicit contract (demand, periodic, event or emergency) between an ANSP and an aircraft. It is mainly used in the provision of ATS over transcontinental or transoceanic areas (low traffic levels)(SKYbrary, 2017).

- An enhancement of capacity and efficiency in traffic flows within a given airspace is assured since time-dependent reference trajectories are given.

- An optimal update of tactical trajectories due to weather or conflict avoidance can be made since the reference trajectory is shared between all ATM actors. Since an optimal trajectory is more likely to be used, and they are usually shorter than the original path, reductions of CO_2 emission and fuel burn are expected.

- Flight predictability and safety are increased due to the use of GNSS and ground systems.

2.2.2.1 Implementation of TBO

Continuous Descent and Continuous Climb Operations (CDO and CCO) are clear examples of the use of TBO, where optimal flight paths are intended in order to achieve the best economic/environmental benefits (see Figure 2.12). These operations could save from 50 to 200kg of fuel per flight using a single CCO or CDO, compared to a non-optimized profile (Eurocontrol, 2017l). Moreover, according to (NASA, 2013), data from the 27 busiest airports in the U.S.A. indicates that 188 million gallons of fuel per year could be saved with continuous climbs, and 218 million with continuous descents.

CDO procedures were first evaluated at Louisville-Standiford International Airport, tested at Atlanta/Hartsfield-Jackson International Airport, and demonstrated at the Miami International Airport in May 2008. However CDO interaction with non-CDO flights, pilot adjustments to drag-generating devices (throttle changes, flap settings, landing gear extension), and further studies on the benefits of these operations, have provoked delays in their full implementation.

On the other hand, CCOs are expected to be included as a part of a SID(Standard Instrument Departure), so ATC and flight crews have a fixed procedure defined in advance.

Ideally, CDOs use minimum engine thrust in a low drag configuration prior to landing, while CCOs use climb engine thrust and speeds until reaching cruise altitude (faster than step climbs). Both CDOs and CCOs are highly encouraged in Europe. In consequence, their associated ICAO manual have been issued, (*ICAO* 2010), (*ICAO* 2013), respectively.

In addition to CCO and CDO techniques, 4D operations have been addressed in both SESAR and Next-Gen projects, where the time integration as an extra dimension to a 3D trajectory allows to consider delays as distortions from the reference trajectory.

The 4D concept relies on RBT (Reference Business Trajectory) that airspace users choose to fly, and ANSPs to provide. This 4D (time-based) operations are considered as milestones towards Trajectory-Based Operations due to their level of information sharing between ATC and flight crews, as well as the required avionics, and required levels of on-board automation.

In the SESAR context, 4D trajectory management is divided in two stages, initial 4D (i4D), and Full 4D.

The i4D consists in using airborne computed predictions in ground systems to define a target time of arrival at a merging point to each aircraft converging to this point (e.g. Initial Approach Fix), such that traffic is sequenced. This implies fewer tactical interventions and improved de-confliction situation.

Although Controlled Time of Arrival (CTA) is a functionality available in modern
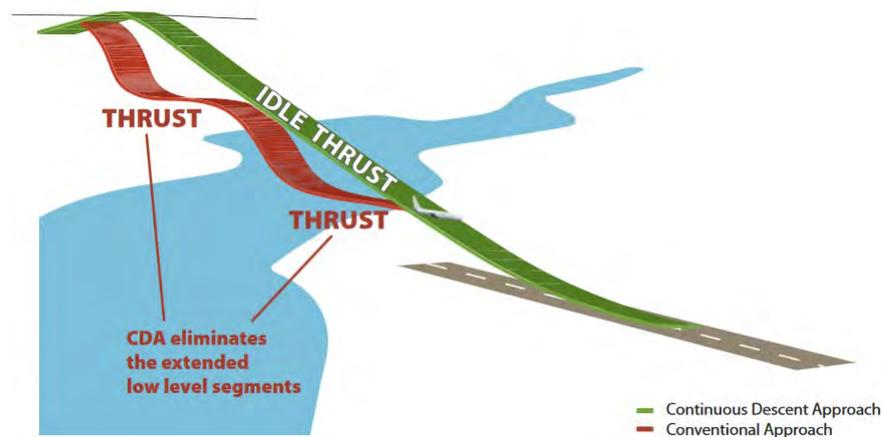
FIGURE 2.12: Concept of CDO (*Eurocontrol* October 2011).

Flight Management Systems, its use to improve efficiency in traffic management has been explored only recently. According to (Klooster, Amo, and Manzi, 2009), the wind data available to the FMS, the speed and altitude constraints, and configuration for landing, are determinant factors that have a substantial impact on the CTA accuracy. Therefore, higher wind modelling accuracy may considerably improve the accuracy of the CTA operation.

Implementation of the i4D was performed successfully the 10th February of 2012 with an A320 test aircraft flying from Toulouse to Copenhagen, Stockholm, and then back to Toulouse, underlying the datalink interoperability (exchange of trajectory predictions between an advanced aircraft FMS and the ground automation systems) as a key element (Mutuel, Paricaud, and Neri, 2013), (*SESAR Factsheet* 2012).

Regarding the Full 4D Trajectory Management concept of SESAR (4D gate-to-gate), it was initially planned to start the implementation between 2017 and 2019, but it was delayed due to its impact on airborne and ground systems, as well as in the existent procedures.

In order to advance towards full 4D trajectories, some requirements for on-board systems and crew procedures need to be accomplished. For example: advanced features for FMS (improved wind modelling and update in the FMS), improved FMS ability to meet time constraints, improvement of personalized, filtered, information sharing like datalink (CPDLC and ADS-C EPP) for transmission of altitude, time, speed predictions, aircraft gross weight, etc., and introduction of SWIM (System-wide Information Management), just to mention a few.

Moreover, considering that:

- Conflict detection is more complex since trajectories will no longer follow standard airways, making conflicting points moving locations.

- TBO improvement in only a part of the trajectory will limit the benefit.

- Action of controllers will have an impact in the trajectory as a whole, since the reach of control points needs to be done in time and not later or earlier.

cost benefit analysis are being developed to ensure that costs associated with 4D avionics are justified by the potential benefits.

2.3 Conclusion

A summary regarding the current air traffic organization has been provided, describing the main features of the CNS-ATM and MET services. Then, after recognizing the imminent growth of air traffic, the solutions adopted by the European Union and the United States of America were described as a part of a modern air traffic organization.

The advantages of a modern organization of air traffic have been pointed out, and the gradual shift from fixed routes and ATC clearances towards flexible trajectories, higher levels of on-board automation, reduced aviation congestion, and improved safety, has been described.

Moreover, the use of new technologies such as ADS-B/C, Global Navigation Satellite Systems (GNSS), and their interaction with current ATM has also been described.

Taking into account that the main goal of SESAR and Next-Gen projects is focused on enhancing the airspace capacity while maintaining safety, the nearest concept to be implemented is TBO, therefore, the Continuous Climb/Descent Operations and the 4D concept are of great interest. This is expected since the Freeflight concept for high traffic regions will result in an increase of air conflicts, and automatic conflict resolutions may end in a permanent state of routes reconfiguration.

Furthermore, certain similarities between the objectives of this thesis with respect to the expected benefits of TBO are found.

Chapter 3

Flight Dynamics of Transport Aircraft under Wind Disturbances

In this chapter, the nonlinear differential equations describing the behaviour of transport aircraft are described, such that they serve not only as a basis for further chapters, but also as a formal introduction for understanding the relation between different frames, variables, and physical phenomena that contribute to explain aircraft flight. To begin with, an aircraft is considered as a rigid body with six degrees of freedom (6 DOF) flying through a quasi-stationary flow field. The principal notation and nonlinear differential equations describing the aerodynamic forces and moments as well as the motion of the aircraft are given based on (Etkin, 1972), (Etkin and Reid, 1996), (Stevens and Lewis, 1992). This aircraft model hinges upon the Newton's 2nd law.

In Section 3.1, the reference frames and their respective rotation matrices between each other are given. Then, Section 3.2 gives the rigid body equations, constructed by a set of nonlinear differential equations split into guidance and attitude dynamics. Moreover, a brief description of the aerodynamic force and moment coefficients that define the behaviour of the aircraft is provided. In spite of the fact that these equations are called the complete mathematical model, some subsystems such as the engines or the control surfaces are bypassed. Therefore, towards a more realistic approach, first-order dynamics are proposed to govern the control surfaces and the engines. Besides, considering that some of the main disturbances during flights are caused by wind gusts, it seems natural to take into account their effects while modelling the aircraft dynamics. In this manner, flight dynamics are expressed assuming wind contributions.

Once the complete aircraft model is built up, it is a common practice in the literature to simplify these equations into longitudinal and lateral motions, opening the door to a less complex analysis of flight mechanics. Stated this, one may infer that these simplified models are only valid for a limited domain of the behaviour of the aircraft. Thus, Section 3.3 presents the reduced equations of motion.

In Section 3.4, an insight in aerodynamics regarding the force and moments coefficients is provided to better understand the nature of the aircraft behaviour. Simultaneously, it will serve as a basis for further chapters where numerical values are proposed for these coefficients. In addition to this, considering that transport aircraft are intended to look after passengers comfort, and structural limitations have to be attended, the flight maneuvers are restricted by load factor boundaries. Hence, the relations to express the load factor depending on the aircraft variables are also given in Section 3.5. Finally, a compilation of the relevant equations is presented in Section 3.6 for the reader's convenience, and conclusions are given in Section 3.7.

3.1   Reference Frames

It is common to observe how not all variables are convenient to be expressed in only one reference frame, yielding to the choice of multiple frames to easily describe a physical phenomena. In this work, only the necessary ones to express the aircraft dynamics are described.

3.1.1   Adopted frames

3.1.1.1   Inertial Frame

The inertial reference frame, represented by $F_I = (O_I, x_I, y_I, z_I)$, has the origin on the center of the earth. The z_I axis points north, the x_I points towards the vernal equinox, and y_I is perpendicular to both in a right-handed rotation. The WGS84 (World Geodetic System) is considered. In the perspective of flight dynamics, since the relevant motions regarding dynamic stability have a very short duration compared to the motion of the earth itself, this frame is of minimal use, therefore will be ignored.

3.1.1.2   Earth-fixed Reference Frame

The local earth reference frame is considered for the description of the trajectories that an aircraft is flying, as well as the trajectories that the aircraft is supposed to follow. This frame is denoted by $F_E = (O_E, x_E, y_E, z_E)$, and its origin is arbitrarily located on the ground. It is worth to say that the trajectory to be followed by the aircraft, referred to it as a 4D reference trajectory, is defined by three functions associated with the coordinates of the center of gravity of the aircraft supposed to follow it. These functions are parameterized by time: $x_R(t), y_R(t), z_R(t), t \in [t_{init}, t_{end}]$.

3.1.1.3   Body Reference Frame

A third reference frame is considered to represent the fast dynamics of the aircraft. It is attached to the body's c.g. and is defined as $F_B = (C, x_B, y_B, z_B)$, referred to it as the body frame. The x_B axis goes from tail to nose of the aircraft while the z_B axis, perpendicular to the latter, points downwards and lies in the symmetry plane of the aircraft. To complete the triad, the direction of y_B can be obtained by the cross product $\vec{z_B} \times \vec{x_B}$. Figure 3.1 represents graphically the body and earth frame.

3.1.1.4   Stability Reference Frame

This frame, denoted by $F_S = (C, x_S, y_S, z_S)$, has its axes chosen such that Cx_B is aligned with the aircraft velocity vector relative to the surrounding air mass (better known as airspeed, V_a) by performing only a rotation around the y_B axis.

3.1.1.5   Wind Reference Frame

Lastly, denoted by $F_W = (C, x_W, y_W, z_W)$, the wind frame is introduced since it allows to represent the aerodynamic forces on the aircraft. This frame has its x_W axis aligned with the airspeed. The difference between x_B and x_S, which is the projection of x_W in the Cx_Bz_B plane, gives birth to the angle of attack (α) (short notation: AoA). Also, the angle created by the projection of V_a in the Cx_By_B plane and the x_B axis, is known as the sideslip angle (β). In the Figure 3.2 are represented
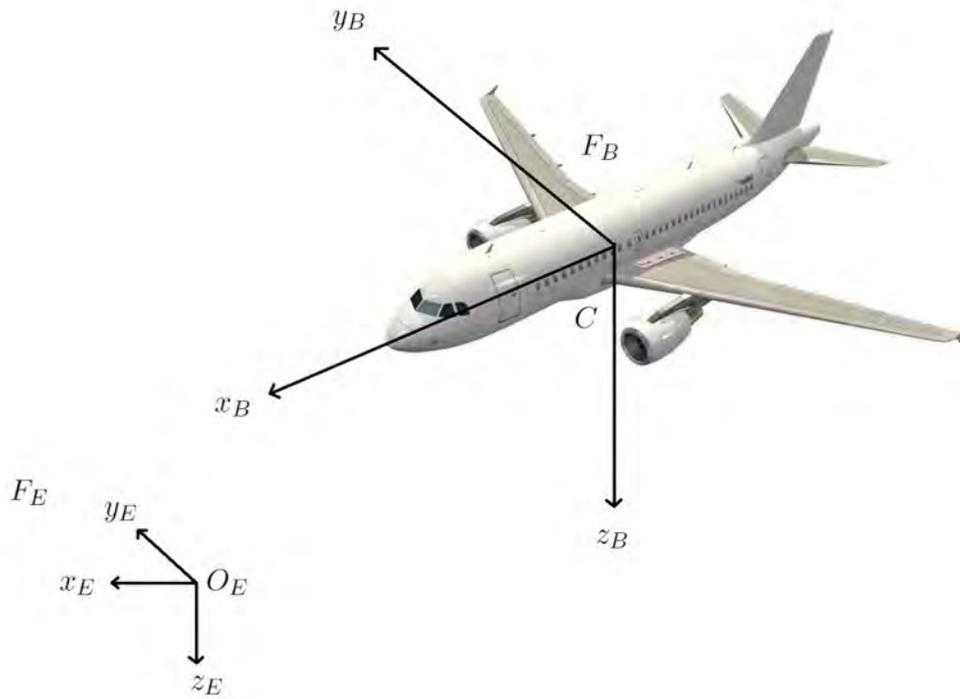
FIGURE 3.1: Earth frame and Body frame.

the wind and stability frames with respect to the body frame.
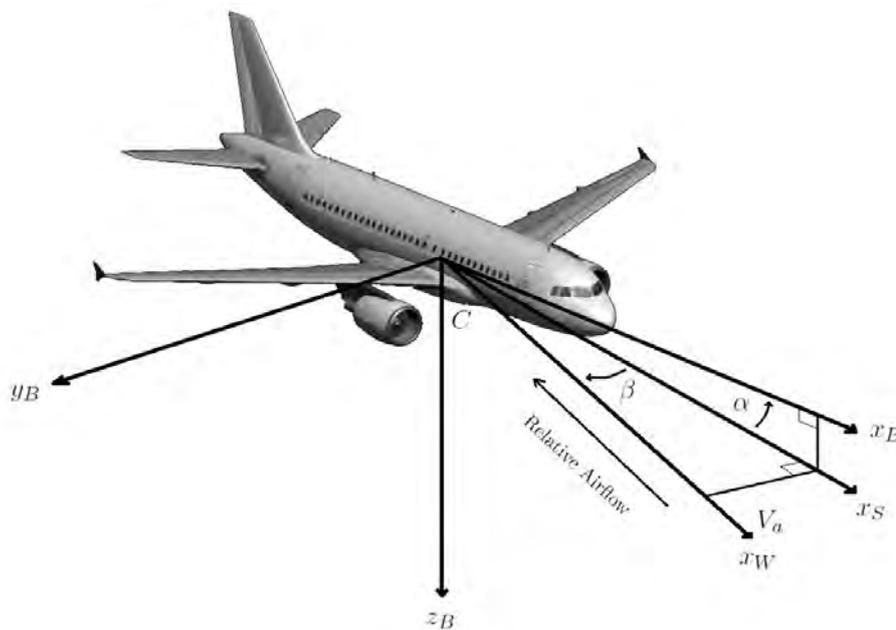
FIGURE 3.2: Wind frame and Stability frame. AoA and Sideslip angle
in the positive sense.

3.1.2   Rotation Matrices between frames

The interaction between different variables attached to different reference frames is described mathematically thanks to the rotation matrices. These rotation matrices allow the mapping of variables from one frame to another. Consider the case of mapping variables from the body frame into the wind frame, passing through the stability frame. This is done by making a rotation around two axes, denoted by

$$
\begin{bmatrix} x_S \\ y_S \\ z_S \end{bmatrix} = \begin{bmatrix} c_\alpha & 0 & s_\alpha \\ 0 & 1 & 0 \\ -s_\alpha & 0 & c_\alpha \end{bmatrix} \begin{bmatrix} x_B \\ y_B \\ z_B \end{bmatrix} \tag{3.1a}
$$

$$
\begin{bmatrix} x_W \\ y_W \\ z_W \end{bmatrix} = \begin{bmatrix} c_\beta & s_\beta & 0 \\ -s_\beta & c_\beta & 0 \\ 0 & 0 & 1 \end{bmatrix} \begin{bmatrix} x_S \\ y_S \\ z_S \end{bmatrix} \tag{3.1b}
$$

Thus, in the inverse sense, physical quantities from the wind frame can be mapped into the body frame by the following rotation matrix:

$$
L_{BW} = \left(\begin{bmatrix} c_\beta & s_\beta & 0 \\ -s_\beta & c_\beta & 0 \\ 0 & 0 & 1 \end{bmatrix} \begin{bmatrix} c_\alpha & 0 & s_\alpha \\ 0 & 1 & 0 \\ -s_\alpha & 0 & c_\alpha \end{bmatrix} \right)^T = \begin{bmatrix} c_\alpha c_\beta & -c_\alpha s_\beta & -s_\alpha \\ s_\beta & c_\beta & 0 \\ s_\alpha c_\beta & -s_\alpha s_\beta & c_\alpha \end{bmatrix} \tag{3.2}
$$

For more details on rotation matrices, see Appendix A.

Therefore, in the case of the airspeed, which has only one component in the axes of the wind frame $\left(V_{aw} = [V_a, 0, 0]^T \right)$, it can be represented in the body frame as

$$
V_{ab} = L_{BW} V_{aw} \tag{3.3a}
$$

$$
V_{ab} = \begin{bmatrix} V_a c_\alpha c_\beta \\ V_a s_\beta \\ V_a s_\alpha c_\beta \end{bmatrix} \tag{3.3b}
$$

Moreover, if the wind components in the body frame are taken into account as $V_w = [V_{w_x}, V_{w_y}, V_{w_z}]^T$, the inertial velocity of the aircraft in the body frame is denoted by.

$$
V_B = \begin{bmatrix} u \\ v \\ w \end{bmatrix} = \begin{bmatrix} V_a c_\alpha c_\beta + V_{w_x} \\ V_a s_\beta + V_{w_y} \\ V_a s_\alpha c_\beta + V_{w_z} \end{bmatrix} \tag{3.4}
$$

Hence, the following relations are extracted from (3.4):

$$
\alpha = arctan \left(\frac{w - V_{w_z}}{u - V_{w_x}} \right) \tag{3.5a}
$$

$$
\beta = arcsin \left(\frac{v - V_{w_y}}{V_a} \right) \tag{3.5b}
$$

$$
V_a = \sqrt{(u - V_{w_x})^2 + (v - V_{w_y})^2 + (w - V_{w_z})^2} \tag{3.5c}
$$

The vector $R = [\alpha, \beta, V_a]^T$ is defined for simplicity in further equations.

In the same tenor, the angles created from the difference between the body frame and the earth frame are the euler angles $\left(\eta = [\phi, \theta, \psi]^T \right)$, used to describe the attitude of the aircraft.

The euler angles are born as follows: It is a fact that the F_B frame rotates, while F_E

is fixed, so the rotated frame F_B can be imagined to be initially aligned with F_E, before undergoing three elemental rotations (rotations about the axes of a coordinate system) represented by the Euler angles. Any target orientation for F_B can be achieved by composing three elemental rotations, these rotations occur around the axes of the frame F_B, attached to the moving body. Therefore, the rotation matrix from the body to the earth frame considering a rotation around the axes in the order $z_B y_B x_B$, is given by:

$$L_{EB} = \begin{bmatrix} c_\theta c_\psi & s_\phi s_\theta c_\psi - c_\phi s_\psi & c_\phi s_\theta c_\psi + s_\phi s_\psi \\ c_\theta s_\psi & s_\phi s_\theta s_\psi + c_\phi c_\psi & c_\phi s_\theta s_\psi - s_\phi c_\psi \\ -s_\theta & s_\phi c_\theta & c_\phi c_\theta \end{bmatrix} \tag{3.6}$$

where the euler angles are bounded as $\phi\{-\pi, \pi\}$; $\theta\{-\frac{\pi}{2}, \frac{\pi}{2}\}$; $\psi\{-\pi, \pi\}$, and limits are never reached during normal operation for transportation aircraft.
Consequently, the velocity of the aircraft in the earth frame is given by:

$$V_E = \begin{bmatrix} \dot{x_E} \\ \dot{y_E} \\ \dot{z_E} \end{bmatrix} = L_{EB} \begin{bmatrix} u \\ v \\ w \end{bmatrix} \tag{3.7}$$

The rotation matrices used here belong to the SO_3 group. Thus, the inverse of any of these matrices equals to its transpose.

3.2   Equations of motion

The four principal forces on an aircraft are shown in Figure 3.3, where the Thrust (F_{thr}) is provided by the engines in the opposite direction of the Drag (D), and the Weight of the aircraft (W) is compensated by the Lift (L).

 Lift and Drag of the wing are assumed to act in the wing's pressure center, so that
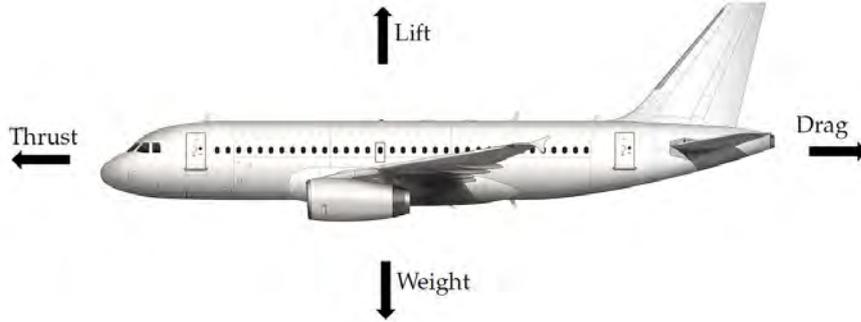
FIGURE 3.3: Forces acting on an aircraft.

if a frame has its origin in this point of the aircraft, the pitching moment is equal to zero. This decision is far from being the optimal due to the changing location of the centre of pressure along the wing as the angle of attack changes. In order to avoid this problem, a point called aerodynamic center (a.c.) is defined, where the pitching moment is almost invariant relative to the AoA variation (within permitted limits). In subsonic velocities (Mach<1), the a.c. is at 1/4 of the wind chord, which is geometrically forward the centre of pressure, such that if a frame is chosen with its origin in the a.c., it will cause an approximately constant nose-down (negative) moment relative to the AoA positive variation when static stability is positive. As the the center of gravity (c.g.) of the aircraft moves ahead the a.c., the more positive static stability is obtained.

Therefore, considering the body frame attached to the c.g. of the aircraft, the equations of motion are split into guidance equations, assumed to be the slow dynamics, and in attitude equations, considered as the fast dynamics. Moreover, first order models for the actuators are considered.

3.2.1   Guidance Dynamics

Considering the Newton's 2nd law with f_E as the resultant force acting on the aircraft, one should obtain the external and internal forces acting on the aircraft. However, the internal forces (those exerted by one small aircraft's mass element upon another), all occur in equal and opposite pairs, such that by Newton's third law, they contribute nothing to the resultant force. Consequently, f_E is the resultant *external force* acting on the aircraft, and it is obtained by:

$$f_E = m\dot{V}_E \tag{3.8a}$$

$$L_{EB}f_B = m\frac{d}{dt}\left(L_{EB}V_B\right) = m\left(\dot{L}_{EB}V_B + L_{EB}\dot{V}_B\right) \tag{3.8b}$$

Then, denoting the angular rates by $\Omega = [p, q, r]^T$, the Euler property is given by

$$\dot{L}_{EB} = L_{EB}\tilde{\Omega} = L_{EB} \begin{bmatrix} 0 & -r & q \\ r & 0 & -p \\ -q & p & 0 \end{bmatrix} \tag{3.9}$$

Therefore, (3.8b) can be rewritten as

$$f_B = m\left(\dot{V}_B + \Omega \times V_B\right) \tag{3.10}$$

where m is the aircraft mass, and f_B is the vector of *external forces* in the body frame, conformed by the aerodynamic forces, the thrust, which is assumed to be aligned with the x_B axis, and the gravitational force projected in the body frame, yielding

$$f_B = mL_{BE} \begin{bmatrix} 0 \\ 0 \\ g \end{bmatrix} + \begin{bmatrix} F_{x_a} \\ F_{y_a} \\ F_{z_a} \end{bmatrix} + \begin{bmatrix} F_{thr} \\ 0 \\ 0 \end{bmatrix} \tag{3.11}$$

where the aerodynamic forces, generated in the wind frame as Lift, Drag, and Side-force (Y), are denoted in the body frame using (3.2) such that

$$\begin{bmatrix} F_{x_a} \\ F_{y_a} \\ F_{z_a} \end{bmatrix} = L_{BW} \begin{bmatrix} -D \\ Y \\ -L \end{bmatrix} \tag{3.12}$$

which are simultaneously related with their aerodynamic force coefficients by:

$$\begin{bmatrix} D \\ Y \\ L \end{bmatrix} = \frac{1}{2}\rho SV_a^2 \begin{bmatrix} C_D \\ C_Y \\ C_L \end{bmatrix} \tag{3.13}$$

with ρ as the air density and S wing area. Some authors prefer to use the *free-stream dynamic pressure*, denoted by $\bar{q} = \frac{1}{2}\rho V_a^2$. However, the full notation will be kept in this work. The aerodynamic force coefficients $C_{D,Y,L}$ will be addressed later.

Thus, an acceleration equation in the body frame using (3.10) and (3.11) is denoted by:

$$\begin{bmatrix} \dot{u} \\ \dot{v} \\ \dot{w} \end{bmatrix} = \begin{bmatrix} \frac{1}{m}\left(F_{x_a} + F_{thr}\right) - gs_\theta + rv - qw \\ \frac{1}{m}F_{y_a} + gc_\theta s_\phi + pw - ru \\ \frac{1}{m}F_{z_a} + gc_\theta c_\phi + qu - pv \end{bmatrix} \tag{3.14}$$

While in the Earth frame, (3.8a) is rewritten as:

$$\begin{bmatrix} \ddot{x}_E \\ \ddot{y}_E \\ \ddot{z}_E \end{bmatrix} = L_{EB} \begin{bmatrix} F_{x_a} + F_{thr} \\ F_{y_a} \\ F_{z_a} \end{bmatrix} \frac{1}{m} + \begin{bmatrix} 0 \\ 0 \\ g \end{bmatrix} \tag{3.15}$$

3.2.2 Attitude Dynamics

Concerning the attitude of the aircraft, the angular rates are produced by the deflection of ailerons, elevator and rudder, denoted by $[\delta_{ail}, \delta_{ele}, \delta_{rud}]^T$. Hence, the total angular momentum h_E (not the same as moment) with respect to the aircraft's c.g. needs to be obtained, since this quantity remains constant unless an external moment actuates on the aircraft. For a moving point other than the mass center, the

following equations do not apply.

Using a similar argument to that used for the forces, the total angular momentum is shown to be the resultant *external moment* about de aircraft's c.g., and it is related with the rolling, pitching and yawing aerodynamic moments ($M_{ext} = [L', M, N]^T$) by

$$M_{ext_E} = \dot{h}_E \tag{3.16a}$$

$$L_{EB}M_{ext} = \frac{d}{dt}(L_{EB}h_B) = \dot{L}_{EB}h_B + L_{EB}\dot{h}_B \tag{3.16b}$$

Knowing that $h_B = I\Omega$, and that I stands for the inertia matrix, assumed to be constant, with some components equal to zero due to the aircraft symmetry, and denoted by

$$I = \begin{bmatrix} A & 0 & -E \\ 0 & B & 0 \\ -E & 0 & C \end{bmatrix} \tag{3.17}$$

equation (3.16b) can be written as

$$M_{ext} = I\dot{\Omega} + \Omega \times (I\Omega) \tag{3.18}$$

Then, rearranging for the angular rates like in (Lombaerts et al., May-June 2009), the rotational equations of the aircraft can be expressed by:

$$\dot{\Omega} = I^{-1}M_{ext} - I^{-1}\Omega \times (I\Omega) \tag{3.19}$$

with

$$I^{-1} = \frac{1}{B(AC - E^2)} \begin{bmatrix} BC & 0 & BE \\ 0 & AC - E^2 & 0 \\ BE & 0 & AB \end{bmatrix} \tag{3.20}$$

It is known that the aerodynamic moments are dependent in part on the deflection of control surfaces, aircraft velocity, air density, and other parameters such as certain aerodynamic moment coefficients. The relations for these aerodynamic moments are given by:

$$M_{ext} = \begin{bmatrix} L' \\ M \\ N \end{bmatrix} = \frac{1}{2}\rho S V_a^2 \left(\begin{bmatrix} bC_l \\ \bar{c}C_m \\ bC_n \end{bmatrix} + C_\delta \begin{bmatrix} \delta_{ail} \\ \delta_{ele} \\ \delta_{rud} \end{bmatrix} \right) \tag{3.21}$$

where

$$C_\delta = \begin{bmatrix} bC_{l_{\delta ail}} & 0 & bC_{l_{\delta rud}} \\ 0 & \bar{c}C_{m_{\delta ele}} & 0 \\ bC_{n_{\delta ail}} & 0 & bC_{n_{\delta rud}} \end{bmatrix} \tag{3.22}$$

with b as the wingspan and $\bar{c}$ as the mean chord. The rolling, pitching and yawing aerodynamic moment coefficients (C_l, C_m, C_n, respectively) are denoted by:

$$\begin{bmatrix} C_l \\ C_m \\ C_n \end{bmatrix} = \begin{bmatrix} C_{l_\beta}\beta + C_{l_p}\frac{bp}{2V_a} + C_{l_r}\frac{br}{2V_a} \\ C_{m0} + C_{m_\alpha}\alpha + C_{m_q}\frac{cq}{2V_a} \\ C_{n_\beta}\beta + C_{n_p}\frac{bp}{2V_a} + C_{n_r}\frac{br}{2V_a} \end{bmatrix} \tag{3.23}$$

where $C_{l_{\beta,p,r,\delta ail,\delta rud}}$, $C_{m_{0,\alpha,q,\delta ele}}$, $C_{n_{\beta,p,r,\delta ail,\delta rud}}$, will be addressed later.
Then, equation (3.19) can be rewritten using (3.21) as

$$\dot{\Omega} = I^{-1} \left(\frac{1}{2}\rho V_a^2 S \left(\begin{bmatrix} bC_l \\ \bar{c}C_m \\ bC_n \end{bmatrix} + C_\delta \begin{bmatrix} \delta_{ail} \\ \delta_{ele} \\ \delta_{rud} \end{bmatrix} \right) + \begin{bmatrix} (B-C)qr + Epq \\ (C-A)pr - E(p^2 - r^2) \\ (A-B)pq - Erq \end{bmatrix} \right)$$
(3.24)

or in a compact form by introducing (3.20) as

$$\dot{\Omega} = \frac{1}{B(AC - E^2)} \begin{bmatrix} BC & 0 & BE \\ 0 & AC - E^2 & 0 \\ BE & 0 & AB \end{bmatrix} \begin{bmatrix} (B-C)qr + Epq + L' \\ (C-A)pr - E(p^2 - r^2) + M \\ (A-B)pq - Erq + N \end{bmatrix}$$
(3.25)

Moreover, the rotation speed components are related with the attitude angular rates by the Euler equations, given by:

$$\begin{bmatrix} \dot{\phi} \\ \dot{\theta} \\ \dot{\psi} \end{bmatrix} = \begin{bmatrix} 1 & tg_\theta s_\phi & tg_\theta c_\phi \\ 0 & c_\phi & -s_\phi \\ 0 & \frac{s_\phi}{c_\theta} & \frac{c_\phi}{c_\theta} \end{bmatrix} \begin{bmatrix} p \\ q \\ r \end{bmatrix}$$
(3.26)

Positive sense of forces, moments and velocities can be seen in Figure 3.4.
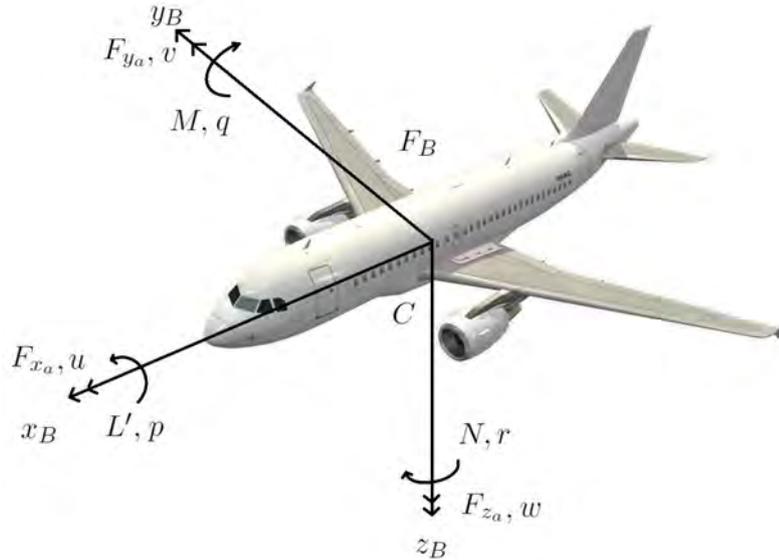
FIGURE 3.4: Positive sense of velocities and aerodynamic forces and moments.

3.2.3   Dynamics in the wind frame

In order to express the flight dynamics in the wind frame, (3.5a) is differentiated, and using (3.4), (3.12), (3.14), the rate of change of the AoA is given by:

$$
\begin{aligned}
\dot{\alpha} &= \frac{(u - V_{w_x})(\dot{w} - \dot{V}_{w_z}) - (w - V_{w_z})(\dot{u} - \dot{V}_{w_x})}{(u - V_{w_x})^2 + (w - V_{w_z})^2} \\
&= \frac{1}{V_a c_\beta} \left[c_\alpha(\dot{w} - \dot{V}_{w_z}) - s_\alpha(\dot{u} - \dot{V}_{w_x}) \right] \\
&= \frac{1}{V_a c_\beta} \left(g_1 - \frac{1}{m}(L + F_{thr} s_\alpha) \right) + p \left(-tan_\beta c_\alpha - \frac{V_{w_y} c_\alpha}{V_a c_\beta} \right) \\
&\quad + q \left(1 + \frac{V_{w_x} c_\alpha + V_{w_z} s_\alpha}{V_a c_\beta} \right) + r \left(-tan_\beta s_\alpha - \frac{V_{w_y} s_\alpha}{V_a c_\beta} \right) + \frac{1}{V_a c_\beta} \left(\dot{V}_{w_x} s_\alpha - \dot{V}_{w_z} c_\alpha \right)
\end{aligned}
\tag{3.27}
$$

with:

$$
g_1 = g \left(c_\alpha c_\theta c_\phi + s_\alpha s_\theta \right)
$$

Similarly, differentiating (3.5b), and using (3.4), (3.12), (3.14), the rate of change of the sideslip angle is given by:

$$
\begin{aligned}
\dot{\beta} &= \frac{V_a(\dot{v} - \dot{V}_{w_y}) - (v - V_{w_y})\dot{V}_a}{V_a \sqrt{V_a^2 - (v - V_{w_y})^2}} \\
&= \frac{c_\beta(\dot{v} - \dot{V}_{w_y}) - c_\alpha s_\beta(\dot{u} - \dot{V}_{w_x}) - s_\alpha s_\beta(\dot{w} - \dot{V}_{w_z})}{V_a} \\
&= \frac{1}{V_a} \left(g_2 + \frac{1}{m}(Y - F_{thr} c_\alpha s_\beta) \right) + p \left(s_\alpha + \frac{V_{w_z} c_\beta + V_{w_y} s_\alpha s_\beta}{V_a} \right) \\
&\quad + q \left(\frac{V_{w_z} c_\alpha s_\beta - V_{w_x} s_\alpha s_\beta}{V_a} \right) + r \left(-c_\alpha - \frac{(V_{w_y} c_\alpha s_\beta + V_{w_x} c_\beta)}{V_a} \right) \\
&\quad + \frac{1}{V_a} \left(\dot{V}_{w_x} c_\alpha s_\beta - \dot{V}_{w_y} c_\beta + \dot{V}_{w_z} s_\alpha s_\beta \right)
\end{aligned}
\tag{3.28}
$$

with:

$$
g_2 = g \left(c_\beta c_\theta s_\phi + s_\beta c_\alpha s_\theta - s_\alpha s_\beta c_\theta c_\phi \right)
$$

Then, from (3.5c), and using (3.4), (3.12), (3.14), it is obtained:

$$
\begin{aligned}
\dot{V}_a &= \frac{(u - V_{w_x})(\dot{u} - \dot{V}_{w_x}) + (v - V_{w_y})(\dot{v} - \dot{V}_{w_y}) + (w - V_{w_z})(\dot{w} - \dot{V}_{w_z})}{V_a} \\
&= g_3 + \frac{1}{m}(F_{thr} c_\alpha c_\beta - D) + p \left(V_{w_z} s_\beta - V_{w_y} s_\alpha c_\beta \right) + q \left(V_{w_x} s_\alpha c_\beta - V_{w_z} c_\alpha c_\beta \right) \\
&\quad + r \left(V_{w_y} c_\alpha c_\beta - V_{w_x} s_\beta \right) - \dot{V}_{w_x} c_\alpha c_\beta - \dot{V}_{w_y} s_\beta - \dot{V}_{w_z} s_\alpha c_\beta
\end{aligned}
\tag{3.29}
$$

with:

$$
g_3 = g \left(-c_\alpha c_\beta s_\theta + s_\beta c_\theta s_\phi + s_\alpha c_\beta c_\theta c_\phi \right)
$$

The expression in matrix form of relations (3.27), (3.28) and (3.29), rearranged for Ω is denoted by:

$$
\begin{bmatrix} \dot{\alpha} \\ \dot{\beta} \\ \dot{V}_a \end{bmatrix} = \begin{bmatrix} H_{11} & H_{12} & H_{13} \\ H_{21} & H_{22} & H_{23} \\ H_{31} & H_{32} & H_{33} \end{bmatrix} \begin{bmatrix} p \\ q \\ r \end{bmatrix} + \begin{bmatrix} Q_1 \\ Q_2 \\ Q_3 \end{bmatrix}
\tag{3.30}
$$

where

$$H_{11} = -\left(tan_\beta c_\alpha + \frac{V_{w_y} c_\alpha}{V_a c_\beta}\right)$$

$$H_{12} = 1 + \frac{V_{w_x} c_\alpha + V_{w_z} s_\alpha}{V_a c_\beta}$$

$$H_{13} = -\left(tan_\beta s_\alpha + \frac{V_{w_y} s_\alpha}{V_a c_\beta}\right)$$

$$H_{21} = s_\alpha + \frac{V_{w_z} c_\beta + V_{w_y} s_\alpha s_\beta}{V_a}$$

$$H_{22} = \frac{V_{w_z} c_\alpha s_\beta - V_{w_x} s_\alpha s_\beta}{V_a}$$

$$H_{23} = -\left(c_\alpha + \frac{V_{w_y} c_\alpha s_\beta + V_{w_x} c_\beta}{V_a}\right)$$

$$H_{31} = V_{w_z} s_\beta - V_{w_y} s_\alpha c_\beta$$

$$H_{32} = V_{w_x} s_\alpha c_\beta - V_{w_z} c_\alpha c_\beta$$

$$H_{33} = V_{w_y} c_\alpha c_\beta - V_{w_x} s_\beta$$

$$Q_1 = \frac{1}{V_a c_\beta}\left(g_1 - \frac{1}{m}\left(L + F_{thr} s_\alpha\right)\right) + \frac{1}{V_a c_\beta}\left(\dot{V}_{w_x} s_\alpha - \dot{V}_{w_z} c_\alpha\right)$$

$$Q_2 = \frac{1}{V_a}\left(g_2 + \frac{1}{m}\left(Y - F_{thr} c_\alpha s_\beta\right)\right) + \frac{1}{V_a}\left(\dot{V}_{w_x} c_\alpha s_\beta - \dot{V}_{w_y} c_\beta + \dot{V}_{w_z} s_\alpha s_\beta\right)$$

$$Q_3 = g_3 + \frac{1}{m}\left(F_{thr} c_\alpha c_\beta - D\right) - \dot{V}_{w_x} c_\alpha c_\beta - \dot{V}_{w_y} s_\beta - \dot{V}_{w_z} s_\alpha c_\beta$$

which can be written as:

$$\dot{R} = H\left(R\right)\Omega + Q\left(R\right) \tag{3.31}$$

It can be easily verified that if the wind components are zero, the equations (3.27), (3.28) and (3.29) take the form:

$$\dot{\alpha} = q - tan(\beta)\left(pc_\alpha + rs_\alpha\right) + \frac{1}{V_a c_\beta}\left[g_1 - \frac{1}{m}\left(L + F_{thr} s_\alpha\right)\right] \tag{3.32a}$$

$$\dot{\beta} = ps_\alpha - rc_\alpha + \frac{1}{V_a}\left[\frac{1}{m}\left(Y - F_{thr} c_\alpha s_\beta\right) + g_2\right] \tag{3.32b}$$

$$\dot{V}_a = g_3 + \frac{1}{m}\left(F_{thr} c_\alpha c_\beta - D\right)$$

$$\tag{3.32c}$$

3.2.4 Actuator Dynamics

Let a first-order model be adopted for the aerodynamic actuators, writing δ_i^d ($i = ail, ele, rud$) as the commanded positions of the control surfaces, and δ_i as the current positions of the control surfaces:

$$\dot{\delta}_i = \frac{1}{\xi_i}\left(\delta_i^d - \delta_i\right) \tag{3.33}$$

where ξ_i are the time-constants. Also, the resultant thrust produced by the engines is supposed to behave as a first-order system, denoted by

$$\dot{F}_{thr} = \frac{1}{\xi_T} \left(F_{thr}^d - F_{thr} \right) \tag{3.34}$$

where the F_{thr}^d is the desired thrust and F_{thr} the current thrust. Besides, the time-constants of the actuators keep the relation: $\xi_T >> \xi_i$.

3.3 Reduced equations of motion

Nowadays, the Flight Management System is in charge of designing the route that an aircraft is going to fly from the departure airport to the arrival airport, better known as the *flight plan* (Walter, 2014). The resultant flight plan, constructed from way-points, bearings, geographical locations or distances inserted by the crew, is created in two separate plans, the *lateral* and *vertical*. Consequently, it is a common practice to split the complete aircraft dynamics in longitudinal and lateral-directional motions, such that flight controls are also separated. The longitudinal motion is used to follow the vertical flight plan, and the lateral-directional to follow the lateral flight plan.

By splitting the aircraft dynamics, there is the advantage of reducing the number of nonlinear differential equations describing either the longitudinal or lateral behaviour. On the other hand, the natural coupling of both motions is lost (for a non symmetric flight situation). It is also interesting that for steady level flight, climbing, or descending, the lateral dynamics are decoupled from the longitudinal dynamics, reducing considerably the complexity of the equations of motion.

3.3.1 Longitudinal Motion

In order to obtain the longitudinal equations, given by the movement in the $Cx_B z_B$ plane, some assumptions have to be made. It is assumed that the sideslip angle is zero, as well as the bank angle, consequently, the angular rates p and r are inexistent and the pitch rate is given by the reduction of equation (3.26) as

$$\dot{\theta} = q \tag{3.35}$$

Moreover, from (3.25) it is obtained that

$$\dot{q} = \frac{M}{B} \tag{3.36}$$

Applying these considerations to equations (3.27) and (3.29), and introducing the Flight Path Angle (f.p.a.), depicted in Figure 3.5 and denoted by

$$\gamma = \theta - \alpha \tag{3.37}$$

the vertical motion in the wind frame is given by:

FIGURE 3.5: Flight Path Angle.

$$\dot{\gamma} = \frac{1}{mV_a}\left(L + F_{thr}s_\alpha - mgc_\gamma\right) - q\left(\frac{V_{w_x}c_\alpha + V_{w_z}s_\alpha}{V_a}\right) + \frac{1}{V_a}\left(\dot{V}_{w_z}c_\alpha - \dot{V}_{w_x}s_\alpha\right)$$

(3.38a)

$$\dot{V}_a = \frac{1}{m}\left(F_{thr}c_\alpha - D - mgs_\gamma\right) + q\left(V_{w_x}s_\alpha - V_{w_z}c_\alpha\right) - \dot{V}_{w_x}c_\alpha - \dot{V}_{w_z}s_\alpha \qquad (3.38b)$$

Furthermore, (3.2) becomes

$$L_{BW} = \begin{bmatrix} c_\alpha & 0 & -s_\alpha \\ 0 & 1 & 0 \\ s_\alpha & 0 & c_\alpha \end{bmatrix} \qquad (3.39)$$

Therefore, it is extracted from (3.12) that

$$\begin{bmatrix} F_{x_a} \\ F_{z_a} \end{bmatrix} = \begin{bmatrix} Ls_\alpha - Dc_\alpha \\ -Lc_\alpha - Ds_\alpha \end{bmatrix} \qquad (3.40)$$

and consequently, from substituting (3.40) in (3.14), it is obtained

$$\dot{u} = \frac{1}{m}\left(F_{thr} + Ls_\alpha - Dc_\alpha\right) - gs_\theta - qw \qquad (3.41a)$$

$$\dot{w} = -\frac{1}{m}\left(Lc_\alpha + Ds_\alpha\right) + gc_\theta + qu \qquad (3.41b)$$

In the same way, considering $\phi = 0$ in (3.6), the following relations are extracted from (3.7):

$$\dot{x}_E = uc_\theta c_\psi + ws_\theta c_\psi \qquad (3.42a)$$

$$\dot{z}_E = -us_\theta + wc_\theta \qquad (3.42b)$$

Then, if $\beta = 0$ in (3.4), it is obtained that

$$u = V_a c_\alpha + V_{w_x} \qquad (3.43a)$$

$$w = V_a s_\alpha + V_{w_z} \qquad (3.43b)$$

Thus, if (3.42) and (3.43) are combined, yields

$$\dot{x}_E = V_a c_\psi (c_\alpha c_\theta + s_\alpha s_\theta) + V_{w_x} c_\theta c_\psi + V_{w_z} s_\theta c_\psi \qquad (3.44a)$$

$$\dot{z}_E = V_a (s_\alpha c_\theta - c_\alpha s_\theta) - V_{w_x} s_\theta + V_{w_z} c_\theta \qquad (3.44b)$$

which can be rewritten using the f.p.a. γ as

$$\dot{x}_E = V_a c_\gamma c_\psi + V_{w_x} c_\theta c_\psi + V_{w_z} s_\theta c_\psi \qquad (3.45a)$$

$$\dot{z}_E = -V_a s_\gamma - V_{w_x} s_\theta + V_{w_z} c_\theta \qquad (3.45b)$$

It can be easily verified that if the wind components are neglected, (3.38a) and (3.45) are reduced to

$$\dot{\gamma} = \frac{1}{mV_a}\left(L + F_{thr}s_\alpha - mgc_\gamma\right) \qquad (3.46a)$$

$$\dot{V}_a = \frac{1}{m}\left(F_{thr}c_\alpha - D - mgs_\gamma\right) \qquad (3.46b)$$

$$\dot{x}_E = V_a c_\gamma c_\psi \qquad (3.46c)$$

$$\dot{z}_E = -V_a s_\gamma \qquad (3.46d)$$

One last generalization can be pulled of the longitudinal equations, this is when the aircraft is flying at constant altitude.

3.3.1.1 Level Flight

Assume that the aircraft is flying at constant altitude, hence, the f.p.a. dynamics are zero. In consequence, from (3.46a) and (3.46b) is obtained that

$$mg = F_{thr}s_\alpha + L \tag{3.47a}$$

$$\dot{V}_a = \frac{1}{m}\left(F_{thr}c_\alpha - D\right) \tag{3.47b}$$

and, if the velocity is assumed constant

$$F_{thr}c_\alpha = D \tag{3.48}$$

3.3.2 Lateral-directional Motion

Moving on to the lateral equations, given by the movement in the Cx_By_B plane, they are obtained by assuming that $\theta = q = 0$, such that from (3.26) it is obtained that

$$\dot{\phi} = p \tag{3.49a}$$

$$\dot{\psi} = rc_\phi \tag{3.49b}$$

and from (3.25)

$$\dot{p} = \frac{1}{AC - E^2}\left(CL' + EN\right) \tag{3.50a}$$

$$\dot{r} = \frac{1}{AC - E^2}\left(EL' + AN\right) \tag{3.50b}$$

Therefore, under these assumptions, the lateral motion in the wind frame is given by the reduction of (3.28) as

$$
\dot{\beta} = \frac{1}{V_a}\left(g\left(c_\beta s_\phi - s_\alpha s_\beta c_\phi\right) + \frac{1}{m}\left(Y - F_{thr}c_\alpha s_\beta\right)\right) + p\left(s_\alpha + \frac{V_{w_z}c_\beta + V_{w_y}s_\alpha s_\beta}{V_a}\right)
$$
$$
+ r\left(-c_\alpha - \frac{(V_{w_y}c_\alpha s_\beta + V_{w_x}c_\beta)}{V_a}\right) + \frac{1}{V_a}\left(\dot{V}_{w_x}c_\alpha s_\beta - \dot{V}_{w_y}c_\beta + \dot{V}_{w_z}s_\alpha s_\beta\right) \tag{3.51}
$$

Furthermore, since the rotation matrix L_{BW} remains as (3.2), the aerodynamic force obtained from (3.12) is expressed by

$$F_{y_a} = -Ds_\beta + Yc_\beta \tag{3.52}$$

Then, substituting (3.52) in (3.14) yields to

$$\dot{v} = \frac{1}{m}\left(-Ds_\beta + Yc_\beta\right) + gs_\phi + pw - ru \tag{3.53}$$

In this manner, if $\phi = 0$ in (3.6), it is extracted from (3.7) the relation:

$$\dot{y}_E = uc_\theta s_\psi + vc_\psi + ws_\theta s_\psi \tag{3.54}$$

and substituting (3.4) in (3.54), considering $\beta = 0$ yields to

$$\dot{y}_E = V_a s_\psi \left(c_\theta c_\alpha + s_\theta s_\alpha \right) + V_{w_x} c_\theta s_\psi + V_{w_y} c_\psi + V_{w_z} s_\theta s_\psi \tag{3.55}$$

Finally, if the wind components are neglected, (3.51) and (3.55) turn into

$$\dot{\beta} = \frac{1}{V_a} \left(g \left(c_\beta s_\phi - s_\alpha s_\beta c_\phi \right) + \frac{1}{m} \left(Y - F_{thr} c_\alpha s_\beta \right) \right) + p s_\alpha - r c_\alpha \tag{3.56a}$$

$$\dot{y}_E = V_a c_\gamma s_\psi \tag{3.56b}$$

One last generalization of the lateral movement is when the transport aircraft perform equilibrated turns.

3.3.2.1   Steady turn

Considering that the aircraft is turning at constant altitude with a non-zero heading rate, the body-axis angular rates are given by:

$$\Omega = \begin{bmatrix} p \\ q \\ r \end{bmatrix} = L_{BE} \begin{bmatrix} 0 \\ 0 \\ \dot{\psi} \end{bmatrix} \tag{3.57}$$

and the AoA, sideslip angle, and the wind components are zero. It is obtained from (3.4) that $V_B = [u, v, w]^T = [V_a, 0, 0]^T$. Thus, from the force equations in y_B given by (3.14), if is considered that the aerodynamic force is zero, the expression

$$\dot{v} = \frac{1}{m} F_{y_a} + g c_\theta s_\phi + p w - r u \tag{3.58}$$

turns into

$$s_\phi = \frac{V_a r}{g c_\theta} \tag{3.59}$$

In consequence, using the yaw rate of (3.57), the heading rate is obtained:

$$\dot{\psi} = \frac{g}{V_a} tan_\phi \tag{3.60}$$

This relation denotes how banked turns can be performed through the coupling of rolling and yawing motions. Moreover, since banked turns can be performed either as a coordinated turn (coordination of the ailerons and rudder), or uncoordinated turn (skidding or sliding turn), a brief analysis about this subject is provided later.

3.4 Dimensionless Aerodynamic Coefficients

In Section 3.2, the equations (3.13) and (3.21) were given to describe the aerodynamic forces and moments.

$$\begin{bmatrix} D \\ Y \\ L \end{bmatrix} = \frac{1}{2}\rho S V_a^2 \begin{bmatrix} C_D \\ C_Y \\ C_L \end{bmatrix}$$

and

$$\begin{bmatrix} L' \\ M \\ N \end{bmatrix} = \frac{1}{2}\rho S V_a^2 \left(\begin{bmatrix} bC_l \\ \bar{c}C_m \\ bC_n \end{bmatrix} + C_\delta \begin{bmatrix} \delta_{ail} \\ \delta_{ele} \\ \delta_{rud} \end{bmatrix} \right)$$

where

$$C_\delta = \begin{bmatrix} bC_{l_{\delta ail}} & 0 & bC_{l_{\delta rud}} \\ 0 & \bar{c}C_{m_{\delta ele}} & 0 \\ bC_{n_{\delta ail}} & 0 & bC_{n_{\delta rud}} \end{bmatrix}$$

These aerodynamic forces and moments, can be expressed in terms of the *dimensional stability derivatives* (also called aerodynamic derivatives), which are the changes of an aerodynamic force or moment due to a motion variable like (u, v, w, p, q, r). In addition to this, the dimensional stability derivatives are expressed in terms of *nondimensional stability derivatives*, which are the partial derivatives of the force or moment aerodynamic coefficients with respect to a nondimensional motion quantity $(\hat{u}, \hat{v}, \hat{w}, \hat{p}, \hat{q}, \hat{r})$. These nondimensional quantities are given by (Etkin and Reid, 1996) as

$$\hat{u} = \frac{u}{V_a} \quad \hat{v} = \frac{v}{V_a} \quad \hat{w} = \frac{w}{V_a}$$

$$\hat{p} = \frac{pb}{2V_a} \quad \hat{q} = \frac{q\bar{c}}{2V_a} \quad \hat{r} = \frac{rb}{2V_a}$$

An example to clarify this is provided for the aerodynamic rolling moment $L' = \frac{1}{2}\rho V_a^2 S b C_l$. Note that the aerodynamic moments generated by the ailerons and ruder are neglected for the example. Thus, the rolling moment is expressed using the dimensional stability derivatives as

$$L' = L'_v v + L'_p p + L'_r r \tag{3.61}$$

where the derivative L'_r, for example, represents the change in the rolling moment due to the angular velocity r, given by the partial derivative

$$L'_r = \frac{\partial L'}{\partial r} = \frac{1}{2}\rho V_a^2 S b \frac{\partial C_l}{\partial r} \tag{3.62}$$

Thus, considering that the partial derivative can be expressed in terms of a nondimensional quantity, if the expression for $\hat{r} = rb/2V_a$ is included (hence $\partial r = \frac{2V_a}{b}\partial\hat{r}$), (3.62) is rewritten using $C_{l_r} = \frac{\partial C_l}{\partial \hat{r}}$ as

$$L'_r = \frac{1}{4}\rho V_a S b^2 C_{l_r} \tag{3.63}$$

Analogously for the other dimensional derivatives, it is obtained that

$$L'_v = \frac{1}{2}\rho V_a b S C_{l_\beta} \tag{3.64a}$$

$$L'_p = \frac{1}{4}\rho V_a b^2 S C_{l_p} \tag{3.64b}$$

$$L'_r = \frac{1}{4}\rho V_a b^2 S C_{l_r} \tag{3.64c}$$

where C_{l_β}, C_{l_p} and C_{l_r} are the nondimensional stability derivatives. Therefore, (3.61) is rewritten as

$$L' = \frac{1}{2}\rho V_a^2 S b \left(C_{l_\beta}\frac{v}{V_a} + C_{l_p}\frac{pb}{2V_a} + C_{l_r}\frac{rb}{2V_a} \right) \tag{3.65}$$

leading to an expression of the form

$$L' = \frac{1}{2}\rho V_a^2 S b C_l \tag{3.66}$$

where

$$C_l = \left(C_{l_\beta}\frac{v}{V_a} + C_{l_p}\frac{pb}{2V_a} + C_{l_r}\frac{rb}{2V_a} \right) \tag{3.67}$$

Then, considering that $\beta = \frac{v}{V_a}$ by linearizing (3.5b), and neglecting wind effects, it is obtained that

$$C_l = \left(C_{l_\beta}\beta + C_{l_p}\frac{pb}{2V_a} + C_{l_r}\frac{rb}{2V_a} \right) \tag{3.68}$$

In this manner, when the same logic is applied for all the aerodynamic moments, the expression (3.23) is found, denoted by

$$\begin{bmatrix} C_l \\ C_m \\ C_n \end{bmatrix} = \begin{bmatrix} C_{l_\beta}\beta + C_{l_p}\frac{bp}{2V_a} + C_{l_r}\frac{br}{2V_a} \\ C_{m0} + C_{m_\alpha}\alpha + C_{m_q}\frac{cq}{2V_a} \\ C_{n_\beta}\beta + C_{n_p}\frac{bp}{2V_a} + C_{n_r}\frac{br}{2V_a} \end{bmatrix}$$

On the other hand, when the same process is followed for the aerodynamic forces, it is found that the main contribution for the Lift coeficient C_L is given by the AoA (C_{L_α}), for the Sideforce coefficient is the sideslip angle (C_{Y_β}), and the Drag coefficient is obtained from the Lift coefficient. This is denoted by:

$$\begin{bmatrix} C_L \\ C_Y \\ C_D \end{bmatrix} = \begin{bmatrix} C_{L_\alpha}\alpha \\ C_{Y_\beta}\beta \\ C_D(C_L) \end{bmatrix} \tag{3.69}$$

where each nondimensional stability derivative contribution is briefly explained in the next chapter, along with numerical values used for the simulation of a 6DOF transport aircraft.

3.5 Load factor

The load factor, commonly expressed in g units, refers to the fact that an observer on board an aircraft will experience an apparent acceleration of gravity relative to its frame of reference. For example, an observer on board an aircraft performing a turn with a load factor of 2, i.e., a 2g turn, will see objects falling to the aircraft floor at twice the normal acceleration of gravity. Consequently, the observer will have an apparent weight of twice his actual weight.

Since transport aircraft are designed to flight smooth trajectories, some limitations on the load factor have to be respected for the well being and comfort of passengers. According to (*FAA* May 2017), on a typical flight, the load factor is limited to +2.5g and -1g for regular maneuvers, or up to 3.8g in maximum takeoff weight. The expressions for the load factor (in the body frame) of an aircraft are given by

$$n_{cg} = \frac{1}{mg}W_{app} = \frac{1}{mg}\left(mg \begin{bmatrix} -s_\theta \\ c_\theta s_\phi \\ c_\theta c_\phi \end{bmatrix} + mV_B \times \Omega \right) \tag{3.70}$$

where W_{app} is the apparent weight of the aircraft. Some relations can be extracted from assumptions on these equations. The case of a steady turn is considered first. Thus, rewriting (3.70) in a scalar form yields to

$$n_x = -s_\theta + \frac{(rv - qw)}{g} \tag{3.71a}$$

$$n_y = c_\theta s_\phi + \frac{(pw - ru)}{g} \tag{3.71b}$$

$$n_z = c_\theta c_\phi + \frac{(qu - pv)}{g} \tag{3.71c}$$

Separately, under the assumptions of a steady turn given by (3.57), it was obtained the relation (3.60). This relation can also be obtained by assuming $n_y = 0$ and using (3.57).

Hence, using (3.57) and (3.60) in (3.71c), it is obtained that

$$n_z = \frac{c_\theta}{c_\phi} \tag{3.72}$$

Note that the bigger value of n_z is obtained when $\theta = 0$. In this way, the maximum bank angle before reaching a 2.5g limit is 66.5°.

Another analysis that can be done is the one involving the centrifugal acceleration (see Figure 3.6), yielding

$$\frac{mV_a^2}{R} = Ls_\phi \tag{3.73a}$$

$$Lc_\phi = W \tag{3.73b}$$

Therefore, (3.73b) can be rewritten as

$$\frac{L}{W} = \frac{1}{c_\phi} = n_z \tag{3.74}$$
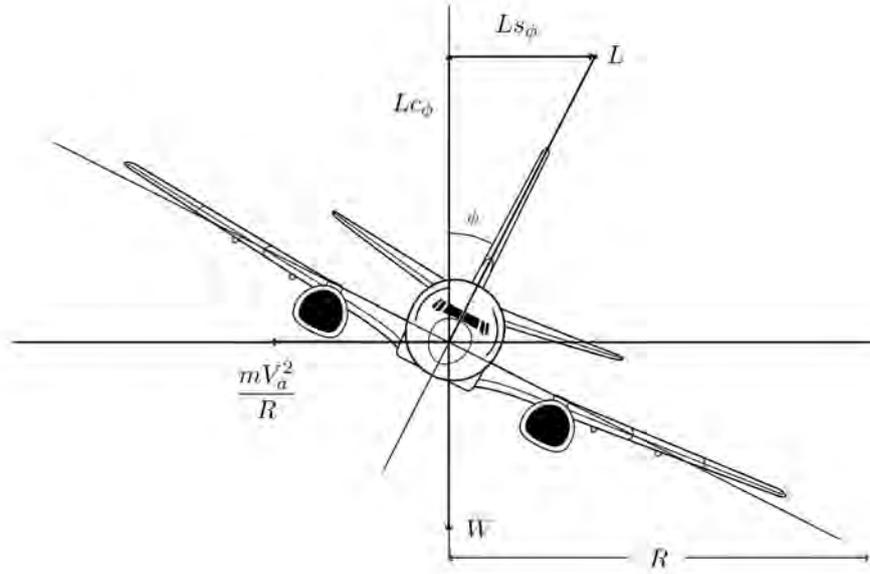
FIGURE 3.6: Steady turn forces.

which is also when $\theta = 0$ in (3.72). Then, using this relation into (3.73a), the load factor can be related with the radius of an horizontal curvature R as

$$R = \frac{1}{n_z} \frac{V_a^2}{g s_\phi} \tag{3.75}$$

Moreover, using (3.74) and the Pythagorean identity, it is obtained

$$\frac{1}{n_z^2} + s_\phi^2 = 1 \tag{3.76}$$

such that

$$s_\phi = \sqrt{1 - \frac{1}{n_z^2}} \tag{3.77}$$

In consequence, (3.75) is expressed completely in terms of the load factor as

$$R = \frac{V_a^2}{g \sqrt{n_z^2 - 1}} \tag{3.78}$$

Arriving to an expression relating the load factor that an aircraft would experience if a curved horizontal path of radius R was flown, at a given speed.

On the other hand, if a pitch up motion is assumed (see Figure 3.7), the considerations of $\phi = p = 0$, $u = V_a$, and $\theta = 0$ for a maximum load factor, applied to (3.71c) yield to

$$n_z = 1 + \frac{q V_a}{g} \tag{3.79}$$

which can be expressed as

$$q = \frac{(n_z - 1) g}{V_a} = \frac{V_a}{R'} \tag{3.80}$$

where R' is the radius of the vertical curve.

As a remark, consider the case of a flight at constant altitude. This can be repre-

FIGURE 3.7: Pitch up motion.

sented as a pitch up motion with an infinite radius $R' = \infty$. Thus, from (3.80), it can be said that since V_a is a given non-zero value, the expression $(n_z - 1)\, g \approx 0$ must be true. Therefore, since g is the gravity, the only solution is $n_z = 1$, which corresponds to a flight with constant altitude.

3.6   Compilation of equations

3.6.1   Complete Aircraft Dynamics

3.6.1.1   Guidance equations

$$\begin{bmatrix} \dot{u} \\ \dot{v} \\ \dot{w} \end{bmatrix} = \begin{bmatrix} \frac{1}{m}\left(F_{x_a} + F_{thr}\right) - gs_\theta + rv - qw \\ \frac{1}{m}F_{y_a} + gc_\theta s_\phi + pw - ru \\ \frac{1}{m}F_{z_a} + gc_\theta c_\phi + qu - pv \end{bmatrix} \tag{3.81}$$

$$\begin{bmatrix} F_{x_a} \\ F_{y_a} \\ F_{z_a} \end{bmatrix} = L_{BW} \begin{bmatrix} -D \\ Y \\ -L \end{bmatrix} \tag{3.82}$$

$$\begin{bmatrix} D \\ Y \\ L \end{bmatrix} = \frac{1}{2}\rho S V_a^2 \begin{bmatrix} C_D \\ C_Y \\ C_L \end{bmatrix} \tag{3.83}$$

$$V_E = \begin{bmatrix} \dot{x_E} \\ \dot{y_E} \\ \dot{z_E} \end{bmatrix} = L_{EB} \begin{bmatrix} u \\ v \\ w \end{bmatrix} \tag{3.84}$$

$$V_B = \begin{bmatrix} u \\ v \\ w \end{bmatrix} = \begin{bmatrix} V_a c_\alpha c_\beta + V_{w_x} \\ V_a s_\beta + V_{w_y} \\ V_a s_\alpha c_\beta + V_{w_z} \end{bmatrix} \tag{3.85}$$

$$\begin{bmatrix} \ddot{x}_E \\ \ddot{y}_E \\ \ddot{z}_E \end{bmatrix} = L_{EB} \begin{bmatrix} F_{x_a} + F_{thr} \\ F_{y_a} \\ F_{z_a} \end{bmatrix} \frac{1}{m} + \begin{bmatrix} 0 \\ 0 \\ g \end{bmatrix} \tag{3.86}$$

3.6.1.2   Attitude equations

$$\begin{bmatrix} \dot{p} \\ \dot{q} \\ \dot{r} \end{bmatrix} = \frac{1}{B(AC - E^2)} \begin{bmatrix} BC & 0 & BE \\ 0 & AC - E^2 & 0 \\ BE & 0 & AB \end{bmatrix} \begin{bmatrix} (B-C)qr + Epq + L' \\ (C-A)pr - E(p^2 - r^2) + M \\ (A-B)pq - Erq + N \end{bmatrix} \tag{3.87}$$

$$\begin{bmatrix} L' \\ M \\ N \end{bmatrix} = \frac{1}{2}\rho S V_a^2 \left(\begin{bmatrix} bC_l \\ \bar{c}C_m \\ bC_n \end{bmatrix} + \begin{bmatrix} bC_{l_{\delta ail}} & 0 & bC_{l_{\delta rud}} \\ 0 & \bar{c}C_{m_{\delta ele}} & 0 \\ bC_{n_{\delta ail}} & 0 & bC_{n_{\delta rud}} \end{bmatrix} \begin{bmatrix} \delta_{ail} \\ \delta_{ele} \\ \delta_{rud} \end{bmatrix} \right) \tag{3.88}$$

$$\begin{bmatrix} \dot{\phi} \\ \dot{\theta} \\ \dot{\psi} \end{bmatrix} = \begin{bmatrix} 1 & tg_\theta s_\phi & tg_\theta c_\phi \\ 0 & c_\phi & -s_\phi \\ 0 & \frac{s_\phi}{c_\theta} & \frac{c_\phi}{c_\theta} \end{bmatrix} \begin{bmatrix} p \\ q \\ r \end{bmatrix} \tag{3.89}$$

$$\begin{bmatrix} \dot{\alpha} \\ \dot{\beta} \\ \dot{V}_a \end{bmatrix} = \begin{bmatrix} H_{11} & H_{12} & H_{13} \\ H_{21} & H_{22} & H_{23} \\ H_{31} & H_{32} & H_{33} \end{bmatrix} \begin{bmatrix} p \\ q \\ r \end{bmatrix} + \begin{bmatrix} Q_1 \\ Q_2 \\ Q_3 \end{bmatrix} \tag{3.90}$$

3.6.1.3   Actuator equations

$$\dot{\delta}_i = \frac{1}{\xi_i}\left(\delta_i^d - \delta_i\right) \tag{3.91}$$

$$\dot{F}_{thr} = \frac{1}{\xi_T} \left(F_{thr}^d - F_{thr} \right) \tag{3.92}$$

3.6.2   Reduced Aircraft Dynamics

3.6.2.1   Longitudinal motion

$$\dot{\gamma} = \frac{1}{mV_a} \left(L + F_{thr}s_\alpha - mgc_\gamma \right) - q\left(\frac{V_{w_x}c_\alpha + V_{w_z}s_\alpha}{V_a} \right) + \frac{1}{V_a}\left(\dot{V}_{w_z}c_\alpha - \dot{V}_{w_x}s_\alpha \right) \tag{3.93}$$

$$\dot{V}_a = \frac{1}{m}\left(F_{thr}c_\alpha - D - mgs_\gamma \right) + q\left(V_{w_x}s_\alpha - V_{w_z}c_\alpha \right) - \dot{V}_{w_x}c_\alpha - \dot{V}_{w_z}s_\alpha \tag{3.94}$$

$$\dot{x}_E = V_a c_\gamma c_\psi + V_{w_x}c_\theta c_\psi + V_{w_z}s_\theta c_\psi \tag{3.95}$$

$$\dot{z}_E = -V_a s_\gamma - V_{w_x}s_\theta + V_{w_z}c_\theta \tag{3.96}$$

$$\dot{\theta} = q \tag{3.97}$$

$$\dot{q} = \frac{M}{B} \tag{3.98}$$

3.6.2.2   Lateral motion

$$\dot{\beta} = \frac{1}{V_a} \left(g\left(c_\beta s_\phi - s_\alpha s_\beta c_\phi \right) + \frac{1}{m}\left(Y - F_{thr}c_\alpha s_\beta \right) \right) + p\left(s_\alpha + \frac{V_{w_z}c_\beta + V_{w_y}s_\alpha s_\beta}{V_a} \right)$$
$$+ r\left(-c_\alpha - \frac{\left(V_{w_y}c_\alpha s_\beta + V_{w_x}c_\beta \right)}{V_a} \right) + \frac{1}{V_a}\left(\dot{V}_{w_x}c_\alpha s_\beta - \dot{V}_{w_y}c_\beta + \dot{V}_{w_z}s_\alpha s_\beta \right) \tag{3.99}$$

$$\dot{y}_E = V_a c_\gamma s_\psi + V_{w_x}c_\theta s_\psi + V_{w_y}c_\psi + V_{w_z}s_\theta s_\psi \tag{3.100}$$

$$\dot{\psi} = \frac{g}{V_a}tan_\phi \tag{3.101}$$

$$\dot{\phi} = p \tag{3.102}$$

$$\dot{\psi} = rc_\phi \tag{3.103}$$

$$\dot{p} = \frac{1}{AC - E^2}\left(CL' + EN \right) \tag{3.104}$$

$$\dot{r} = \frac{1}{AC - E^2}\left(EL' + AN \right) \tag{3.105}$$

3.6.3   Load Factor equations

$$n_x = -s_\theta + \frac{(rv - qw)}{g} \tag{3.106}$$

$$n_y = c_\theta s_\phi + \frac{(pw - ru)}{g} \tag{3.107}$$

$$n_z = c_\theta c_\phi + \frac{(qu - pv)}{g} \tag{3.108}$$

3.7   Conclusion

The principal reference frames and their corresponding rotation matrices were provided. They allow a particular representation of a 6DOF aircraft motion using a set of nonlinear differential equations. These equations were rearranged so they fit into the purposes of this work. A clear example is the wind consideration in the AoA, sideslip and airspeed, instead of a wind disturbance directly in the aircraft position. Furthermore, an introduction to the aerodynamic coefficients of an aircraft was provided. Nevertheless, this topic is complemented in Chapter 4.

In addition to this, load factor assumptions for the pitching motion and steady turns have been considered, such that instead of expressing the load factor of an aircraft depending on the aircraft state, it was expressed depending on the curvature of the trajectory that is following. Thus, the obtained expressions could be used for path generation purposes.

No aeroelasticity effects were considered, nor the effects of high lift devices or drag generating elements such as flaps, slats or landing gear.

Chapter 4

6DOF Transport Aircraft Simulation using MATLAB

After obtaining all the nonlinear differential equations that describe the full behaviour of a transport aircraft, these are used to develop a six degree of freedom Matlab (Matlab, 2017) model, described in this chapter. The aircraft parameters were chosen similar to an aircraft type Boeing 737-200 or an Airbus 320-200, flying in an International Standard Atmosphere model with uniform gravity.

One of the main challenges of simulating a full aircraft is in obtaining the aerodynamic nondimensional coefficient values. This is because each coefficient is composed by one or more nondimensional stability derivatives, and that they differ from plane to plane. In general, resources like fluid analysis, wind tunnel tests, or data bases are available to obtain these values. However, issues are encountered for each option.

In this work, the lack of wind tunnels and need of an aircraft mock up, as well as steakholders not sharing easily enough this information, has led to software analysis.

Hence, data bases were obtained only from public domain softwares, such that anyone is able to reproduce or modify the presented approach. First, the static stability, control and dynamic derivative characteristics of the chosen aircraft are computed using the methods contained in the USAF Stability and Control DATCOM. Then, the obtained data is compared and refined using the corresponding JSBSim open source Flight Dynamic Model (FDM). JSBSim is employed to drive the motion-base research simulators of many universities worldwide.

Furthermore, due to the complexity and size of the data bases, two-layer feed-forward neural networks with sigmoid hidden neurons and linear output neurons were trained to obtain the values of the coefficients: $C_{D,Y,L}, C_{l_{\beta,p,r,\delta ail,\delta rud}}; C_{m_{0,\alpha,q,\delta ele}}; C_{n_{\beta,p,r,\delta ail,\delta rud}}$, allowing to develop a complete aircraft model.

As a result, Section 4.1 of this chapter is subdivided in three subsections. Subsections 4.1.1 and 4.1.2 are an extensive background on machine learning towards supervised learning, in order to better understand the neural networks used in the simulation. Subsection 4.1.3, regards to relevant information about the stability derivatives as well as their numerical values for our case study.

Section 4.2 shows the aircraft behaviour in open loop, so that the model is verified according to the theory presented.

Finally, conclusions are given in Section 4.4.

4.1 Aerodynamic Coefficients using Neural Networks

The theory in Subsections 4.1.1 and 4.1.2 is an extract from (Bishop, 2006), presented in order to provide the necessary elements for the neural networks developed in this chapter.

4.1.1 Introduction to Machine Learning

Consider the example of recognizing handwritten digits, the goal is to build a machine that will take an image as an input, and will produce as output the digit from 0 to 9 corresponding to the image, this is a nontrivial problem due to the variability of handwriting, so a machine learning algorithm suits the example. Lets consider for this algorithm a large set N of handwritten digits $\{x_1, \ldots, x_N\}$, called the *training set*, used to tune the parameters of an adaptive model. The desired output of the training set is known in advance, typically by inspecting them individually and labelling the corresponding digits manually, this output set is called the *target vector* $\{t_1, \ldots, t_N\}$.

By running the machine learning algorithm, a function $y(x)$ can be obtained which takes an input x and generates an output y, encoded in the same way as the target vector. The form of $y(x)$ is determined in the training phase, using the training data. Once the model is trained, it can determine numbers from handwritten images, so tests of the performance of the model are done using the *test set*. This is known as *generalization*: the ability to categorize new examples that differ from those used for training. Both the training set and the test set are obtained from a labelled data base. The training set is used to train the model and obtain the candidate algorithms. Then, a model is selected based on the best performing approach (*model selection*). Finally the accuracy of the selected approach is computed using the test set.

Applications where the training data comprises examples of the input vectors along with their corresponding target vectors are known as *Supervised Learning* problems. If the desired output consists of one or more continuous variables, then the task is called *regression*. An example of regression is the typical polynomial curve fitting, briefly described as follows.

4.1.1.1 Polynomial Curve fitting

Suppose that a curve $f(x)$ is to be fitted on a set of data. To perform the task, a training set comprising N observations in x of the curve $(x_1, \ldots, x_N)^T$, along with its target vector $(t_1, \ldots, t_N)^T$, given by the value of $f(x)$ with some added noise, are supposed to be given. Then, a basic curve fitting can be proposed by the function:

$$y(x, w) = w_0 + w_1 x + w_2 x^2 + \ldots + w_M x^M = \sum_{j=0}^{M} w_j x^j \qquad (4.1)$$

where M is the order of the polynomial, and x^j denotes x raised to the power of j. The coefficients $w_0, \ldots, w_M$ (*weights*) are denoted by the vector w. Note that $y(x, w)$ is a nonlinear function of x, but is a linear function of the coefficients w. So functions such as the polynomial, linear in the unknown parameters w, are called *linear models*. The values of w are determined by fitting the polynomial to the training set by minimizing an *error function*.

Assuming that x_n are the values of x for $n = 1, \ldots, N$, a common error function is

given by the sum of the squares of the error between the predictions $y(x_n, w)$ for each data point x_n and the corresponding target values t_n:

$$E(w) = \frac{1}{2} \sum_{n=1}^{N} \{y(x_n, w) - t_n\}^2 \tag{4.2}$$

The curve fitting problem can be solved by choosing values for w, such that $E(w)$ is as small as possible. Since the error function is a quadratic function of the coefficients w, its derivatives with respect the coefficients will be linear in the elements of w, and so the minimization of the error function has a unique solution w^*, which can be found in closed form. The resulting polynomial will be given by $y(x, w^*)$. Then, the remaining problem is to choose the order M of the polynomial, in other words, the model selection. Some problems of the model selection are a poor representation of the curve to be fitted, and the *over-fitting* phenomenon, which will happen if $E(w^*) = 0$, but the polynomial does not fit properly the curve proposed. Since the goal is to make a good generalization by making accurate predictions for new data, a good model selection can be made by evaluating for each choice of M, the residual value of $E(w^*)$ (given by (4.2)) for the training data. Moreover, $E(w^*)$ can be evaluated for the test set to measure how well the model is predicting the values of t for new data observations of x. It is convenient to use the root-mean-square error, measured in the same scale and units as the target variable t, defined by:

$$E_{RMS} = \sqrt{2E(w^*)/N} \tag{4.3}$$

As the size of N increases, the more complex model can be used to fit to the data. In addition to this, it will be seen that the use of least squares to find the model parameters represents a specific case of *maximum likelihood*, and the over-fitting problem can be understood as a general property of maximum likelihood. Therefore, in order to avoid the over-fitting problem, a Bayesian approach can be adopted.

Another technique often used to control the over-fitting problem is the *regularization*, which involves adding a penalty term to the error function (4.2) in order to discourage the coefficients from reaching large values. The simplest expression of the new error function under this idea is expressed by:

$$\tilde{E}(w) = \frac{1}{2} \sum_{n=1}^{N} \{y(x_n, w) - t_n\}^2 + \frac{\lambda}{2} \|w\|^2 \tag{4.4}$$

where $\|w\|^2 = w^T w = w_0^2 + w_1^2 \ldots + w_M^2$, and the coefficient λ handles the relative importance of the regularization term compared with the sum-of-squares error term. The particular case of a quadratic regularizer is called *ridge regression*. Besides, an effect of the regularization is to reduce the magnitude of the coefficients w.

In gerneral, the training set will be used to determine the coefficients w, and the validation set will be used to optimize the model complexity (M, λ).

4.1.1.2 Bayesian Approach

Imagine two boxes, one red, one blue, with the red box containing 2 apples and 6 oranges, and the blue containing 3 apples and 1 orange. Suppose that one of the boxes is picked randomly, and one fruit is selected from the box. Then, after seeing the sort of fruit that was picked, it is put back in the box. Assume that the red box is picked the 40% of time and the blue the other 60%. By denoting the random

variables B for box, F for fruit, and the values of $r = red$, $b = blue$, $a = apple$, and $o = orange$, the probability of selecting the red box is expressed as $p(B = r) = 4/10$ and $p(B = b) = 6/10$. Note that all probabilities must lie in the interval $[0, 1]$, and that the probability of an event is defined as the fraction of times that the event occurs out of the total number of trials, in the limit that the total number of trials tends to infinity. Note also that $p(B = r) + p(B = b) = 1$.

In the same way, it is known that the probability of selecting an apple from the blue box is $3/4$, so the *conditional* probabilities, starting with the latter mentioned are:

- $p(F = a|B = b) = 3/4$

- $p(F = a|B = r) = 1/4$

- $p(F = o|B = b) = 1/4$

- $p(F = o|B = r) = 3/4$

Again, lets note that

$$p(F = a|B = r) + p(F = o|B = r) = p(F = a|B = b) + p(F = o|B = b) = 1 \quad (4.5)$$

and using the rules of sum and product of probability, the overall probability of choosing an apple can be evaluated by:

$$p(F = a) = p(F = a|B = r)p(B = r) + p(F = a|B = b)p(B = b)$$
$$= \frac{1}{4} \times \frac{4}{10} + \frac{3}{4} \times \frac{6}{10} = \frac{11}{20} \quad (4.6)$$

so, $p(F = o) = 1 - 11/20 = 9/20$.

Now, lets assume that a fruit has been selected and it is an orange, and it is desired to know from which box it came from, one can solve the problem of reversing the conditional probability by using the *Bayes theorem*. This yields:

$$p(B = r|F = o) = \frac{p(F = o|B = r)p(B = r)}{p(F = o)}$$
$$= \frac{3}{4} \times \frac{4}{10} \times \frac{20}{9} = \frac{2}{3} \quad (4.7)$$

so, $p(B = b|F = o) = 1 - 2/3 = 1/3$.

An important interpretation of the Bayes theorem can be provided. If it would have been asked which box had been chosen before being told the selected fruit, then the most complete information available is provided by the probability $p(B)$. This is called the *prior probability*, because it is the probability available before the observation of the identity of the fruit. Once it is known that the fruit is an orange, the Bayes theorem can be used to compute the probability $p(B|F)$, which will be called the *posterior probability*, because is the probability obtained after the observation of F. Note that the prior probability of selecting the red box was $4/10$, so it is more likely to select the blue box. However, once it was observed that the selected fruit is an orange, the posterior probability of the red box is now $2/3$, so that it is now more likely that the box selected was in fact the red one. Corroborating that the observation that the fruit was an orange, provides significant evidence favouring the red box. Moreover, this evidence is strong enough to outweigh the prior probability of selecting the blue box.

Now, after pointing out the advantages of a *Bayesian* approach, where probabilities

provide a quantification of uncertainty rather than the typical *frequentist* interpretation of probability based on frequencies of random, repeatable events, let us reconsider the polynomial curve fitting example.

In the polynomial fitting, assumptions about the parameters w can be made before observing the data, in the form of a prior probability distribution $p(w)$. Then, the effect of the observed data $D = \{t_1, \dots, t_N\}$ is expressed through the conditional probability $p(D|w)$, and it will be shown how this can be represented explicitly. Hence, the Bayes theorem takes the form of

$$p(w|D) = \frac{p(D|w)p(w)}{p(D)} \tag{4.8}$$

which allows the evaluation of the uncertainty in w after the observation of D in the form of the posterior probability $p(w|D)$.

The quantity $p(D|w)$ of (4.8) is evaluated for the observed data set D and can be viewed as a function of the parameter vector w, in which case it is called the *likelihood function*. It expresses how probable the observed data set is for different settings of the parameter vector w. Note that the likelihood is not a probability distribution over w. Hence, its integral with respect to w does not (necessarily) equal to one. In other words, the Bayes theorem can be expressed as:

$$posterior \propto likelihood \times prior$$

where all these are viewed as functions of w. The term $p(D)$ in (4.8) is the normalization constant, which ensures that the left hand-side of the equation is a valid probability density and integrates to one.

In both Bayesian and frequentist paradigms, the likelihood function $p(D|w)$ is fundamental but is used differently depending on the approach. For the frequentist setting, w is considered to be a fixed parameter, which is determined by some "estimator", and error bars on this estimate are obtained by considering the distribution of possible data sets D. On the other hand, for the Bayesian approach, there is only a single data set D, which is the one observed, and the uncertainty in the parameters is expressed through a probability distribution over w.

In the *maximum likelihood* frequentist estimator, w is set to the value that maximizes the likelihood function. This corresponds to choosing w such that the probability of the observed data set is maximized.

In the machine learning literature, the monotonically decreasing function given by the negative log of the likelihood function is the error function, because maximizing the likelihood is equivalent to minimizing the error.

The advantage of the Bayesian approach can be seen in the inclusion of prior knowledge. Suppose for example that a coin is flipped three times, and every time it lands heads. The classical maximum likelihood estimate of the probability of landings heads would be 1, implying that all future tosses will be heads. In contrast, the Bayesian approach with reasonable prior information will lead to a less extreme conclusion.

Therefore, in the curve fitting problem viewed from a probabilistic perspective, the goal is to make predictions for the target variable t given a new value of the scalar input variable x, using a training set comprising N input observation values $\mathfrak{X} = (x_1, \dots, x_N)^T$ and their corresponding target values $\mathfrak{T} = (t_1, \dots, t_N)^T$. In this manner, the uncertainty over the value of the target variable can be expressed using a probability distribution. For this purpose, it is assumed that, given the value of x,

the corresponding value of t has a Gaussian distribution[1] with a mean equal to the value $y(x, w)$ of the polynomial curve given by (4.1). Thus:

$$p(t|x, w, \beta) = \mathcal{N}(t|y(x, w), \beta^{-1}) \tag{4.9}$$

where β corresponds to the inverse variance of the Gaussian distribution.

Now, the values of the unknown parameters w and β are determined using the training data $\{\mathfrak{X}, \mathfrak{T}\}$ via maximum likelihood. If the training data is assumed to be taken independently from the distribution (4.9), then the likelihood function is given by

$$p(\mathfrak{T}|\mathfrak{X}, w, \beta) = \prod_{n=1}^{N} \mathcal{N}(t_n|y(x_n, w), \beta^{-1}) \tag{4.10}$$

As shown in the Appendix B.2, where the maximum likelihood approach is used to perform a regression of a Gaussian distribution, it is convenient to maximize the logarithm of the likelihood function. In this manner, using (B.1), which describes mathematically the Gaussian distribution, it is obtained

$$\ln p(\mathfrak{T}|\mathfrak{X}, w, \beta) = -\frac{\beta}{2} \sum_{n=1}^{N} \{y(x_n, w) - t_n\}^2 + \frac{N}{2}\ln\beta - \frac{N}{2}\ln(2\pi) \tag{4.11}$$

The first maximum likelihood solution for the polynomial coefficients will be denoted by w_{ML}, obtained by maximizing (4.11) with respect to w. Some interesting results are derived from this. Note that the last 2 terms of the right-hand side can be omitted, as they do not depend on w. Then, scaling the log likelihood by a positive constant coefficient β, does not alter the location of the maximum with respect to w. Consequently, $\beta/2$ can be replaced by $1/2$. Finally, instead of maximizing the log likelihood, is equivalent to minimize the negative log likelihood. Therefore, it is clearly seen that maximizing the likelihood to obtain the parameters w is the same as minimizing the *sum-of-squares error function*, defined previously in (4.2). Thus the sum-of-squares error function is a consequence of maximizing the likelihood under the assumption of a Gaussian noise distribution.

Also, maximizing (4.11) with respect to the precision parameter β of the Gaussian conditional distribution yields

$$\frac{1}{\beta_{ML}} = \frac{1}{N} \sum_{n=1}^{N} \{y(x_n, w_{ML}) - t_n\}^2 \tag{4.12}$$

Now that the parameters w and β have been determined, predictions for new values of x can be made. Since a probabilistic model is obtained, the predictions are expressed by a *predictive distribution* that gives the probability distribution over t rather than simply a point estimate. Hence (4.9) turns into

$$p(t|x, w_{ML}, \beta_{ML}) = \mathcal{N}(t|y(x, w_{ML}), \beta_{ML}^{-1}) \tag{4.13}$$

Therefore, in order to advance towards a Bayesian approach, it is introduced a Gaussian prior distribution over the polynomial coefficients w, given by

$$p(w|\alpha) = \mathcal{N}(w|0, \alpha^{-1}\mathrm{I}) = \left(\frac{\alpha}{2\pi}\right)^{(M+1)/2} \exp\left\{-\frac{\alpha}{2}w^T w\right\} \tag{4.14}$$

---

[1] For more information on Gaussian distribution, refer to Appendix B.1

where α is the precision of the distribution, and $M+1$ is the total number of elements in the vector w for an Mth order polynomial. Variables such as α, which control the distribution of model parameters, are called *hyperparameters*. Then, using the Bayes theorem, the posterior distribution for w is proportional to the product of the prior distribution and the likelihood function, denoted by

$$p(w|\mathfrak{X}, \mathfrak{T}, \alpha, \beta) \propto p(\mathfrak{T}|\mathfrak{X}, w, \beta)p(w|\alpha) \tag{4.15}$$

In this manner, w can be determined by finding the most probable value of w given the data. This, therefore, involves maximizing the posterior distribution, and using the technique is called *maximum posterior*. Taking the negative logarithm of (4.15) and using (4.11) and (4.14), the maximum of the posterior is given by the minimum of

$$\frac{\beta}{2}\sum_{n=1}^{N}\{y(x_n, w) - t_n\}^2 + \frac{\alpha}{2}w^T w \tag{4.16}$$

At this point, it is clear that maximizing the posterior distribution is equivalent to minimizing the regularized sum-of-squares error function encountered in (4.4), with a regularization parameter denoted by $\lambda = \alpha/\beta$

4.1.1.3 Bayesian curve fitting

Knowing the training data $\mathfrak{X}$ and $\mathfrak{T}$, along with a new test point x, the goal is to predict the value of t. Therefore, the predictive distribution $p(t|x, \mathfrak{X}, \mathfrak{T})$ needs to be evaluated. It is assumed that the parameters α and β are known in advance. Thus, the predictive distribution can be written as

$$p(t|x, \mathfrak{X}, \mathfrak{T}) = \int p(t|x, w)p(w|\mathfrak{X}, \mathfrak{T})dw \tag{4.17}$$

where $p(t|x, w)$ is given by (4.9), omitting the dependence on α and β to reduce notation. Here $p(w|\mathfrak{X}, \mathfrak{T})$ is the posterior distribution over parameters, and can be found by normalizing the right-hand side of (4.15). This posterior distribution will turn out to be a Gaussian and can be evaluated analytically. Similarly, the integration in (4.17) can also be performed analytically with the result that the predictive distribution is given by a Gaussian of the form

$$p(t|x, \mathfrak{X}, \mathfrak{T}) = \mathcal{N}(t|\mu(x), \sigma^2(x)) \tag{4.18}$$

where the mean (μ) and variance (σ^2) are given by

$$\mu(x) = \beta\phi(x)^T S\sum_{n=1}^{N}\phi(x_n)t_n \tag{4.19}$$

$$\sigma^2(x) = \beta^{-1} + \phi(x)^T S\phi(x) \tag{4.20}$$

and the matrix S is expressed by

$$S^{-1} = \alpha I + \beta \sum_{n=1}^{N}\phi(x_n)\phi(x)^T \tag{4.21}$$

where I is the unit matrix, and the vector $\phi(x)$ is defined with the elements $\phi_i(x) = x^i$ for $i = 0, \ldots, M$. The mean and the variance of the predictive distribution in (4.18)

are dependent on x.

In this manner, the first term in (4.20) represents the uncertainty in the predicted value of t due to the noise of the target variables and was expressed in the maximum likelihood predictive distribution (4.13) through β^{-1}. However, the second term comes from the uncertainty in the parameters w and is a consequence of the Bayesian treatment.

4.1.1.4 Model Selection

In the polynomial curve fitting example using least squares, the optimal order of the polynomial is the one that gives the best generalization, and the order (M) of the polynomial controls the number of free parameters (w) in the model, and therefore, the model complexity. In the case of regularized least squares, the regularization co-efficient (λ) also controls the complexity of the model, and for more complex models, there may be multiple parameters governing complexity. In a practical application, the values of these coefficients must be determined such that the best prediction performance on new data is achieved.

It has been seen in the maximum likelihood approach that the performance on the training set is not a good indicator of predictive performance on unseen data due to the over-fitting problem. So one approach is to use some of the available data to train a range of models, or a given model with a range of values for its complexity parameters. Then, the models are compared using independent data, called a *validation set*, and finally the model with the best predictive performance is selected.

If the validation set is too small, it will give a relatively noisy estimate of predictive performance, so one solution to this is *cross validation*. The cross validation technique consists in dividing the available data in S groups and taking $S - 1$ groups to train a set of models that are evaluated in the remaining group. This is repeated for all S possible choices, and then the scores from the S runs are averaged. The disadvantage of this approach is that the computational complexity is increased as the number of training runs is increased by a factor S, and exponentially increased if several parameters are tested in different combinations.

4.1.1.5 Linear Models for Regression

Consider that the goal of regression is to predict the value of one or more target variables t given the value of a $D-$dimensional vector x of input variables. Given a training data set comprising N observations $\{x_n\}$, where $n = 1, \ldots, N$, together with their correspondent target values t_n, the goal is to predict the value of t for a new value of x. Note that $x = (x_1, \ldots, x_D)^T$.

The simplest linear model for regression is a linear combination of the input variables:

$$y(x, w) = w_0 + w_1 x_1 + \ldots + w_D x_D \tag{4.22}$$

This is known as *linear regression*, with a linear function of the parameters $w_0, \ldots, w_D$ and a linear function of the inputs variables $x_1, \ldots, x_D$. However, much more useful class of functions can be obtained by taking linear combinations of a fixed set of nonlinear functions of the input variables, known as *basis functions*. Hence:

$$y(x, w) = w_0 + \sum_{j=1}^{M-1} w_j \phi_j(x) \tag{4.23}$$

where $\phi_j(\text{x})$ are the basis functions. By denoting the maximum value of the index j by $M-1$, the total number of parameters will be M.

The parameter w_0, called *bias*, allows to introduce a fixed offset in the data. It is useful to define an additional basis function $\phi_0(\text{x}) = 1$ so that

$$y(\text{x}, w) = \sum_{j=0}^{M-1} w_j \phi_j(\text{x}) = w^T \phi(\text{x}) \tag{4.24}$$

where $w = (w_0, \dots, w_{M-1})^T$ and $\phi = (\phi_0, \dots, \phi_{M-1})^T$.

By using nonlinear basis functions, $y(\text{x}, w)$ is allowed to be a nonlinear function of the input vector x.

An example of a linear model is the polynomial regression for fitting a curve, where instead of having an input vector x, a single input variable x is needed, so the basis functions take the form $\phi_j(x) = x^j$.

There are many other possible choices for the basis functions, for example

$$\phi_j(x) = exp\left\{-\frac{(x-\mu_j)^2}{2s^2}\right\} \tag{4.25}$$

where μ_j governs the locations of the basis functions in input space, and the parameter s governs their spatial scale. This is known as a Gaussian basis function. Another possibility is the sigmoidal basis function:

$$\phi_j(x) = \sigma\left(\frac{x-\mu_j}{s}\right) \tag{4.26}$$

where

$$\sigma(a) = \frac{1}{1 + exp(-a)} \tag{4.27}$$

Equivalently, the hyperbolic tangent ($tanh$) function can be used, knowing that

$$tanh(a) = 2\sigma(a) - 1 \tag{4.28}$$

Another possible choice of basis functions is the Fourier basis, which leads to an expansion in sinusoidal functions. Also, a class of functions known as wavelets are more applicable for signal processing problems.

4.1.2 Neural Networks Model

So far, models for regressions comprising linear combinations of fixed basis functions have been considered. However, as they are limited by dimensionality, the basis functions can be adapted to the data. One approach to do this is to fix the number of basis functions in advance but allowing them to be adaptive. In other words, to use parametric forms for the basis functions in which the parameters values are adapted during training. The most successful model of this is the *feed-forward neural network*, also known as the *multilayer perceptron*, which gives a compact, fast model, with high generalization performance.

The linear models for regression are based on linear combinations of fixed nonlinear

basis functions $\phi_j(\text{x})$ with the form

$$y(\text{x}, w) = f\left(\sum_{j=1}^{M} w_j \phi_j(\text{x})\right) \tag{4.29}$$

where $f(\cdot)$ is a nonlinear activation function equal to the identity in the case of regression. Neural networks (NNs) use basis functions that follow the same form as (4.29). Therefore, each basis function is itself a nonlinear function of a linear combination of the inputs, where the coefficients in the linear combination are adaptive parameters.

Then, it is time to provide the basic neural network model.

First, M linear combinations of the input variables $x_1, \ldots, x_D$ are constructed in the form

$$a_j = \sum_{i=1}^{D} w_{ji}^{(1)} x_i + w_{j0}^{(1)} \tag{4.30}$$

where $j = 1, \ldots, M$, and the superscript (1) indicates that the corresponding parameters are in the first layer of the network. From now on, $w_{ji}^{(1)}$ are referred to as *weights*, and the parameters $w_{j0}^{(1)}$ as *biases*. The quantities a_j are known as *activations*. Each of them is transformed using a differentiable nonlinear activation function $h(\cdot)$ to give

$$z_j = h(a_j) \tag{4.31}$$

These quantities correspond to the outputs of the basis functions in (4.29), referred to as *hidden units*. The typical choice for the nonlinear functions $h(\cdot)$ are sigmoidal functions. Thus, following (4.29), these values are again linearly combined to give *output unit activations*

$$a_k = \sum_{j=1}^{M} w_{kj}^{(2)} z_j + w_{k0}^{(2)} \tag{4.32}$$

where $k = 1, \ldots, K$, and K is the total number of outputs. This transformation corresponds to the second layer of the network. Finally, the output unit activations are transformed using an appropriate activation function to give a set of network outputs y_k. The activation function is the identity in regression problems, such that

$$y_k = a_k \tag{4.33}$$

Combining the stages, the overall network function for a regression problem takes the form

$$y_k(\text{x}, \text{w}) = \sum_{j=1}^{M} w_{kj}^{(2)} h\left(\sum_{i=1}^{D} w_{ji}^{(1)} x_i + w_{j0}^{(1)}\right) + w_{k0}^{(2)} \tag{4.34}$$

where the set of all weight and bias parameters have been grouped together into a vector w. Thus, the neural network model is a nonlinear function from a set of input variables x_i to a set of output variables y_k, controlled by a vector w of adjustable parameters. The neural network architecture is shown in Figure 4.1.

This network, being the most commonly used in practice, may be described as a 2-layer feed-forward neural network, because it is the number of layers of adaptive weights. A two-layer network with linear outputs can uniformly approximate any continuous function on a compact input domain.
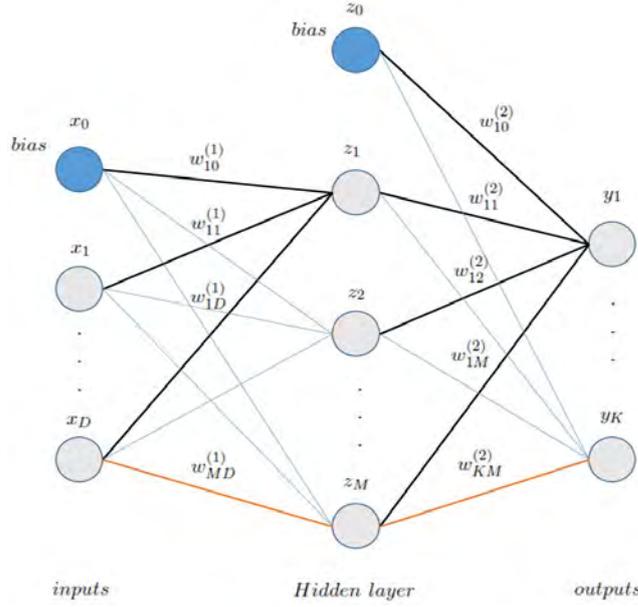
FIGURE 4.1: Neural Network architecture.

Determining the neural network parameters within a maximum likelihood framework involves the solution of a nonlinear optimization problem. This requires the evaluation of derivatives of the log likelihood function with respect to the network parameters, obtained efficiently using the *error back propagation* technique. This training technique is not covered in this manuscript.

4.1.3 Aerodynamic Coefficients

According to (Stevens and Lewis, 1992), the various dimensionless aerodynamic coefficients are primarily dependent on the AoA and sideslip angle, and less dependent on other variables. Nevertheless, the dependence of the coefficients on angular velocities is taken into account for this work since they play an important role in the aircraft motion. The relations describing the aerodynamics coefficients were given in the previous chapter as

$$
\begin{bmatrix} C_L \\ C_Y \\ C_D \end{bmatrix} = \begin{bmatrix} C_{L_\alpha}\alpha \\ C_{Y_\beta}\beta \\ C_D(C_L) \end{bmatrix}
$$

$$
\begin{bmatrix} C_l \\ C_m \\ C_n \end{bmatrix} = \begin{bmatrix} C_{l_\beta}\beta + C_{l_p}\frac{bp}{2V_a} + C_{l_r}\frac{br}{2V_a} \\ C_{m_0} + C_{m_\alpha}\alpha + C_{m_q}\frac{\bar{c}q}{2V_a} \\ C_{n_\beta}\beta + C_{n_p}\frac{bp}{2V_a} + C_{n_r}\frac{br}{2V_a} \end{bmatrix}
$$

where each one of the nondimensional coefficients is composed by one or more nondimensional stability derivatives.

Furthermore, the contributions of the control surfaces moments is included in (3.21), which is

$$
M_{ext} = \begin{bmatrix} L' \\ M \\ N \end{bmatrix} = \frac{1}{2}\rho S V_a^2 \left(\begin{bmatrix} bC_l \\ \bar{c}C_m \\ bC_n \end{bmatrix} + \begin{bmatrix} bC_{l_{\delta ail}} & 0 & bC_{l_{\delta rud}} \\ 0 & \bar{c}C_{m_{\delta ele}} & 0 \\ bC_{n_{\delta ail}} & 0 & bC_{n_{\delta rud}} \end{bmatrix} \begin{bmatrix} \delta_{ail} \\ \delta_{ele} \\ \delta_{rud} \end{bmatrix} \right)
$$

The numerical values of these nondimensional stability derivatives change from plane to plane, and the means to obtain these values are computation of fluid dynamics, wind tunnel tests, or data bases gathering this information. When numerical simulations are carried out, it is a common practice to assume the values of these derivatives as constants, loosing accuracy but gaining simplicity in the simulation. In this work, a group of neural networks, one for each nondimensional stability derivative is proposed.

From now on, the nondimensional stability derivatives will be referred to just as the stability derivatives.

At this point, the reader may wonder why the use of Neural Networks is preferred instead of N-dimensional lookup tables with interpolation between values. The answer is quite simple, a Neural Networks approach provides a significant simplicity when multi-input / multi-output data is handled. Also, the possibility of online improvement of the neural networks with new airborne information in case of abnormal situations (icing, disfigurations in profile, major inertial matrix changes, etc.) is of great interest.

Thus, as neural networks need a data base to be trained, it is imperative to obtain a data base of the aerodynamic coefficients or the stability derivatives. Unfortunately, since access to experimental data bases of this coefficients is almost impossible due to enterprises privacy policies, and the use of wind tunnels to measure this coefficients is also unfeasible, the only resource left is software simulation.

Consequently, data bases were obtained from the United States Air Force (USAF) Stability and Control Digital DATCOM (Data Compendium) (Williams and Vukelich, April 1979). This Public Domain Aeronautical Software computes the static stability, control and dynamic derivative characteristics of fixed-wing aircrafts using the methods contained in the USAF Stability and Control DATCOM. Furthermore, the data sets were compared and refined using the JSBSim open source Flight Dynamics Models (FDM) (JSBsim, 2016), used in several open source simulators and also employed to drive the motion-base research simulators of many universities worldwide.

The first step in the coefficient obtention is to draw the aircraft using built-in commands provided in the DATCOM software, which resulted in Figure 4.2 (dimensions are in feet). Then, the aircraft geometry in the form of a script is processed by the program and the aerodynamic data is provided in tables.

 After the datasets are obtained for each stability derivative, the training, validation and test sets are defined to be the 70, 15 and 15 percent, respectively, of the available data. The training algorithm used is the Bayesian Regularization and the number of hidden neurons is selected by trial and error trying to improve the performance as much as possible.

All simulations performed here are at subsonic speeds, and the stability derivatives are computed per-radian.

Furthermore, the performance of the neural networks developed to fit the available data is given in Appendix C, using the Mean Squared Error of the training and testing data sets.

The reader must have in mind that all the stability derivatives are the result of approximated models and neural networks with limited datasets.

This model was created using publicly available data, publicly available technical reports, textbooks, and estimates. It contains no proprietary or restricted data. If this model has been validated at all, it would be only to the extent that it seems to "fly right", and that it possibly complies with published, publicly known, performance data. Thus, this model is meant for educational and entertainment purposes only.
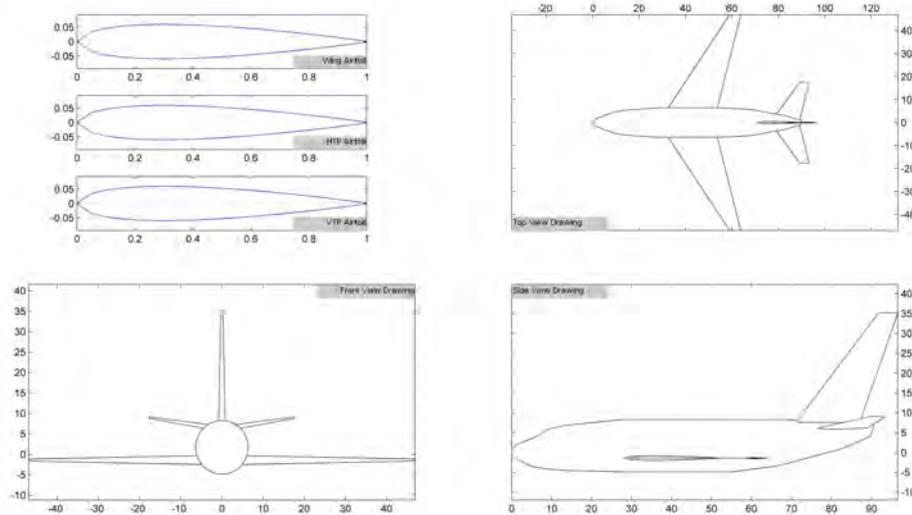
FIGURE 4.2: Aircraft drawing (Dimensions in feet).

This simulation model is not endorsed by the manufacturer. This model is not to be sold.

4.1.3.1 Lift and Drag Coefficients

Regarding the Lift coefficient, a dependence on the AoA is shown in Figure 4.3, where it can be seen how as the AoA increases, so does the Lift coefficient. Thus, if the stability derivative C_{L_α} was obtained, it would have a positive value. Note that high Lift devices such as flaps or slats are not considered. Thus, for take-off and landing, the coefficient would have to be modified with the corresponding effects.
Once that the Lift coefficient is known, the Drag coefficient can be obtained from it, this is done using a parabolic equation of the form

$$C_D = C_{D0} + C_{Di}C_L^2 \tag{4.35}$$

where $C_{D0} = .0176$ is the parasitic drag coefficient, and $C_{Di} = .0515$ is the induced drag coefficient. Note that this equation is only valid for nominal conditions. For landing or approaching, where flaps or the landing gear have drag contributions, other coefficients should be considered.
The resultant Drag coefficient is plot in Figure 4.4. Note that the Drag coefficient increases as the AoA increases. Therefore, a derivative C_{D_α} would be also positive.

4.1.3.2 Sideforce Coefficient

Regarding the lateral force C_Y, the main contribution is supposed to be given by the sideslip angle, such that the nondimensional stability derivative C_{Y_β} is its main component. The variation of this derivative with respect to the airspeed and the angle of attack is provided in Figure 4.5.
 Since C_{Y_β} has a negative value, and the coefficient C_Y is given by the product of $C_{Y_\beta}\beta$, this means that a positive sideslip angle (sideslip to the right), will generate a negative lateral force (force to the left). This force is due to the drag of the aircraft vertical surfaces such as the fuselage or vertical fin.
Moreover, a lateral force due to the rudder deflection could be taken into account,
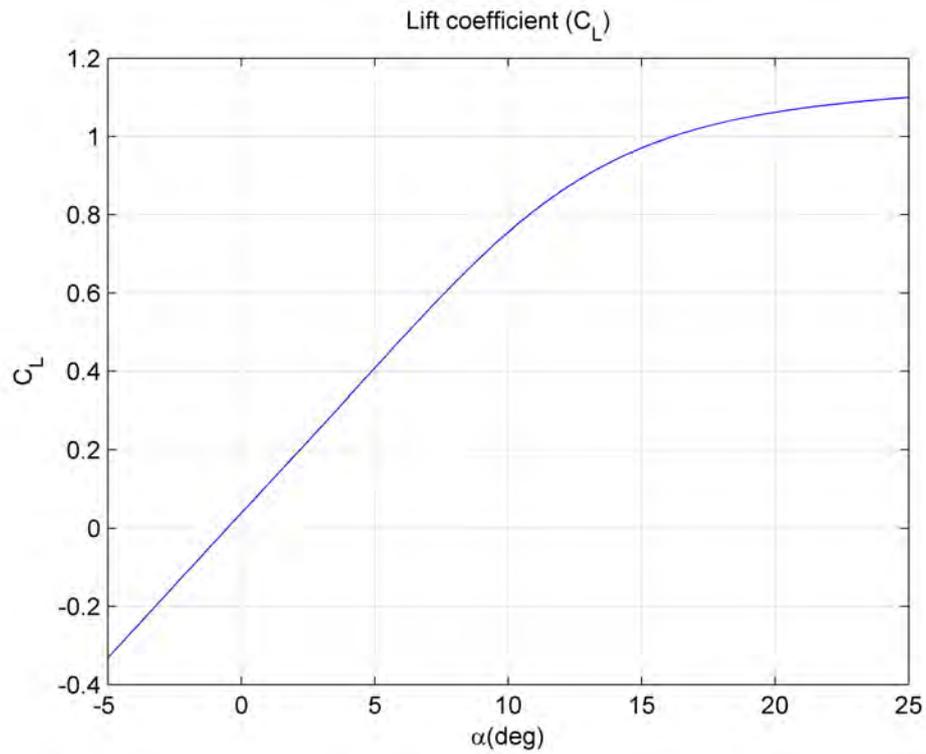
FIGURE 4.3: Coefficient C_L.
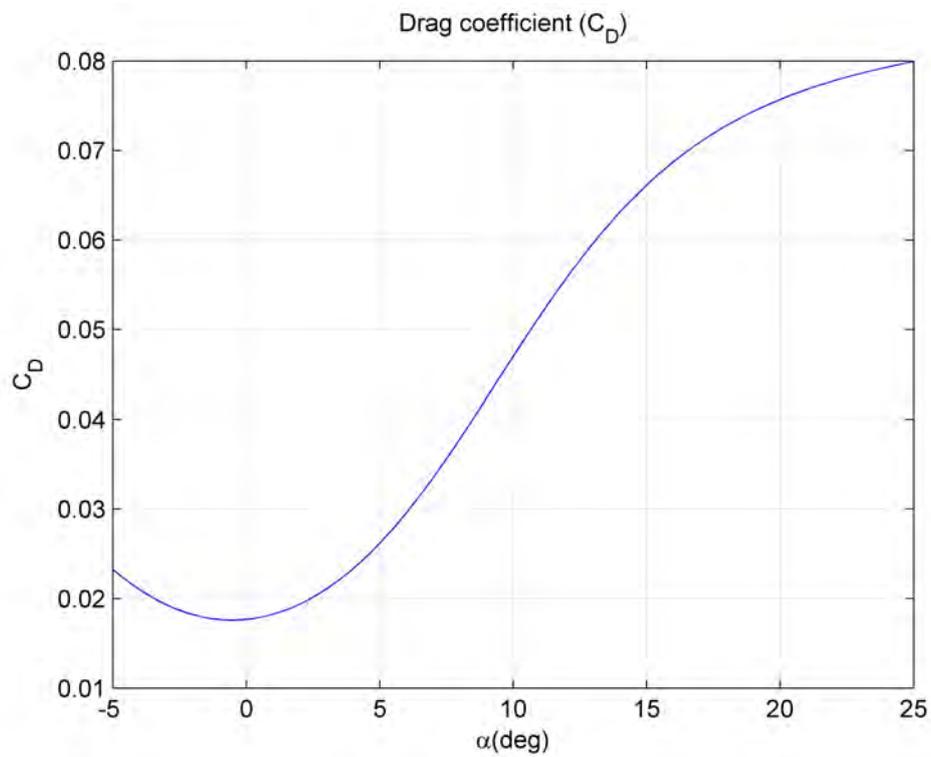
FIGURE 4.4: Coefficient C_D.
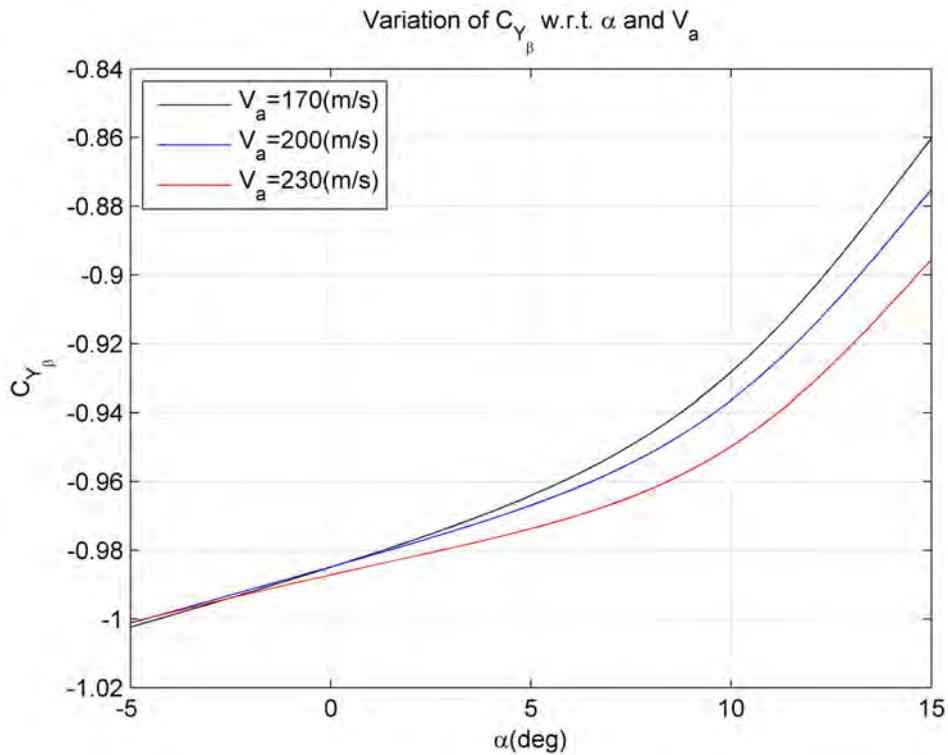
FIGURE 4.5: Coefficient C_{Y_β}.

but as its influence is weaker than the one of the sideslip angle, this force is neglected.

4.1.3.3 Rolling moment

Figure 4.6 is provided to follow this subsection easily.
To begin, the rolling coefficient is considered to be given by
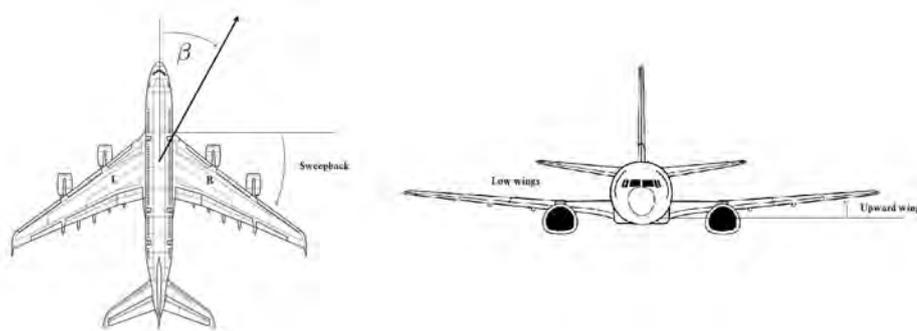
FIGURE 4.6: Top and front view of a plane showing a positive β. The right and left wings are in low positions and are denoted by R, L, respectively. Positive sweep angle of the wings along with a positive wing dihedral is also shown.

$$C_l = C_{l_\beta}\beta + C_{l_p}\frac{bp}{2V_a} + C_{l_r}\frac{br}{2V_a}$$

where the first contribution, C_{l_β}, is the combination of four influences:

- The wing dihedral effect:
  For a positive sideslip in an aircraft with positive wing dihedral (upward), the AoA of the right wing is increased, and the AoA of the left wing is decreased. Therefore, the lift of the right wing is more than the one on the left wing, creating a negative rolling moment (to the left).

- The wing sweep angle:
  For a positive sideslip in an aircraft with positive sweep of the wings (sweepback), the speed of the right wing is lightly increased with respect to the left wing, provoking more lift on the right wing compared to the left wing. This creates a negative rolling moment (to the left).

- The wing position (high/low):
  In this component, the *high* position refers to wings above the fuselage, and *low* to wings situated below the fuselage.
  For a positive sideslip in the high wing position, the pressure increase on the right wing lower surface, creating more lift in this side of the wing. Consequently, a negative rolling moment is created.
  For a positive sideslip in the low wing position, the pressure increase on the right wing upper surface, creating less lift in this side of the wing. Consequently, a positive rolling moment is created.

- The vertical tail:
  Since the vertical tail's centre of pressure is typically above the Cx_B axis, a positive sideslip will generate a drag force due to the vertical tail drag actuating in the upper part of the rotation axis, creating a negative rolling moment. Hence, the placement of vertical fins below the Cx_B axis will counteract this component with a positive rolling moment.

Since the wing dihedral effect is the most significant, sometimes this nondimensional stability derivative is called the *dihedral effect*. Thus, the general behaviour of the aircraft is a negative rolling motion at positive sideslip angles (yielding a negative value of the derivative).
Note 1: 1° of dihedral angle has the same effect as 6° of sweep angle.
Note 2: The horizontal stabilizer also contributes to this derivative; it can feature dihedral, sweep and high/low position.
The variation of this derivative with respect to the airspeed and the angle of attack is provided in Figure 4.7.
  The second component of the rolling moment is the one induced by a roll rate, given by the derivative C_{l_p}. Considering an initial positive roll rate, additional velocity components affect the wings. The right wing is dropping and increasing its AoA, and the left wing is rising and decreasing its AoA. This generates more lift in the right wing than in the left one, creating a negative rolling moment counteracting the initial motion. Thus, this component of the rolling moment can be seen as a damping, helping to the static stability of the aircraft. Therefore, the derivative will have a negative value.
The variation of this derivative with respect to the airspeed and the AoA is provided in Figure 4.8.
  The third component of the rolling moment is the one induced by the yaw rate, involving the derivative C_{l_r}. Considering an initial positive yaw rate, the velocity on the right wing is decreased and in the left wing is increased, generating more lift
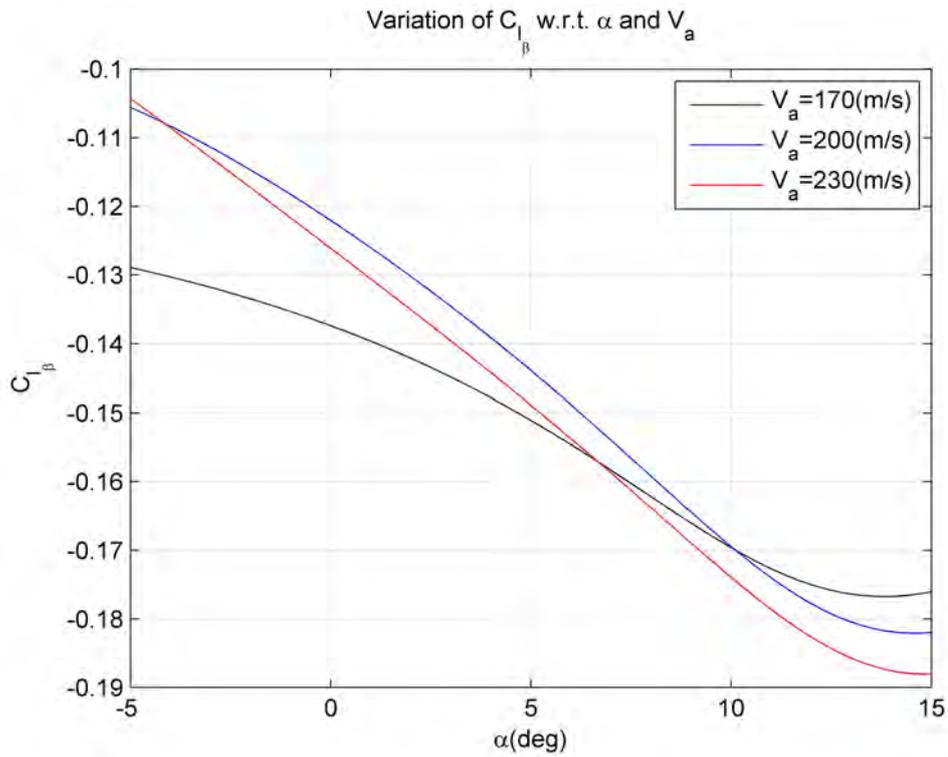
FIGURE 4.7: Coefficient C_{l_β}.
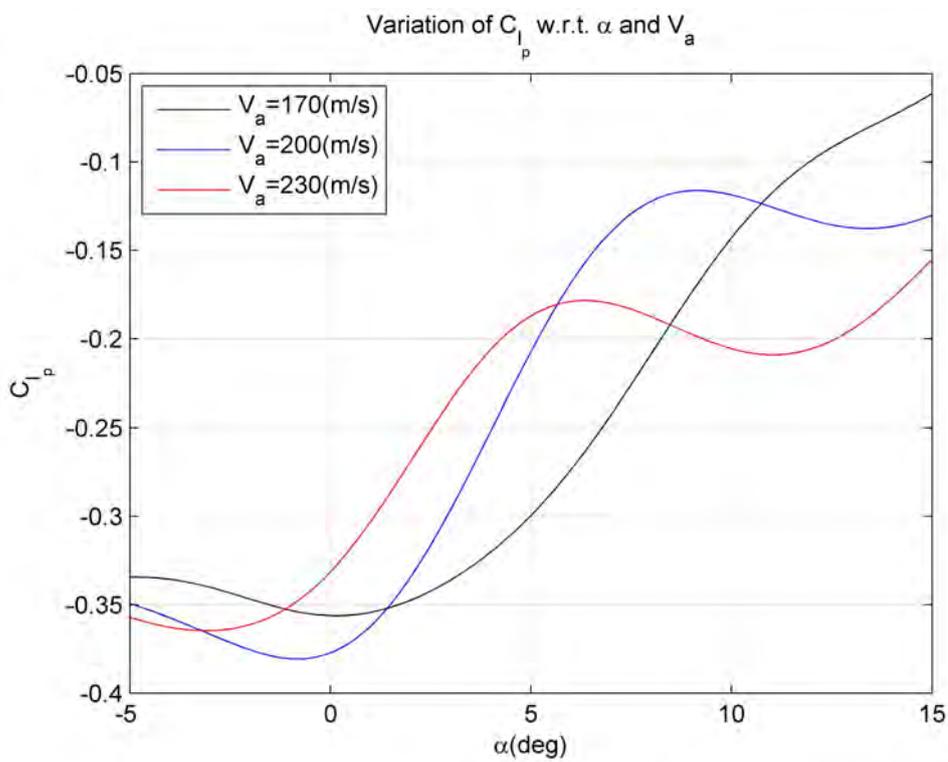
FIGURE 4.8: Coefficient C_{l_p}.

in the left wing compared to the right wing, provoking a positive rolling moment. In this manner, this derivative with positive value, acts in the opposite sense as the one produced by the roll rate, not helping to the static stability.

The variation of this derivative with respect to the airspeed and the AoA is provided in Figure 4.9.

 Regarding the moments generated by the control surfaces, the first to be considered

FIGURE 4.9: Coefficient C_{l_r}.

is the rolling moment provoked by the ailerons deflection. When the right aileron is lowered and the left aileron is raised, denoted by a positive δ_{ail}, the lift is spoiled in the left wing and the lift is increased on the right wing, making the airplane turn to the left due to a negative rolling moment. Thus, the value of the derivative expressing this effect is negative. In our simulation, this is a constant value of $C_{l_{\delta ail}} = -.02$. On the other hand, the moment generated by the rudder deflection involves the derivative $C_{l_{\delta rud}}$. Considering a deflection of the rudder to the left, denoted by a positive δ_{rud} (clockwise from a top-view of the aircraft with the nose in the upper part), it will create an added drag component above the Cx_B axis. Hence, since this drag force will act in the upper part of the rotation axis, it will generate a positive rolling moment, named *adverse roll*, and a negative yawing motion. In consequence, the value of $C_{l_{\delta rud}}$ should be positive. This adverse effect is weak, and a value of zero is defined for this derivative in the simulation such that the moment produced is neglected.

4.1.3.4 Yawing Coefficient

The yawing coefficient is considered to be given by

$$C_n = C_{n_\beta}\beta + C_{n_p}\frac{bp}{2V_a} + C_{n_r}\frac{br}{2V_a}$$

where the first contribution C_{n_β} is also called the *weathercock effect*, and is the contribution of four influences

- The vertical tail and fins:
  Considering a positive sideslip angle (to the right), the vertical tail experiences a change in its "AoA". Thus, a sideforce appears on the tail (towards the left), provoking a positive yawing moment (to the right). An interesting remark is that if the sideslip angle is too big, the vertical tail may stall.

- The wing sweep angle:
  As seen in the rolling moment created by the dihedral effect, a sweepback angle of the wings and a positive sideslip angle, will create an increase in the speed of the right wing compared to the left, provoking more lift on the right wing and consequently, more drag. Thus, since more drag is produced in the right wing with respect to the left wing, a positive yawing moment is generated.

- The fuselage:
  Considering a positive sideslip angle, a side force appears on the fuselage, provoking a positive yawing moment dependent on the center of pressure position.

- The c.g. position:
  All forces applied in front of the aircraft's c.g. will generate a negative yawing moment when a positive sideslip angle is considered.

In general, the contribution of the weathercock effect, is such that for positive sideslip angles, positive yawing moments are generated, causing a positive static stability. Thus, the derivative has a positive value.
The variation of this derivative with respect to the angle of attack is provided in Figure 4.10.
The second contribution term is the one involving the derivative C_{n_p}. Considering an initial roll in the positive sense, the left wing will be rising, decreasing its AoA. On the other hand, the right wing will be dropping and increasing its AoA, provoking more Drag in the right wing than the left. This means that a positive roll rate, creates a positive yawing motion, called *induced yaw*. Thus, the derivative has a positive value. The effect of this induced yaw is weak.
The variation of this derivative with respect to the AoA and airspeed is provided in Figure 4.11.
The third contribution term is the one induced by the yaw rate C_{n_r}. Considering an initial rate of yaw to the right, the right wing decreases its speed, and consequently decreases its drag with respect to the left wing. On the other hand, the left wing increases its speed and drag. All combined provokes a negative yawing motion. This component of the yawing moment can be seen as a damping, helping to the dynamic stability of the aircraft. Therefore, the derivative will have a negative value.
The variation of this derivative with respect to the AoA and airspeed is provided in Figure 4.12.
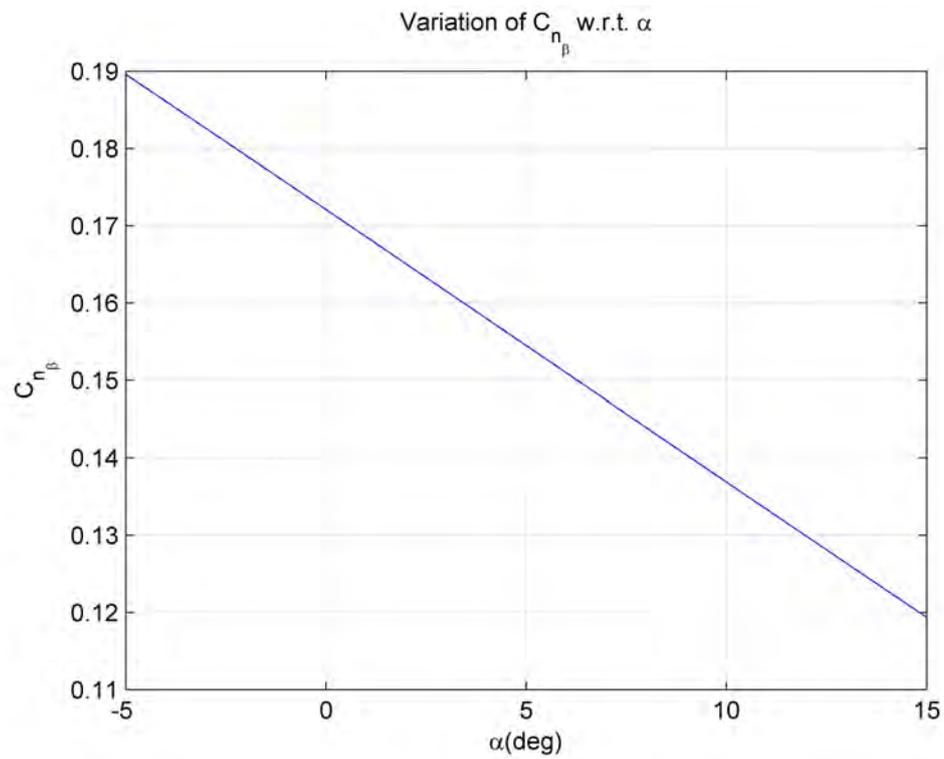
FIGURE 4.10: Coefficient C_{n_β}.
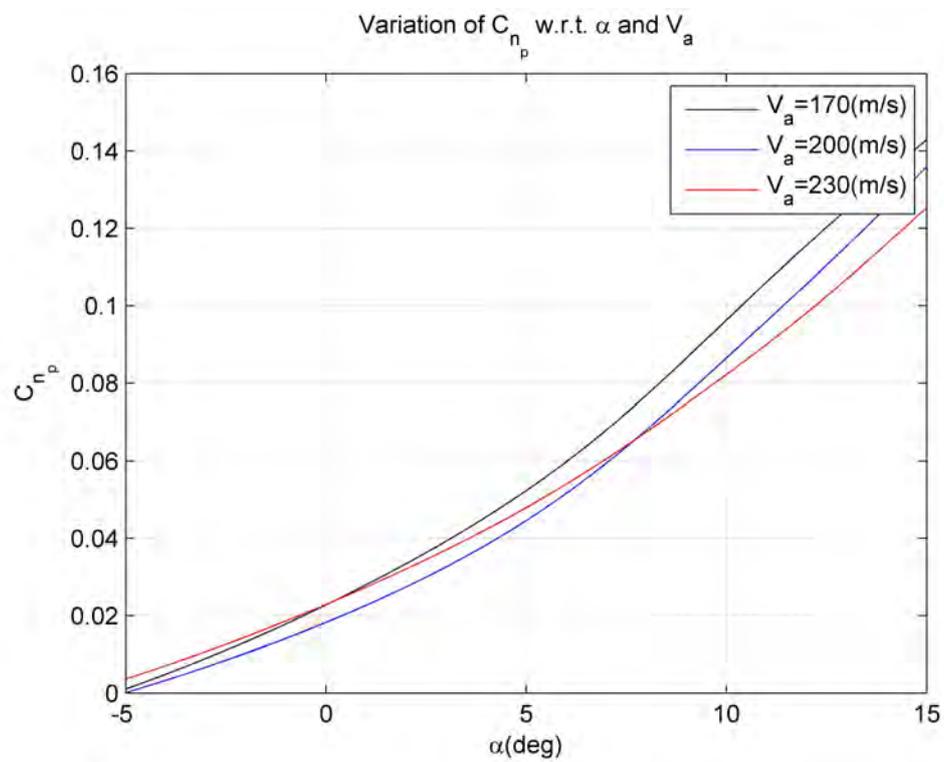
FIGURE 4.11: Coefficient C_{n_p}.
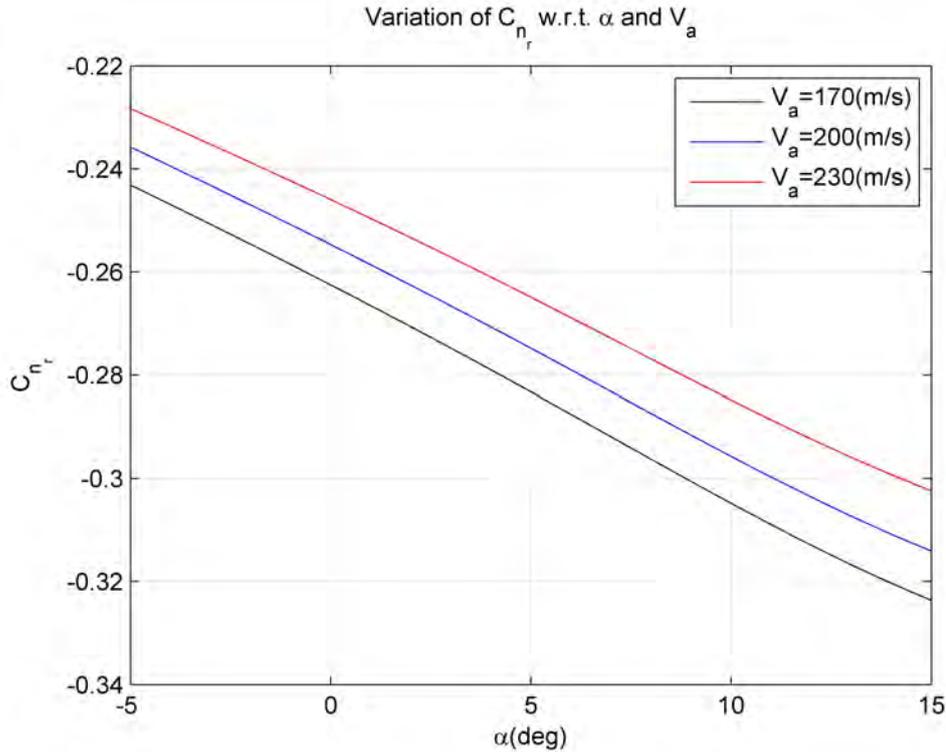
FIGURE 4.12: Coefficient C_{n_r}.
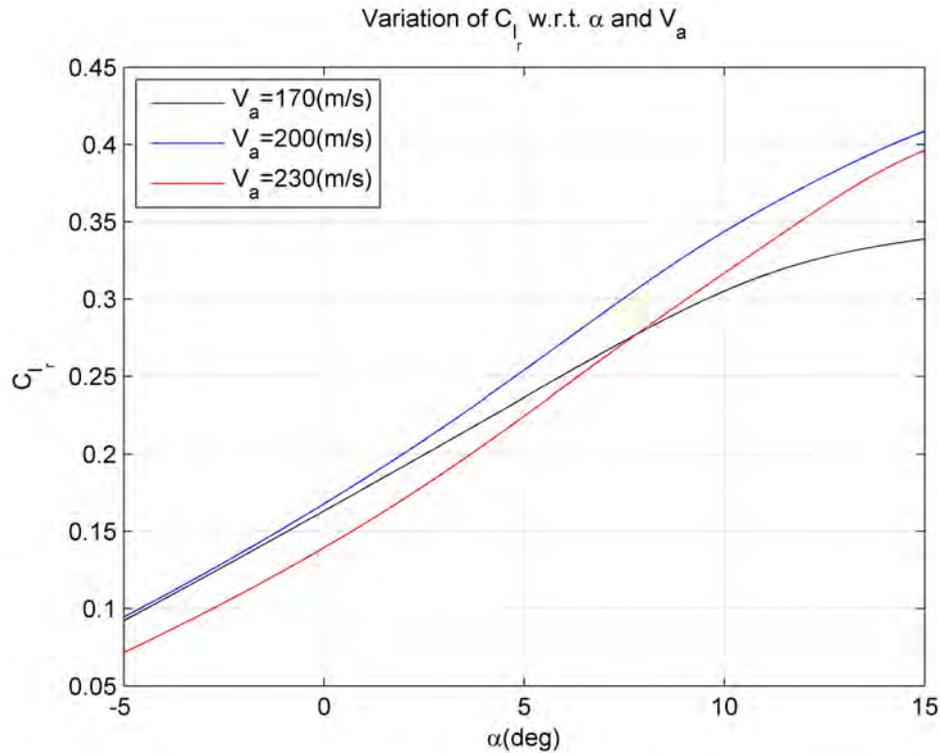
Regarding the moments generated by the control surfaces, the first to be considered is the yawing moment provoked by the ailerons deflection. When the right aileron is lowered and the left aileron is raised (positive δ_{ail}), the raised aileron actuates as a camber decrease which decreases the drag force, and the dropped aileron acts as a camber increase, increasing the drag. Thus, banking to the left provokes a positive yawing motion, called *adverse yaw*. The value of the derivative expressing this effect is positive. In our simulation, this is a constant value of $C_{n_{\delta ail}} = .002$.

On the other hand, the moment generated by the rudder deflection involves the derivative $C_{n_{\delta rud}}$. Considering a deflection of the rudder to the left, denoted by a positive δ_{rud}, it will create a strong moment to the left, since it is the very function of the rudder. Thus, the value of the derivative is negative. In our simulation, this is a constant value of $C_{n_{\delta rud}} = -.07$.

4.1.3.5 Pitching Coefficient

The pitching coefficient is considered to be given by

$$C_m = C_{m_0} + C_{m_\alpha}\alpha + C_{m_q}\frac{\bar{c}q}{2V_a}$$

Before continue with each term of the pitching coefficient, three important considerations are pointed out:

- When c.g. is ahead a.c.: Positive static stability.

- When c.g. is behind a.c.: Negative static stability (Instability).

- When c.g. is at a.c.: Neutral static stability.

The location of the c.g. moving backwards is limited by the a.c. position for stability reasons. Also, the more forward the c.g. position, the larger the elevator deflection is needed to pitch the aircraft. In this manner, a forward c.g. position limit is defined due to controllability reasons. Moreover, one should consider that at larger elevator deflection, larger drag is generated, leading to more fuel consumption.

The first term of the pitching coefficient corresponds to the intrinsic pitching moment of any wing profile. For the simulation in this work, $C_{m_0} = -.094$.

The second term of the pitching coefficient is the one due to the angle of attack, involving the derivative C_{m_α}. An increase of the AoA creates a nose up or nose down moment depending on the aerodynamic center position relative to the c.g. position. This derivative has often a negative value, meaning that the c.g. is ahead the a.c., giving positive static stability to the aircraft.

The variation of this derivative with respect to the AoA and airspeed is provided in Figure 4.13.

Before passing to the third term of the coefficient, the moment generated by the
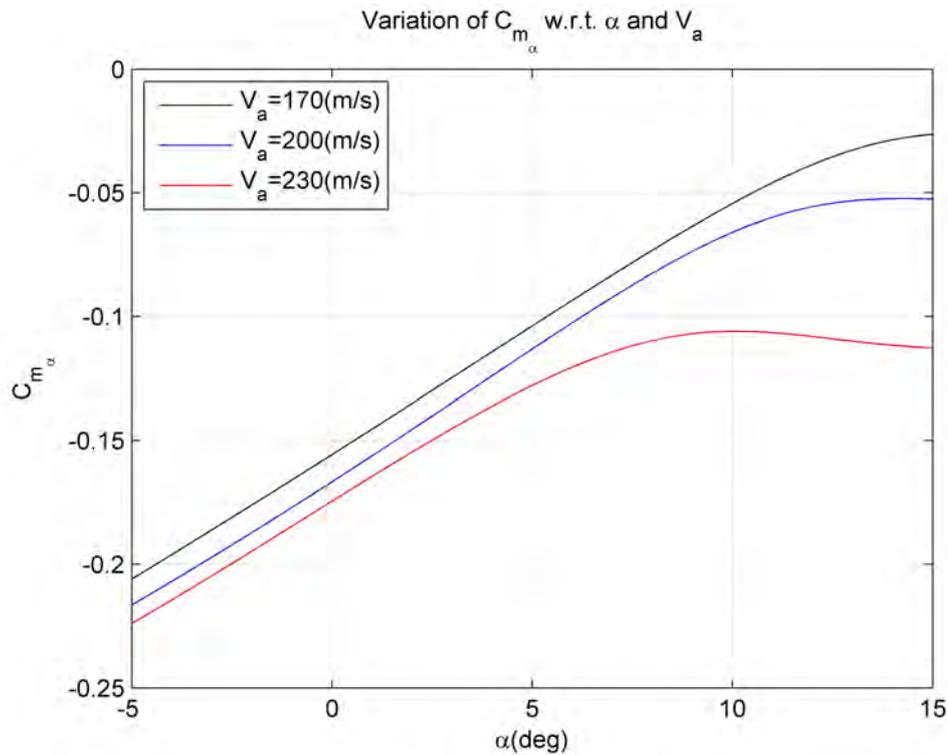
FIGURE 4.13: Coefficient C_{m_α}.

the control surface is addressed. The drop of the elevator, denoted by a positive δ_{ele}, provokes a negative pitching moment. Thus, the value of this derivative is negative. In our simulation, this is a constant value of $C_{m_{\delta ele}} = -.003$.

The third term is the one involving the derivative C_{m_q}. Considering an initial nose down moment (produced by the drop of the elevator), the horizontal stabilizer goes up, so its effective AoA decreases, provoking a positive (nose up) pitching moment. This can be seen as a damping effect, helping to the static stability of the aircraft. The fuselage and wing also have a damping effect. The value of this derivative is negative.

The variation of this derivative with respect to the airspeed is provided in Figure 4.14.
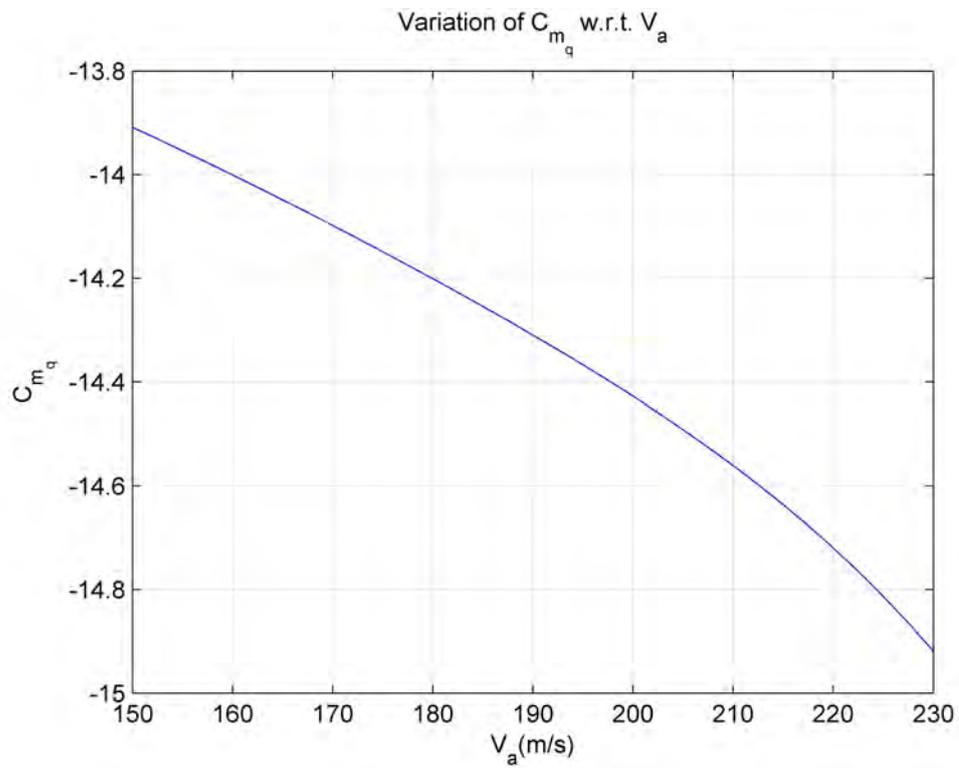
FIGURE 4.14: Coefficient C_{m_q}.

4.2   Simulation of Aircraft Dynamics in Open Loop

In this part, the behaviour of an aircraft with the aerodynamic forces and moment coefficients, as well as the parameters provided in the List of Physical Constants (provided within the first pages of this work) is analyzed.
A general block diagram of the aircraft simulation is provided in Figure for the reader's convenience.
 Furthermore, in spite of the fact that the inertia matrix of the aircraft is taken as
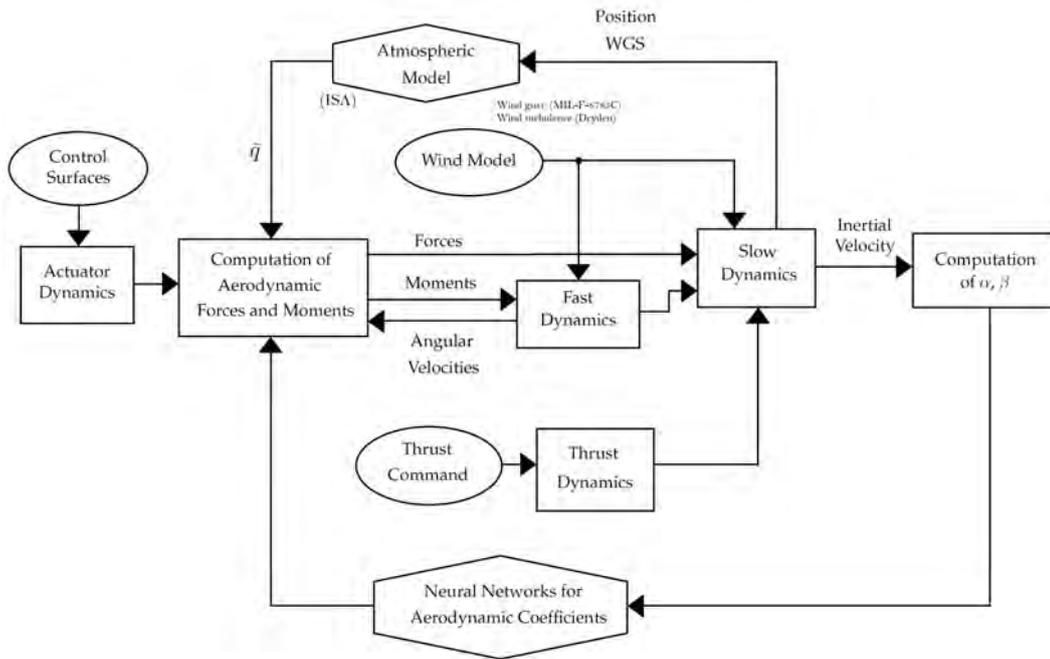
FIGURE 4.15: Block diagram of the aircraft simulation.

constant due to its relatively small rate of change, small decrements of the aircraft's mass are considered. The inertia matrix I, is given in $kg \cdot m^2$ by

$$I = \begin{bmatrix} 1,278,369.56 & 0 & -135,588.17 \\ 0 & 3,781,267.79 & 0 \\ -135,588.17 & 0 & 4,877,649.98 \end{bmatrix} \tag{4.36}$$

Consequently, considering that the Lift and Drag coefficients are known, also their corresponding aerodynamic forces are known, such that if a cruise situation with small AoA is considered, the ratio of (3.48) and (3.47a) will give the expression

$$F_{thr} = mg\frac{C_D}{C_D s_\alpha + C_L c_\alpha} \approx mg\frac{C_D}{C_L} \tag{4.37}$$

which, along with the last expression of (3.13) rewritten as

$$V_a = \sqrt{\frac{2L}{\rho S C_L}} \tag{4.38}$$

can be used to obtain the relation between the Thrust and Speed. Note the key role that the air density plays in this computation. For example, around FL320

($\rho = .41kg/m^3$), the Thrust-Speed relation is shown in Figure 4.16. On the other hand, for a FL020 ($\rho = 1.112kg/m^3$), the relation is shown in Figure 4.17. The value of the AoA required to fly at the minimum Thrust value is expressed by α_m.

Hence, if a cruise flight is to be maintained at FL320 with a velocity of 200m/s, an
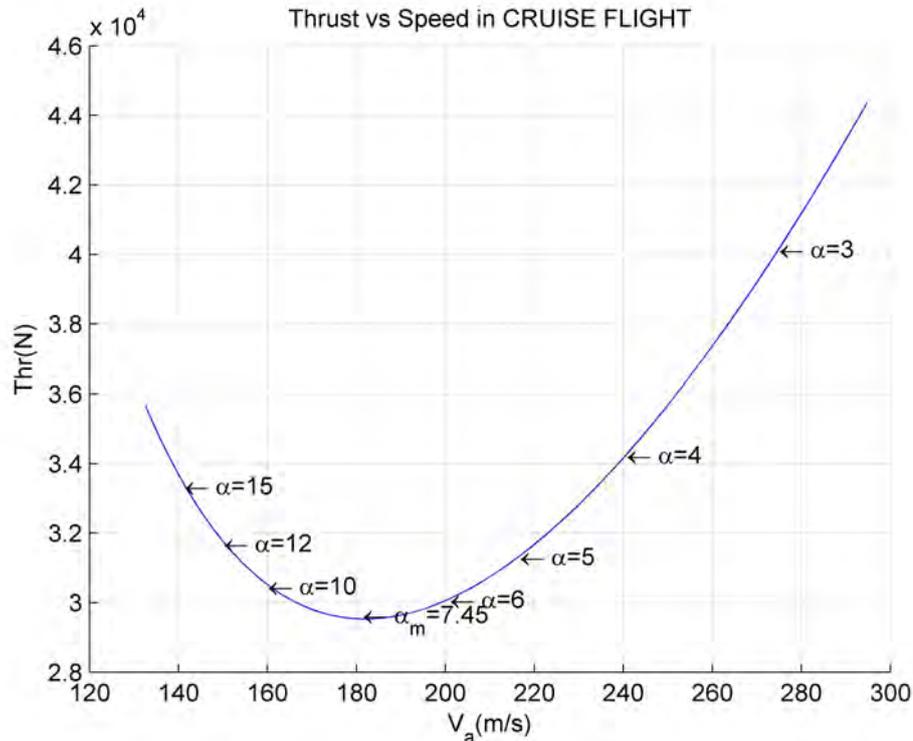
FIGURE 4.16: Thrust vs Airspeed graph indicating values of AoA at FL320.

approximate value of $\alpha = 6°$ with a Thrust of $F_{thr} = 30,000$N are needed.

In order to corroborate these computations, an open loop flight simulation is carried-on with an initial value for $\theta = 5°$. The results obtained when the control surfaces are set at zero degrees and $F_{Th} = 30,000$N are shown in Figure 4.18.

As expected, the behaviour of the aircraft is stable, with decreasing phugoid mode with a 85s period.

Concerning the short period, a zoom in the time scale (see Figure 4.19) shows a self-stabilized behaviour in around 15s with a frequency of .42rad/s.

Regarding the lateral response of the aircraft, an impulse of $1°$/s in the roll rate is applied, results are shown in Figure 4.20.

Furthermore, since the ailerons, elevator and rudder are considered to have first order dynamics, a time response of 50ms is proposed when the control surfaces are moved. Concerning the Thrust, a time response of 2.5s is assumed.
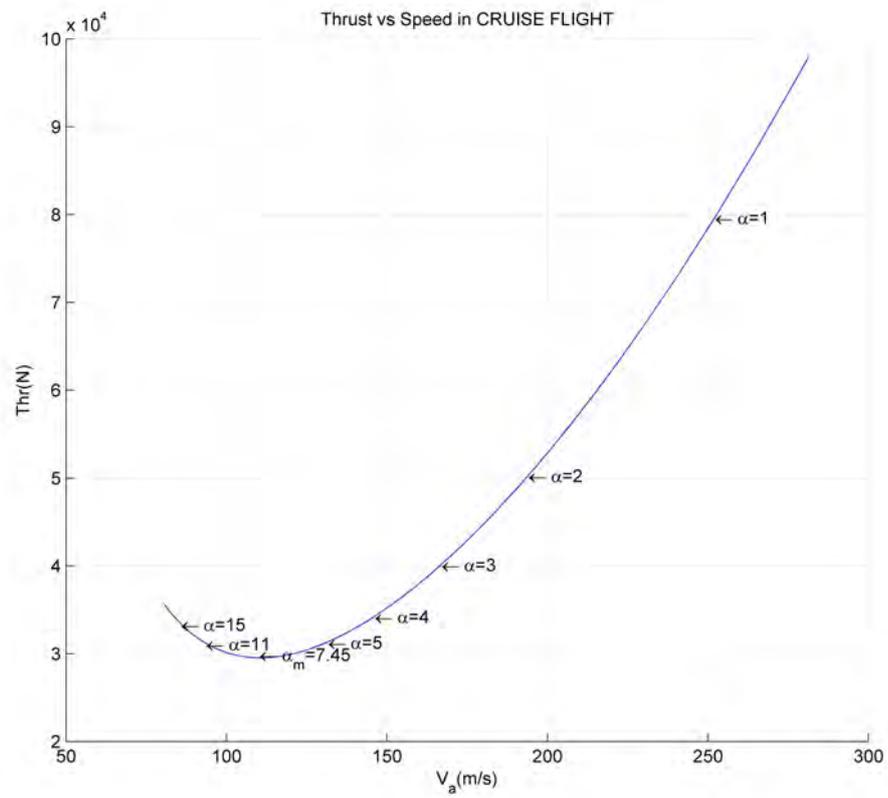
FIGURE 4.17: Thrust vs Airspeed graph indicating values of AoA at FL020.
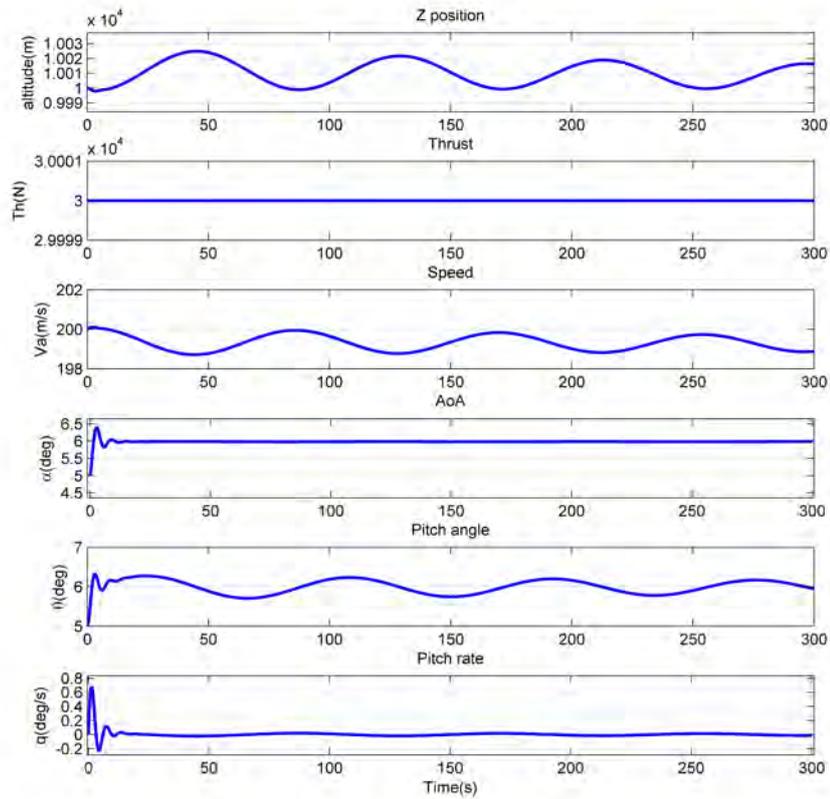
FIGURE 4.18: Longitudinal response of aircraft.
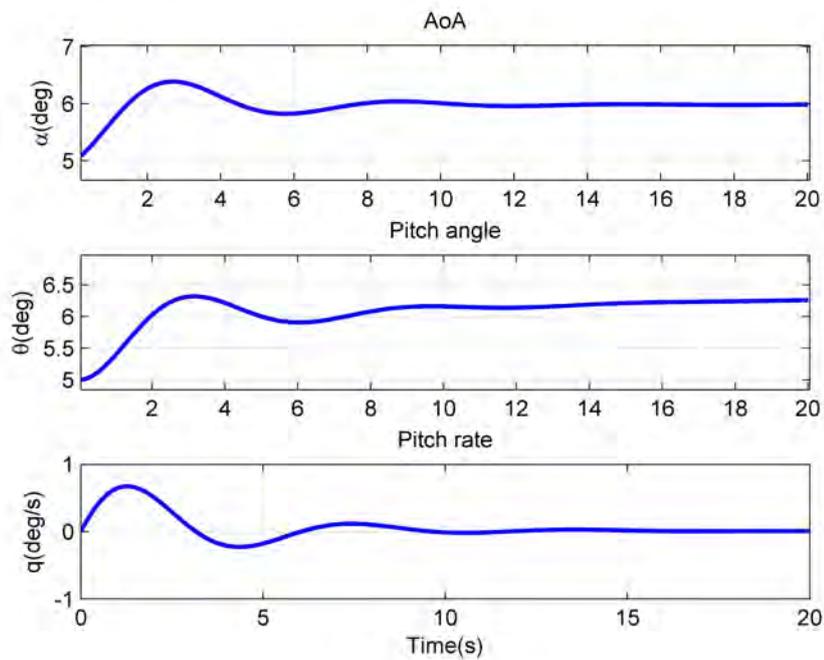
FIGURE 4.19: Longitudinal response of aircraft (zoom).
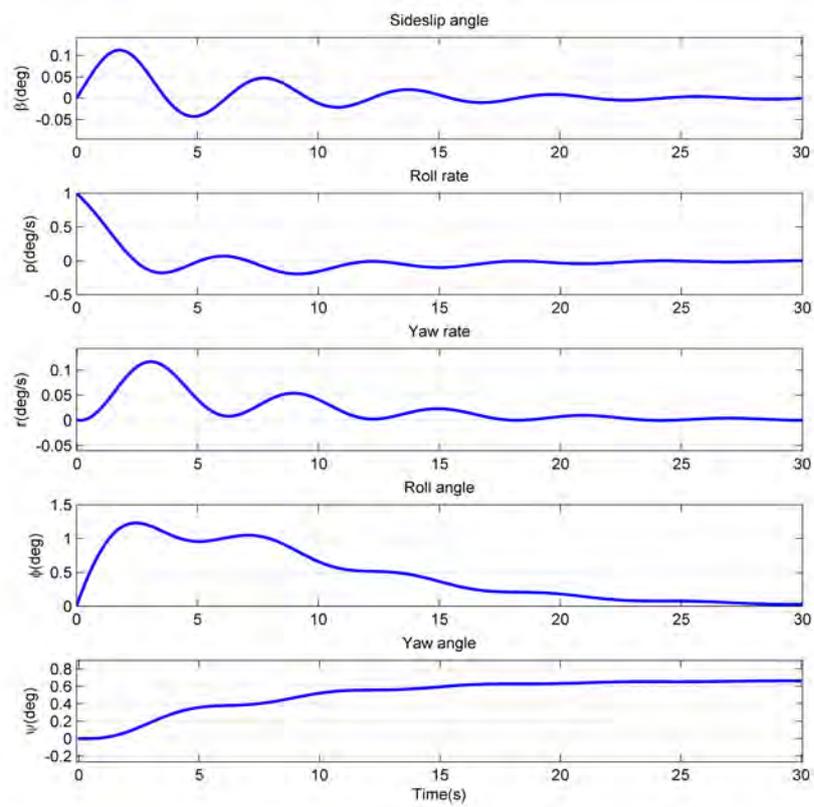
FIGURE 4.20: Lateral response of aircraft.

4.3 Data Visualization through FlightGear flight simulator

In order to facilitate the visualization of the aircraft behaviour and flight variables such as the position, attitude and other representative variables, an interface between Matlab and the flight simulator FlightGear (FlightGear, 2017) was created. FlightGear is an open-source flight simulator endowed with world Scenery, time of day and date modeling (current computer clock or other), seasonal effects (24hr day during summer at north pole), and animated, operational, and interactive 3d cockpits and instruments.

In this way, the whole Flight Dynamic Model is provided by Matlab, but a graphic visualization of the aircraft states can be seen through FlightGear simulator (see Figure 4.21). A short video[2] is available showing a step change in the lateral position using Matlab, but visualized in FlightGear.

(a) .

(b) .

(c) .

(d) .
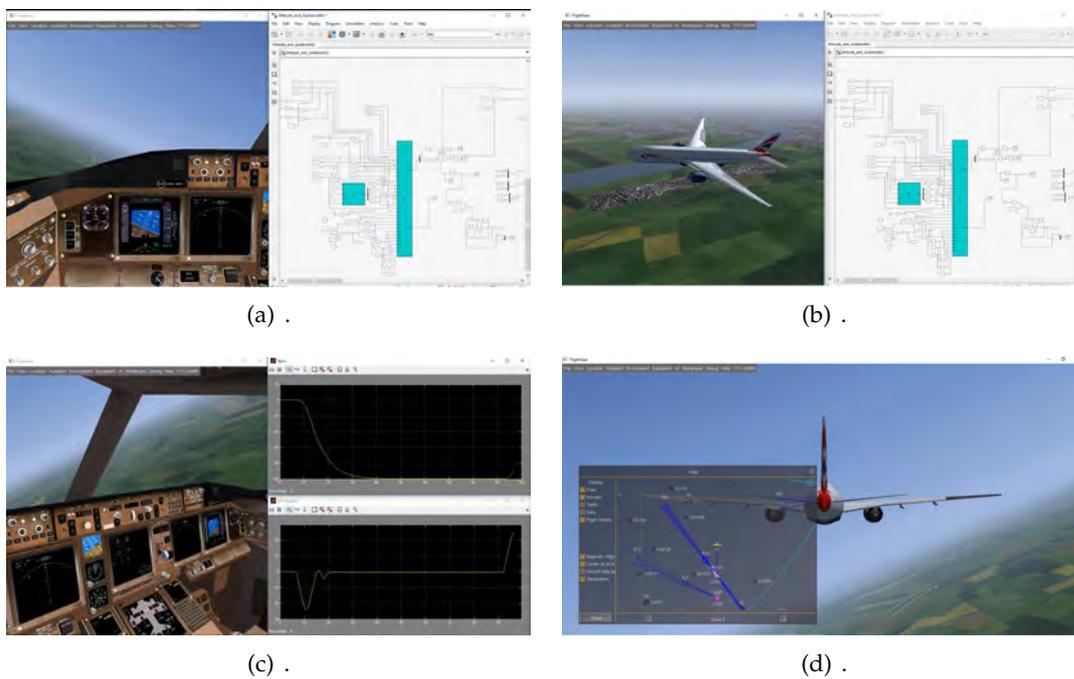
FIGURE 4.21: FlightGear Simulation using Matlab dynamic model.

---

[2]https://www.youtube.com/watch?v=Nf4E0uFFTIc

4.4 Conclusions

A full 6DOF Matlab simulation for an aircraft similar to an aircraft type B737-200 / A320-200 has been described.

Since the values of the aerodynamic coefficients play a key roll in the aircraft simulation, special emphasis was put on their effects and their estimation through the use of Neural Networks. In consequence, an extensive background on Neural Networks has been provided.

In spite of the fact that other approaches like N-dimensional lookup tables with interpolation between values could have been used for the obtention of the aerodynamic coefficients, a Neural Networks approach was chosen due to the simplicity of multi-input / multi-output data handling, and also due to the possibility of on-line improvement of the neural networks with new airborne information in case of abnormal situations (icing, disfigurations in profile, major inertial matrix changes, etc.).

The aircraft simulation was tested in an open loop configuration (no input of the control surfaces is applied) at different Flight Levels, behaving as expected.

Chapter 5

4D Trajectory Generation for Transport Aircraft using Bezier curves

With the increase in air traffic in the upcoming years, new concepts have been introduced to organize and better manage air traffic flows (free flight, flow-corridors, etc.) with the view of increasing traffic safety and airspace capacity by solving air traffic conflicts. Therefore, ad-hoc descriptions and parametrization of more complex and flexible transport aircraft trajectories with new characteristics are needed.

The trajectories generated in this chapter are meant to be seen as a complement to regular flight plans, such that modifications to a general trajectory in order to solve air traffic conflicts or enhance air capacity by a better timing due to the 4D generated trajectories are done.

In Section 5.1, the motivation and trajectory generation problem is introduced, along with a state of the art with respect to transport aircraft trajectory generation techniques. In this manner, since a smooth path generation from pre-existing control points based on Bezier curves is the elected approach, Bezier Curves are briefly described along with the fundamentals of continuity and curvature of a curve in Section 5.2.

Consequently, the adopted trajectory generation method is described in Section 5.3. The approach consists in stitching several Bezier curves together while assuring G^2 continuity at the joints. Then, since the aircraft is supposed to follow a desired 4D trajectory, a reference flight starting time $t_{init} = 0$ along with an ending time t_{end} are considered. In this way, considering velocity and time constraints, the obtained path based on Bezier curves is re-parameterized with respect to time and open the way to 4D guidance along these curves.

Furthermore, in order to control the Euclidian distance between the control points and the proposed trajectory, an reshaping of the trajectory using a distance range defined by the user is performed in Section 5.4.

Moreover, since flyable trajectories depend heavily on the load factor they induce on aircraft, the tradeoff between curvature, speed, and load factor is briefly analyzed in Section 5.5.

In Section 5.6, the proposed approach is used to reproduce a full flight profile, and the addition of multiple parallel trajectories to the reference trajectory is considered. This is done looking forward to extend the method not only as a complement to regular flight plans, but to full trajectories compatible with the flow-corridors concept. Finally, conclusions are given in Section 5.7.

Numerical simulations using Matlab to corroborate the feasibility of the approach are provided troughout the chapter, showing promising results for different types of trajectories.

5.1   Introduction

Current guidance and path generation systems are based on an airborne database of waypoints (latitude and longitude), transitions between waypoints, and constraints in speed and altitude. However, new functionalities to improve procedures, airspace, and air traffic operations are required for the implementation of up-to date Performance Based Navigation systems. Some of these path generation functionalities are:

- Fixed radius paths:

  1 Radius to fix (RF): Used when there is a requirement for a specific curved path radius in a terminal or approach procedure. It is defined by radius, arc length and fix.

  2 Fixed radius transition (FRT): Intended to be used in en-route procedures. It refers to turns with 22.5 NM radius for high altitude routes (above FL195), and 15 NM radius for low altitude routes.

- Fly-by turns:
  Uses information of the aircraft speed, bank angle, wind and yaw rate to calculate a smooth transition from one path segment to the next. Since speed, wind, an other parameters affecting the turn radius can vary, the turn initiation point and turn area can vary.

- Holding pattern:
  Consists of an oval course definition attached to a holding waypoint, where turn direction and leg time or distance on the straight segments is specified, as well as the ability to plan the exit from the hold. Improvements include fly-by entry into the hold, minimising the necessary protected airspace on the non-holding side of the holding pattern.

- Offset flight path:
  Provides the capability to specify a lateral offset from a defined route. Generally, lateral offsets can be specified in increments of 1 NM up to 20 NM. When a lateral offset is activated, the aircraft will depart the defined route and typically intercept the offset at an angle of 45° or less. When the offset is cancelled, the aircraft returns to the defined route in a similar manner. This functionality is discontinued in the terminal area or at the beginning of an approach procedure, at hold, and during course changes of 90° or greater.

Consequently, a quick and efficient 4D trajectory generation device capable of recreating the needed functionalities of PBN operations is crucial for implementing 4D guidance, always taking into account compatibility with FMS.

In addition to this, (ICAO, March 2014) states that the unpredictability of aircraft operations eliminates the possibility of an intended flight path (trajectory) free of conflicts, even if a de-conflicted path from all other trajectories is defined at the initial setup of a Reference Business Trajectory (RBT). Besides, since unpredictability grows in time, long-term de-confliction of individual trajectories is pointless. In this manner, aircraft separation is not assured, since trajectory predictions that may appear free of conflict, still have the possibility to led to a separation loss due to their unpredictability and/or associated inaccuracy.

Nowadays, in order to cope with separation loss, additional measures such as the ACAS/TCAS systems are considered, but even with operating TCAS, aircraft are exposed to collisions or near mid air collisions, like the ones stated in Section 2.1.1.1.1.

Furthermore, TCAS (III and IV) versions, capable to give Vertical and/or Horizontal direction RAs, were abandoned for one main reasons: 1) The imminent replacement of the radar concept (used in TCAS) with an improved version of the ADS-B concept, named ADS-C EPP (Extended Projected Profile). This ADS-C EPP reports a maximum of 128 waypoints with associated estimates of position, time, and speed, so ground systems know the intended trajectory (ICAO, October 2014[a]).

This stated, it is clear that reference trajectories are essential for flight plans which meet a large set of overfly or profile constraints, which vary in general from flight to flight. Hence, the generation of reference trajectories at short term, and their capability of being modified in case of potential conflicts, should allow the implementation of procedures with the purpose of allowing aircraft to fly closer.

As a result, the generation of flyable and efficient trajectories has been considered by several authors (Bakolas, Zhao, and Tsiotras, August 2011), (Anderson, Beard, and McLain, May 2005), (Judd and McLain, August 2001), (Yang et al., 28-2 September-October 2015), (Yang and Sukkarieh, June 2010), (Delahaye et al., 2014).

Current path generation for transport aircraft is based on a sequence of objective points in a 2D or 3D space given to connect two geographical locations (Walter, 2014). Then, using diagrams like Voronoi, or Delaunay triangulation, or any other method, a piecewise path is constructed using straight lines denominated *legs*. This path may be offered by a high-level path planner from techniques such as Dijkstra's, A*, probabilistic roadmaps, genetic algorithms (Sahingoz, April 2014), or Rapidly exploring random tree star (RRT*) (Webb and Berg, May 2013), just to mention a few.

However, since path differential requirements have to be satisfied, the initial trajectory needs to be reshaped in order to provide a flyable trajectory for transport aircraft. The problem of designing a flyable path over or close to the objective points while satisfying constraints such as maximum curvature and/or G^2 continuity (curvature continuity), has been addressed using different approaches.

As a pioneer, Dubins assured that the shortest path between two points involves circles and straight line path segments (Dubins, July 1957). However, curvature continuity at the joints of lines and circular arcs is not satisfied.

Techniques to solve this track transition problem are addressed using Clothoids (Scheuer and Fraichard, September 1997), but as they do not have closed-form expressions, the computation complexity is increased.

Circular arcs as transitions tracks have been also proposed (Anderson, Beard, and McLain, May 2005), where a 2D real-time trajectory is generated satisfying curvature and velocity constraints. Also, the deviation between the generated circular path and the associated control points is minimized using a parameter $\kappa \in [0, 1]$. If $\kappa = 0$, the distance is zero, so the plane will fly exactly over the waypoint, and if $\kappa = 1$, minimum-time transitions between control points are achieved. However, the election of this parameter κ becomes an issue when a range of distance needs to be chosen as a permitted deviation from the generated path.

Furthermore, Dubins-like approaches generate paths limited to straight lines and arcs of circles without parametrization. Thus, the method shows disadvantages in the generation of several arcs without curvature continuity or with high computation complexity.

Another tool to generate smooth flyable paths is the method of splines, defined by series of low order polynomials. In (Judd and McLain, August 2001), after finding the best path from a UAV position location to a target location using a Voronoi diagram and a Dijkstra's algorithm, the 2D path is smoothed using cubic splines.

In the general use of splines, the optimal locations of the middle knots of the curve are crucial for the shape of the segments. However, the optimal computation of these

points is very time-consuming unless a set of cases are defined a priori.

As an attractive approach, Bezier curves are able to generate continuous-curvature paths, having the advantage of passing through initial and final points while the whole curve always lies within the convex hull that is constructed by the control points. Moreover, the initial and final piecewise straight lines of the control polygon are always tangent to the Bezier curve at the starting and ending control points.

An example is given in (Lee, Kim, and Kim, October 2016), where the authors present the generation of a 3D path obtained from a combination of Rapidly exploring random tree star (RRT*) using a C^2 class Bezier curve and Dynamic Movement Primitives (DMP's), that allow cooperative aerial manipulators to avoid known and unknown obstacles.

In this manner, since the final Bezier curve is a barycentric combination of the polygon vertices formed by the control points, it may be thought that a trajectory could not be accurately generated if the control point positions form a zig-zag. However, this aspect can be handled by stitching several Bezier curves to form a bigger path while assuring G^2 continuity at the joints.

In (Yang et al., 28-2 September-October 2015), after a Guiding Attraction based Random Tree (GART) is used to obtain control points in a 2D plane, a kinematic smoother based on sixth order Bezier curves to achieve second derivative continuity (curvature continuity) is proposed. Finally, a local optimal reshaping of the path, minimizing length and curvature cost is performed.

In (Yang and Sukkarieh, June 2010), an algorithm based on cubic Bezier curves for 3D path smoothing, satisfying G^2 continuity and maximum curvature constraints is presented. Also, instead of addressing a direct solution for the 3D path smoothing, a 2D path smoothing for consecutive triplets of control points is applied, considering each triplet as a 2D plane thanks to the Frenet frame. Nevertheless, deviation from the resulting trajectory with respect to the control points is not controlled at all.

In this chapter, assuming velocity and time constraints, a time-parametrized smooth trajectory is developed by stitching several Bezier curves while assuring G^2 continuity at the joints. Furthermore, the Euclidian distance between the control points and the proposed trajectory is controlled taking into account a tradeoff between path curvature and aircraft intended speed. Thus, the aircraft stays within load factor limits, yielding an 4D path valid for 4D guidance.

The approach proposed in this chapter generates 4D trajectories from given control points, assuring a proper handling of aircraft in position and time. In this manner, air traffic conflicts can be avoided or addressed if present, taking into account load factor limits to look after passengers comfort.

The proposed approach is compatible with the Flow Corridor concept, which consist in long and narrow air highways intended to be used by aircraft while producing minimal interference with other traffic. In addition to this, the quick computation of Bezier curves and their proposed time-parametrization represents a key point to enable the use of slots along the defined trajectories, as well as the path modification if necessary.

A non-exhaustive block diagram of the proposed Trajectory Generation method is presented in Figure 5.1 for the reader's convenience.

 Since the core of the approach is contained in the block *Trajectory Generation (Regular or Reshaped)*, a non-exhaustive coding schema of this part will be provided.

Regarding the other blocks, they are implemented either by the computation of a defined equation, or by a straightforward operation. Thus, these blocks are described with no coding at all through the chapter.
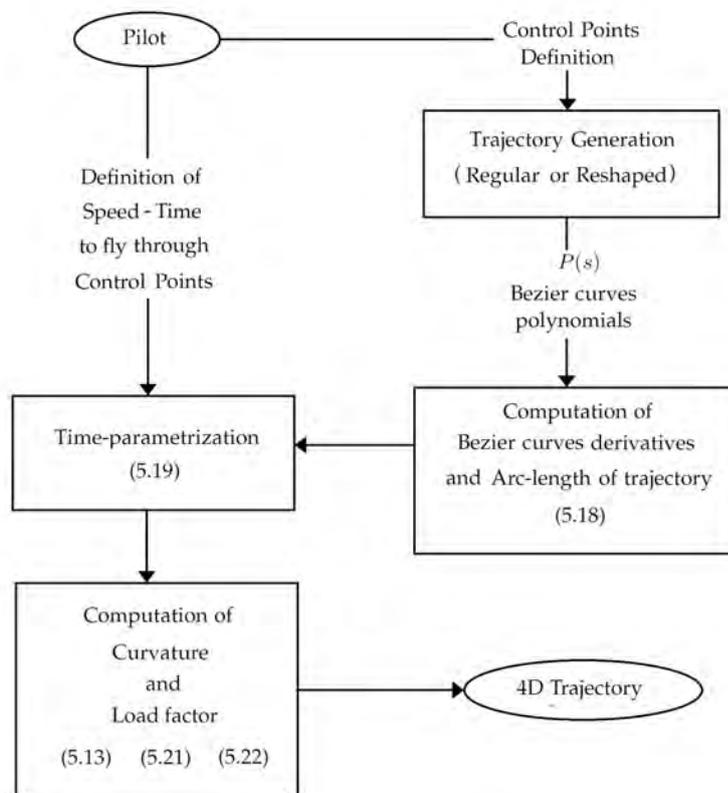
FIGURE 5.1: Block diagram of the Trajectory Generation algorithm.

5.2   Bezier Curves Definition

A Bezier curve $P(s)$ of degree n, obtained from $n + 1$ control points $(P_0, \ldots, P_n)$, is described by

$$P(s) = \sum_{i=0}^{n} B_i^n(s) P_i \qquad s \in [0, 1] \tag{5.1}$$

where $B_i^n(s)$ is the ith Bernstein polynomial of degree n, given by

$$B_i^n(s) = \binom{n}{i} s^i (1 - s)^{n-i} \qquad i \in \{0, 1, \ldots, n\} \tag{5.2}$$

and

$$\binom{n}{i} = \frac{n!}{i! \, (n - i)!} \tag{5.3}$$

Note that

$$P(0) = P_0 \tag{5.4a}$$
$$P(1) = P_n \tag{5.4b}$$

Consequently, differentiating (5.1), and using the property $(n - 1)! = \frac{n!}{n}$, yields

$$P'(s) = \frac{dP(s)}{ds} = \sum_{i=0}^{n} \frac{dB_i^n(s)}{ds} P_i$$
$$= \sum_{i=0}^{n-1} B_i^{n-1}(s) \left(n \left(P_{i+1} - P_i \right) \right) \tag{5.5}$$

Meaning that if a new polygon is defined with its control points as

$$Q_i = n \left(P_{i+1} - P_i \right) \tag{5.6}$$

the first derivative of the Bezier curve is defined by another Bezier curve of the form

$$P'(s) = \sum_{i=0}^{n-1} B_i^{n-1}(s) Q_i \tag{5.7}$$

Analogously, like in (5.4), note that

$$P'(0) = n \left(P_1 - P_0 \right) \tag{5.8a}$$
$$P'(1) = n \left(P_n - P_{n-1} \right) \tag{5.8b}$$

The second derivative of the Bezier curve, obtained from differentiating one more time (5.7), is denoted by

$$P''(s) = \sum_{i=0}^{n-2} B_i^{n-2}(s) \left((n - 1) \left(Q_{i+1} - Q_i \right) \right)$$
$$= \sum_{i=0}^{n-2} B_i^{n-2}(s) \left(n \left(n - 1 \right) \left(P_{i+2} - 2P_{i+1} + P_i \right) \right) \tag{5.9}$$

Note also that

$$P''(0) = n(n-1)(P_2 - 2P_1 + P_0) \tag{5.10a}$$
$$P''(1) = n(n-1)(P_n - 2P_{n-1} + P_{n+2}) \tag{5.10b}$$

As an example, consider the 2D points: $P_0 = [0,0]$, $P_1 = [1,1]$, $P_2 = [2,0]$. A Bezier curve to fit these points will be given by

$$P(s) = B_0^2 P_0 + B_1^2 P_1 + B_2^2 P_2$$
$$= (1-s)^2 P_0 + 2s(1-s)P_1 + s^2 P_2 \qquad s \in [0,1]$$

Therefore, using the control points yields to

$$P_x(s) = (1-s)^2 * 0 + 2s(1-s) * 1 + s^2 * 2$$
$$P_y(s) = (1-s)^2 * 0 + 2s(1-s) * 1 + s^2 * 0$$

In this manner, the two Bezier curves (one for each axe) that fit the control points is given by

$$P(s) = [2s, 2s(1-s)] \qquad ; \quad s \in [0,1]$$

Since three control points are used, a 2nd order curve is generated. Figure 5.2 depicts the control points and the obtained polynomial curve.
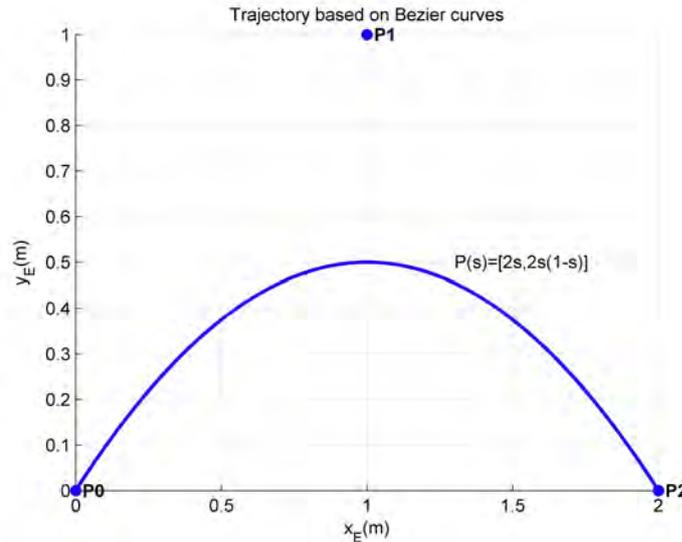
FIGURE 5.2: Second order Bezier curve example.

5.2.1 Continuity and Curvature of a Curve

According to (Barsky and DeRose, October 1984), it is defined:

Definition 1 *(C^n and regularity). A scalar function $g(x)$ belongs to the class C^n on an interval I if it is n-times continuously differentiable on I. It is regular on I if:*

$$\frac{dg(x)}{dx} \neq 0 \qquad \forall x \in I \tag{5.11}$$

Definition 2 *(C^n Continuity). Let $P(s_0, s_1 : s)$ and $Q(t_0, t_1 : t)$ be regular C^n parametrizations such that $P(s_1) = Q(t_0) = J$. That is, the right endpoint of P agrees with the left endpoint of Q. They meet with nth order parametric continuity (C^n) at J if:*

$$\frac{d^k P}{ds^k}|_{s_1} = \frac{d^k Q}{dt^k}|_{t_0} \qquad k = 1, ..., n \tag{5.12}$$

Definition 3 *(G^n Continuity). Let C_P and C_Q be two curves, and let $P(s_0, s_1 : s)$ and $Q(t_0, t_1 : t)$ be regular C^n parametrizations such that $P(s_1) = Q(t_0) = J$, where J is a simple point of $C_P \cup C_Q$. They meet with nth-order geometric continuity (G^n) at J if the natural parametrizations of P and Q meet with C^n continuity at J.*

In this way, G^2 continuity is the second-order geometric continuity, implying the second derivative continuity of two curves at the joint.

Moreover, it is considered that the curvature of a curve, is to be taken as the tendency to change the direction of the path, in other words, what distinguishes a circle from a line.

Hence, let $P(s) = (x(s), y(s), z(s))$ be a regular parametrization of a curve in an interval $I = [a, b] \to R^3$. An expression for the curvature is obtained from the normal and tangential acceleration, expressed by:

$$\kappa(s) = \frac{\|P'(s) \times P''(s)\|}{\|P'(s)\|^3} \tag{5.13}$$

If $\kappa(s) = 0$, $P(s)$ is a straight line. Otherwise, the curve will have a curvature radius of $1/\kappa(s)$. Curvature is always positive or zero.

Thus, let a Bezier curve $C(s)$ with $m + 1$ control points $(C_0, \ldots, C_m)$, and a second Bezier curve $D(s)$ with $n + 1$ control points $(D_0, \ldots, D_n)$ be joined. According to the definitions presented above, C^0 continuity is guaranteed if:

$$C_m = D_0 \tag{5.14}$$

Then, knowing that the first curve is tangent to the last leg, and the second curve is tangent to the first leg, a smooth transition is assured if (5.14) is satisfied and C_m, D_0, C_{m-1}, D_1 are on the same line.

Furthermore, C^1 continuity is guaranteed if the tangent vector of the first curve at $s = 1$ is identical to the tangent vector of the second curve at $s = 0$, meaning that:

$$C'(1) = m(C_m - C_{m-1}) = n(D_1 - D_0) = D'(0) \tag{5.15}$$

This states that the ratio $\left(\frac{C_m - C_{m-1}}{D_1 - D_0}\right)$, involving the length of the last leg of the first curve ($\|C_m - C_{m-1}\|$), and the length of the first leg of the second curve ($\|D_0 - D_1\|$), must be $\frac{n}{m}$.

Therefore, since n and m are fixed numbers, the positions of C_{m-1} and D_1 can be rearranged to be not only at the same line, but also at the proper distance to assure C^1 continuity.

In the same tenor, C^2 and G^2 continuity are guaranteed at the joint if it is verified that

$$\begin{aligned} C''(1) &= m(m - 1)(C_m - 2C_{m-1} + C_{m-2}) \\ &= n(n - 1)(D_2 - 2D_1 + D_0) = D''(0) \end{aligned} \tag{5.16}$$

Hence, to assure G^2 continuity, the locations of C_m, C_{m-1}, C_{m-2}, D_0, D_1, D_2, where (5.14)-(5.16) are satisfied, need to be proposed.

In order to better understand these definitions, different continuity degrees are depicted in Figure 5.3.
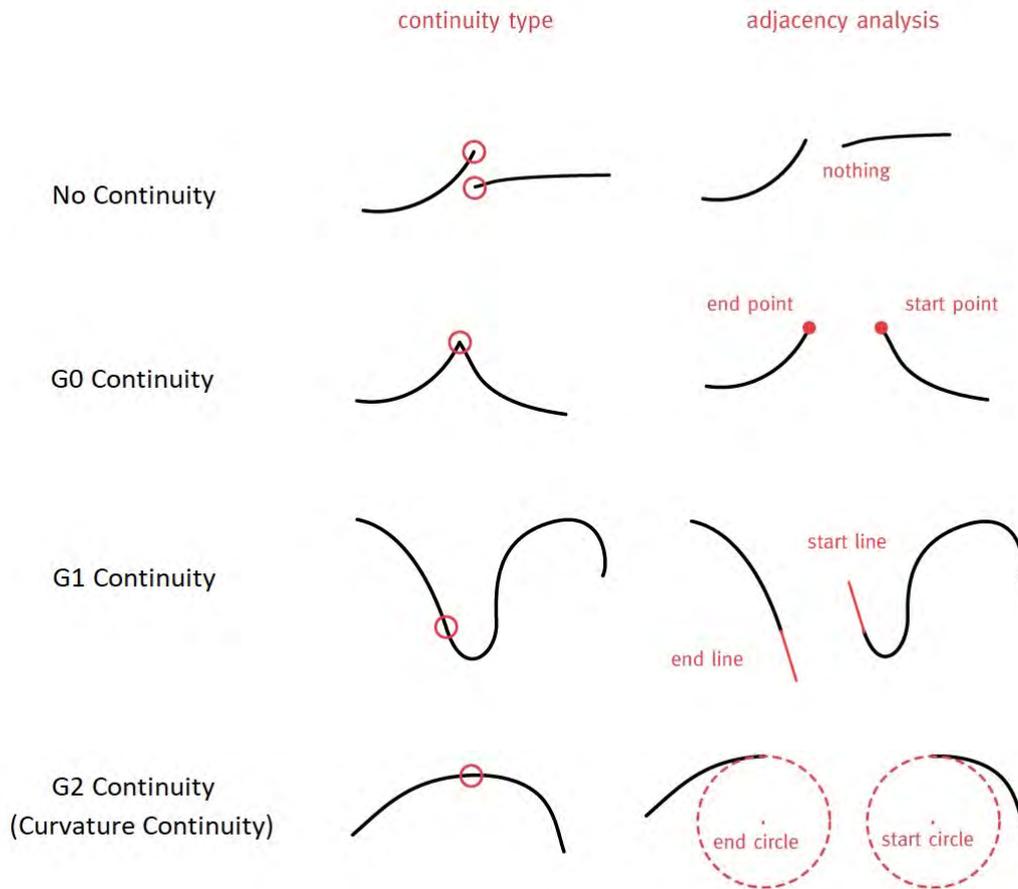
FIGURE 5.3: Different types of continuity in a curve.

5.3   Trajectory Generation

5.3.1 G^2 Continuity Path Generation

In order to handle the curvature while the torsion (what distinguishes a circle from a helix) is zero, the 3D path is decomposed into several 2D planar trajectories laying on the tangent/normal plane of the frenet frame, as some authors have proposed (Yang and Sukkarieh, June 2010). Since three control points are required to form a plane, at least h control points $(P_1, \ldots, P_h, h \geq 3)$ are defined, and then divided into $h - 2$ triplets. Moreover, in order to assure an accurate generation of the path even in zig-zags, several quintic Bezier curves, one for each triplet of control points, are stitched together to form a bigger path while assuring G^2 continuity at the joints.

For the reader's convenience, a pseudocode of the trajectory generation algorithm is provided (see Algorithm 1). Then, a numerical example for a triplet of control points is used to clarify the approach.

Consider a triplet of control points (P_1, P_2, P_3), like the ones depicted in Figure 5.4,

---

Algorithm 1 Trajectory Generation (Regular G^2 Continuity)

Input: Control Points $P_h = [Px_h, Py_h, Pz_h]$, for $k = 1, \ldots, h$
Output: Sets of 5th order Bezier curve polynomials $P_k(s) = [x(s), y(s), z(s)]$, for $k = 1, \ldots, h - 2$

1: **procedure** BEZIER(P_h)   ▷ Insert matrix input
2:     **for** $< i = 1 : 1 : (h - 2)>$ **do**   ▷ Divide control points in triplets
3:         $C = [P_i, P_{i+1}, P_{i+2}]$ ▷ Define the current Triplet
4:         $\delta_1 = \frac{\|P_{i+1} - P_i\|}{4}$ ▷ Compute distances to assure curvature continuity
5:         $\delta_2 = \frac{\|P_{i+1} - P_{i+2}\|}{4}$
6:         $Q_0 = P_i + .5(P_{i+1} - P_i)$ ▷ Interpolate Q_j points (for $j = 0, \ldots, 5$)
7:         $Q_1 = Q_0 + \delta_1 \left(\frac{P_{i+1} - Q_0}{\|P_{i+1} - Q_0\|} \right)$
8:         $Q_2 = Q_1 + \delta_1 \left(\frac{P_{i+1} - Q_0}{\|P_{i+1} - Q_0\|} \right)$
9:         $Q_3 = Q_4 + \delta_2 \left(\frac{P_{i+1} - Q_5}{\|P_{i+1} - Q_5\|} \right)$
10:        $Q_4 = Q_5 + \delta_2 \left(\frac{P_{i+1} - Q_5}{\|P_{i+1} - Q_5\|} \right)$
11:        $Q_5 = P_{i+1} + .5(P_{i+2} - P_{i+1})$
12:        $B(s) = [x(s), y(s), z(s)] \leftarrow \sum_{m=0}^{n=5} B_m^n(s) Q_m$ ▷ Compute curve
13:        $P_i(s) \leftarrow B(s)$ ▷ Save the polynomials
14:        **if** $<i = 1>$ **then**   ▷ Beginning triplet
15:            $Q_{init} = [P_i, Q_0]$
16:            $Bi(s) \leftarrow \sum_{m=0}^{n=1} B_m^n(s) Q_{init_m}$ ▷ Line from P_1 to first Q_0
17:        **end if**
18:        **if** $<i = h - 2>$ **then**   ▷ Ending triplet
19:            $Q_{end} = [Q_5, P_{i+2}]$
20:            $Be(s) \leftarrow \sum_{m=0}^{n=1} B_m^n(s) Q_{end_m}$ ▷ Line from last Q_5 to P_h
21:        **end if**
22:     **end for**
23:     $P(s) = [Bi(s); B(s); Be(s)]$ ▷ Complete total curve with straight segments
24:     **return** $P(s)$ ▷ Full Curve
25: **end procedure**

G^1 continuity can be achieved by interpolating four points (Q_0, Q_1, Q_4, Q_5), and for G^2 continuity, six points are interpolated $(Q_i; i \in \{0, \ldots, 5\})$. After the interpolation

of these auxiliary control points, a quintic Bezier curve is adjusted to them in the case of the G^2 continuity path.

The points are interpolated as follows:

Q_0 and Q_5 are defined to be at the middle point of $(\bar{P_1 P_2})$ and $(\bar{P_2 P_3})$ respectively,
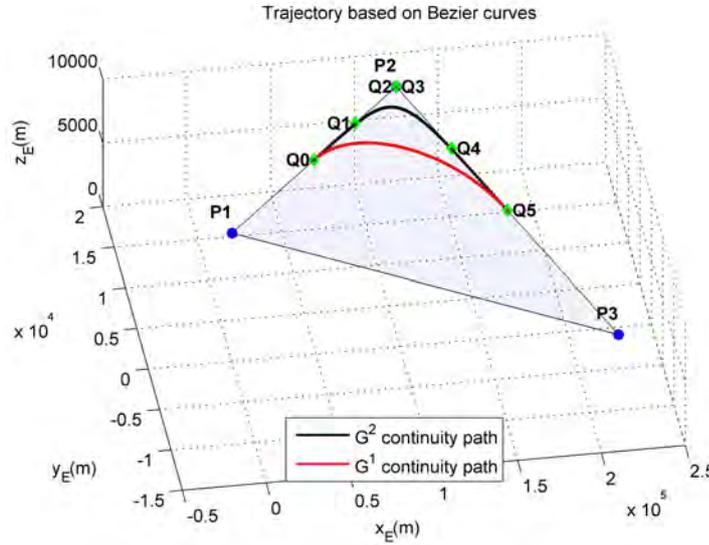
FIGURE 5.4: G^2 and G^1 continuity path with auxiliary control points.

forcing a past and following Bezier curve formed by the past and next triplet of control points, to finish and start at Q_0 and Q_5 control points. In other words, a next triplet of points conformed by (P_2, P_3, P_4) will have a Bezier curve starting at Q_5, and a past triplet of points conformed by (P_0, P_1, P_2) will have a Bezier curve ending at Q_0, so (5.14) is fulfilled.

For Q_1 and Q_4, they are computed to be also in the same line of $(\bar{P_1 P_2})$ and $(\bar{P_2 P_3})$, respectively, but separated by a δ_1 distance from Q_0 in the case of Q_1, and a distance δ_2 from Q_5 in the case of Q_4.

Note that the number of auxiliary interpolated points to compute the Bezier curves are the same for all the triplet of points, so m and n from (5.15) are equal. Hence, to fulfill G^1 continuity, it only remains to guarantee that the distance δ_2 of a certain triplet of control points is equal to the distance δ_1 of the next triplet of control points. Finally, if the positions of Q_2 and Q_3 are computed also in the same line of $(\bar{P_1 P_2})$ and $(\bar{P_2 P_3})$, respectively, separated by the same distances δ_1 from Q_1, and δ_2 from Q_4, if it is proposed:

$$\delta_1 = \frac{\bar{P_1 P_2}}{4} \tag{5.17a}$$

$$\delta_2 = \frac{\bar{P_2 P_3}}{4} \tag{5.17b}$$

equations (5.15), (5.16) are satisfied, assuring G^2 continuity by forcing the curvature to be zero at the joints between Bezier curves.

Furthermore, knowing that the first and last Bezier curves forming the *total* path will start and end at the middle point of their corresponding control points, since straight lines have zero curvature, the path can be completed with straight lines without affecting the G^2 continuity (see Figure 5.5).
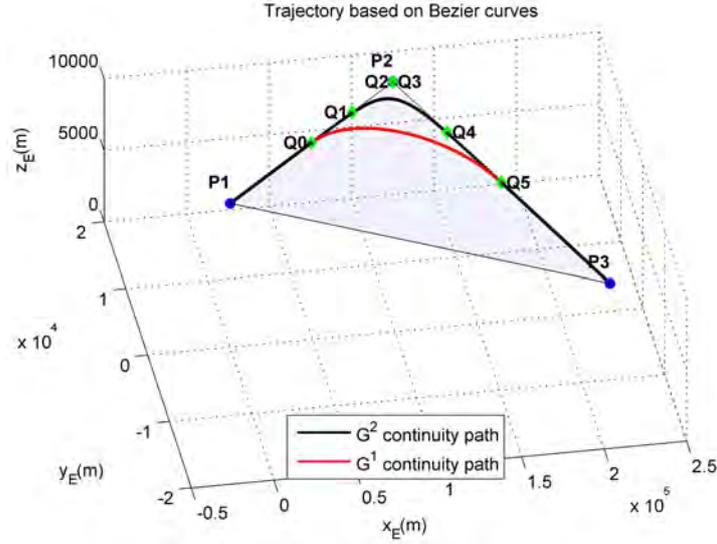
FIGURE 5.5:   Bezier curve completed with starting and ending straight lines.

5.3.2   Time-Parametrization of the Path

Taking into account that several Bezier curves form the total path, and each Bezier curve is parameterized by $s \in [0, 1]$, a time re-parametrization needs to be done for the creation of a flyable path for transport aircraft.

Considering that the timing in which each Bezier curve is used needs to be known to parameterize the curve, the computation of the arc length of each Bezier curve is inherent. Therefore, the arc-length of each Bezier curve is calculated by integrating from zero to one the norm of the first derivative of the Bezier curves.

$$\int_0^1 \|P'(s)\| ds \tag{5.18}$$

For example, the Bezier polynomial given for the Figure 5.2 ($P(s) = [2s, 2s(1 - s)]$), have an arc-length of:

$$\int_0^1 4\sqrt{s^2 - s + \frac{1}{2}} ds = 2.29$$

Once the arc-lengths are obtained, a velocity for the aircraft to follow the path can be chosen, or as an alternative way, the time in which the aircraft is supposed to fly over the joints of the Bezier curves is defined.

As a first numerical example, some control points were chosen, given in Table 5.1. These points are used to generate a G^1 and G^2 path, depicted in Figure 5.6.

  Regarding the joints of the G^2 Bezier curves, and assuming that the path is intended to be followed at a constant $200m/s$ velocity, Figure 5.7 shows the arc-lengths ($l_i; i \in [1, 6]$) and their accumulative times ($t_j; j \in [0, 6]$) assigned. Note that these values of time, are the times where the Bezier curves are joined. The values of l_i and t_j are given in Table 5.2.

  However, since Bezier curves are not parameterized by time, an operation is performed such that:

$$s = \frac{t - t_i}{t_{i+1} - t_i} \qquad i \in [0, 1, ..., 5] \tag{5.19}$$

TABLE 5.1: Control Points.

	X(m)	Y(m)	Z(m)
P_1	0	0	10,000
P_2	120,843	16,983	9,300
P_3	210,332	-14,779	9,000
P_4	272,744	-759	8,200
P_5	388,920	-11,130	9,500
P_6	478,501	12,964	9,800
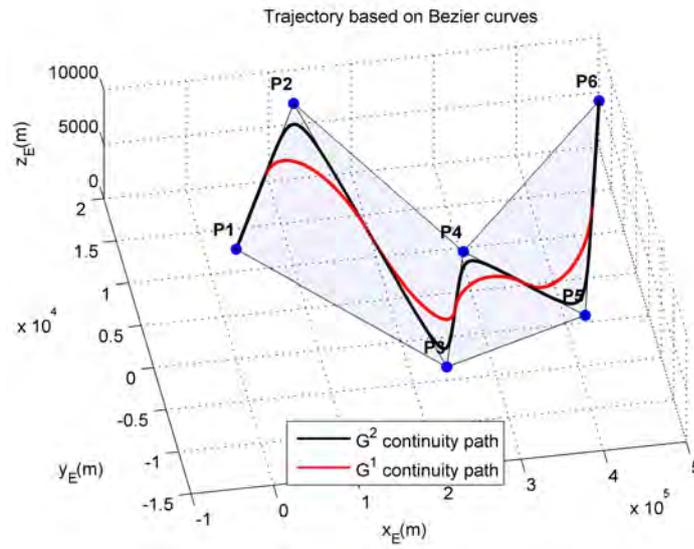
FIGURE 5.6: Generated path based on quintic Bezier curves.
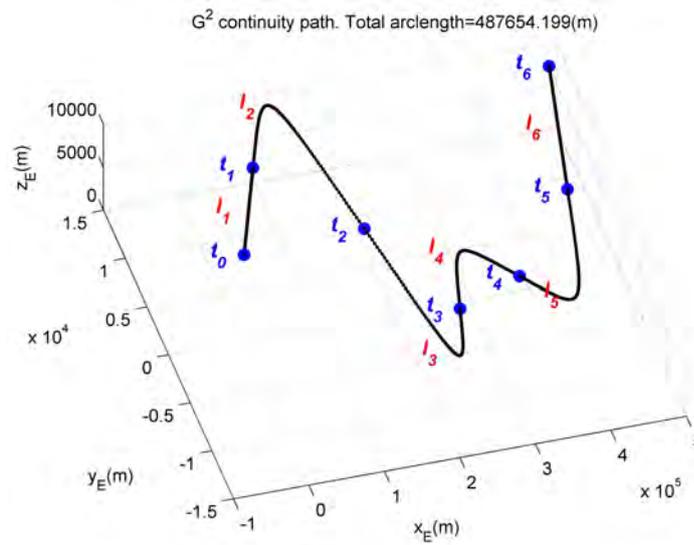
FIGURE 5.7: Generated path showing arc lengths and joints of Bezier curves.

So that the multiple Bezier curves parameterized by $s \in [0,1]$, can be used at the proper time intervals $[t_i, t_{i+1}]$.

TABLE 5.2: Times and Arc lengths.

	Arc length(m)		*Accumulative Time(s)*
		t_0	0
l_1	61,016	t_1	305.1
l_2	107,536	t_2	842.8
l_3	78,523	t_3	1,235.4
l_4	89,990	t_4	1,685.3
l_5	104,206	t_5	2,206.4
l_6	46,383	t_6	2,438.3

Finally, comparing the curvatures of the G^1 and G^2 continuity paths (see Figure 5.8), it is clearly seen how the G^2 path has continuity in the curvature at the joints of the different Bezier curves, and that these joints occur at the assigned time, represented by asterisks in the corresponding axis.
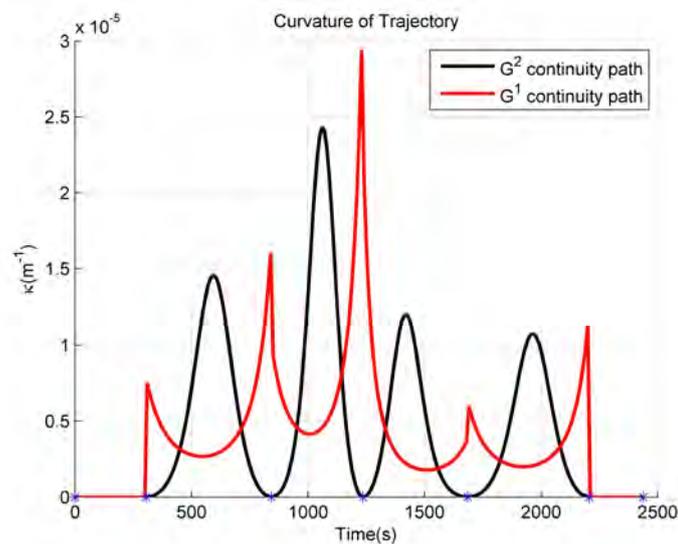
FIGURE 5.8: Curvature of the G^1 and G^2 continuity paths.

5.4 Reshaping of the Trajectory

Depending on the application, some aircraft may need to fly directly over the control points or at least near a defined range of distance from the control points. In order to achieve this demand, the Euclidian distance from the G^2 continuity path with respect to the nearest control point is controlled. For this special case, an extra auxiliary point (Q_3 in Figure 5.9) is computed such that a reshaped path based on sixth order Bezier curves is obtained. The other auxiliary control points are conserved as before in order to not affect curvature continuity, but the position of the heptic auxiliary point is moved gradually until the generated path passes within a distance range defined by the user. The direction in which the extra point moves is denoted by:

$$a\vec{u}x = \frac{(Q_2 \vec{-} Q_1) + (Q_4 \vec{-} Q_5)}{\|(Q_2 \vec{-} Q_1) + (Q_4 \vec{-} Q_5)\|} \tag{5.20}$$

For the reader's convenience, a pseudocode of the reshaped trajectory generation algorithm is provided (see Algorithm 2). Then, a numerical example for a triplet of control points is used to clarify the approach.

In Figure 5.9, a $100m$ maximum deviation for a triplet of control points is commanded, meaning that the reshaped path will be generated such that it will pass no further than $100m$ away the control point P_2. In this case, the reshaping algorithm stopped at a distance of $92.48m$. The distance at which the algorithm stops depends on the step size in which Q_3 is moved away in the direction of $a\vec{u}x$. For a small step size, the path will be closer to the distance defined by the user, in this case $100m$, but the computation time will be increased. The curvature of the reshaped path, and the initial G^1 path are shown in Figure 5.10.

Now, for a complete trajectory, using the control points of Table 5.1, a $100m$ max-
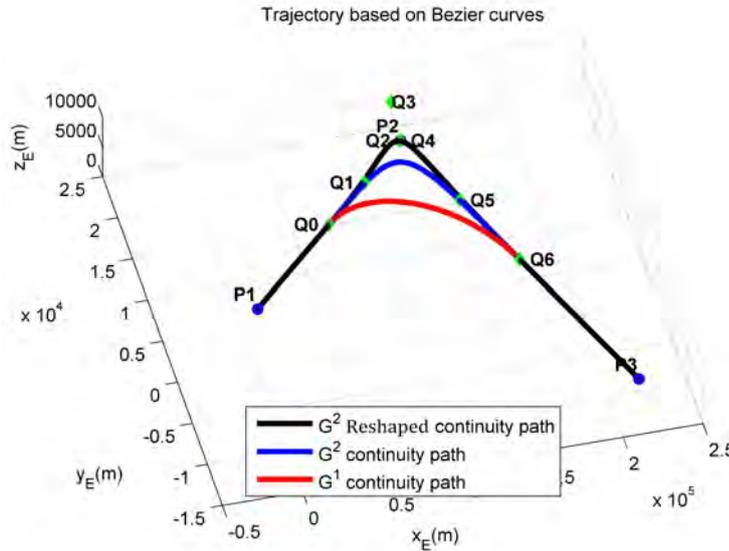
FIGURE 5.9: $100m$ deviation reshaped path for a triplet of control points using an auxiliary control point (Q_3).

imum deviation is commanded, the resultant path is shown in Figure 5.11 and the curvature of the reshaped path in Figure 5.12.

The Euclidian distance from the generated trajectory to the closest control points is

---

Algorithm 2 Trajectory Generation (Reshaped G^2 Continuity)

Input 1: Control Points $P_h = [Px_h, Py_h, Pz_h]$, for $k = 1, \ldots, h$

Input 2: Maximum distance from path to trajectory ddc

Output: Sets of 6th order Bezier curve polynomials $P_k(s) = [x(s), y(s), z(s)]$, for $k = 1, \ldots, h - 2$

1: **procedure** BEZIER RESHAPED(P_h)   ▷ Insert matrix input
2:      **for** $< i = 1 : 1 : (h - 2)>$ **do**   ▷ Divide control points in triplets
3:          $C = [P_i, P_{i+1}, P_{i+2}]$ ▷ Define the current Triplet
4:          $\delta_1 = \frac{\|P_{i+1} - P_i\|}{4}$ ▷ Compute distances to assure curvature continuity
5:          $\delta_2 = \frac{\|P_{i+1} - P_{i+2}\|}{4}$
6:          $Q_0 = P_i + .5(P_{i+1} - P_i)$ ▷ Interpolate Q points
7:          $Q_1 = Q_0 + \delta_1 \left(\frac{P_{i+1} - Q_0}{\|P_{i+1} - Q_0\|} \right)$
8:          $Q_2 = Q_1 + \delta_1 \left(\frac{P_{i+1} - Q_0}{\|P_{i+1} - Q_0\|} \right)$
9:          $Q_4 = Q_4 + \delta_2 \left(\frac{P_{i+1} - Q_5}{\|P_{i+1} - Q_5\|} \right)$ ▷ Note that Q_3 is not calculated
10:          $Q_5 = Q_5 + \delta_2 \left(\frac{P_{i+1} - Q_5}{\|P_{i+1} - Q_5\|} \right)$
11:          $Q_6 = P_{i+1} + .5(P_{i+2} - P_{i+1})$
12:          $B(s) = [x(s), y(s), z(s)] \leftarrow \sum_{m=0; m \not\ni 3}^{n=6} B_m^n(s) Q_m$ ▷ Compute curve
13:          $d = min \left(\sqrt{(Px_{i+1} - x(s))^2 + (Py_{i+1} - y(s))^2 + (Pz_{i+1} - z(s))^2} \right)$ ▷
     Compute distance from path to control point
14:          **while** $<d \geq ddc>$ **do**   ▷ current distance from path to control point is compared with the desired distance
15:              $\varepsilon = cte$ ▷ Step size that Q_3 moves in $a\vec{u}x$ direction
16:              $Q_3 = P_{i+1} + \varepsilon \left(\frac{(Q_2 - Q_1) + (Q_4 - Q_5)}{\|(Q_2 - Q_1) + (Q_4 - Q_5)\|} \right)$ ▷ Compute Q_3 position
17:              $B(s) = [x(s), y(s), z(s)] \leftarrow \sum_{m=0}^{n=6} B_m^n(s) Q_m$ ▷ Compute curve
18:              $d = min \left(\sqrt{(Px_{i+1} - x(s))^2 + (Py_{i+1} - y(s))^2 + (Pz_{i+1} - z(s))^2} \right)$
19:          **end while**
20:          $P_i(s) \leftarrow B(s)$ ▷ Save the polynomials
21:          **if** $<i = 1>$ **then**   ▷ Beginning triplet
22:              $Q_{init} = [P_i, Q_0]$
23:              $Bi(s) \leftarrow \sum_{m=0}^{n=1} B_m^n(s) Q_{init_m}$ ▷ Line from P_1 to first Q_0
24:          **end if**
25:          **if** $<i = h - 2>$ **then**   ▷ Ending triplet
26:              $Q_{end} = [Q_6, P_{i+2}]$
27:              $Be(s) \leftarrow \sum_{m=0}^{n=1} B_m^n(s) Q_{end_m}$ ▷ Line from last Q_6 to P_h
28:          **end if**
29:      **end for**
30:      $P(s) = [Bi(s); B(s); Be(s)]$ ▷ Complete total curve with straight segments
31:      **return** $P(s)$ ▷ Full Curve
32: **end procedure**
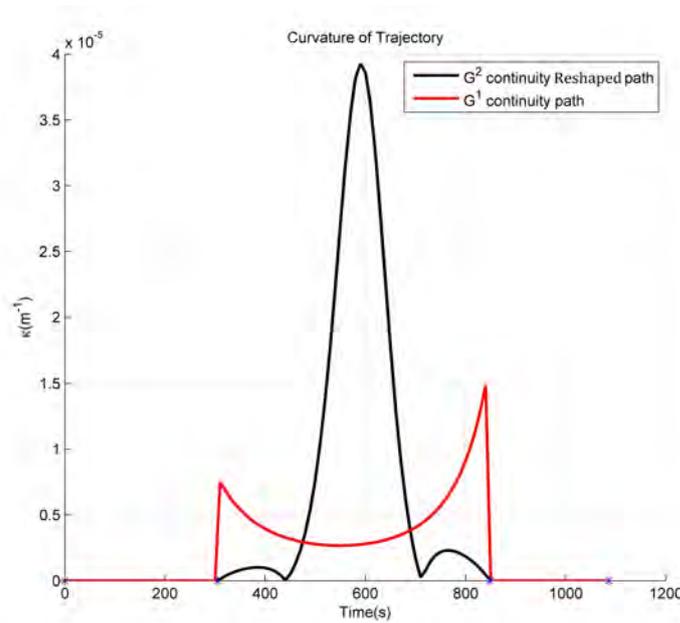
FIGURE 5.10: Curvature for a triplet of control points of the $100m$ deviation reshaped G^2 path, and the G^1 initial path.

given by Table 5.3.
 Assuring that the maximum deviation distance is achieved.

TABLE 5.3: Distance of curve from control points.

From		P_2	P_3	P_4	P_5
Distance(m)	*Initial*	2800.77	2351.04	1449.10	2010.67
	Reshaped	92.48	99.72	96.09	79.53

 Note that at as close as the reshaped path is to the control points, the curvature increases. In this manner, a tradeoff between the deviation of the path from the control points, and maximum curvature constraints, needs to be established.
It is straightforward to see that maximum curvature constraints are strongly related to limitations of the load factor for transport aircraft. Moreover, since the curvature is the inverse of the radius of the trajectory, the interaction of the load factor and the curvature, or the radius of the trajectory (dependent on the aircraft velocity) is analyzed.
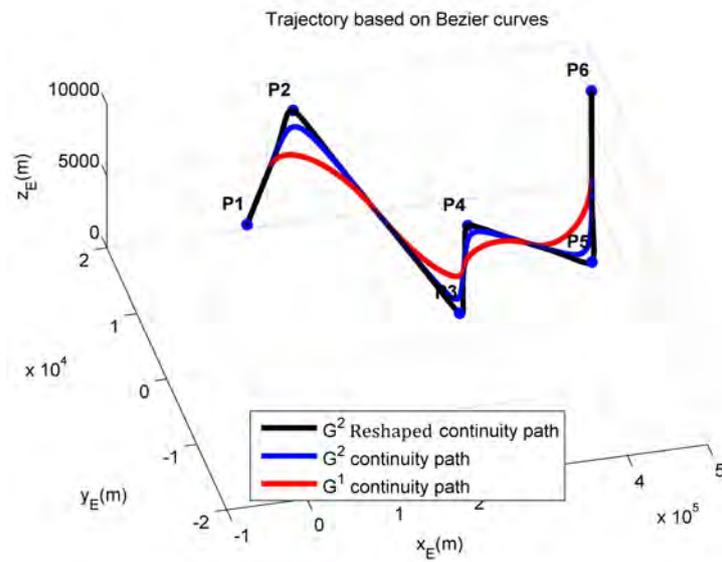
FIGURE 5.11: $100m$ deviation reshaped path.
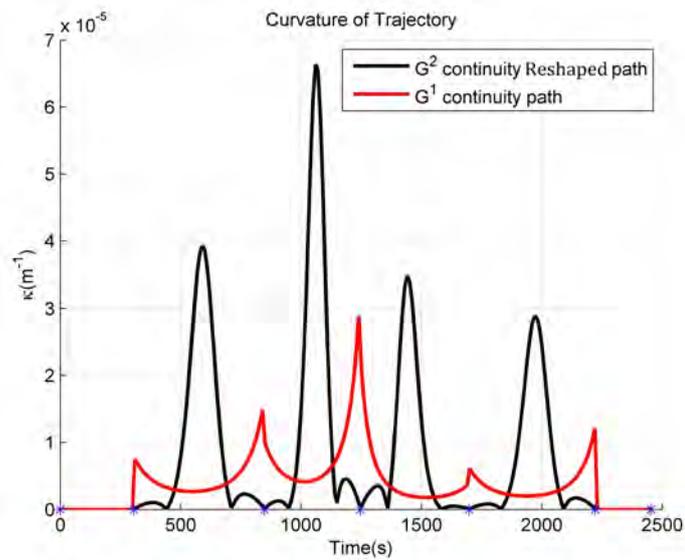
FIGURE 5.12: Curvature of reshaped path.

5.5   Load Factor and Curvature of the Trajectory

In Section 3.5, the expression relating the load factor that an aircraft would experience if a curved horizontal path of radius R was flown, at a given speed, was stated by:

$$R = \frac{V_a^2}{g\sqrt{n_z^2 - 1}} \tag{5.21}$$

Moreover, the equation relating the load factor and speed with the radius R' of the path in a pitch up motion was denoted by:

$$\frac{(n_z - 1)\,g}{V_a} = \frac{V_a}{R'} \tag{5.22}$$

Therefore, since the path has a curvature radius of $1/\kappa$, the curvature κ of the path is directly related to (5.21) and (5.22). In this manner, for independent lateral or vertical maneuvers, the path that an aircraft can follow without infringing load factor limits can be computed, taking into account the speed of the aircraft and the curvature of the path generated by the position of the control points. Then, path constraints regarding the maximum curvature can be established for different flyability requirements based on load factor limits.

According to (5.21) and (5.22), maximum radius of curvature for circular motions can be computed for different speeds after defining load factor limits. For example, a $2.5g$ load factor at $200\mathrm{m/s}$ is generated by a circular trajectory of a radius of $1,779.55\mathrm{m}$, equivalent to a roll angle of $66.5°$ using (3.75). This angle happens to be the maximum roll angle permitted for transport aircraft.

To better exemplify the relation of the load factor with respect to the velocity, consider a scenario of the trajectory of an aircraft changing airways by changing its heading (fly-by turn). Three control points located at the same altitude and separated by 50 nautical miles (nm) from each other are used (see Table 5.4). The control

TABLE 5.4: Control points for an aircraft changing airways.

1nm=1852m	X(m)	Y(m)	Z(m)
P_1	0	92,600	10,000
P_2	92,600	92,600	10,000
P_3	92,600	0	10,000

points are shown in Figure 5.13, along with the computed Bezier curves of G^2 continuity. Moreover, the arc-lengths of each curve and the points where the Bezier curves are joined (using their timestamps) are shown.

Now, consider three different speeds for an aircraft to go through these control points, the numerical values of the timestamps where the Bezier curves are joined change according to Table 5.5. Furthermore, the transition between legs will generate different load factors depending on the speed, shown in Figure 5.14. On the other hand, independent from the speed, the curvature of the path remains constant (see Figure 5.15).

Once that the relation of the load-factor and velocity has been shown, we can explore the curvature constraints due to load factor limits while keeping a constant velocity.

In the example above, the distance from the trajectory to the point P_2 is $7,161.66\mathrm{m}$. Thus, consider a trajectory to allow an aircraft to turn closer to P_2 with a constant velocity of $200\mathrm{m/s}$. The first guess is to use the path reshaping proposed in Section 5.4.
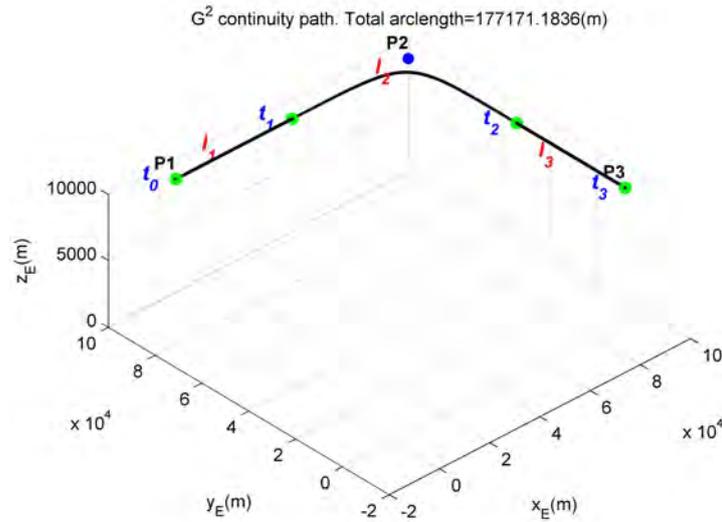
FIGURE 5.13: Control points of example, Arc lengths, and Times.

TABLE 5.5: Arc lengths and times at different velocities

	Arc length(m)		170m/s	200m/s	230m/s
			Time(s)		
		t_0	0	0	0
l_1	46,300	t_1	272.35	231.5	201.30
l_2	84,571	t_2	769.83	654.35	569
l_3	46,300	t_3	1,042.18	885.85	770.3
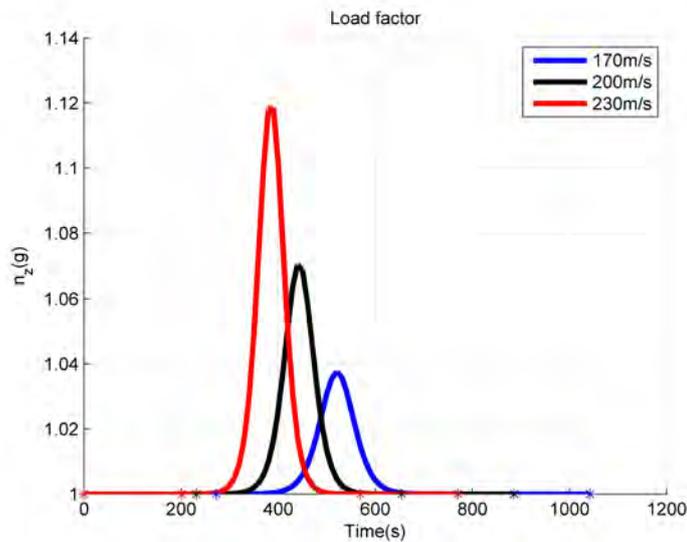
FIGURE 5.14: Load factor at different velocities.

However, due to the design of the algorithm, even if the trajectory is to be designed with a maximum deviation of 10m from P_2, the algorithm modifies the trajectory such that the load factor remains within bounds. This scenario is depicted in Figure 5.16, where a zoom to P_2 shows how the generated trajectory curves before and
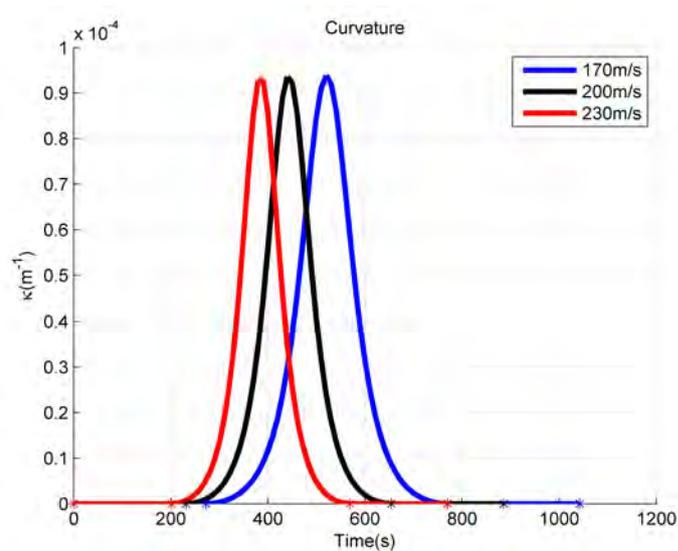
FIGURE 5.15: Curvature at different velocities.

after the control point to satisfy the maximum deviation constraint. This trajectory corresponds to an "optimized" fly-by turn. The load factor of the generated trajectory, shown in Figure 5.17(a), reaches a peek of $\approx 1.425g$. The curvature of the path, shown in Figure 5.17(b), reaches a value of $\approx 2.5 \times 10^{-4}(\text{m}^{-1})$. The distance from this trajectory to P_2 is 1.36m.

Consequently, in order to have a trajectory close to the control point P_2 while in-
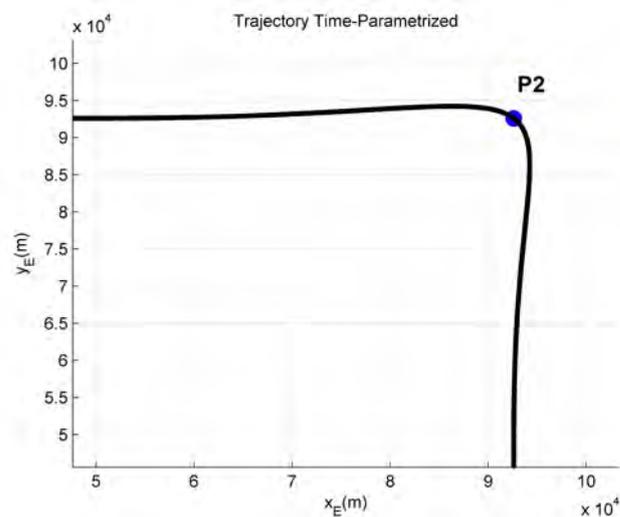
FIGURE 5.16: Zoom to the generated trajectory close to the control point P_2 with a 10m maximum deviation.

creasing significantly the load factor, two auxiliary control points are added (see Table 5.6), such that the direction of the path is not curved, as in the case when the reshaping is done. This trajectory corresponds to a regular fly-by turn. A zoom in close to the control point P_2 shows the generated trajectory, which passes at a distance of $1,203$m from P_2 (see Figure 5.18). Under this conditions, the load factor, shown in Figure 5.19(a) reaches its $2.5g$ limit. The curvature of the path pikes

(a) Load factor.
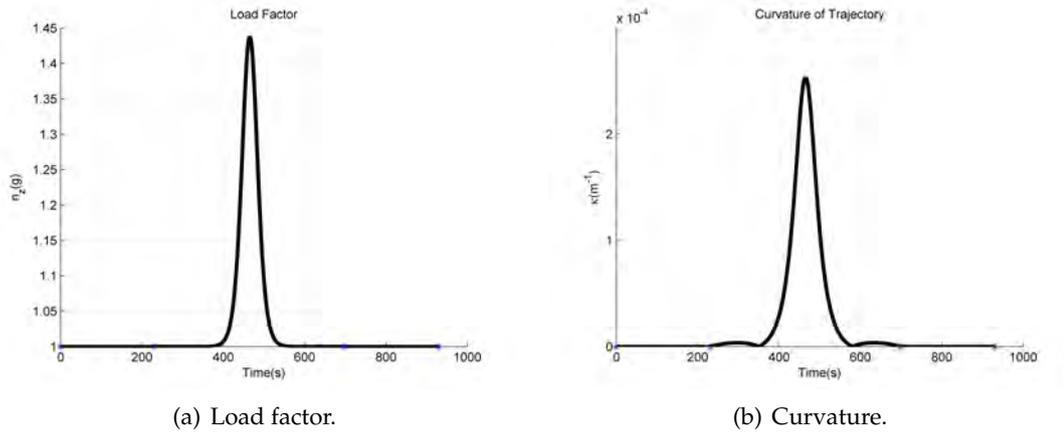
(b) Curvature.

FIGURE 5.17: Load factor and Curvature of the trajectory with a 10m maximum deviation.

at $\approx 5.6\mathrm{x}10^{-4}(\mathrm{m}^{-1})$ (see Figure 5.19(b)), which is close enough to the $1,779\mathrm{m}$ radius limit for circular trajectories, stated before.

Thus, if an aircraft flying at $200\mathrm{m/s}$ is commanded to pass through three control points distributed in a "L" shape, a single turn maneuver leaves the aircraft at a distance of $1,203\mathrm{m}$ from the middle control point before infringing load factor limits. On the other hand, the proposed reshaping algorithm generates a flyable trajectory at $1.36\mathrm{m}$ from the same control point, achieving an "optimal" fly-by turn. Numerical computations can be done for any other velocity and for the pitching motion.

TABLE 5.6: Auxiliary control points to force a high load factor

	X(m)	Y(m)	Z(m)
P_{aux1}	77,043.2	92,600	10,000
P_{aux2}	92,600	77,043.2	10,000
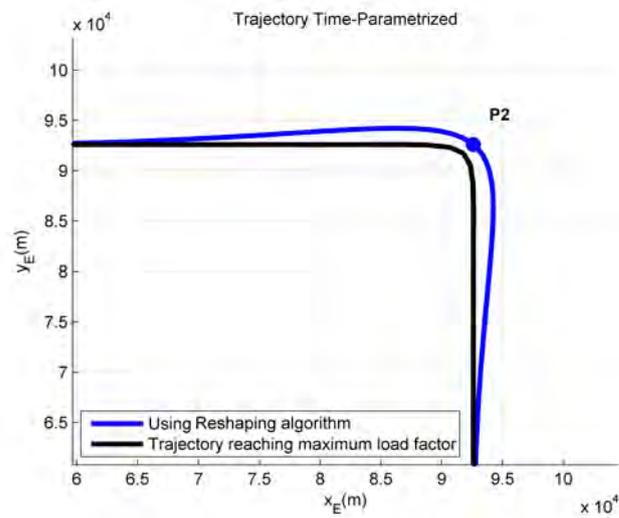
FIGURE 5.18: Zoom to the generated trajectory close to the control point P_2 forcing a maximum load factor compared with Reshaping algorithm.

(a) Load factor.
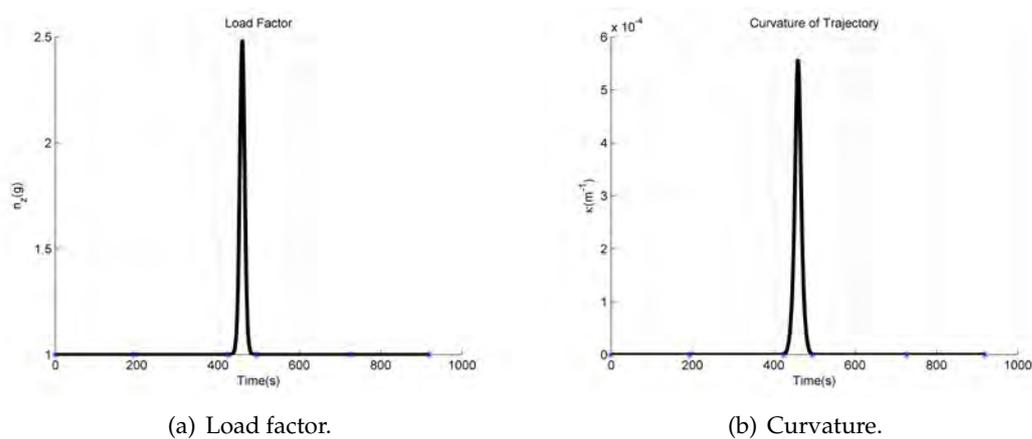
(b) Curvature.

FIGURE 5.19: Load factor and Curvature of the trajectory close to the control point P_2 with a maximum load factor.

5.6 Generation of a full Flight Profile

In this Section, the use of Bezier curves to generate a full flight profile is presented. Consider the profile flown by an A320-200 from Toulouse airport (TLS) to Paris Charles de Gaulle airport (CDG) the 16th November 2017. The vertical and lateral flight profiles are shown in Figures 5.20 and 5.21, while the flight is summarized in Table 5.7.

Introducing the control points in the approach based on Bezier curves, the flight

FIGURE 5.20: Vertical profile from flight AF7527 (Flightradar24, 2017).
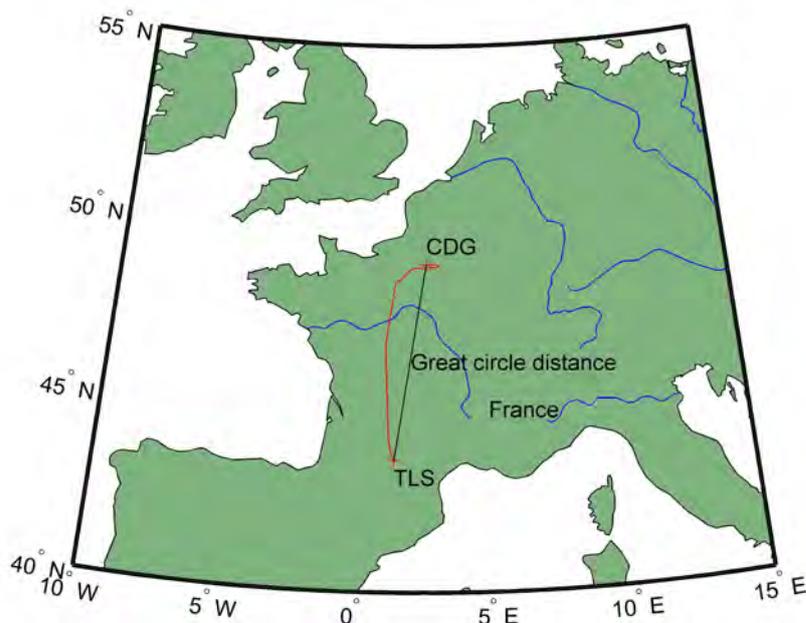
FIGURE 5.21: Lateral profile from flight AF7527.

profile is reproduced.

Considering a geodetic reference system (WGS 84), the latitude and longitude points are transformed into the North-East-Down frame (NED), where the x axis is East, and the y axis North. Then, a G^2 continuity path is generated. The resultant path has a distance of $731,909$m. A comparison between the original path and the reproduced path is given in Figure 5.22(a), and the continuous curvature of the generated path is shown in Figure 5.22(b). The generated trajectory is time-parameterized according to the velocities attached to each control point. In this manner, the proposed
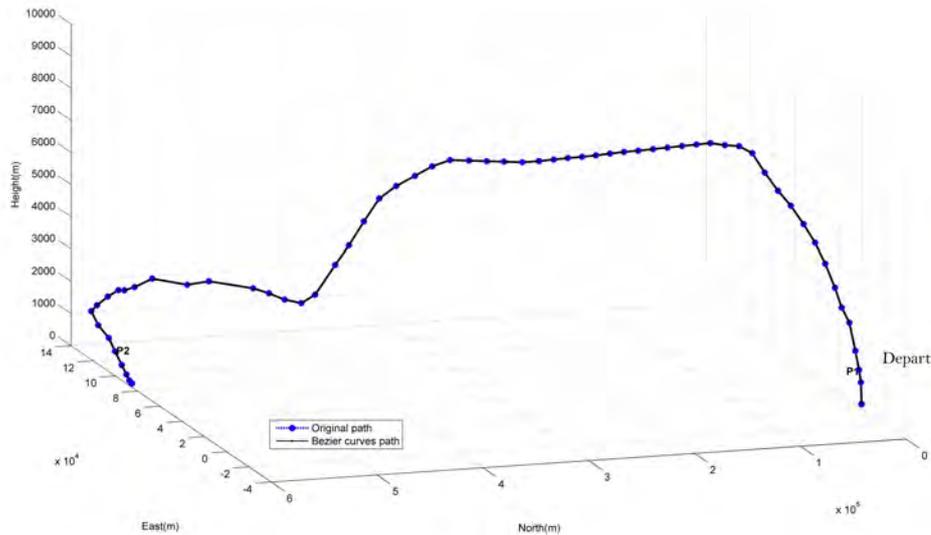
(a) Originial and Generated Trajectory of a full flight profile.
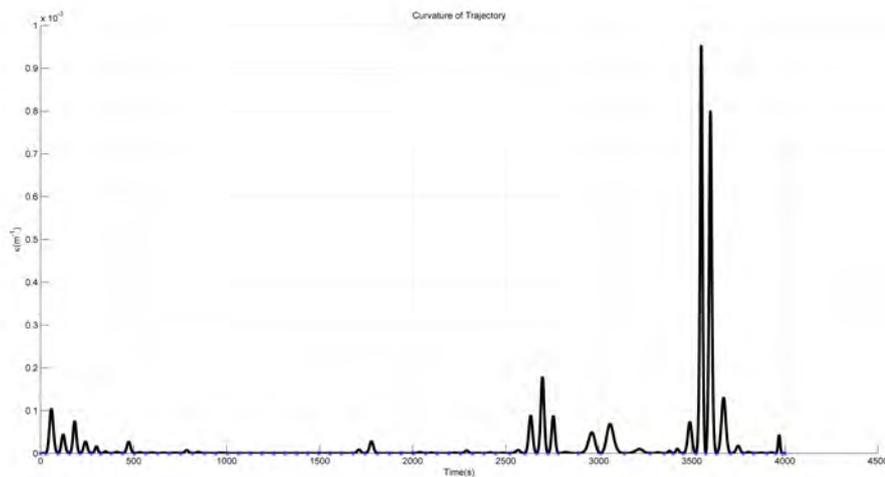
(b) Curvature of the path.

FIGURE 5.22: Reproduction of the lateral/vertical profile of the flight AF7527.

approach is shown to be suitable for optimizing a given path, and valid for generating a complete flight profile from pre-defined control points.

TABLE 5.7: Flight Profile of AF7527.

Control Point	Latitude	Longitude	Altitude (m)	Speed (knot)	Time
1	43.630074	1.371411	0	0	20:21
2	43.63591	1.359239	145	153	20:26
3	43.665951	1.326599	892	143	20:27
4	43.70813	1.292528	1356	205	20:28
5	43.769669	1.252697	2042	266	20:29
6	43.838753	1.228441	2979	275	20:30
7	43.921337	1.205553	3513	331	20:31
8	43.99054	1.189973	4176	338	20:32
9	44.090195	1.167297	4991	350	20:33
10	44.193714	1.144148	5700	365	20:34
11	44.297714	1.13608	6317	378	20:35
12	44.410461	1.12851	6927	390	20:36
13	44.525215	1.120739	7437	402	20:37
14	44.644455	1.112627	8047	403	20:38
15	44.755737	1.105107	8694	395	20:39
16	44.87352	1.097063	8954	418	20:41
17	44.999813	1.088383	9030	447	20:42
18	45.130859	1.079474	9144	446	20:43
19	45.254837	1.07084	9144	445	20:44
20	45.382874	1.061881	9144	450	20:45
21	45.512447	1.052812	9144	450	20:46
22	45.642002	1.043633	9144	450	20:47
23	45.774628	1.034294	9144	450	20:48
24	45.902161	1.025413	9152	450	20:49
25	46.026432	1.016647	9144	450	20:50
26	46.152355	1.007584	9136	450	20:51
27	46.276276	0.998589	9136	450	20:52
28	46.403137	0.989506	9144	450	20:53
29	46.529938	0.980324	9144	450	20:54
30	46.661125	0.970848	9144	450	20:55
31	46.803131	0.969543	9144	450	20:56
32	46.939087	0.996803	9144	450	20:57
33	47.067154	1.022855	9144	450	20:58
34	47.198914	1.049881	9144	450	20:59
35	47.338348	1.078651	9144	450	21:00
36	47.469921	1.106027	8931	454	21:01
37	47.597763	1.132553	8618	461	21:02
38	47.736572	1.161593	8283	463	21:04
39	47.861797	1.188002	7879	408	21:05
40	47.97562	1.211947	7148	390	21:06
41	48.086552	1.235399	6393	377	21:07
42	48.188595	1.257212	5784	359	21:08
43	48.336456	1.288781	4839	337	21:09
44	48.438629	1.310894	4564	345	21:10
45	48.532059	1.382024	4572	353	21:11
46	48.577789	1.507733	4564	353	21:12
47	48.643616	1.605342	4564	353	21:13
48	48.830246	1.87824	4359	355	21:16
49	48.893631	2.053287	3962	332	21:17
50	48.915741	2.446843	3482	314	21:20
51	48.918674	2.655656	2858	305	21:22
52	48.919922	2.778696	2545	282	21:23
53	48.920582	2.848711	2431	261	21:24
54	48.921841	2.975777	2012	249	21:25
55	48.937901	3.083689	1562	238	21:26
56	48.989136	3.083144	1394	233	21:27
57	49.013222	2.965152	1166	227	21:28
58	49.007542	2.844881	975	195	21:29
59	49.00396	2.775493	678	189	21:30
60	48.999954	2.698951	381	130	21:31
61	48.997253	2.647127	175	127	21:32
62	48.995499	2.614394	46	128	21:33
63	48.993996	2.58569	0	128	21:34
64	49.008286	2.566229	0	0	21:42

5.6.1 Multiplicity of trajectories

Since the generated path is defined by several Bezier curves, and each curve is a polynomial, the generation of parallel trajectories to a reference one is straight forward. An example of parallel trajectories to the full flight profile is given in Figure 5.23. These trajectories are separated according to the flow corridors organization, with 8NM lateral and 1000ft vertical distances for each path.

In this manner, the trajectory generation algorithm is compatible with current FMS
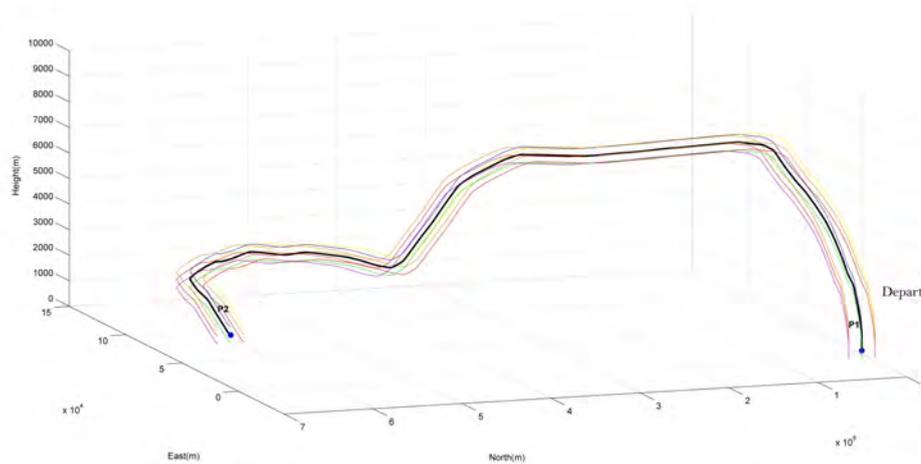
FIGURE 5.23: Multiplicity of the flight profile.

functions, and valid for its usage in flow corridors design, where several aircraft follow a reference track in parallel lanes.

5.7 Conclusion

In this chapter, the problem of trajectory generation was addressed using several Bezier curves while assuring G^2 continuity at the joints. Since the curvature of the path is forced to zero at the joints between Bezier curves, the G^2 continuity could be guaranteed. Moreover, since the time interval for each Bezier curve needs to be known for the time-parametrization, velocity/time constraints were assumed, leading to an inherent computation of the arc length of each Bezier curve.

A reshaping was performed to control the deviation of the generated path with respect to the control points, allowing to adjust the distance at which the aircraft is supposed to fly through the control points. The closer the reshaped path is to the control points, the bigger the curvature becomes, such that a maximum curvature is defined and controlled by the deviation distance defined by the user. In this manner, a tradeoff between the curvature, speed and load factor of the trajectory could be established.

Furthermore, the control points were shown to be related with path constraints issues as well as flyability constraints, corroborating that a wise choice of control points, allowed the proposed algorithm to generate trajectories within load factor limits.

A formal approach for the design of 4D smooth trajectories for commercial aircraft has been developed, opening the way to 4D guidance along these time-parameterized Bezier curves.

The proposed trajectories, in spite of the fact of being designed to complement flight plans, can be used to generate a full flight profile. In addition to this, parallel trajectories to a reference one can be easily generated.

Thanks to the free choice of the control points to generate the reference trajectory, the quick computation of Bezier curves, their proposed time-parametrization, and their multiplicity, the approach is compatible with the Flow Corridor concept, slot usage, and path modification. In this manner, the adoption of these trajectories could ease air traffic management in congested areas, helping to solve air traffic conflicts and improving on-board guidance systems performance.

Chapter 6

Aircraft Mass Estimation

In the perspective of SESAR and NextGen projects, new applications of ATM/ATC are centered on TBO, such as the current development of the Full 4D Trajectory Management concept, or Continuous Descent/Climb Operations (CDO/CCO), where parameter sharing through improved datalink services is critical for online optimization of trajectory prediction. Considering that the prediction of the vertical profile is roughly divided in climb, cruise and descent, special attention is paid to the climb phase, which is a significant part of commercial flights, and offers the opportunity for trajectory optimization, where savings from 50 to 200kg of fuel per flight using a single CCO, compared to a non-optimized profile can be achieved (Eurocontrol, 2017l). Moreover, data from the 27 busiest airports in the U.S.A. indicates that 188 million gallons of fuel per year could be saved with direct climbs.

This said, it is important to underline the importance of the knowledge of aircraft mass at all time during the climb phase, since this value is critical for advanced features in the FMS (needed for TBO), trajectory prediction enhancement, and strategic/tactical computations to enhance the aircraft performance.

(Suchkov, Swierstra, and Nuic, June 2003) explains that without full knowledge of the Take-Off Weight (TOW), Air Traffic Management Decision Support Tools (ATM DSTs) have to consider average (nominal) TOWs for aircraft, leading to rough approximations with uncertainties associated to fuel, passenger, and cargo weight. It is also claimed that, based on data from Airline Operations Center (AOC) flight plans, a same aircraft type can show a variation of -27% to $+56\%$ of the mean GTOW (Gross TOW) depending on destination. Also, worldwide airlines revealed that some times, the GTOW (even recorded by AOC) can be $5,000$-$6,000$lbs off the actual GTOW, which could result in serious problems like discrepancies in path distance and time to reach a desired altitude, or wrong computation of rotation speed during take-off. Therefore, the uncertainty in aircraft mass, not only affects the vertical plane, but also the horizontal plane. Hence, the mass estimation problem is deeply related to the extension of the flexibility in separation between aircraft, and therefore, to the increase of air traffic capacity.

In this chapter, the state-of-the-art in mass estimation and the fuel consumption models for the B737-200 / A320-200 are presented in Section 6.1. Then, a mass estimation method is proposed in Section 6.2, based on the knowledge of approximative models for the Drag/Lift forces, and a reduced longitudinal aircraft model. Once the mass estimates are computed, and a fuel consumption model is assumed, Section 6.3 describes an approach based on least squares to estimate the initial mass of the aircraft, allowing to recalculate the mass estimations. The mass estimations based on the longitudinal motion will be referred to as *mass inferences*, while the ones based on least squares as *mass estimations*. Accuracy of the mass inferences and mass estimations is compared using Matlab. Finally, conclusions are given in Section 6.4.

6.1   Introduction

Given a vertical flight plan formed by waypoints (with associated speed, altitude or time constraints), a trajectory prediction function of the FMS computes the optimal vertical profile within the specified flight plan. This flight profile is constantly updated due to non-forecasted conditions, reserved airspace, or upcoming tactical maneuvers for conflicts resolution. Therefore, on-board prediction of the aircraft behaviour in the vertical motion is considered a challenging task.

Besides, even if trajectory predictions before take-off can be considered reliable due to the accuracy and computing power of on-ground systems, not all on-board variables are transmitted to ground stations for processing or use. This is the case of the aircraft mass, which remains unavailable for the public as it is considered a commercially sensitive parameter by airlines.

Moreover, even if weight and balance procedures are performed to control the aircraft's c.g. positions and maximum take-off/landing weights, according to predefined tables given in Pilot's Operating Handbooks (POH), some categories among the different weights of transport aircraft (see Figure 6.1) still represent a strong source of uncertainty. In this work, passengers and freight weight are considered

FIGURE 6.1: Different weights of an aircraft (StackExchange, 2017c).

as sources of uncertainty. Since each passenger is considered to weight an average of 170lb (sometimes different for children, men and women), and baggage weight approximations (depending on the airline) are assumed, uncertainty is present in the aircraft TOW. In addition to this, considering that the amount of fuel and its consumption are important modifiers of the aircraft mass over long periods of time,

their effects are also considered.

Perhaps, the mass accuracy problem could be considered unworthy to study, but an improvement on the mass estimation accuracy, besides improving the aircraft performance (mainly during climb/descent phases), extended to countless flights for countless hours, represents massive savings for stakeholders.

Generally, the mass estimation problem is analyzed for the climb or descent phase. Thus, a flight phase identification would have to be addressed first. In (Sun, Ellerbroek, and Hoekstra, June 2016[a]), Flightradar24 (Flightradar24, 2017) datasets are used to cluster aircraft location, velocity, identity, and timestamp into small sets of continuous flight trajectories. Then, a flight phase identification is performed using fuzzy logic. In this manner, in spite of the fact that fuzzy logic methods depend on the tuning quality of their membership functions, the flight phase identification issue is considered solved in this work.

Several authors have performed aircraft mass estimation based on the Aircraft Performance Models from the Eurocontrol's Base of Aircraft Data (BADA) (Eurocontrol, 2017f), the ICAO Engine Emission Databank (EASA, 2017), ATC Centers data, ADS-B messages, or information from the Flight Data Recorder (FDR), sometimes considering fuel flow consumptions.

In (Schultz, Thipphavong, and Erzberger, August 2012) and (Alligier, Gianazza, and Durand, May 2012), using adaptive and least squares methods, respectively, the aircraft weight is adjusted such that the modeled energy rate fits the observed energy rate. These methods use simplified point-mass equations of motion of an aircraft in climb to model the energy rate. Then, after adding a fuel flow model to the least squares approach, both methods are compared in (Alligier, Gianazza, and Durand, June 2013) and (Alligier et al., May 2014), using simulated and real data, respectively. Furthermore, mass estimations have been used to improve the trajectory predictions during the climb phase (Alligier, Gianazza, and Durand, November 2013), (Thipphavong et al., January-February 2013).

In the same way, from an operational view, computation of the TOW have been done by approximating different components of aircraft weight, i.e. fuel weight, payload weight and Operating Empty Weight (OEW).

In (Gloudemans, 2016), with an aim to perform ATM simulations, the OEW is assumed to be known while the fuel and payload weight are computed.

In (Lee and Chatterji, September 2010), closed-formed fuel consumption models for climb, cruise and descent are provided (maneuver and reserve fuel are taken into account) in order to compute the total fuel weight as the sum of the fuel weight for each flight segment. Then, considering a known Zero-Fuel Weight (ZFW), the TOW is calculated. The fuel consumption models are based on the altitude, speed, BADA parameters, and other.

Analogously, educated guesses had been established, for instance, the rule of thumb saying that the total fuel burned during flight is the same as the fuel burned on a cruising flight with the same length, but adding an extra ten percent to compensate for the fuel burned during climb. Thus, the rule of thumb allows the estimation of the aircraft mass based on the typical landing weight. This is according to (Gerretsen and Swierstra, January 2003), where the sensitivity of aircraft performance with respect to different input data is analyzed (data is produced using the performance programs from Airbus and Boeing, PEPC and the INFLT, respectively).

Furthermore, regarding 4D conflict free trajectories, aircraft need to assure their self-separation such that ATC workload is reduced. In this case, the need of an aircraft to predict accurately other aircraft trajectories without the help of ATC is mandatory.

(Vilardaga and Prats, October 2015) describes how an aircraft, using ADS-B messages, simplified dynamic models, and assumptions of other aircraft (required unknown parameters like mass are filled with nominal values), predicts the trajectories of surrounding traffic . Then, and as time goes by, since a bad mass assumption would lead to very inaccurate trajectory predictions, intruder trajectories are continuously updated and the mass of other aircraft is estimated, allowing a more accurate estimation of conflict-free trajectories while assuring autonomous self-separation. This corroborates the relevance of mass uncertainty in aircraft performance for conflict free trajectories.

In (Sun, Ellerbroek, and Hoekstra, June 2016[b]), two methods to estimate the TOW at the lift-off moment are provided. These methods use ADS-B data from Flightradar24 corresponding to the take-off phase, and the mass is a function of the acceleration and velocity of the aircraft. Moreover, parameters such as the Lift and Drag coefficients are required in advance.

In (Sun, Ellerbroek, and Hoekstra, June 2017), using a linearized energy model of the aircraft, different mass estimations are computed during different phases and specific points of the flight (take-off, lift-off, approach, climb, descent and landing-breaking). Then, with two fuel flow models (ICAO and BADA3), the initial mass of the aircraft is obtained using a Bayesian method.

Regarding the fuel flow models, it is stated that the ICAO fuel flow model (available at take-off, climb-out, approach, idle, and provided by manufactures from static engine test) differs from the operational fuel consumption. Thus, a quadratic fuel flow profile dependent on the fraction between the actual thrust and maximum static thrust is proposed, allowing the computation of the fuel flow as a function of the Mach, altitude, and time. On the other hand, the BADA3 fuel flow model is used at its three phases: minimal (idle thrust at descent), cruise, and nominal (other flight phases). In this manner, having two fuel flow models and several mass estimations, a Bayesian approach is used to infer the initial mass value using prior information.

In the same way, machine learning algorithms have been used to obtain mass predictions.

In (Alligier, Gianazza, and Durand, December 2015), data from the Paris Air Traffic Control Center is used to develop five machine learning algorithms: multiple linear regression, ridge regression, principal component regression, single-layer neural network, and stochastic gradient boosting tree.

In (Chati and Balakrishnan, June 2017), using Flight Data Recorder (FDR) information during the takeoff ground roll, a machine learning approach based on Gaussian Process Regression (GPR) is used to obtain the TOW. Then, the TOW is considered as the input to estimate the fuel flow rate during climb. This GPR model is compared with the Aircraft Noise and Performance database (Eurocontrol, 2017c) from Eurocontrol.

In general, the mass estimation problem for most approaches relies on performance data bases, ATC Centers data, or ADS-B messages to obtain the aircraft mass at specific points/phases of flights. From this point, an estimation of the initial mass (TOW) can be found by considering the mass lost during flight, obtained by machine learning techniques or by extrapolating fuel consumption models based on mathematical models or educated estimates. Nevertheless, difficulties are encountered when the aircraft mass is estimated, either for an ATM or on-board point of view, considering that FMS data has never been presented, nor analyzed in the scientific literature, only in industrial practice.

In this work, since the mass estimation methods are based on fuel consumption

models provided either by the BADA aircraft performance model, or the ICAO Engine Emission Databank, both models are described.

6.1.1 Base of Aircraft Data (BADA)

The BADA provides a set of ASCII files containing performance and operating procedure coefficients for 438 different aircraft types. The coefficients include those used to calculate thrust, drag, fuel flow, and those used to specify nominal cruise, climb, and descent speeds. All data provided by BADA is organised into six types of files:

- Synonym File
  Provides a list of all the aircraft types which are supported by BADA and indicates whether the aircraft type is supported directly (through provision of parameters in other files) or supported by equivalence (through indicating an equivalent aircraft type that is supported directly).

- Operations Performance File (OPF)
  Provided for each aircraft type which is directly supported. This file specifies parameter values for the mass, flight envelope (maximum value for different parameters like speed, altitude, maximum TOW, etc.), drag, engine thrust, and fuel consumption.

- Airline Procedure File (APF)
  Provided for each directly supported aircraft type. This file specifies the recommended speed procedures for climb, cruise and descent.

- Performance Table File (PTF)
  Provided for each directly supported aircraft type. This file contains a summary table of speeds, climb/descent rates and fuel consumption at various flight levels:
  For cruise: Flight Level (FL), True Airspeed (TAS) at nominal mass, and fuel consumption (at low, nominal and high mass).
  For climb: TAS(nominal mass), rate of climb with reduced power (at low, nominal and high mass), and fuel consumption (nominal mass).
  For descent: TAS, rate of descent, and descent fuel consumption (all at nominal mass).

- Performance Table Data File (PTD)
  Provided for each directly supported aircraft type. In addition to the PTF file, this file contains more detailed climb and descent computed performance data at various flight levels. Data for low, nominal and high mass climb performance, as well as nominal mass descent performance is given through: FL, temperature, pressure, air density, speed of sound, TAS, Calibrated Airspeed (CAS), Mach number, aircraft mass, Thrust, fuel flow, rate of climb/descent, etc.

- Global Parameter File
  Contains parameters that are valid for all aircraft or a group of aircraft (for instance all civil flights or all jet aircraft), such as maximum acceleration, nominal and maximum bank angles, etc.

The reader must keep in mind that the data gathered in BADA comes from the computation of different formulas (simplified equations of aircraft model) using measured variables during flights.

For the purposes of this Section and according to (BADA, August 2014), the BADA fuel consumption model for turboprop engines is provided for three phases: minimal (idle Thrust at descent), cruise, and nominal (other flight phases).

6.1.1.1   BADA Fuel Consumption Model

First, the thrust specific fuel consumption, $\mu\,[\mathrm{kg/min} \cdot kN]$, is defined as a function of the True Airspeed $V_{TAS}\,[knot]$ as

$$\mu = c_{f1}\left(1 - \frac{V_{TAS}}{c_{f2}}\right)\frac{V_{TAS}}{1{,}000} \tag{6.1}$$

Then, the nominal fuel flow, $f_{nom}\,[\mathrm{kg/min}]$, which can be perceived as the mass lost during nominal fuel flow, is defined as a function of the Thrust $F_{thr}\,[kN]$.

$$f_{nom} = \mu F_{thr} \tag{6.2}$$

The coefficients c_{f1} and c_{f2} provoke a mass decrease in $\mathrm{kg/min}$.
The minimum fuel flow, $f_{min}\,[\mathrm{kg/min}]$, corresponding to the mass lost during idle Thrust at descent, is a function of the geopotential pressure altitude $H_p\,[ft]$.

$$f_{min} = c_{f3}\left(1 - \frac{H_p}{c_{f4}}\right) \tag{6.3}$$

For the approach and landing phases, the fuel consumption is based on the nominal fuel flow, and limited to the minimum fuel flow

$$f_{app/ld} = max\left(f_{nom}, f_{min}\right) \tag{6.4}$$

Finally, the cruise fuel flow, $f_{cr}\,[\mathrm{kg/min}]$, is the nominal fuel flow with a gain factor

$$f_{cr} = \mu F_{thr} c_{fcr} \tag{6.5}$$

The coefficients used to compute these fuel flows are summarized in Table 6.1. The needed coefficients can be extracted from the OPF file. However, access to the BADA files needs to be granted by EUROCONTROL.

An extract of the PTF file corresponding to the proposed fuel consumption of an

TABLE 6.1: Fuel flow coefficients

Coefficient	Dimensions
c_{f1}	$\left[\frac{\mathrm{kg}}{\mathrm{min}\cdot kN \cdot knot}\right]$
c_{f2}	$[knot]$
c_{f3}	$[\mathrm{kg/min}]$
c_{f4}	$[ft]$
c_{fr}	dimensionless

A320 is shown in Figure 6.2, provided publicly by Eurocontrol.

6.1.2   Fuel Consumption Model of the ICAO Engine Emission Databank

The database provided by ICAO consists of information regarding engine operation and performance, voluntarily provided by the manufacturers. In Table 6.2, an extract of data corresponding to fuel consumption during the principal flight phases is

```
                    BADA PERFORMANCE FILE              98/03/12

AC/Type: A320__              Last BADA Revision:   3.0
                            Source OPF File:       3.0      98/03/12
                            Source APF file:       3.0      98/03/12

Speeds:   CAS(LO/HI)  Mach   Mass Levels [kg]        Temperature:   ISA
climb   - 250/300     0.78   low     -  50160
cruise  - 250/300     0.78   nominal -  62000        Max Alt. [ft]:  39000
descent - 250/300     0.78   high    -  73500
```

FL	CRUISE				CLIMB				DESCENT		
	TAS [kts]	fuel [kg/min]			TAS [kts]	ROCD [fpm]			fuel [kg/min]	TAS [kts]	ROCD [fpm]	fuel [kg/min]

FL	TAS [kts]	lo	nom	hi	TAS [kts]	lo	nom	hi	fuel nom	TAS [kts]	ROCD nom	fuel nom
0					157	2180	2140	1890	129.4	142	1100	9.4
5					158	2160	2120	1870	128.1	143	1100	9.3
10					159	2150	2100	1850	126.8	149	1100	9.3
15					166	2250	2180	1910	125.5	160	1100	9.2
20					167	2230	2160	1890	124.2	192	1150	9.2
30	261	35.9	40.4	45.7	190	2620	2450	2140	121.6	230	1330	9.1
40	265	35.8	40.4	45.7	225	3100	2800	2440	119.1	233	1340	9.0
60	272	35.8	40.4	45.7	272	3690	3010	2520	114.1	240	1370	8.8
80	280	35.7	40.3	45.7	280	3540	2880	2400	109.1	280	1640	8.6
100	289	35.7	40.3	45.7	289	3390	2750	2270	104.1	289	1680	8.4
120	356	44.6	47.8	51.6	356	3260	2670	2230	99.4	356	2310	8.1
140	366	44.4	47.6	51.5	366	3060	2490	2070	94.6	366	2340	7.9
160	377	44.2	47.5	51.3	377	2860	2310	1900	89.8	377	2370	7.7
180	388	44.0	47.3	51.2	388	2650	2130	1740	85.1	388	2400	7.5
200	400	43.8	47.1	51.0	400	2430	1940	1560	80.5	400	2740	7.3
220	412	43.5	46.9	50.8	412	2220	1740	1390	76.0	412	2760	7.1
240	425	43.2	46.6	50.6	425	1990	1550	1210	71.6	425	2770	6.9
260	438	43.0	46.4	50.4	438	1770	1350	1030	67.2	438	2780	6.7
280	452	42.7	46.1	50.2	452	1540	1150	840	62.9	452	2790	6.5
300	459	41.5	45.1	49.3	459	1880	1360	950	58.6	459	3830	6.3
320	455	39.1	43.0	47.7	455	1690	1170	750	54.5	455	3620	6.1
340	451	37.0	41.3	46.4	451	1480	970	540	50.4	451	3430	5.8
360	447	35.2	40.0	45.6	447	1250	750	320	46.3	447	3270	5.6
380	447	33.8	39.0	44.1	447	940	470	70	42.4	447	2910	5.4
400	447	32.6	38.3	40.0	447	710	240	0	38.5	447	2840	5.2

FIGURE 6.2: Performance Table file of an A320 (Eurocontrol, 2017d).

provided for a set of engines similar to the ones used for the B737-200, or its equivalent, the A320-200. These fuel flow models are obtained from static engine test, and each flight phase is defined only by a rough assumption of the percentage of thrust associated to it (see Table 6.4). Furthermore, the maximum thrust provided by some engines is shown in Table 6.3. Note that this is data extracted for a single engine, and the mentioned aircraft models posses two of them. Therefore, a fuel consumption model using only the ICAO Engine Emission Databank will result in an interpolation based on only 4 Thrust measures with no adjustments with respect to altitude.

TABLE 6.2: Fuel Consumption data.

Engine	Fuel flow (kg/s)				Fuel per LTO^a cycle (kg)	Atmospheric Conditions		
	Take-off	Climb-out	Approach	Idle		Barometer (kPa)	Temperature (K)	Humidity (kg water/kg dry air)
V2500-A1	1.113	.924	.334	.124	442	101.3	286	.0048
CFM56-5-A1	1.051	.862	.291	.1011	385	94.7-95.6	280-291	.0026-.0034
CFM56-5B4	1.166	.961	.326	.107	421	97.49-98.18	283.4-293.9	.0067-.0076
CFM56-5B4/2	1.18	.975	.335	.121	447	100.67-101.01	293-299	.0114-.0129
JT8D-7	.9892	.8113	.2861	.1291	419	-	270-311	-

^{a}LTO stands for Landing/Take-Off.

TABLE 6.3: Maximum Thrust provided by engines used in A320-200/B737-200

Engine	Maximum Thrust (kN)
V2500-A1	111.2
CFM56-5-A1	111.2
CFM56-5B4	117.88
CFM56-5B4/2	117.9
JT8D-7	62.27

TABLE 6.4: Percentage of Thrust used in different flight phases

Flight Phase	Thrust (%)
Take-off	100
Climb-out	85
Approach	30
Idle	7

6.2 Mass Estimations based on the longitudinal equations of motion

The mass estimations based on the longitudinal aircraft model will be referred to as *mass inferences*, while the ones based on least squares (described later) as *mass estimations*, even if both are mass estimation processes. Also, for the reader's convenience throughout the chapter, a non-exhaustive scheme of the mass estimation processes is provided in Figure 6.3.

According to the aircraft performance model proposed by BADA, the computa-
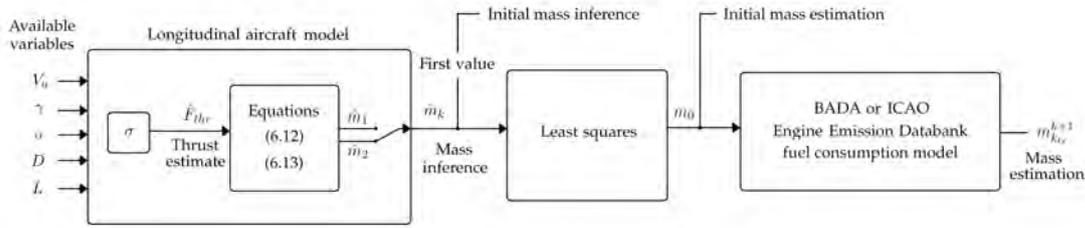
FIGURE 6.3: Mass estimation scheme.

tion of the lift coefficient is directly dependent on the aircraft mass, and the drag coefficient is directly dependent on the lift (see (6.6)).

$$C_L = \frac{2mg}{\rho V_a^2 S cos(\phi)} \tag{6.6a}$$

$$C_D = C_{D0} + C_{Di} C_L^2 \tag{6.6b}$$

Therefore, when these coefficients are used analytically to obtain mass inferences, a certain inaccuracy is self-induced when standard mass values are considered.

In spite of the fact that this inaccuracy is corrected by taking into account observations of the flown trajectory, this section describes an algorithm capable of providing mass and thrust inferences without the use of mass-dependent lift and drag coefficients. Thus, the proposed approach relies on machine learning techniques, more specifically, in the neural networks proposed in Section 4.1.3, to first estimate the lift and drag coefficients, and then infer the aircraft mass using a reduced longitudinal aircraft model. In this scenario, the training part of the neural networks becomes crucial, as it is determinant for the neural network performance.

Assuming that a well-trained neural network is available for the lift and drag coefficients, which could be feasible thanks to wind tunnel testing, experimental-aircraft measures, or any other, a mass estimation can be performed as follows.

The assumption of a zero bank angle ($\phi \approx 0$) as well as no yawing motion ($\psi \approx 0$), produce a reduced three degrees of freedom longitudinal aircraft model, expressed in the wind frame by

$$\dot{V}_a = \frac{F_{thr}c_\alpha - D}{m} - gs_\gamma \tag{6.7a}$$

$$\dot{\gamma} = \frac{F_{thr}s_\alpha + L}{mV_a} - \frac{g}{V_a}c_\gamma \tag{6.7b}$$

Assuming that V_a, γ and α are measured or computed at a sample time $t_{k+1} = t_k + \Delta t$, the system (6.7) is discretized using the Euler method, such that the following

equations are obtained:

$$V_{a_{k+1}} = V_{a_k} + \Delta t \left(\frac{F_{thr_k} c_{\alpha_k} - D_k}{m_k} - g s_{\gamma_k} \right) \tag{6.8a}$$

$$\gamma_{k+1} = \gamma_k + \Delta t \left(\frac{F_{thr_k} s_{\alpha_k} + L_k}{m_k V_{a_k}} - \frac{g}{V_{a_k}} c_{\gamma_k} \right) \tag{6.8b}$$

Besides, it is assumed that the aerodynamic forces D and L are known using approximated models. On the other hand, the thrust force and mass are assumed to be unknown and unmeasurable. Thus, an on-line inference of these variables can be proposed.

For this purpose, (6.8a) and (6.8b) are rearranged as

$$\frac{V_{a_{k+1}} - V_{a_k}}{\Delta t} + g s_{\gamma_k} = \frac{F_{thr_k} c_{\alpha_k} - D_k}{m_k} \tag{6.9a}$$

$$V_{a_k} \left(\frac{\gamma_{k+1} - \gamma_k}{\Delta t} \right) + g c_{\gamma_k} = \frac{F_{thr_k} s_{\alpha_k} + L_k}{m_k} \tag{6.9b}$$

Then, dividing (6.9a) by (6.9b), an auxiliary variable σ_k is defined as

$$\sigma_k = \frac{F_{thr_k} c_{\alpha_k} - D_k}{F_{thr_k} s_{\alpha_k} + L_k} \tag{6.10a}$$

$$= \frac{\frac{V_{a_{k+1}} - V_{a_k}}{\Delta t} + g s_{\gamma_k}}{\frac{V_{a_k}(\gamma_{k+1} - \gamma_k)}{\Delta t} + g c_{\gamma_k}} \tag{6.10b}$$

Hence, after manipulating (6.10a), an estimate of the thrust force at the instant t_k, but computed at the instant t_{k+1}, can be expressed as

$$\hat{F}_{thr_k} = \frac{D_k + \sigma_k L_k}{c_{\alpha_k} - \sigma_k s_{\alpha_k}} \tag{6.11}$$

where σ_k can be computed from (6.10b). Finally, introducing (6.11) into (6.8a) and (6.8b), two possible expressions for mass inference are obtained:

$$\hat{m}_{1_k} = \frac{\hat{F}_{thr_k} c_{\alpha_k} - D_k}{\frac{V_{a_{k+1}} - V_{a_k}}{\Delta t} + g s_{\gamma_k}} \tag{6.12}$$

$$\hat{m}_{2_k} = \frac{\hat{F}_{thr_k} s_{\alpha_k} + L_k}{\frac{V_{a_k}(\gamma_{k+1} - \gamma_k)}{\Delta t} + g c_{\gamma_k}} \tag{6.13}$$

where $\hat{m}_{1_k}$ is feasible at any flight condition with the exception of constant speed and zero flight path angle. In this case, the $\hat{m}_{2_k}$ value can be used. Therefore, the inferred mass at the instant t_k, referred to it as $\hat{m}_k$ is known at the instant t_{k+1}.

In order to corroborate the feasibility of this mass inference, data corresponding to the climb phase of a 10min simulated flight using the model described in Chapter 4 was obtained. The aircraft climbs from $1,000$m to approximately $4,000$m (FL30 to FL130) (see Figure 6.4), starting with an airspeed (TAS) of 100m/s ($194 knot$) and finishing at 122m/s ($237.5 kn$). During the whole simulation, a pitch angle of $10°$ is maintained. The variables used to infer the aircraft mass and the Thrust are shown in Figure 6.5. The quality of these data is assumed to be reliable (accurate, integral, continuous and available), thanks to the use of up-to-date navaids+GNSS and
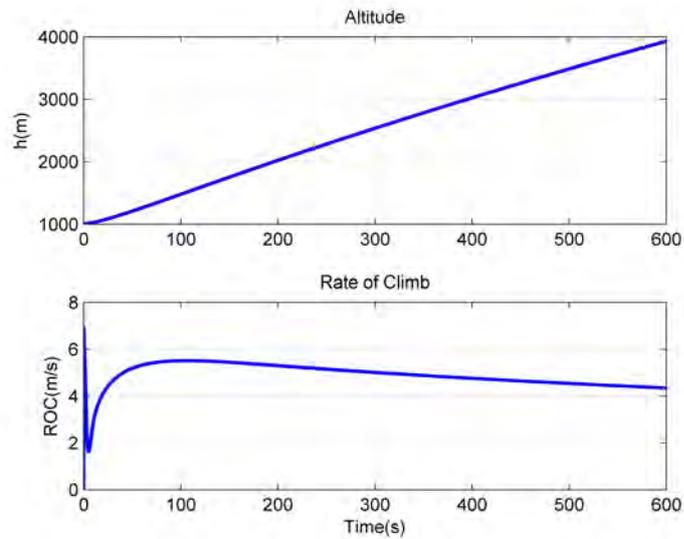
FIGURE 6.4: Altitude and Rate of Climb for mass inference.
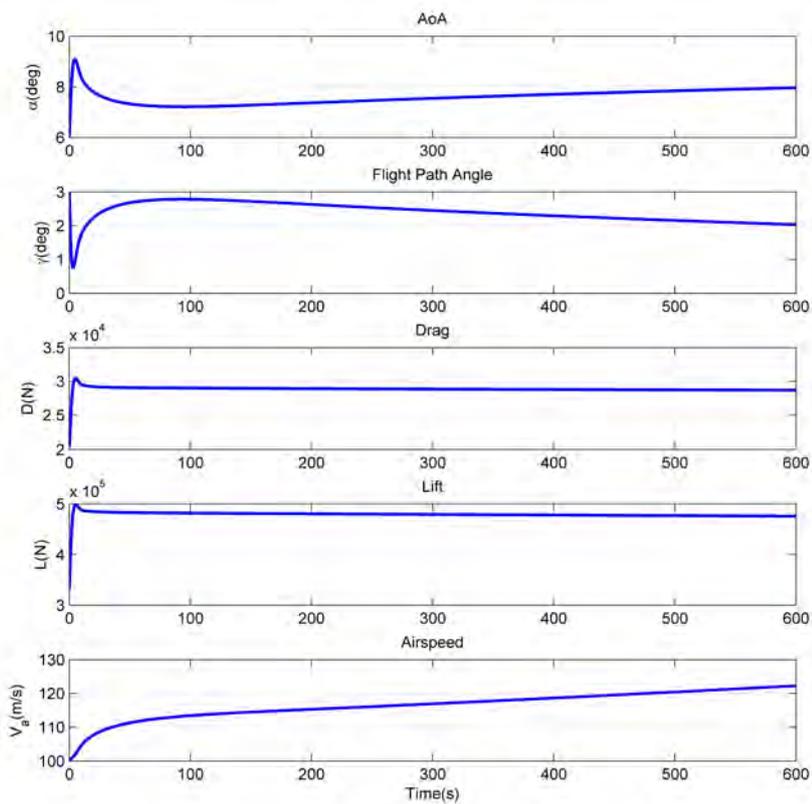
FIGURE 6.5: Variables used to infer aircraft mass and Thrust profile.

ADIRS systems.

Regarding the aircraft mass, it is assumed that a measure of this parameter is subject to uncertainty. Therefore an initial mass of $50,000$kg, decreasing under the
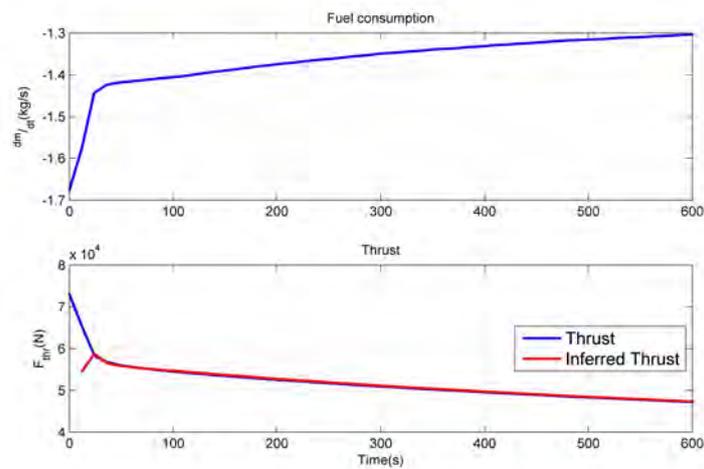
FIGURE 6.6: Fuel consumption and Thrust profile inference.

effects of a gaussian noise (with standard deviation of 100kg to avoid the simulation of an ideal measure), provoked by a fuel consumption dependent on the thrust and airspeed, is considered as the "real" mass of the aircraft during the climb. Concerning the "real" thrust profile, it is dependent on the altitude, speed, and drag. The fuel consumption associated to the real mass behaviour and the inferred thrust under a 12s sampling are shown in Figure 6.6. Although the generation of the thrust profile is out of the scope of this section, it must be noted that as the altitude increases, the fuel consumption and the thrust decrease, always maintaining a growing airspeed, which fits the general behaviour of aircraft during the climb phase.

Regarding the mass inference, since different values of Δt affect the inference, in Figure 6.7 are shown the results of mass inferences at different sampling times with respect to the real mass. For a sampling at 1s, the inferred mass converges within a bounded error of ± 400kg, and for 2, 5, and 12s, bounds of ± 300, ± 300, and ± 200kg are sufficient. This error reduction is thought to be related to the low-pass filter effect that the increase in the sampling time has on the variables affected by the gaussian noise added to avoid an ideal measure of the mass. The error of these inferences with respect to to an average value of the real mass (an accurate mass measure), is analyzed later.

Hence, it could be assumed that the mass is now available for further treatment, but in addition to this, thanks to a method based on least squares and the computed mass inference, the initial mass of the aircraft can be estimated.
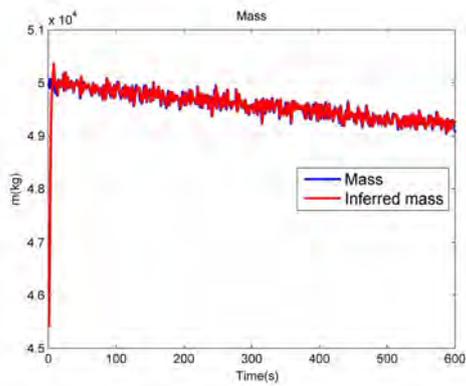
(a) Sampling time of 1s.
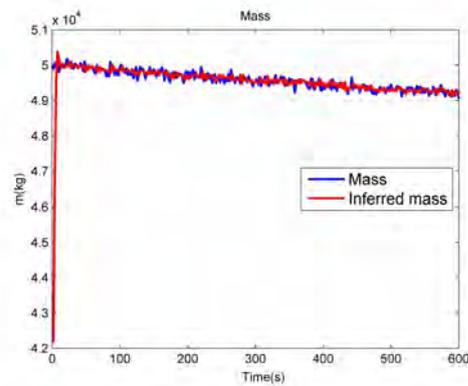
(b) Sampling time of 2s.
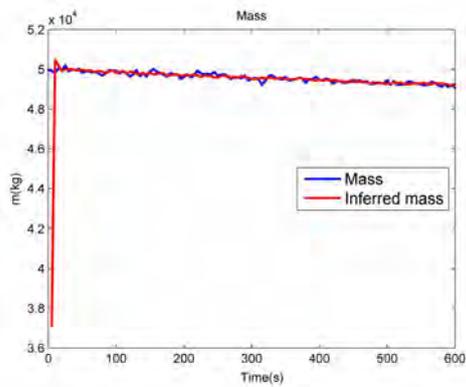
(c) Sampling time of 5s.
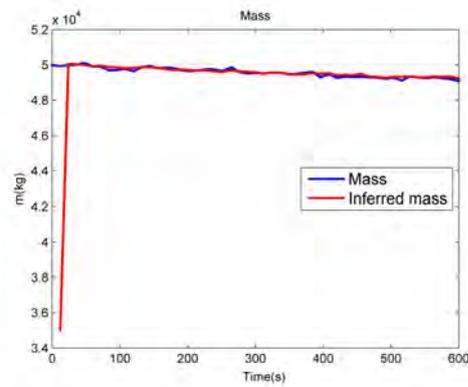
(d) Sampling time of 12s.

FIGURE 6.7: Mass inference at different sampling times.

6.3   Mass Estimation based on Least Squares

Since the aircraft mass has been inferred repeatedly by the previous approach, refer-ring to the kth value (known at the instant t_{k+1}) as $\hat{m}_k$. These inferences can be used to propose an initial mass that minimizes the error (in a least squares sense) between the real mass, and the inferred mass.

Let the aircraft mass be modeled by the BADA expression

$$\dot{m} = -\mu F_{thr} \tag{6.14}$$

where the aircraft mass decreases depending on the Thrust force and a thrust specific fuel consumption μ. This coefficient μ can be extracted from the BADA files, or the ICAO engine databank.

Assuming μ is measured or computed at a sample time $t_{k+1} = t_k + \Delta t$, the mass dynamic is discretized using the Euler method, such that the following equation is obtained:

$$m_{k+1} = m_k - \Delta t \mu_k F_{thr_k} \tag{6.15}$$

In this manner, from a general point of view, the measure of the aircraft mass can be assumed to come from the substraction of the weight of the burned fuel (given by equation (6.15)) to an unknown initial mass.

Therefore, assuming that a vector of inferred masses has been computed with the approach based on the longitudinal aircraft model in Section 6.2, the fuel consump-tion model makes possible the knowledge of the initial aircraft mass by adding all the fuel consumed until a determined time. In other words, the initial mass of an aircraft can be estimated using a fuel consumption model and the mass inferences known until the instant t_{k+1}, denoted as m_0^{k+1}.

This is possible by minimizing the least-squared error (E_{ls}) given by

$$min\,(E_{ls}) = min \left\{ \sum_{l=0}^{k} \left[\hat{m}_l - \left(m_0 - \sum_{h=0}^{l} \Delta t_h \mu_h F_{thr_h} \right) \right]^2 \right\} \approx 0 \tag{6.16}$$

where $\hat{m}_l$ is the vector containing all the mass inferences, and the term

$$m_0 - \sum_{h=0}^{l} \Delta t_h \mu_h F_{thr_h} \tag{6.17}$$

represents the real mass, given by the substraction of the weight of the burned fuel (given by equation (6.15)) to the initial mass m_0, considered unknown.

Hence, to solve this minimum problem, the first and second derivatives of (6.16) with respect to m_0 are obtained. The first derivative is given by

$$2 \sum_{l=0}^{k} \left(\hat{m}_l - m_0 + \sum_{h=0}^{l} \mu_h \Delta t_h F_{thr_h} \right) \sum_{l=0}^{k} (-1) = 0 \tag{6.18}$$

and by differentiating one more time (6.18), it is found that the second derivative is positive

$$2 \left[\sum_{l=0}^{k} (-1) \right]^2 > 0 \tag{6.19}$$

Thus, the minimum of (6.16), is found by equalizing to zero equation (6.18) and solving for m_0, leading to

$$m_0^{k+1} = \frac{1}{k} \left[\sum_{l=0}^{k} \left(\hat{m}_l + \sum_{h=0}^{l} \Delta t_h \mu_h F_{thr_h} \right) \right] \tag{6.20}$$

In order to test the approach, the flight simulation of the 10min climb from the previous section was used. Hence, assuming a known fuel consumption, provided by BADA or the ICAO Engine Emission Databank, the initial mass estimation using three different sampling times (2s, 5s, and 10s) is shown in Figure 6.8. It can be seen how as the available data to solve the least squares problem increases in size, the initial mass estimation becomes more accurate.

Moreover, the first value of the mass inferences (using the longitudinal equations)
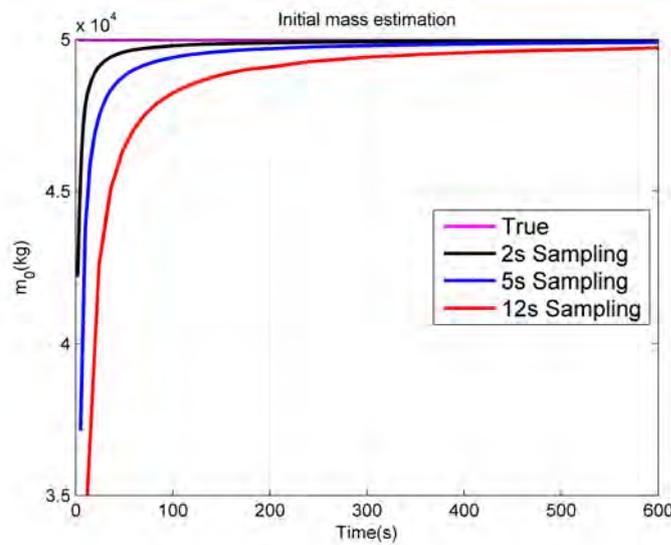
FIGURE 6.8: Initial mass estimation.

and the initial mass estimation (using the least squares), are compared with respect to the true initial mass. This errors, named initial mass inference error, and initial mass estimation error, are compared in Figure 6.9. The superior performance of the least squares approach at different sampling times is clear.

It must be noted that the presented approach differs completely from a least squares fitting application. If a fitting problem was considered, a polynomial function would be adapted to the mass inferences, such that the polynomial describing the mass evolution would dictate a fuel consumption disregarding any available prior information such as the BADA or the ICAO Engine Emission Databank model. In our case, the solution of a least squares method is used, but no polynomial is adjusted to fit the data.

At this point, since the initial mass estimation and the fuel consumption are considered known, a recalculation of the mass until the instant t_k can be computed at t_{k+1} (using the mass dyanmic model (6.15)), denoted as $m_{k_{ls}}^{k+1}$. This computation, will be increasing its accuracy as every new estimation of the initial mass comes closer to the true value, this is depicted in Figure 6.10. Note that the mass estimation is smoother than the mass inference.

(a) Original plot   (b) Zoom
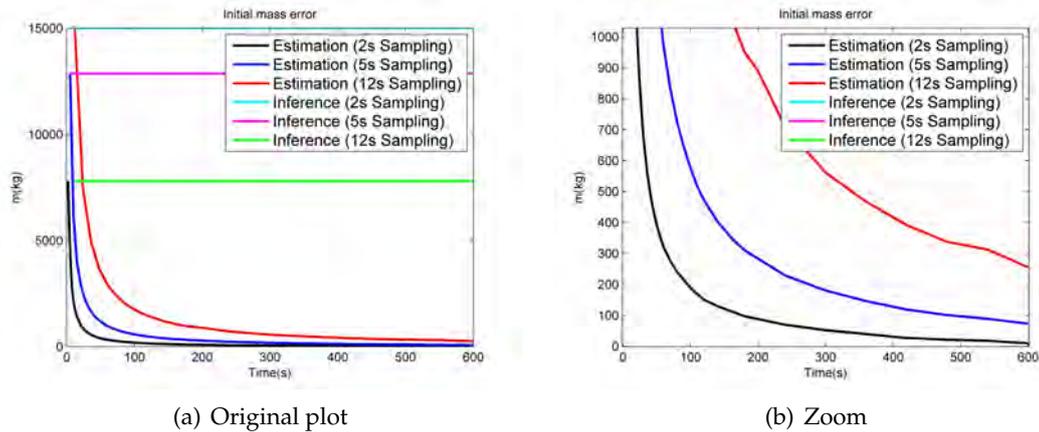
FIGURE 6.9: Initial mass estimation and initial mass inference errors
at different sampling times.

Let now the error of the mass estimation (using m_0^{k+1}) and mass inference be compared with respect to an accurate mass measure (represented by the simulated real mass without the gaussian noise). These errors are shown at different sampling times in Figure 6.11.
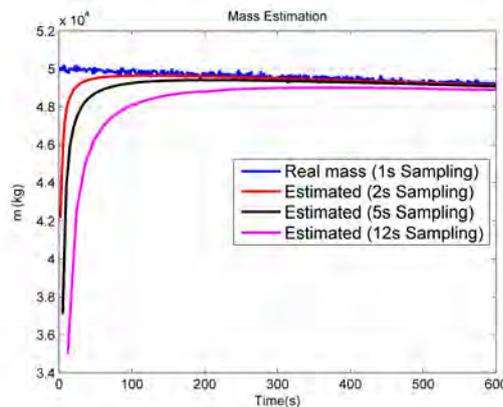
FIGURE 6.10: Mass estimation using initial mass estimations.

(a) Original plot   (b) Zoom
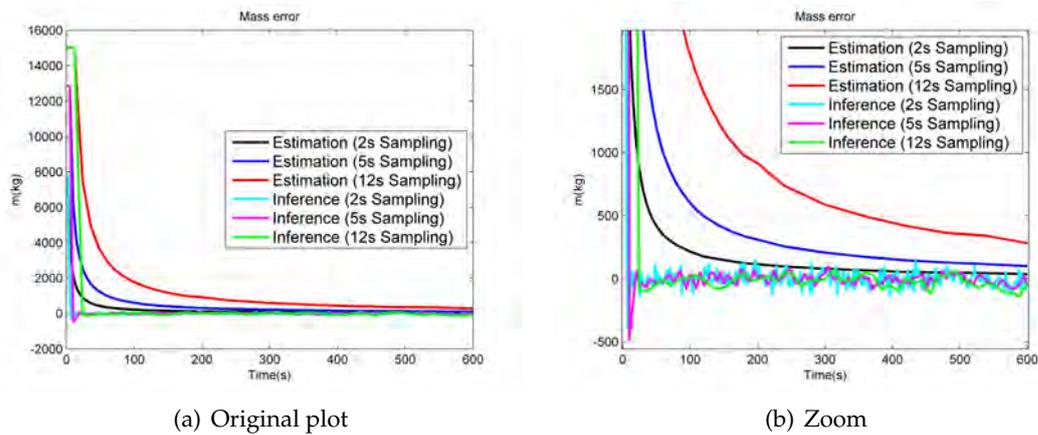
FIGURE 6.11: Mass estimation and mass inference errors at different sampling times.

6.4   Conclusions

A new method for online mass estimation, and initial mass estimation was proposed. The mass estimation using the longitudinal equations, despite beginning far away from the true value, converged faster than the mass estimation based on least squares. However, the inclusion of initial guesses into the mass estimation based on least squares approach could significantly improve its convergence time.

The least squares approach provided an accurate initial mass estimation, not only equally accurate, but also smoother, compared to the mass inferences approach (mass estimations using the longitudinal equations). Since the mass estimation process was proposed as a recursive and discrete algorithm, sampling times affected the behaviour of it.

The approach to estimate the mass relied heavily on previous knowledge of the fuel consumption model, such that the inaccuracy or complete ignorance of this parameter would have affected severely the method. Nevertheless, an adaptive estimation of the fuel consumption model to solve this issue could be addressed.

Moreover, since the fuel consumption models are well defined for the different flight phases, the method could be easily adjusted to complete flights and not limited to the climb phase.

The implementation of the proposed mass estimation methods could improve aircraft trajectory prediction, and ease the guidance efforts to follow a desired trajectory. In addition to this, it completed the simulation of the transport aircraft described in previous chapters.

Chapter 7

Introduction to Control Theory

The first feedback control system ever developed by the human being is though to be the Egyptian water clock of Ktesibios in Alexandria, around the third century b.c., since then, driven by curiosity, need, entertainment or even mistake, mankind has carried on to develop new control systems regardless of the discipline throughout history.

Nowadays, considering the ubiquity of mathematics to describe physical phenomena, control theory has gained great interest when a defined system, referred to as plant, need to fulfil some closed-loop behavior. In this manner, the design of a controller that allows a system to meet the desired characteristics has been the subject of worldwide research.

Control theory can be roughly divided in two branches, classic and modern. The first one, performs an analysis of physical systems using the Laplace transform as a key tool, and the second, allows the analysis of systems based mainly on Lyapunov theory. System analysis is done using the state-space representation, either for SISO (Single-Input/ Single-Output) or MIMO (Multi-Input/ Multi-Output) systems.

According to (Slotin and Li, 1991), physical systems are nonlinear most of the time, and they can be classified in terms of their mathematical properties as continuous or discontinuous. In the case where the operating range to be analyzed is small, and the nonlinearities within this range are smooth, the system may be approximated by a linear one. However, there are "hard" nonlinearities (described by discontinuous functions) that cannot be approximated by linear functions, such as the Coulomb friction, saturation, dead-zones, backlash, and hysteresis.

In this manner, nonlinear and linear control laws are designed depending on the system.

It is a fact that linear control laws are likely to perform poorly, or even lead to unstable behaviours when large range of systems operation are required. Thus, nonlinear control laws are of great interest. Furthermore, many control problems involving model uncertainties can be tolerated using nonlinear control theory. Nevertheless, when a linearized system is able to represent fairly enough a nonlinear one, the complexity can be reduced significantly and a linear control law is sufficient.

In this chapter, after providing the essentials about Linear Time-Invariant (LTI) systems and Linear control techniques in Section 7.1, nonlinear systems theory and nonlinear control techniques are given in Section 7.2. This background of linear / nonlinear systems is stated considering that aircraft dynamics are highly nonlinear, and that flight control systems are based on control theory, either linear or nonlinear.

Moreover, the flight guidance systems of modern aircraft are briefly described in Section 7.3. Finally, conclusions are given in Section 7.4.

7.1   Linear Systems Theory

In the late 40's, frequency response methods based on the root locus, and therefore, in the Laplace transform were developed. The root locus consists in plotting the poles of a closed loop transfer function in the complex s-plane as a function of a gain parameter (in a feedback system). Hence, since the roots of a system change when the gain varies, the stability of the system can be analyzed, establishing the basis of classical control theory, developed by Walter R. Evans.

The main contribution of the root locus analysis can be denoted by the description of 1st and 2nd order linear systems.

This Section is a compilation from extracts of different sources. For 1st and 2nd order systems (MIT, 2017) and (Ogata, 1998) are used, while (Chen, 2013) is used for the solution, stability, controllability and observability of LTI systems.

7.1.1   First and Second Order Systems

7.1.1.1   First Order Systems

Consider any phenomenon described by a first order differential equation:

$$\tau \dot{y}(t) + y(t) = f(t) \tag{7.1}$$

The system is defined by the parameter τ, referred to as the system time-constant, and $f(t)$, which is a forcing function.

It is common to separate the response of liner systems in *zero-state* response (initial conditions are zero), and *zero-input* response (input is zero).

Thus, the zero-input response, or homogeneous response of (7.1) is found by setting $f(t) = 0$, such that using the Laplace transform

$$\tau\left(sy(s) - y(0)\right) + y(s) = 0 \tag{7.2a}$$

$$y(s) = \frac{y(0)}{s + \frac{1}{\tau}} \tag{7.2b}$$

where the single root $\lambda = -1/\tau$ provokes the system response to an initial condition $y(0)$:

$$y_h(t) = y(0)e^{\lambda t} = y(0)e^{-t/\tau} \tag{7.3}$$

Note that for $\tau > 0$, the system behaviour is an exponential decay from the initial value $y(0)$ to zero, described as an *stable* system. Otherwise, for $\tau < 0$, the response grows exponentially, and the system is referred to as *unstable*.

The constant τ has time units, and denotes the general behaviour of 1st order systems. In this way, the homogeneous response of stable first order systems is depicted using a normalized time t/τ, and a normalized magnitude response $y(t)/y(0)$ in Figure 7.1, where it can be seen how after a time of $t = 0, \tau, 2\tau, 3\tau, 4\tau$, the output reaches the $0, 63.21, 86.47, 95.02, 98.17\%$ of its final value, respectively.

On the other hand, the zero-state responses, or solutions to a given $f(t)$ and the initial condition $y(0) = 0$, are referred to as *characteristic responses*.

In this way, the total response of the system $(y(t))$ is denoted by the sum of the homogeneous solution $(y_h(t))$ and a particular solution $(y_p(t))$ for an input $f(t)$, given by:

$$y(t) = y_h(t) + y_p(t) = Ce^{-t/\tau} + y_p(t) \tag{7.4}$$
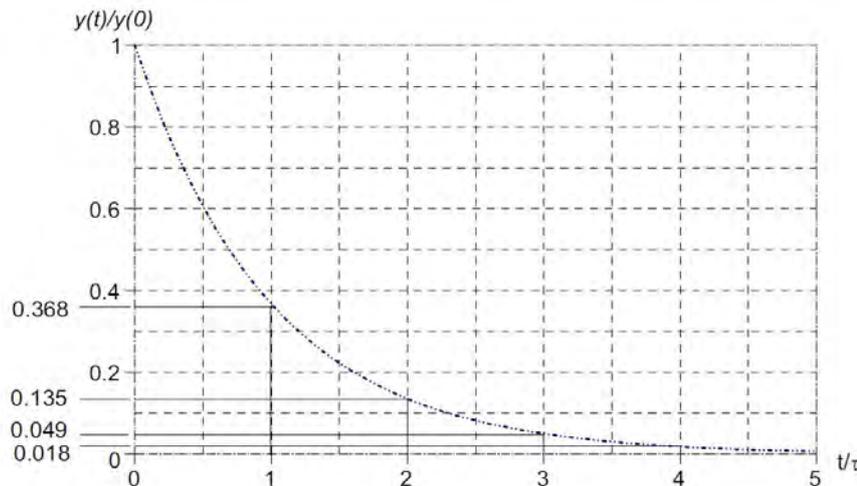
FIGURE 7.1: First order linear systems zero-input response (MIT, 2017).

where C is a constant to be found from the initial condition.

The first response analyzed is the step response $(y_s(t))$. The step $u_s(t)$ is defined for being $u_s(t < 0) = 0$ and $u_s(t \geq 0) = 1$, such that the particular solution has the form $y_p(t) = K = 1$. Then, with the requirement of $y_s(0) = 0$, the constant C is -1. Thus, the total response of a system under a step input, is given by

$$y_s(t) = 1 - e^{-t/\tau} \tag{7.5}$$

This can also be obtained from solving $\tau \dot{y}(t) + y(t) = 1$ using the laplace transform with the initial condition $y_s(0) = 0$.

The step response is usually divided in the transient region, where the system is still responding dynamically, and the steady-state region, where the system has reached its final value (y_{ss}). The initial slope of the response is $1/\tau$. Moreover, a normalized response is given in Figure 7.2.

The impulse function $\delta(t)$ is defined as a pulse of duration T and amplitude $1/T$ as
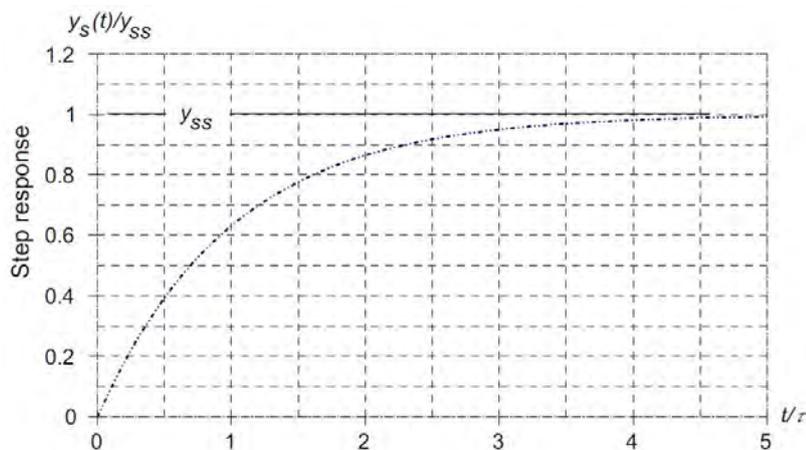
FIGURE 7.2: Step response of 1st order systems (MIT, 2017).

$T \to 0$. Then, since the impulse is considered the derivative of the step function, the total response of a 1st order system under an impulse response is given by

$$y_\delta(t) = \frac{1}{\tau}e^{-t/\tau} \qquad for \quad t \geq 0 \tag{7.6}$$

The normalized response is plotted in Figure 7.3.

Finally, considering that the unit ramp $u_r(t) = t$ for $t \geq 0$ is the integral of the unit
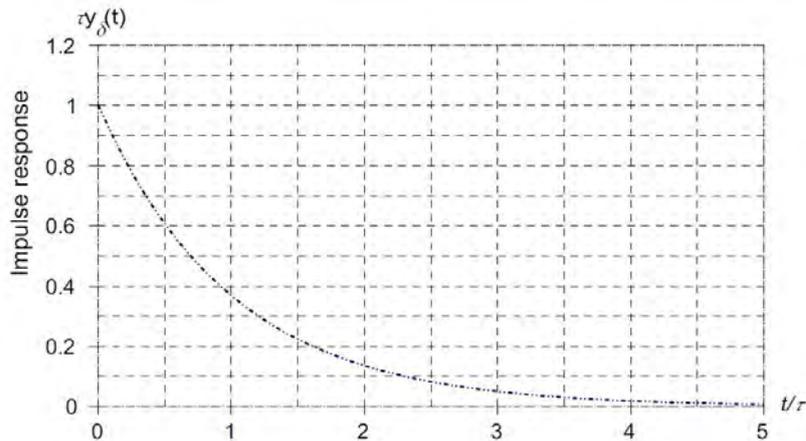
FIGURE 7.3: Impulse response of 1st order systems (MIT, 2017).

step, the total response of 1st order systems to a unit ramp input is obtained as

$$y_r(t) = t - \tau\left(1 - e^{-t/\tau}\right) \tag{7.7}$$

The response is plotted in Figure 7.4. Note that for large values of t compared to τ, the exponential converges to zero, and the response becomes $y_r(t \gg \tau) = t - \tau$.

When systems become more complex, with multiple inputs/outputs, representing
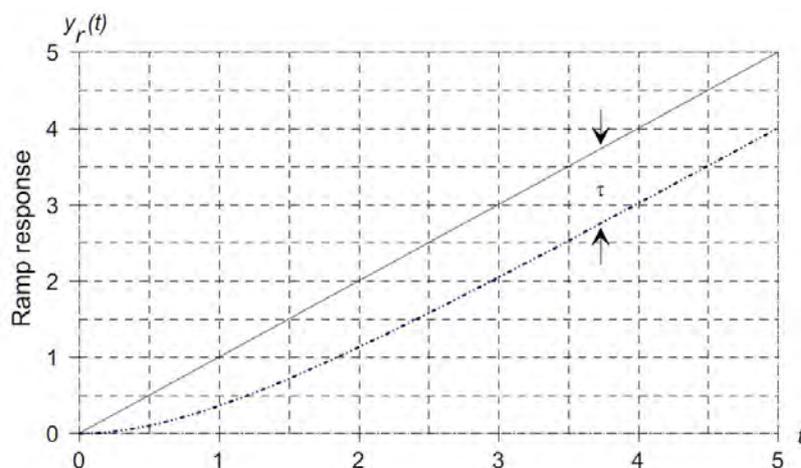
FIGURE 7.4: Unit ramp response of 1st order systems (MIT, 2017).

them with differential equations or transfer functions becomes more and more difficult. Therefore, the *state-space representation* of a system replaces a n-order differential

equation with a single first order matrix equation.

7.1.1.2 State-Space Representation and General Solution of Linear Time Invariant Systems

The state-space representation of a system is given by the state equation and the output equation:

$$\dot{X}(t) = A(t)X(t) + B(t)U(t) \tag{7.8a}$$

$$Y(t) = C(t)X(t) + D(t)U(t) \tag{7.8b}$$

where, in the case of a nth order system (represented by an nth order differential equation) with r inputs and m outputs, $A_{n \times n}$ is the state matrix, $B_{n \times p}$ is the input matrix, $U_{p \times 1}$ is the input vector, $X_{n \times 1}$ is the state vector, $C_{m \times n}$ is the output matrix, $D_{m \times p}$ the direct transition (or feedthrough) matrix, and $Y_{m \times 1}$ is the output vector. Linear control theory has been predominantly concerned with the study of Linear Time-Invariant (LTI) control systems, which is the case where the matrices, A, B, C, D are constants. The Linear Time-Varying (LTV) equations are not covered in this work.

According to (Chen, 2013), the general solution of the LTI state-space equations hinges around the exponential matrix e^{At}, more specifically, in the properties:

$$\frac{d}{dt}e^{At} = Ae^{At} = e^{At}A \tag{7.9a}$$

$$\left(e^{-At}\right)^{-1} = e^{At} \tag{7.9b}$$

$$e^0 = I \tag{7.9c}$$

such that pre-multiplying both sides of (7.8a) with e^{-At} is obtained

$$e^{-At}\dot{X}(t) - e^{-At}AX(t) = e^{-At}BU(t) \tag{7.10a}$$

$$\frac{d}{dt}\left(e^{-At}X(t)\right) = e^{-At}BU(t) \tag{7.10b}$$

and integrating from $\tau = 0$ to t, yields

$$e^{-A\tau}X(\tau)|_{\tau=0}^{t} = \int_0^t e^{-A\tau}BU(\tau)d\tau \tag{7.11a}$$

$$e^{-At}X(t) - e^0X(0) = \int_0^t e^{-A\tau}BU(\tau)d\tau \tag{7.11b}$$

In consequence, using the exponential matrix properties, the solution is obtained

$$X(t) = e^{At}X(0) + \int_0^t e^{A(t-\tau)}BU(\tau)d\tau \tag{7.12}$$

In order to verify this result, it is straightforward to check that at $t = 0$, the initial conditions are satisfied. Moreover, (7.12) can be differentiated using the Leibnitz's equation, given by

$$\frac{d}{dt}\int_{\alpha(t)}^{\beta(t)} f(t,\tau)d\tau = f(t,\beta(t))\frac{d}{dt}\beta(t) - f(t,\alpha(t))\frac{d}{dt}\alpha(t) + \int_{\alpha(t)}^{\beta(t)}\left(\frac{d}{dt}f(t,\tau)\right)d\tau \tag{7.13}$$

to return to (7.8a). Furthermore, if (7.12) is substituted in (7.8b), yields

$$Y(t) = Ce^{At}X(0) + C\int_0^t e^{A(t-\tau)}BU(\tau)d\tau + DU(t) \tag{7.14}$$

reaching the solutions of the LTI system.

Note that after a similarity transformation applied to the matrix A using its eigen vectors, the exponential matrix is easily computed since the new A would be in a Jordan form representation. Also, the computation of the exponential matrix can be done using a polynomial approximation based on the Cayley-Hamilton theorem, or using power series.

Another path to reach the general solutions for LTI systems is using the Laplace transformation to (7.8a) and (7.8b), such that

$$X(s) = (sI - A)^{-1}[X(0) + BU(s)] \tag{7.15a}$$
$$Y(s) = C(sI - A)^{-1}[X(0) + BU(s)] + DU(s) \tag{7.15b}$$

and by computing the inverse of Laplace, where $e^{At} = \mathcal{L}^{-1}\left\{(sI - A)^{-1}\right\}$, the time solution is obtained.

Note that

$$(sI - A)^{-1} = \frac{1}{det\,[sI - A]}adj\,(sI - A) \tag{7.16}$$

7.1.1.3   Second Order Systems

A 2nd order linear system can be seen as a system with a single output and two coupled first order differential equations expressed using two state variables, denoted by

$$\dot{x} = \begin{bmatrix} \dot{x}_1 \\ \dot{x}_2 \end{bmatrix} = \begin{bmatrix} a_{11} & a_{12} \\ a_{21} & a_{22} \end{bmatrix}\begin{bmatrix} x_1 \\ x_2 \end{bmatrix} + \begin{bmatrix} b_1 \\ b_2 \end{bmatrix}u \tag{7.17}$$

such that with the laplace transform

$$x(s) = (sI - A)^{-1}Bu(s) \tag{7.18}$$

it is rearranged such that

$$det\,(sI - A)\,x(s) = \begin{bmatrix} s - a_{22} & a_{12} \\ a_{21} & s - a_{11} \end{bmatrix}\begin{bmatrix} b_1 \\ b_2 \end{bmatrix}u \tag{7.19}$$

from which

$$\ddot{x}_1 - (a_{11} + a_{22})\dot{x}_1 + (a_{11}a_{22} - a_{12}a_{21})x_1 = b_1\dot{u} + (a_{12}b_2 - a_{22}b_1)u \tag{7.20a}$$
$$\ddot{x}_2 - (a_{11} + a_{22})\dot{x}_2 + (a_{11}a_{22} - a_{12}a_{21})x_2 = b_2\dot{u} + (a_{21}b_1 - a_{11}b_2)u \tag{7.20b}$$

Therefore, defining two parameters: the *undamped natural frequency* ω_n in $\mathrm{rad/s}$, and the *damping ratio* ζ (dimensionless). If it is considered that

$$\omega_n = \sqrt{a_{11}a_{22} - a_{12}a_{21}} \tag{7.21a}$$
$$\zeta = -\frac{1}{2\omega_n}(a_{11} + a_{22}) \tag{7.21b}$$

equations (7.20) turn into

$$\ddot{x}_1 + 2\zeta\omega_n\dot{x}_1 + \omega_n^2 x_1 = b_1\dot{u} + (a_{12}b_2 - a_{22}b_1)\,u \tag{7.22a}$$

$$\ddot{x}_2 + 2\zeta\omega_n\dot{x}_2 + \omega_n^2 x_2 = b_2\dot{u} + (a_{21}b_1 - a_{11}b_2)\,u \tag{7.22b}$$

Then, using the output equation, given by a scalar equation of the form

$$y(t) = c_1 x_1(t) + c_2 x_2(t) + du(t) \tag{7.23}$$

It is obtained that, following a similar procedure than the one for the states:

$$\ddot{y} + 2\zeta\omega_n\dot{y} + \omega_n^2 y = d\ddot{u} + (c_1 b_1 + c_2 b_2 - d\,(a_{11} + a_{22}))\,\dot{u} + (c_1\,(-a_{22}b_1 + a_{12}b_2)$$
$$+c_2\,(-a_{11}b_2 + a_{21}b_1) + d\,(a_{11}a_{22} - a_{12}a_{21}))\,u \tag{7.24}$$

such that the scalar form given by

$$\ddot{y} + 2\zeta\omega_n\dot{y} + \omega_n^2 y = f(t) \tag{7.25}$$

is the equation to describe 2nd order systems under a forcing input $f(t)$.
The undamped natural frequency and the damping factor play an important role in the second order systems response, similar to the time-constant τ in first order systems.
In this work, the undamped natural frequency will be referred to just as natural frequency, unless indicated the contrary.
Hence, the homogeneous solution (zero-input) of a 2nd order system equation denoted by

$$\ddot{y} + 2\zeta\omega_n\dot{y} + \omega_n^2 y = 0 \tag{7.26}$$

is given by

$$y_h(t) = C_1 e^{\lambda_1 t} + C_2 e^{\lambda_2 t} \tag{7.27}$$

where C_1, C_2 are constants defined so the system fits the initial conditions, and the eigen values λ_1, λ_2 are the roots obtained from the characteristic equation:

$$det\,[sI - A] = \lambda^2 + 2\zeta\omega_n\lambda + \omega_n^2 = 0 \tag{7.28}$$

such that

$$\lambda_{1,2} = -\zeta\omega_n \pm \omega_n\sqrt{\zeta^2 - 1} \tag{7.29}$$

In the case where $\zeta = 1$, the two roots are equal ($\lambda_1 = \lambda_2 = \lambda$) such that (7.27) is replaced by

$$y_{h_2}(t) = C_1 e^{\lambda t} + C_2 t e^{\lambda t} \tag{7.30}$$

Thus, considering the initial conditions $y(0) = y_0$ and $\dot{y}(0) = 0$, the solutions of the homogeneous system can be obtained using equations (7.27) and (7.30), along with their derivatives, such that

$$y_h(0) = y_0 = C_1 + C_2 \tag{7.31a}$$

$$\dot{y}_h(0) = 0 = \lambda_1 C_1 + \lambda C_2 \tag{7.31b}$$

$$y_{h_2}(0) = y_0 = C_1 \tag{7.31c}$$

$$\dot{y}_{h_2}(0) = 0 = \lambda C_1 + C_2 \tag{7.31d}$$

Therefore, $C_1 = \frac{\lambda_2}{\lambda_2 - \lambda_1} y_0$ and $C_2 = \frac{\lambda_1}{\lambda_1 - \lambda_2} y_0$ are the constants for $\zeta \neq 1$, and $C_1 = y_0$ and $C_2 = -\lambda y_0$ otherwise.

Thus, substituting these constants in (7.27) and (7.30), the homogeneous response for 2nd order systems is obtained

$$y_h(t) = y_0 \frac{\lambda_1 \lambda_2}{\lambda_2 - \lambda_1} \left[\frac{1}{\lambda_1} e^{\lambda_1 t} - \frac{1}{\lambda_2} e^{\lambda_2 t} \right] \qquad for \quad \zeta \neq 1 \qquad (7.32)$$

$$y_{h_2}(t) = y_0 \left[e^{\lambda t} - \lambda t e^{\lambda t} \right] \qquad for \quad \zeta = 1 \qquad (7.33)$$

This zero-input behaviour can be categorized depending on the damping factor.

7.1.1.3.1 Overdamped System ($\zeta > 1$)

Two real and negative roots

$$\lambda_{1,2} = \omega_n \left(-\zeta \pm \sqrt{\zeta^2 - 1} \right) \qquad (7.34)$$

When these roots are substituted in the homogeneous response (equation (7.32)), the solution is the sum of two decaying real exponentials (with time constants $-1/\lambda_1$ and $-1/\lambda_2$), with no overshoot or oscillation. This response is shown in a normalized time and output scale in Figure 7.5.
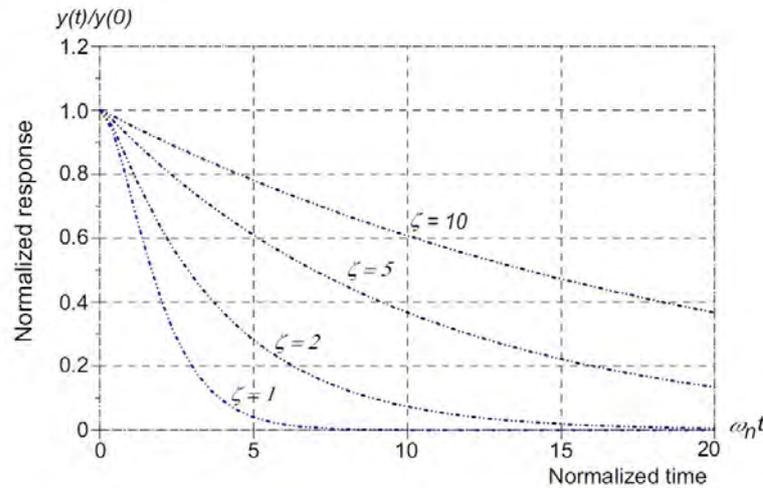
FIGURE 7.5: Overdamped and critically damped zero-input response of 2nd order systems with $y(0) = 1$ and $\dot{y}(0) = 0$ (MIT, 2017).

7.1.1.3.2 Critically damped System ($\zeta = 1$)

Real and identical roots

$$\lambda_{1,2} = \omega_n \qquad (7.35)$$

When these roots are substituted in the homogeneous response (equation (7.33)), the solution marks the transition between the non-oscillatory response of overdamped systems, an the oscillatory response of underdamped systems. This response is shown in Figures 7.5 and 7.6 in normalized axes.

7.1.1.3.3   Underdamped System ($0 \leq \zeta < 1$)

Two complex conjugate roots with negative real parts

$$\lambda_{1,2} = -\zeta\omega_n \pm j\omega_n\sqrt{1-\zeta^2} = -\zeta\omega_n \pm j\omega_d \tag{7.36}$$

where $j = \sqrt{-1}$, and $\omega_d = \omega_n\sqrt{1-\zeta^2}$ is the *damped natural frequency*.
When these roots are substituted in the homogeneous response (equation (7.32)), the euler identities (involving the *sin* and *cos* with the exponential) are used to describe the response as a damped cosine function, oscillating at a ω_d frequency and a decay rate of $e^{-\zeta\omega_n t}$. For this case, the normalized response is shown in Figure 7.6.
Note that the closer the damping is to zero, the more oscillations in the response are produced. If the damping is zero ($\zeta = 0$), the response is a pure oscillation of the form $y_h(t) = y_0 cos(\omega_n t)$. Note also that $\omega_d = 0$ when $\zeta = 1$.
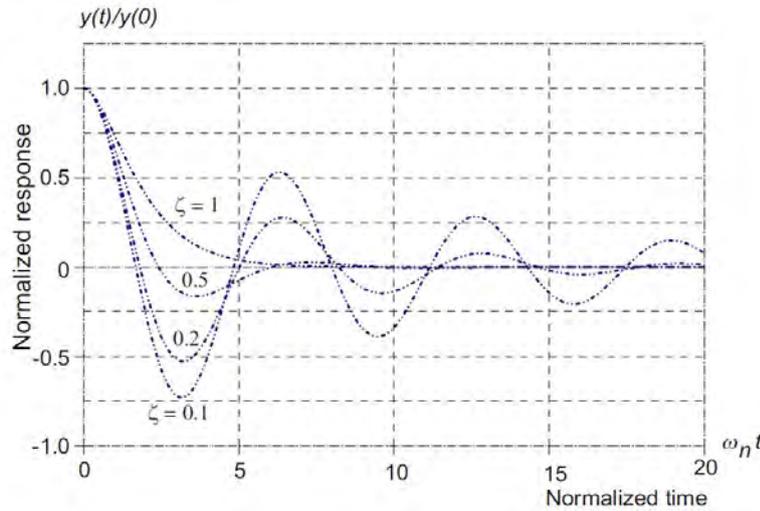
FIGURE 7.6: Underdamped and critically damped zero-input response of 2nd order systems with $y(0) = 1$ and $\dot{y}(0) = 0$ (MIT, 2017).

7.1.1.3.4   Unstable System ($\zeta < 0$)

Two roots with real positive parts. Since the roots are on the right side of the real / complex plane, the response grows exponentially in amplitude.
The root location in the real/complex plane for overdamped, underdamped, and critically damped systems is shown in Figure 7.7.
  In this way, the total response of 2nd order systems is denoted by the sum of the homogeneous solution (equations (7.27) and (7.30)) and a particular solution ($y_p(t)$) for an input $f(t)$, such that

$$y(t) = C_1 e^{\lambda_1 t} + C_2 e^{\lambda_2 t} + y_p(t) \qquad\qquad for \;\; \zeta \neq 1 \tag{7.37}$$
$$y(t) = C_1 e^{\lambda t} + C_2 t e^{\lambda t} + y_p(t) \qquad\qquad for \;\; \zeta = 1 \tag{7.38}$$

where C_1, C_2 are constants defined so the system fit the initial conditions.
The total responses to step, impulse and ramp inputs, under the initial conditions of $y(0) = 0$ and $\dot{y}(0) = 0$, are summarized in Table 7.1, and Figures 7.8 and 7.9, show

(a) $\zeta > 1$.

(b) $\zeta = 1$.

(c) $\zeta < 1$.

(d) $\zeta = 0$.
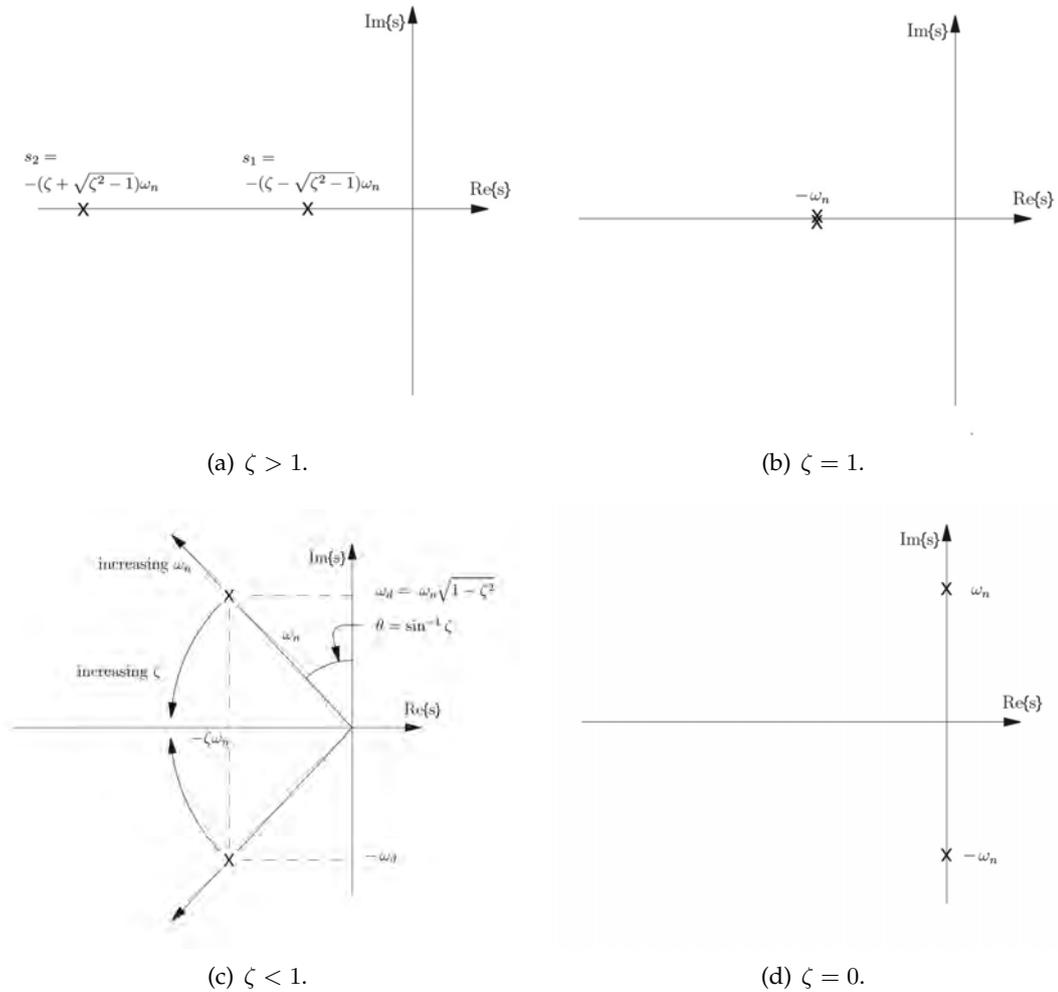
FIGURE 7.7: Poles of 2nd order systems at different damping factors
(MIT, 2017).

the normalized responses for the step and impulse functions, respectively.
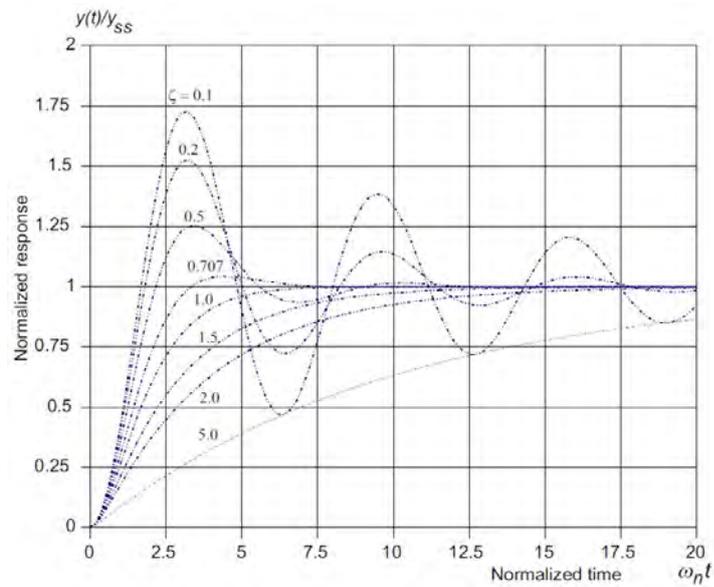
FIGURE 7.8: Step response of 2nd order systems with $y(0) = 0$ and $\dot{y}(0) = 0$ (MIT, 2017).
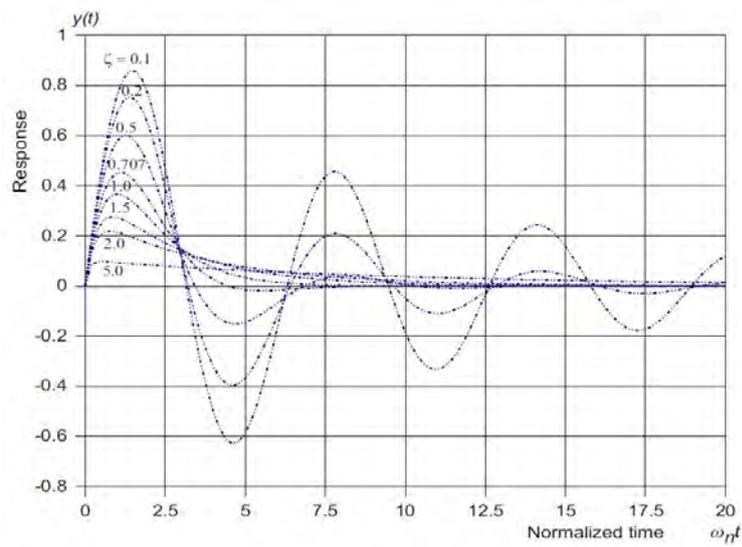
FIGURE 7.9: Impulse response of 2nd order systems with $y(0) = 0$ and $\dot{y}(0) = 0$ (MIT, 2017).

TABLE 7.1: Characteristic responses of $\ddot{y} + 2\zeta\omega_n\dot{y} + \omega_n^2 y = f(t)$ (MIT, 2017).

Damping	Input	Characteristic Response $y(t)$
$0 \leq \zeta < 1$	$u_r(t)$	$y_r(t) = \frac{1}{\omega_n^2}\left[t + \frac{e^{-\zeta\omega_n t}}{\omega_n}\left(2\zeta\cos(\omega_d t) + \frac{2\zeta^2-1}{\sqrt{1-\zeta^2}}\sin(\omega_d t)\right) - \frac{2\zeta}{\omega_n}\right]$
	$u_s(t)$	$y_s(t) = \frac{1}{\omega_n^2}\left[1 - \frac{e^{-\zeta\omega_n t}}{\sqrt{1-\zeta^2}}\cos(\omega_d t - \psi)\right]$
	$\delta(t)$	$y_\delta(t) = \frac{e^{-\zeta\omega_n t}}{\omega_n\sqrt{1-\zeta^2}}\sin(\omega_d t)$
$\zeta = 1$	$u_r(t)$	$y_r(t) = \frac{1}{\omega_n^2}\left[t + \frac{2}{\omega_n}e^{-\omega_n t} + te^{-\omega_n t} - \frac{2}{\omega_n}\right]$
	$u_s(t)$	$y_s(t) = \frac{1}{\omega_n^2}\left[1 - e^{-\omega_n t} - \omega_n te^{-\omega_n t}\right]$
	$\delta(t)$	$y_\delta(t) = te^{-\omega_n t}$
$\zeta > 1$	$u_r(t)$	$y_r(t) = \frac{1}{\omega_n^2}\left[t + \frac{\omega_n}{2\sqrt{1-\zeta^2}}\left(\tau_1^2 e^{-t/\tau_1} - \tau_2^2 e^{-t/\tau_2}\right) - \frac{2\zeta}{\omega_n}\right]$
	$u_s(t)$	$y_s(t) = \frac{1}{\omega_n^2}\left[1 - \frac{\omega_n}{2\sqrt{\zeta^2-1}}\left(\tau_1 e^{-t/\tau_1} - \tau_2 e^{-t/\tau_2}\right)\right]$
	$\delta(t)$	$y_\delta(t) = \frac{1}{2\omega_n\sqrt{\zeta^2-1}}\left(e^{-t/\tau_1} - e^{-t/\tau_2}\right)$

Notes:

The damped natural frequency $\omega_d = \omega_n\sqrt{1-\zeta^2}$

The phase angle $\psi = tan^{-1}(\zeta/\sqrt{1-\zeta^2})$

The time-constants $\tau_1 = 1/\left(\zeta\omega_n - \omega_n\sqrt{\zeta^2-1}\right)$ and $\tau_2 = 1/\left(\zeta\omega_n + \omega_n\sqrt{\zeta^2-1}\right)$

7.1.2 Stability of Linear Systems

The stability of linear systems is divided into BIBO (Bounded Input / Bounded Output) stability for zero-state responses, and Marginal and Asymptotic stability for zero-input responses. Again, the case of Linear Time-Varying systems is not covered.

7.1.2.1 Input-Output Stability of LTI systems

Consider a proper transfer function as a ratio of two polynomials $P(x)/Q(x)$ where the degree of $P(x)$ is less than the degree of $Q(x)$.
A SISO system with a proper transfer function is BIBO stable if its impulse response approaches the origin (zero) as $t \to \infty$. Also, it is BIBO stable if and only if every pole of its transfer function has a negative real part.
A MIMO system is BIBO stable if and only if every component of the impulse response matrix is absolutely integrable in the interval $[0, \infty)$. This is also the case if and only if every pole of the system has a negative real part.
Consider a MIMO system, with a state-space equation (7.15b), rewritten as

$$Y(s) = C\left(sI - A\right)^{-1} X(0) + \left[C\left(sI - A\right)^{-1} B + D\right] U(s) \tag{7.39}$$

The term involving the initial condition $X(0)$ is the zero-input (natural response) contribution to the total response, and the term involving the input $U(s)$ is the zero-state (forced response) contribution.
Hence, since BIBO stability is analyzed for the zero-state response, the transfer function of the forced response is given by:

$$G(s) = \frac{Y(s)}{U(s)} = \frac{1}{det\left[sI - A\right]} C\left[adj\left(sI - A\right)\right] B + D \tag{7.40}$$

In this manner, the system is BIBO stable if the roots of the characteristic polynomial given by $det\left[sI - A\right] = 0$ (i.e. the poles of the system), all have negative real parts. Hence, since every pole of $G(s)$ is an eigen value of A, if every eigen value of A has a negative real part, then every pole has a negative real part and BIBO stability is assured. However, due to possible term cancellation in (7.40), not every eigen value is a pole of the system. Thus, even if A has some eigen values with a zero or positive real part, the system may still be BIBO stable.

7.1.2.2 Internal Stability of LTI systems

Regarding the zero-input response of a system, there is no difference between SISO and MIMO sytems. Consider that the state-space equations are reduced, since $U(t) = 0$, such that the stability of the solution given by $X(t) = e^{At}X(0)$ is analyzed.
The response is marginally stable if and only if all eigen values of A have zero or negative real parts, and those with zero real parts are simple roots of the minimal polynomial[1] of A.
The response is asymptotically stable if and only if all eigen values of A have negative real parts (no eigen value with zero real part is permitted).

---

[1] The minimal polynomial is the smallest (in the sense of divisibility) nonzero polynomial that the matrix satisfies. That is, if A has a minimal polynomial $m(t)$, then $m(A) = 0$, and if $p(t)$ is a nonzero polynomial with $p(A) = 0$, the minimal polynomial $m(t)$ must divide $p(t)$.
The characteristic polynomial, on the other hand, is defined algebraically. If A has a size of $n \times n$, the characteristic polynomial must have a degree n. This is not true for the minimal polynomial.

In this way, asymptotical stability implies BIBO stability, and asymptotical stability is defined for the zero-input response of systems. BIBO stability, in general, does not imply asymptotical stability.

Moreover, the asymptotic stability of the matrix A can also be checked by the *Routh test* (without computing the roots), or introducing the *Lyapunov equation*:

$$A'M + MA = -N \tag{7.41}$$

where A is said to be asymptotically stable if an only if any given positive definite symmetric matrix N, has an unique symmetric solution M, and M is positive definite.

From this theorem, it can be extracted that the $n \times n$ matrix A is asymptotically stable if an only if, for any given $m \times n$ matrix $\bar{N}$ with $m < n$ and with the property

$$rank \mathfrak{O} = rank \left[\bar{N}, \bar{N}A \ldots \bar{N}A^{n-1}\right]^T = n \qquad (full \quad column \quad rank) \tag{7.42}$$

where $\mathfrak{O}$ is an $nm \times n$ matrix, the Lyapunov equation

$$A'M + MA = -\bar{N}'\bar{N} = N \tag{7.43}$$

has a unique symmetric solution M, and M is positive definite.

Furthermore, if the matrix A is asymptotically stable, the Lyapunov equation has an unique solution for every N, and the solution is given by

$$M = \int_0^\infty e^{A't} N e^{At} dt \tag{7.44}$$

7.1.3   Controllability and Observability of Linear Systems

Consider the state-space equation

$$\dot{x}(t) = Ax(t) + Bu(t) \tag{7.45a}$$
$$y(t) = Cx(t) + Du(t) \tag{7.45b}$$

where A, B, C, and D have a size of $n \times n$, $n \times p$, $m \times n$, and $m \times p$ respectively.

The first concept to be analyzed is the controllability. Since the output does not contribute to controllability, it is neglected. The system (7.45), or the pair (A, B) is said to be controllable if for any initial state $x(0) = x_0$ and any final state x_1, there exists an input that transfers x_0 to x_1 in a finite time.

This is assured if the controllability matrix

$$\mathfrak{C} = \left[B, AB, A^2B, \ldots, A^{n-1}B\right] \tag{7.46}$$

has rank n (full row rank).

Concerning the observability, the system (7.45) is said to be observable if for any unknown initial state $x(0)$, there exists a finite $t_1 > 0$ such that the knowledge of the input u and the output y over the interval $[0, t_1]$, suffices to determine uniquely the initial state $x(0)$.

This is assured if the observability matrix

$$\mathfrak{O} = \left[C, CA, \ldots, CA^{n-1}\right]^T \tag{7.47}$$

has rank n (full row rank).

In addition to this, the *Theorem of duality* claims that the pair (A, B) is controllable if and only if the pair (A', B') is observable.

Further information about these topics and the proof to the given theorems is available in (Chen, 2013).

7.1.4 Control Approaches of Linear Systems

The methods analyzed in this section are for the Linear Time Invariant case, and the first to be examined is the State-Feedback approach.

7.1.4.1 State-Feedback

This method is based on the state equation given by

$$\dot{x}(t) = Ax(t) + Bu(t)$$

where the input $u(t) = -Kx(t)$ is proposed, and the size of K is $p \times n$. Therefore:

$$\dot{x}(t) = Ax(t) - BKx(t) \tag{7.48}$$
$$\dot{x}(t) = \bar{A}x(t) \tag{7.49}$$

where $\bar{A} = (A - BK)$, such that the stability of the system is given by the roots of the polynomial given by

$$det\left[sI - \bar{A}\right] \tag{7.50}$$

If these roots are on the left side of the real-imaginary plane, the system is asymptotically stable (Hurwitz stable).

Consider the system

$$\begin{bmatrix} \dot{x}_1 \\ \dot{x}_2 \end{bmatrix} = \begin{bmatrix} 0 & 1 \\ -a & -b \end{bmatrix} \begin{bmatrix} x_1 \\ x_2 \end{bmatrix} + \begin{bmatrix} 0 \\ c \end{bmatrix} u \tag{7.51}$$

choosing the input $u = -[k_1, k_2][x_1, x_2]^T$, the stability of the system depends on the roots of

$$det\left[sI - \bar{A}\right] = \begin{bmatrix} s & -1 \\ a + ck_1 & s + b + k_2c \end{bmatrix} = 0 \tag{7.52a}$$
$$= s^2 + s(b + ck_2) + a + ck_1 = 0 \tag{7.52b}$$

Thus, in order to assure the system stability

$$b + ck_2 > 0 \qquad\qquad a + ck_1 > 0 \tag{7.53}$$

such that

$$k_1 > -\frac{a}{c} \qquad\qquad k_2 > -\frac{b}{c} \tag{7.54}$$

In this manner, the control input given by

$$u = \begin{bmatrix} \frac{a}{c} & \frac{b}{c} \end{bmatrix} \begin{bmatrix} x_1 \\ x_2 \end{bmatrix} = \frac{1}{c}(ax_1 + bx_2) \tag{7.55}$$

TABLE 7.2: Gain Computation for a PID controller (Ziegler-Nichols).

Controller	k_p	k_d	k_i
P	$.5k_u$	-	-
PI	$.45k_u$	$.54\frac{k_u}{T_u}$	-
PID	$.6k_u$	$1.2\frac{k_u}{T_u}$	$\frac{3k_uT_u}{40}$

will guarantee the exponential stability of the system.

In addition to state-feedback controllers, lead and/or lag compensators are important for classical control theory. They rely heavily in the root locus plot since they modify the system response by introducing a pole-zero pair. These pole/zero placement methods help to achieve desired system specifications in terms of settling time, steady state error, rise time, damping ratio, etc.

7.1.4.2 PID control

This is a widely used feedback control method that has the main advantage of not needing a plant model to work. Thus, for non-modeled systems, the PID controller, where PID stands for Proportional–Integral–Derivative, is of great interest. However, the PID can only be implemented for SISO systems, and is very sensitive to noise in the measured variable.

This method is based on the error generated by the desired value of a variable and its measure ($e(t)$), such that the control input is given by

$$u(t) = k_p e(t) + k_i \int_0^t e(\tau)d\tau + k_d \dot{e}(t) \tag{7.56}$$

where k_p, k_i, and k_d are the proportional, integral, and derivative gains, respectively. These gains determine the behaviour of the closed loop system, and each gain has a different impact. For example, the integral term drives the overshoot and the residual steady-state error that occurs with a pure proportional controller, and the derivative term drives the time response of the system. In this manner, the tuning of a PID can result in a hard-working task when performed manually. In consequence, the gains can be computed using existing tuning methods. The most common is the one proposed by Ziegler-Nichols.

In Table 7.2 is summarized the gain computation for different PID forms based on the Ziegler-Nichols method, where k_u is the value of k_p when the systems starts to oscillate (with $u = k_p e(t)$), and T_u is the period of the oscillations provoked by k_u.

The Laplace form of the controller (7.56) is given by

$$G(s) = \frac{u(s)}{e(s)} = k_p + \frac{k_i}{s} + k_d s = \frac{k_d s^2 + k_p s + k_i}{s} \tag{7.57a}$$

$$= k_d \frac{s^2 + \frac{k_p}{k_d}s + \frac{k_i}{k_d}}{s} \tag{7.57b}$$

7.2 Nonlinear Systems Theory

This Section is a compilation of extracts from different sources, such as (Slotin and Li, 1991), (Khalil, 2002).

It is a fact that the behaviour of nonlinear systems is much more complex than the one of linear systems. A clear example of that are the limit cycles (or sustained oscillations), where the amplitude of the excitation is independent from the initial condition, and not easily affected by parameter changes. This is completely different from the sustained oscillations of marginally stable linear systems.

Another example is that besides the multiple equilibrium points of nonlinear systems, the number of equilibrium points can change depending on the system parameters (bifurcation). Moreover, the output of nonlinear systems is extremely sensitive to the initial conditions. In this way, two close initial conditions can generate completely different trajectories (chaos) that may change the stability of the system. In general, nonlinear systems do not satisfy the basic properties of superposition, uniqueness of an equilibrium point, or scalability of output due to an input. Thus, two principal tools for nonlinear systems are briefly described: the phase plane analysis, and the Lyapunov theory.

The phase plane analysis is a graphical method that allows the visualisation of the system behaviour without solving the nonlinear equations analytically. However, it is limited to systems of 2nd order dynamics.

The basic idea of this method is to generate, in a 2D plane (phase plane portrait) with the axes defined by the two states of the system, motion trajectories corresponding to various initial conditions, and then to obtain information concerning stability and other motion patterns of the system. The phase plane can be constructed either for linear or nonlinear systems. The method of isoclines is widely used.

On the other hand, the Lyapunov theory encompasses the direct and indirect method, introduced in the late 19th century by the Russian mathematician Alexander Lyapunov.

The indirect method (or linearization method) states that the stability properties of a nonlinear system in the vicinity of an equilibrium point are the same as those in a linearized approximation around this equilibrium point. This is the reason why linear control laws can be used for nonlinear systems.

In the same tenor, the Lyapunov's direct method relies on the energy of a system, expressing that the motion of a mechanical system is stable if its total mechanical energy decreases all the time. In this manner, a scalar energy-like function (Lyapunov function) is constructed for the system, and the decrease of this function is analyzed. The beauty of this method is the range of applicability of the concept, since its suitable to all control systems. However, this method is limited by the difficulty of finding the proper Lyapunov function for a given system. Lyapunov's direct method is considered to be the main tool for nonlinear systems analysis.

Both Lyapunov's methods form the so-called Lyapunov stability theory.

7.2.1 Autonomous Systems

In this chapter, only the Lyapunov theory for nonlinear systems is covered.

Consider a nonlinear system given by

$$\dot{x} = f(x, t) \tag{7.58}$$

where f is a nonlinear vector function of size $n \times 1$, and x is the state vector of size $n \times 1$. A solution $x(t)$ corresponds to a curve in the state-space as t varies from

$0 \to \infty$. This curve is referred to as the state or system trajectory.

Note that even if (7.58) does not explicitly contain the control input as a variable, the equation remains the same for feedback control systems, since the input can be written in terms of the states and time in the closed loop dynamics.

If the system does not depend explicitly on time, it is considered as autonomous, described by

$$\dot{x} = f(x) \tag{7.59}$$

otherwise, is called non-autonomous. Thus, LTI systems are autonomous and LTV non-autonomous.

Moreover, a system in the form of

$$\dot{x} = f(x, u) = f(x) + g(x)u(t) \tag{7.60}$$

is said to be an *affine* system.

7.2.1.1   Equilibrium point

Consider the autonomous system described by

$$\dot{x} = f(x) \tag{7.61}$$

A state $x^\star$ is said to be an equilibrium point of (7.61) if once $x(t)$ is equal to $x^\star$, it remains equal to $x^\star \; \forall t \geq t_0$.

Matematically, this is found by solving $0 = f(x^\star)$. For example, the system denoted by $\dot{x} = sin(x(t))$ has the equilibrium points of $x^\star(t) = n\pi$ for $n = 0, 1, 2, 3 \ldots \infty$.

7.2.1.2   Stability in the sense of Lyapunov

Let a spherical region B_R defined by $\|x\| < R$ in state-space, and S_R the sphere surface, defined by $\|x\| = R$.

The equilibrium point $x = 0$ is stable in the sense of Lyapunov if, for any $R > 0$, there exists $r > 0$ such that if $\|x(0)\| < r$, then $\|x(t)\| < R$ for all $t \geq 0$. Otherwise, the equilibrium point is unstable.

In other words, the origin is stable in the sense of Lyapunov if a value $r(R)$ is found, such that at time 0, the starting state within the spherical region B_r, stays for the rest of the trajectory $x(t)$ within the spherical region B_R. This can be expressed by

$$\forall R > 0, \exists r > 0, \|x(0)\| < r \Rightarrow \forall t \geq 0, \|x(t)\| < R \tag{7.62}$$

or

$$\forall R > 0, \exists r > 0, x(0) \in B_r \Rightarrow \forall t \geq 0, x(t) \in B_R \tag{7.63}$$

7.2.1.3   Asymptotic and Exponential Stability

7.2.1.3.1   Asymptotic Stability

An equilibrium point $x = 0$ (the trivial solution) is said to be asymptotically stable if besides being stable in the sense of Lyapunov, there exists some $r > 0$ such that $\|x(0)\| < r$ implies that $x(t) \to 0$ as $t \to \infty$.

In other words, if the system is Lyapunov stable and the limit

$$\lim_{t \to \infty} x(t, x_0) = 0 \qquad \forall \|x(0)\| < r \tag{7.64}$$

is true, the system is asymptotically stable.

Hence, considering that a state starting within the ball B_r (close to 0) converges to the origin as time goes to infinity, the ball B_r is called a *domain of attraction* of the equilibrium point.

An equilibrium point which is Lyapunov stable but not asymptotically stable is called *marginally stable*.

7.2.1.3.2 Exponential Stability

The trivial solution of the system ($x = 0$) is exponentially stable if there exist two strictly positive numbers α and λ such that

$$\forall t > 0, \qquad \|x(t)\| \leq \alpha \|x(0)\| e^{-\lambda t} \tag{7.65}$$

in some ball B_r around the origin.

In other words, the state vector converges to the origin faster than an exponential function.

7.2.1.4 Local and Global Stability

The definitions of asymptotic and exponential stability concern the *local* stability of systems, since the state is considered to evolve near the trivial equilibrium point. However, if the concepts of asymptotic or exponential stability hold for any initial state, then the equilibrium point is said to be *Globally* Asymptotically (or Exponentially) Stable.

Linear asymptotic stability is always global and exponential, which explains the refined notions of stability at this point and not before.

7.2.1.5 Lyapunov's Linearization Method

This method serves to analyse the local stability of a nonlinear system around an equilibrium point.

It relies on the assumption that a nonlinear system behaves similarly to its linear approximation in a range close to an equilibrium point. Therefore, based on the stability of the linearized system around an equilibrium point, some inferences about the stability of the nonlinear system can be extrapolated.

Consider the autonomous system

$$\dot{x} = f(x) \tag{7.66}$$

Assuming that $f(x)$ is continuously differentiable, the systems dynamics can be rewritten using the Taylor series as

$$f(x) = f(x_0) + \frac{\partial f}{\partial x}|_{x=x_0} (x - x_0) + \frac{1}{2!} \frac{\partial^2 f}{\partial x^2}|_{x=x_0} (x - x_0)^2 + f_{h.o.t.}(x) \tag{7.67}$$

where $f_{h.o.t.}$ stands for higher-order terms in x.

Hence, since $f(0) = 0$, and 0 is an equilibrium point, the Jacobian matrix

$$A = \frac{\partial f}{\partial x}|_{x=0} = \begin{bmatrix} \frac{\partial f_1}{\partial x_1} & \frac{\partial f_1}{\partial x_2} & \cdots & \frac{\partial f_1}{\partial x_n} \\ \frac{\partial f_2}{\partial x_1} & \frac{\partial f_2}{\partial x_2} & \cdots & \frac{\partial f_2}{\partial x_n} \\ \vdots & \vdots & \ddots & \vdots \\ \frac{\partial f_n}{\partial x_1} & \frac{\partial f_n}{\partial x_2} & \cdots & \frac{\partial f_n}{\partial x_n} \end{bmatrix} \tag{7.68}$$

allows to write

$$\dot{x} = Ax \tag{7.69}$$

which is called the linear approximation of the original nonlinear system at the equilibrium point $x = 0$ (or $x = x^\star$).

In case of a system

$$\dot{x} = f(x, u) \tag{7.70}$$

the Jacobian $B = \frac{\partial f}{\partial u}|_{x=0, u=0}$ allows to form a system in the form $\dot{x} = Ax + Bu$.
Thus:

- If the linearized system is strictly stable (i.e., all eigen values of A are strictly in the left-half complex plane), the equilibrium point of the nonlinear system is asymptotically stable.

- If the linearized system is unstable (i.e., at least one eigen value of A is strictly in the right-half complex plane), the equilibrium point of the nonlinear system is unstable.

- If the linearized system is marginally stable (i.e., all eigen values of A are in the left-half complex plane, but at least one of them is on the $j\omega$ axis), then no conclusion about the nonlinear system can be extracted.

7.2.1.6 Lyapunov's Direct Method

This method is based on the total energy of a mechanical system, assuring that if the energy is continuously dissipated, then the system, linear or nonlinear, must eventually converge to an equilibrium point. In this manner, the stability of the system is determined by the analysis of a single scalar function, called the Lyapunov function (V).

Consider that zero energy corresponds to an equilibrium point. Therefore, asymptotic stability refers to the convergence of the energy to zero, and instability is referred to the growth of mechanical energy.

Hence, the energy-like function has two properties:

- It is strictly positive unless the state variables are zero.

- It is associated with the system dynamics.

Consequently, some definitions are given before enouncing the Lyapunov's direct method.

7.2.1.6.1 Positive Definite Functions and Lyapunov Functions

Consider a ball of radius R_0. A scalar continuous function $V(x)$ is said to be globally positive definite if $V(0) = 0$ and $V(x) > 0$ for any $x \neq 0$. But is said to be locally

positive definite if this is true only in a ball B_{R_0}.

Moreover, is said to be semi-positive definite if $V(0) = 0$ and $V(x) \geq 0$ for any $x \neq 0$. The negative and semi-negative properties can be easily inferred.

Consider the system given by

$$\dot{x} = f(x) \tag{7.71}$$

If in a ball B_{R_0}, the function $V(x)$ is positive definite and has continuous partial derivatives, if its time derivative along any state trajectory of the system (7.71) is negative semi-definite ($\dot{V}(x) \leq 0$), then $V(x)$ is a Lyapunov function.

7.2.1.6.2   Lyapunov theorem for Local Stability

If, in a ball B_{R_0}, there exists a scalar function $V(x)$ with continuous first partial derivatives such that:

- $V(x)$ is positive definite (locally in B_{R_0})

- $\dot{V}(x)$ is negative semi-definite (locally in B_{R_0})

then the equilibrium point 0 is stable.

But, if the derivative $\dot{V}(x)$ is locally negative definite in B_{R_0}, then the stability is asymptotic.

7.2.1.6.3   Lyapunov theorem for Global Stability

Assume that there exists a scalar function $V(x)$ with continuous first order derivatives such that

- $V(x)$ is positive definite

- $\dot{V}(x)$ is negative definite

- $V(x)$ is radially unbounded, meaning that $V(x) \to \infty$ as $\|x\| \to \infty$

then the equilibrium at the origin is Globally Asymptotically Stable.

7.2.1.7   Invariant Set Theorems

It is very common to have a derivative of a Lyapunov function candidate $\dot{V}$, which is only negative semi-definite. Thus, the *invariant set theorems* allow to expand the Lyapunov stability concept to extract conclusions regarding the asymptotic stability to dynamic behaviours, instead of just the equilibrium. For example, the convergence to a limit cycle. This is attributed to Joseph P. La Salle.

Let us define first an *invariant set*.

A set G is an invariant set for a dynamic system if every trajectory of the system which starts from a point in G remains in G for all future time. For example, any equilibrium point is an invariant set, and the domain of attraction of an equilibrium point is also an invariant set.

7.2.1.7.1   Local Invariant Set Theorem

Consider an autonomous system given by

$$\dot{x} = f(x) \tag{7.72}$$

with f continuous. Also, let $V(x)$ be a scalar function with continuous first partial derivatives.
Assume that

- for some $l > 0$, the region Ω_l defined by $V(x) < l$ is bounded

- $\dot{V}(x) \leq 0$ for all x in Ω_l

Let $\mathfrak{R}$ be the set of all points within Ω_l where $\dot{V}(x) = 0$, and $\mathfrak{M}$ be the largest invariant set in $\mathfrak{R}$. Then, every solution $x(t)$ originated in Ω_l tends to $\mathfrak{M}$ as $t \to \infty$.
Note that $\mathfrak{M}$ is the union of all invariant sets within $\mathfrak{R}$ (e.g., equilibrium points). Thus, if the set $\mathfrak{R}$ is invariant (i.e., if once $\dot{V} = 0$, then $\dot{V} = 0$ for all future time), then $\mathfrak{M} = \mathfrak{R}$. Moreover, note that V is not required to be positive definite, even if its often still referred to as a Lyapunov function.
A geometrical meaning of this theorem is shown in a two state example in Figure 7.10, where a trajectory starting in the bounded region Ω_l converges to the largest invariant set $\mathfrak{M}$.
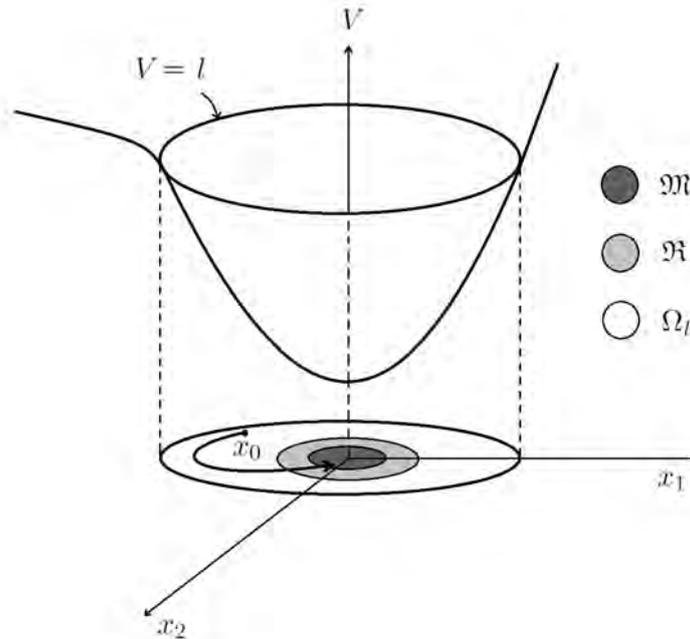

FIGURE 7.10: Convergence to the invariant set $\mathfrak{M}$.

7.2.1.7.2   Global Invariant Set Theorem

Consider an autonomous system given by

$$\dot{x} = f(x) \tag{7.73}$$

with f continuous. Also, let $V(x)$ be a scalar function with continuous first partial derivatives.
Assume that

- $V(x) \to \infty$ as $\|x\| \to \infty$

- $\dot{V}(x) \leq 0$ over the whole state space

Let $\mathfrak{R}$ be the set of all points where $\dot{V}(x) = 0$, and $\mathfrak{M}$ be the largest invariant set in $\mathfrak{R}$. Then, all solutions globally asymptotically converge to $\mathfrak{M}$ as $t \to \infty$.

As stated before, the problem of finding the proper Lyapunov function for a given nonlinear system can result in a difficult task. Thus, some constructive methods have been proposed, like the Krasovskii's method, or the Variable Gradient method. Moreover, considering that the Lyapunov's direct method is a method to analyse the stability of a system, it can be used to propose nonlinear controllers. The idea is to propose a scalar positive function of the system states such that using a proposed control law, make the Lyapunov function decrease, assuring stability of the closed loop. In this case, the Lyapunov function can be constructed empirically or with methods like the Sontag's universal formula.

7.2.2 Non-autonomous Systems

In this work, only the Lyapunov's direct method is tackled for non-autonomous systems. This is due to the non applicability of La Salle's theorems for non-autonomous systems. On the other hand, the Barbalat's Lemma is used.

Before diving into the Barbalat's Lemma, positive definite functions, decreasing functions and some points about asymptotic properties of functions and their derivatives are provided.

7.2.2.1 Preliminaries

A scalar time-varying function $V(x,t)$ is locally positive definite if $V(0,t) = 0$ and there exists a time-invariant positive definite function $V_0(x)$ such that

$$\forall t \geq t_0, \qquad V(x,t) \geq V_0(x) \tag{7.74}$$

Thus, a time-variant function is locally positive definite if it *dominates* a time-invariant locally positive definite function. Global positive definite functions are defined similarly.

A function $V(x,t)$ is negative definite if $-V(x,t)$ is positive definite.

A function $V(x,t)$ is positive semi-definite if it dominates a time-invariant positive semi-definite function.

A function $V(x,t)$ is negative semi-definite if $-V(x,t)$ is positive semi-definite.

A scalar function $V(x,t)$ is decrescent if $V(0,t) = 0$, and if there exists a time-invariant positive definite function $V_l(x)$ such that

$$\forall t \geq 0, \qquad V(x,t) \leq V_l(x) \tag{7.75}$$

In other words, a scalar function $V(x,t)$ is decrescent if it is dominated by a time-invariant positive definite function.

Moreover, consider that for the non-autonomous system

$$\dot{x} = f(x,t) \tag{7.76}$$

and for a time-varying scalar function $V(x,t)$, the derivative $\dot{V}(x,t)$ along the system trajectory is given by

$$\frac{dV}{dt} = \frac{\partial V}{\partial t} + \frac{\partial V}{\partial x}\dot{x} = \frac{\partial V}{\partial t} + \frac{\partial V}{\partial x}f(x,t) \tag{7.77}$$

Regarding the asymptotic properties of functions, consider a differentiable function f of time t. Then:

- $\dot{f}(t) \to 0$ does not imply that $f(t)$ converges to 0 as $t \to \infty$.

- $f(t) \to 0$ as $t \to \infty$ does not imply that $\dot{f}(t) \to 0$.

- If $f(t)$ is lower bounded and decreasing ($\dot{f}(t) \leq 0$), then it converges to a limit.

This result does not say wether the slope of the curve will diminish or not. Consequently, the Barbalat's lemma is used to guarantee the convergence to zero of the derivative of this function.

7.2.2.2 Barbalat's Lemma

If the differentiable function $f(t)$ has a finite limit as $t \to \infty$, and if $\dot{f}$ is uniformly continuous, then $\dot{f}(t) \to 0$ as $t \to \infty$.
A sufficient condition to check that $\dot{f}$ is uniformly continuous is to check that its derivative is bounded. This is expressed as

$$\exists \alpha > 0 \qquad \forall t \geq 0 \qquad such \ \ that \qquad \|\ddot{f}(t)\| \leq \alpha \tag{7.78}$$

where α is a real number.
Thus, using the Barbalat's Lemma for the stability analysis of non-autonomous systems, a Lyapunov's like lemma is stated:
If a scalar function $V(x, t)$ satisfies the following conditions

- $V(x, t)$ is lower bounded

- $\dot{V}(x, t)$ is negative semi-definite

- $\dot{V}(x, t)$ is uniformly continuous in time

then $\dot{V}(x, t) \to 0$ as $t \to \infty$.
For more information (including the proofs of the stated theorems), please refer to (Slotin and Li, 1991).

7.2.3 Control Approaches for Nonlinear systems

Several control approaches for nonlinear systems have been developed, such as nested/separated saturations, backstepping, sliding modes, adaptive control, feedback linearization, just to mention a few. In this work, backstepping and feedback linearization techniques are used.
Since the Backstepping is based on the Lyapunov theory, and it has already been presented, the approach is explained on the fly. However since the Feedback linearization is based on the Lie algebra and linear control techniques, it is explained as follows.

7.2.3.1 Feedback linearization

The feedback linearization method consists in transforming algebraically a nonlinear system into a system with linear dynamics (Slotin and Li, 1991), (Khalil, 2002). This idea is demonstrated initially with a class of nonlinear systems described by the so-called companion form, or controllability canonical form, described by the dynamics

$$x^{(n)} = f(x) + g(x)u(t) \tag{7.79}$$

where x is the scalar output of interest, u the scalar control input, and $f(x)$, $g(x)$ are nonlinear functions. Thus, after putting the system in a multiple-integrator form, a control input of the form

$$u = \frac{1}{g(x)}\left(v - f(x)\right) \tag{7.80}$$

can cancel the nonlinearities and obtain a simple input-output relation in the multiple-integrator form

$$x^{(n)} = v \tag{7.81}$$

Then, a linear control law proposed using $v = -k_0 x - k_1 \dot{x} - \ldots - k_{n-1} x^{(n-1)}$ assures the system stability.

Before considering a more complex system to develop the feedback linearization, some mathematical tools are provided, extracted from (Slotin and Li, 1991).

7.2.3.1.1 Lie Algebra

Given a smooth scalar function $h(x)$ of the state vector x, mapping from $\mathrm{R}^n \to \mathrm{R}$, the gradient of h is denoted by ∇h

$$\nabla h = \frac{\partial h}{\partial x} \tag{7.82}$$

represented by a row-vector of elements $(\nabla h)_j = \partial h / \partial x_j$.

Similarly, given a vector field $f(x)$ in R^n (considered as a vector function mapping from $\mathrm{R}^n \to \mathrm{R}^n$) with continuous partial derivatives, the Jacobian of f is denoted by $\nabla f = \partial f / \partial x$ (like in the Lyapunov's Linearization Method), represented by a $n \times n$ matrix of elements $(\nabla f)_{ij} = \partial f_i / \partial x_j$.

Thus, given a smooth scalar function $h(x)$ and a smooth vector field $f(x)$, a scalar function $L_f h = \nabla h f$ is defined, called the *Lie derivative* of h with respect to f.

Hence, the Lie derivative is the directional derivative of h along the direction of the vector f.

Recursive Lie derivatives are defined as

$$L_f^0 h = h \tag{7.83a}$$

$$L_f^i h = L_f\left(L_f^{i-1} h\right) = \nabla\left(L_f^{i-1} h\right) f \tag{7.83b}$$

Similarly, if g is another vector field, the scalar function $L_g L_f h(x)$ is denoted by

$$L_g L_f h = \nabla\left(L_f h\right) g \tag{7.84}$$

In the same tenor, let f and g be two vector fields. The *Lie bracket* of f and g is a vector field defined by

$$[f, g] = \nabla g f - \nabla f g = ad_f g \tag{7.85}$$

where ad stands for adjoint. Recursive Lie brackets are defined as

$$ad_f^0 g = g \tag{7.86a}$$

$$ad_f^i g = \left[f, ad_f^{i-1} g\right] \tag{7.86b}$$

The properties of the Lie brackets are the:

- Bilinearity

$$[\alpha_1 f_1 + \alpha_2 f_2, g] = \alpha_1 [f_1, g] + \alpha_2 [f_2, g]$$
$$[f, \alpha_1 g_1 + \alpha_2 g_2] = \alpha_1 [f, g_1] + \alpha_2 [f, g_2]$$

  where f, f_1, f_2, g, g_1 and g_2 are smooth vector fields, and α_1 and α_2 are constant scalars.

- Skew-commutativity

$$[f, g] = -[g, f]$$

- Jacobi identity

$$L_{ad_f g} h = L_f L_g h - L_g L_f h$$

where $h(x)$ is a smooth scalar function of x.

7.2.3.1.2   Input-Output Linearization

Consider the SISO system

$$\dot{x} = f(x) + g(x)u \tag{7.87a}$$
$$y = h(x) \tag{7.87b}$$

where $f(x)$ is the nonlinear state equation matrix, $g(x)$ is the controller matrix, $h(x)$ the output matrix, u the input and y the output.

The idea is to obtain and explicit dependence of the input in the output equation. In other words, the output y is differentiated r^{th} times until the input u appears.

Hence, using the Lie derivatives

$$y = h(x) = L_f^0 h(x) \tag{7.88a}$$
$$\dot{y} = \frac{\partial h(x)}{\partial x} \dot{x} = L_f h(x) + L_g h(x) u \tag{7.88b}$$

where, if the term $L_g h(x) u = 0$, means that the first derivative of y is not explicitly related to the input, therefore

$$\dot{y} = L_f h(x) \tag{7.89}$$

and another differentiation needs to be done, yielding

$$\ddot{y} = L_f^2 h(x) + L_g L_f h(x) u \tag{7.90}$$

If $L_g L_f h(x) u = 0$, the differentiation process must continue until for some integer r

$$L_g L_f^{r-1} h(x) \neq 0 \tag{7.91}$$

where r will be called the *relative degree* of the system. Then, a control law of the form

$$u = \frac{1}{L_g L_f^{r-1} h(x)} \left(-L_f^r h(x) + v \right) \tag{7.92}$$

is proposed, which applied to

$$y^{(r)} = L_f^r h(x) + L_g L_f^{r-1} h(x) u \tag{7.93}$$

leads to

$$y^{(r)} = v \qquad (7.94)$$

In this manner, the desired dynamics of the systems are proposed in v, usually with linear control techniques to ensure system stability.

Note that $r \leq n$, where n is the system order. If $r = n$, the input-output linearization yields a full linearization of the system, but in the case where $r < n$, there will be internal dynamics. These internal dynamics need to be bounded to ensure the stability of the system.

Once the SISO case is stated, consider the MIMO case, given by the equations:

$$\dot{x} = f(x) + g(x)u \qquad (7.95a)$$
$$y = h(x) \qquad (7.95b)$$

where x is an $n \times 1$ state vector, u is the $m \times 1$ input vector (of components u_i), y is the $m \times 1$ output vector (of components y_i), $f(x)$ and $h(x)$ are smooth vector fields, and $g(x)$ is an $n \times m$ matrix whose columns are smooth vector fields g_i.

In this case each output y_i is differentiated until the inputs appear. Assume that r_j is the smallest integer such that at least one of the inputs appear in $y_i^{(r_i)}$, then

$$y_i^{(r_i)} = L_f^{r_i} h_i + \sum_{j=1}^{m} L_{g_j} L_f^{r_i-1} h_i u_j \qquad (7.96)$$

with $L_{g_j} L_f^{r_i-1} h_i(x) \neq 0$ for at least one j. This procedure for all the outputs will lead to

$$\begin{bmatrix} y_1^{(r_1)} \\ \vdots \\ y_m^{(r_m)} \end{bmatrix} = \begin{bmatrix} L_f^{r_1} h_1(x) \\ \vdots \\ L_f^{r_m} h_m(x) \end{bmatrix} + \begin{bmatrix} L_{g_1} L_f^{r_1-1} h_1(x) & \cdots & L_{g_m} L_f^{r_1-1} h_1(x) \\ \vdots & \ddots & \vdots \\ L_{g_1} L_f^{r_m-1} h_m(x) & \cdots & L_{g_m} L_f^{r_m-1} h_m(x) \end{bmatrix} \begin{bmatrix} u_1 \\ \vdots \\ u_m \end{bmatrix} \qquad (7.97)$$

which can be expressed as:

$$y^r = \mathrm{L}(x) + \mathrm{J}(x)u \qquad (7.98)$$

where J has to be non-singular to generate the control law given by:

$$u = \mathrm{J}^{-1}(x)\left(v - \mathrm{L}(x)\right) \qquad (7.99)$$

with $v = [v_1, \ldots, v_m]^T$, such that, when the control law is applied to the system, yields:

$$y_i^{(r_i)} = v_i \qquad (7.100)$$

Thus, the desired dynamics of the system are expressed in v.

In MIMO systems, the total relative degree is given by $r = r_1 + \ldots + r_m$. If the total relative degree is equal to n, there is no internal dynamics.

7.3   Modern Flight Guidance Systems

After the generation of a flight plan, taking into account tactical choices entered by the crew through the Multipurpose Control Display Unit (MCDU), the aircraft is endowed with different local objectives depending on the flight phase. If these objectives are to be achieved automatically, a series of guidance modes are induced by the FMS, each one of them with different guidance variables. In other words, if the flight plan is to be followed automatically, the flight guidance system will sequence the corresponding guidance modes using the FMS, this is called the *managed* mode on Airbus aircraft.

On the other hand, the pilot can take over the aircraft control, and can either impose new objectives using the Flight Control Unit (FCU) (*selected* mode), or modify the aircraft control surfaces using the lateral stick (*manual* mode).

All the flight guidance functions on board modern aircraft are embedded in the Flight Management System.

In addition to this, considering that the flight plan objectives are divided into lateral and vertical, the autoguidance modes are also split into lateral and vertical modes. The lateral modes use the roll angle to control the horizontal motion, and the vertical modes use the pitch angle. The speed/thrust is controlled using the auto-thrust.

Moreover, since the aircraft is an underactuated system, and the position is controlled by the orientation, the Flight Control Systems are also split into the Automatic Piloting (Autopilot) and Automatic Guidance (Autoguidance modes). In Figure 7.11, a classical structure of Flight Control Systems is shown.

Furthermore, the lateral guidance modes are roughly summarised as:
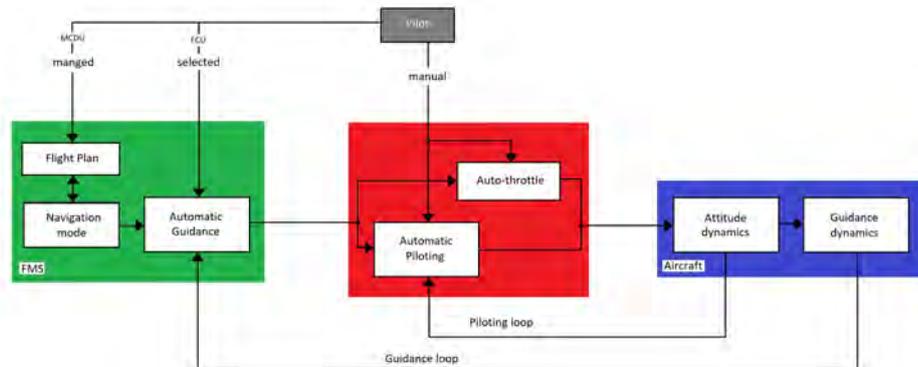
FIGURE 7.11:   Classical structure of Flight Control Systems (Mora-Camino, 2017).

- Runway (RWY) [managed], to follow the runway centreline on take-off.

- Navigation (NAV) [managed], to capture and track the lateral guidance in the en-route phase, as well as SID and STAR routes.

- Approach (APPR) [managed], to capture and track lateral guidance for ILS and VOR during the approach.

- Go Around (GA) [managed], to track a heading reference during Go Around.

- Heading Track (HDG-TRK) [managed/selected], to capture and maintain a selected heading reference.

- Roll Out [managed], to guide the aircraft along the runway during automatic landing.

and the vertical guidance modes as:

- Speed Reference (SRS) [managed], to maintain a speed target using the pitch angle, and guide the aircraft during take-off, initial climb and after Go-Around.

- Climb (CLB) to Descent (DES), to change altitude while maintaining speed, auto-throttle holds a constant thrust. This is known as the pitch mode, and different modes are available:

    1. Open climb/descent (OP CLB/DES) [selected], to reach an altitude with an open rate of climb/descent.
    2. CLB/DES [managed], to level off the aircraft when reaching an altitude constraint.
    3. Expedite climb/descent (EXP CLB/DES) [selected], which is similar to OP CLB/DES but with different speed targets.

- Altitude (ALT), to maintain the pressure altitude. Different modes are available:

    1. ALT and ALT*[selected], to maintain altitude when an altitude target is reached after a climb or descent. The * is for the capture mode.
    2. ALT CRZ [managed], which behaves similar to ALT but the selected altitude has to be at or above the cruise altitude defined in the MCDU.
    3. ALT CST and ALT CST* [managed], which considers a constant altitude.

- Approach (APPR) [managed], to follow the vertical flight plan. It can capture and maintain the Glide Slope of the ILS (G/S and G/S*).

- Vertical Speed (V/S) / Flight Path Angle (FPA) [selected], to maintain a defined vertical speed (positive or negative).

- Flare [managed], to align the aircraft with the runway centerline and adopt a pitch angle to flare.

In this manner, since each autoguidance mode uses only certain guidance variables, a non-exhaustive list of the controlled variables in lateral and vertical guidance for different aircrafts is given:

- Longitudinal modes

    1. Normal load factor (n_z) control (A320/330/340/380).
    2. Pitch angle control (A300/310, B737/747/767).
    3. Acquisition and hold of vertical speed and altitude.
    4. Vertical profile tracking coupled with FMS (climb, cruise, descent).
    5. Acquisition and hold of speed coupled with auto-throttle.
    6. Acquisition and hold of path angle.

- Lateral modes

    1. Roll rate acquisition (A320/330/340/380).

2. Hold of bank angle (A300/310, B737/747/767).

3. Acquisition and hold of heading.

4. Acquisition and hold of radio axis VOR or magnetic route.

5. Acquisition and hold of inertial route coupled with FMS.

Thus, each guidance mode will use different variables to control the aircraft motion. Currently, the flight guidance control laws are based on linear control techniques (P, PI, and PID controllers with scheduled gains depending on the flight conditions). However, when more control loops are added and multivariable dynamics (MIMO systems) are considered, the controller design becomes way more complex for this one-loop-at-a-time design.

On the other hand, modern avionics systems have adopted a linearized aircraft model in the state-space representation, while relying on linear control techniques (state-feedback and output-feedback controllers) (Stevens and Lewis, 1992).

In this work, Nonlinear Control Techniques applied to a Nonlinear aircraft model are addressed.

7.4 Conclusion

Since modern flight guidance systems rely mainly on linear control techniques based on the state space representation, the theory of linear systems and some linear control techniques was provided.

Furthermore, it seems that flight guidance systems are based on "selected" predefined strategies, each one of them based in a decoupled and linear aircraft model. Thus, aiming to the implementation of a 4D guidance strategy, the consideration of a nonlinear aircraft model is mandatory, and therefore, the use of nonlinear control techniques.

In consequence, the theory corresponding to nonlinear systems has been covered, as well as the basis for nonlinear control theory. This is used to develop a complete flight guidance system with an autopilot for transport aircraft in the next chapter, which addresses the formal proposition of a 4D guidance method compliant with the new requirements for Trajectory-Based Operations.

Chapter 8

4D Guidance Control for Transport Aircraft

Since air traffic is predicted to increase dramatically in the upcoming years, new problems and requirements are arising, and those related with the use of 4D trajectories are of most interest for this work.

NextGen (FAA, 2016) and SESAR (Eurocontrol, 2016) control projects, where traffic capacity and safety issues are central, adopt the Trajectory Based Operations (TBO) paradigm, which supposes 4D guidance effectiveness. Therefore, it is not surprising that an important enabler is automation, allowing aircraft to follow with more accuracy flight plans characterized by a 4D reference trajectory.

It is expected that accurate 4D guidance will improve safety by decreasing the occurrence of near mid-air collisions for planned conflict free 4D trajectories, and then diminish the workload associated to a single flight for air traffic controllers. Also, it will result in a fuel usage decrease and reduced CO_2 emissions per flight. Thus, the proposal of a new approach to perform 4D guidance is mandatory for the improvement of future guidance systems.

Until today, no general control framework has been developed for 4D guidance of a transport aircraft and current systems are extensions of 3D guidance with overfly time constraints at some given points. In that case, control laws are based on frequency decoupling and different PID control layers with gain scheduling provisions.

This chapter, considers that the aircraft dynamics are composed of fast dynamics, related with the angular attitude of the aircraft, and slow dynamics, related with the trajectory followed by the aircraft, referenced at its center of gravity.

For modern transportation aircraft with Fly by Wire (FBW) technology, the autopilot is in charge of controlling the aircraft attitude, improving flying qualities through stabilization, and generating automatic protections in dangerous piloting situations. In Section 8.1, two different approaches are studied for the autopilot, which will be considered to be an specific device providing in an integrated way these essential functions. The approaches analyzed are based on backstepping and Non Linear Inversion (NLI), both taking into account wind disturbances.

Once the attitude is controlled, the attention is focused on the autoguidance system, in charge of controlling the slow flight dynamics with the aim of providing 4D guidance. In this manner, Section 8.2 describes two approaches based on NLI (direct and indirect). Finally, conclusions are given in Section 8.3.

Numerical simulation of all control approaches is provided using Matlab.

8.1 Attitude Control

8.1.1 Backstepping

After splitting the aircraft equations in fast and slow dynamics, related with the angular attitude of the aircraft, and the trajectory followed by the aircraft (referenced at its center of gravity), respectively, an attitude control approach based on backstepping is addressed first.

Backstepping architecture is an attractive approach for cascade systems, since it can produce smooth feedback controls which are convenient for aircraft or spacecraft attitude dynamics (Imran, Gianmarco, and Jongrae, February 2010). Furthermore, stabilizing nonlinearities of the system can be retained (Rajput, Weiguo, and Jingping, June 2015). Since backstepping approaches may result in trivial cancellation of terms or excessive control effort at the initial time, enhancements on the method have been done recently. In (Kim and Kim, November 2003), it is shown that when a nonlinear tracking function is proposed instead of a linear tracking function, settling times and peak control efforts are reduced. The backstepping technique has also been applied to design missile autopilots with model uncertainties (Mattei and Monaco, 2014), and can be combined with other control techniques like sliding-modes in order to improve its performance (Wang, Wang, and Xiong, August 2014).

Starting by considering ϕ and α as the link variables with the fast dynamics, in order to integrate properly the attitude controller into a general control framework, these variables are controlled taking into account wind perturbations.

Consider the equations presented in Chapter 3, where an expression for the angular velocities ($\Omega = [p, q, r]^T$) is given by:

$$\dot{\Omega} = \frac{1}{2}\rho V_a^2 S I^{-1} \left(\begin{bmatrix} bC_l \\ \bar{c}C_m \\ bC_n \end{bmatrix} + C_\delta \begin{bmatrix} \delta_{ail} \\ \delta_{ele} \\ \delta_{rud} \end{bmatrix} \right) - I^{-1}\Omega \times (I\Omega) \tag{8.1}$$

where the inputs are the deflection of ailerons, elevator and rudder, denoted by $\delta = [\delta_{ail}, \delta_{ele}, \delta_{rud}]^T$, and ρ is the air density, α the angle of attack (AoA), β sideslip angle, V_a airspeed, S wing area, b wingspan, $\bar{c}$ mean chord, I the inertia matrix, and the rolling, pitching and yawing aerodynamic coefficients (C_l, C_m, C_n, respectively) are denoted by:

$$\begin{bmatrix} C_l \\ C_m \\ C_n \end{bmatrix} = \begin{bmatrix} C_{l_\beta}\beta + C_{l_p}\frac{bp}{2V_a} + C_{l_r}\frac{br}{2V_a} \\ C_{m_0} + C_{m_\alpha}\alpha + C_{m_q}\frac{\bar{c}q}{2V_a} \\ C_{n_\beta}\beta + C_{n_p}\frac{bp}{2V_a} + C_{n_r}\frac{br}{2V_a} \end{bmatrix} \tag{8.2}$$

and

$$C_\delta = \begin{bmatrix} bC_{l_{\delta ail}} & 0 & bC_{l_{\delta rud}} \\ 0 & \bar{c}C_{m_{\delta ele}} & 0 \\ bC_{n_{\delta ail}} & 0 & bC_{n_{\delta rud}} \end{bmatrix} \tag{8.3}$$

Also, the mathematical model under wind conditions for the AoA and sideslip angle, conformed by

$$\begin{bmatrix} \dot{\alpha} \\ \dot{\beta} \end{bmatrix} = \begin{bmatrix} H_{11} & H_{12} & H_{13} \\ H_{21} & H_{22} & H_{23} \end{bmatrix} \begin{bmatrix} p \\ q \\ r \end{bmatrix} + \begin{bmatrix} Q_1 \\ Q_2 \end{bmatrix} \tag{8.4}$$

where

$$H_{11} = -\left(tan_\beta c_\alpha + \frac{V_{w_y} c_\alpha}{V_a c_\beta}\right)$$

$$H_{12} = 1 + \frac{V_{w_x} c_\alpha + V_{w_z} s_\alpha}{V_a c_\beta}$$

$$H_{13} = -\left(tan_\beta s_\alpha + \frac{V_{w_y} s_\alpha}{V_a c_\beta}\right)$$

$$H_{21} = s_\alpha + \frac{V_{w_z} c_\beta + V_{w_y} s_\alpha s_\beta}{V_a}$$

$$H_{22} = \frac{V_{w_z} c_\alpha s_\beta - V_{w_x} s_\alpha s_\beta}{V_a}$$

$$H_{23} = -\left(c_\alpha + \frac{V_{w_y} c_\alpha s_\beta + V_{w_x} c_\beta}{V_a}\right)$$

$$Q_1 = \frac{1}{V_a c_\beta}\left(g_1 - \frac{1}{m}\left(L + F_{thr} s_\alpha\right)\right) + \frac{1}{V_a c_\beta}\left(\dot{V}_{w_x} s_\alpha - \dot{V}_{w_z} c_\alpha\right)$$

$$Q_2 = \frac{1}{V_a}\left(g_2 + \frac{1}{m}\left(Y - F_{thr} c_\alpha s_\beta\right)\right) + \frac{1}{V_a}\left(\dot{V}_{w_x} c_\alpha s_\beta - \dot{V}_{w_y} c_\beta + \dot{V}_{w_z} s_\alpha s_\beta\right)$$

with

$$g_1 = g\left(c_\alpha c_\theta c_\phi + s_\alpha s_\theta\right)$$

$$g_2 = g\left(c_\beta c_\theta s_\phi + s_\beta c_\alpha s_\theta - s_\alpha s_\beta c_\theta c_\phi\right)$$

is complemented by the Euler equation for roll, given by

$$\dot{\phi} = p + tg_\theta s_\phi q + tg_\theta c_\phi r \tag{8.5}$$

Note that wind perturbations are included in the model as $V_w = [V_{w_x}, V_{w_y}, V_{w_z}]^T$. Then, a complete expression for the attitude dynamics of the aircraft is proposed as

$$\dot{x}_1 = f_1(x_1) + f_2(x_1)x_2 \tag{8.6a}$$
$$\dot{x}_2 = f_3(x_1, x_2) + f_4(\cdot)u \tag{8.6b}$$

where $x_1 = [\phi, \alpha, \beta]^T$, $x_2 = \Omega$, $u = \delta$ and

$$f_1(x_1) = [0, Q_1, Q_2]^T \tag{8.7}$$

$$f_2(x_1) = \begin{bmatrix} 1 & tg_\theta s_\phi & tg_\theta c_\phi \\ H_{11} & H_{12} & H_{13} \\ H_{21} & H_{22} & H_{23} \end{bmatrix} \tag{8.8}$$

$$f_3(x_1, x_2) = \frac{1}{2}\rho V_a^2 S I^{-1} \begin{bmatrix} bC_l \\ \bar{c}C_m \\ bC_n \end{bmatrix} - I^{-1}\Omega \times (I\Omega) \tag{8.9}$$

$$f_4(\cdot) = \frac{1}{2}\rho V_a^2 S I^{-1} C_\delta \tag{8.10}$$

with the Euler angles bounded as $\phi\{-\pi, \pi\}$; $\theta\{-\frac{\pi}{2}, \frac{\pi}{2}\}$; $\psi\{-\pi, \pi\}$.

Hence, the problem is the control of the roll angle, AoA and sideslip angle via the control surfaces. In order to tackle this issue, note that the form of the system denoted by (8.6a), (8.6b), is the typical nonlinear affine system, where a backstepping control can be applied.

Following a similar method as (Mattei and Monaco, 2014), let the error $e_1 = x_1^d - x_1$ be defined under the assumption of the existence of a function $\varphi(x_1)$ such that the error dynamics $\dot{e}_1 = \dot{x}_1^d - f_1(x_1) - f_2(x_1)\varphi(x_1)$ is Globally Asymptotically Stable in the sense of Lyapunov under the candidate function $V_1(e_1)$. Hence:

$$
\begin{aligned}
\dot{V}_1(e_1) &= \frac{\partial V_1(e_1)}{\partial e_1}\dot{e}_1 \\
&= \frac{\partial V_1(e_1)}{\partial e_1}\left(\dot{x}_1^d - f_1(x_1) - f_2(x_1)\varphi(x_1)\right) \leq -W(\|e_1\|) \quad (8.11)
\end{aligned}
$$

where $W(\|e_1\|)$ is positive definite. Then, proposing the error $e_2 = x_2 - \varphi(x_1)$ with the desired values of the angular velocities as $\varphi(x_1)$, a new system in terms of errors using (8.6a), (8.6b) is obtained:

$$
\dot{e}_1 = \dot{x}_1^d - f_1(x_1) - f_2(x_1)(e_2 + \varphi(x_1)) \quad (8.12)
$$

$$
\dot{e}_2 = f_3(x_1, x_2) + f_4(\cdot)u - \frac{\partial \varphi(x_1)}{\partial x_1}[f_1(x_1) + f_2(x_1)(e_2 + \varphi(x_1))] \quad (8.13)
$$

Thus, from (8.12), (8.13), an augmented Lyapunov function with its derivative in order to analyse convergence of e_1 and e_2 is defined as:

$$
V_2(e_1, e_2) = V_1(e_1) + \frac{1}{2}e_2^T e_2 \quad (8.14)
$$

$$
\begin{aligned}
\dot{V}_2(e_1, e_2) = {}& \frac{\partial V_1(e_1)}{\partial e_1}\left[\dot{x}_1^d - f_1(x_1) - f_2(x_1)(e_2 + \varphi(x_1))\right] + e_2^T\Big\{f_3(x_1, x_2) + f_4(\cdot)u \\
& - \frac{\partial \varphi(x_1)}{\partial x_1}[f_1(x_1) + f_2(x_1)(e_2 + \varphi(x_1))]\Big\} \\
\leq {}& -W(\|e_1\|) - \frac{\partial V_1(e_1)}{\partial e_1}f_2(x_1)e_2 + e_2^T\Big\{f_3(x_1, x_2) + f_4(\cdot)u \\
& - \frac{\partial \varphi(x_1)}{\partial x_1}[f_1(x_1) + f_2(x_1)(e_2 + \varphi(x_1))]\Big\} \quad (8.15)
\end{aligned}
$$

Accordingly, an expression for u is chosen

$$
\begin{aligned}
u = {}& f_4^{-1}(\cdot)\Big\{\frac{\partial \varphi(x_1)}{\partial x_1}[f_1(x_1) + f_2(x_1)(e_2 + \varphi(x_1))] + \left(\frac{\partial V_1(e_1)}{\partial e_1}f_2(x_1)\right)^T \\
& - k_{e_2}e_2 - f_3(x_1, x_2)\Big\} \quad (8.16)
\end{aligned}
$$

where k_{e_2} is a positive definite matrix gain. Then substituting (8.16) into (8.15), it is obtained

$$
\dot{V}_2(e_1, e_2) \leq -W(\|e_1\|) - e_2^T k_{e_2} e_2 \quad (8.17)
$$

Moreover, in order to perform simple term cancellation, the expression for $\varphi(x_1)$ can be selected as:

$$
\varphi(x_1) = f_2(x_1)^{-1}\left(\dot{x}_1^d - f_1(x_1) + k_{e_1}e_1\right) \quad (8.18)
$$

where k_{e_1} is also a positive definite matrix gain. As a result, with the Lyapunov function $V_1(e_1) = \frac{1}{2}e_1^T e_1$, (8.11) turns into:

$$\dot{V}_1(e_1) = -e_1^T k_{e_1} e_1 \tag{8.19}$$

Consequently, the system (8.12), (8.13) assume the form

$$\begin{bmatrix} \dot{e}_1 \\ \dot{e}_2 \end{bmatrix} = \begin{bmatrix} -k_{e_1} & -f_2(x_1) \\ f_2^T(x_1) & -k_{e_2} \end{bmatrix} \begin{bmatrix} e_1 \\ e_2 \end{bmatrix} \tag{8.20}$$

This system is Globally Asymptotically Stable using the Lyapunov function:

$$V(e_1, e_2) = \frac{1}{2}e_1^T e_1 + \frac{1}{2}e_2^T e_2 \tag{8.21}$$

such that

$$\dot{V}(e_1, e_2) \leq -e_1^T k_{e_1} e_1 - e_2^T k_{e_2} e_2 \tag{8.22}$$

using the control law (8.16).

Finally, LaSalle's invariance principle is used to probe system stability.

Theorem 1. LaSalle's theorem. Let Υ be a compact (closed and bounded) set with the property that every solution of the system (8.6a),(8.6b), which starts in Υ remains in Υ for all future time. Let $V : \Upsilon \to \mathbb{R}$ (8.21) be a continuously differentiable function such that $\dot{V} \leq 0$ in Υ. Let E be the set of all points in Υ where $\dot{V}(e_1, e_2) = 0$. Let ζ be the largest invariant set in E. Then every solution starting in Υ, approaches ζ as $t \to \infty$.

Proof. Convergence of e_1 and e_2 to zero. The proof relies on LaSalle's theorem. Consider the system (8.6a),(8.6b) and the radially unbounded Lyapunov function candidate (8.21). Let us define $\Upsilon = \{V(e_1, e_2) \leq a\}$, where $a \in \mathbb{R}^+$. Let us define the set $E = \{(e_1, e_1)^T \in \Upsilon : \dot{V}(e_1, e_2) = 0\}$.

Equivalently, the expression $\dot{V}(e_1, e_2) = 0$ means that $e_1 = e_2 = 0$, then is easy to verify that every trajectory converges to 0 as $t \to \infty$. Therefore, the following limits are true:

$$\lim_{t \to \infty} e_1 = 0 \qquad\qquad \lim_{t \to \infty} e_2 = 0$$

ensuring the converge of $x_1 \to x_1^d$ and $x_2 \to x_2^d$.

A non-exhaustive block diagram of the proposed controller is shown in Figure 8.1.
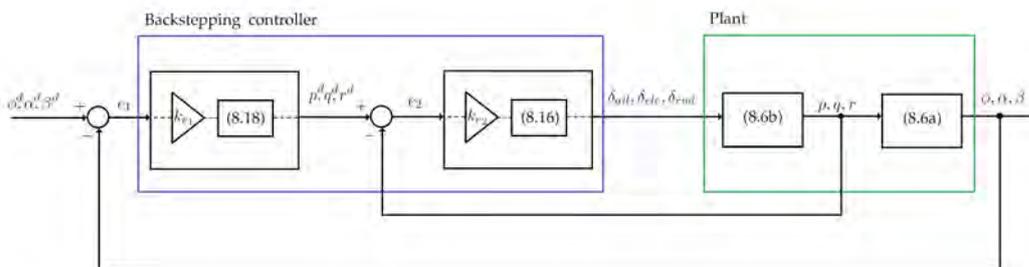

FIGURE 8.1: Block diagram of the backstepping controller.

8.1.1.1 Numerical Simulation

Numerical simulations using a six DOF Matlab model were carried out in order to test the attitude controller. Sinusoidal reference signals were proposed for ϕ, α, and β while wind disturbances were applied. The response of the roll angle, AoA and sideslip angle are given in Figure 8.2, while the corresponding angular velocities and control effort to perform these maneuvers are shown in Figure 8.3(a) and Figure 8.3(b) respectively. The wind disturbances applied are $V_{w_x} = 12\text{m/s}$, $V_{w_y} = 10\text{m/s}$ and $V_{w_z} = 6\text{m/s}$, corresponding to a typical troposphere wind magnitude according to an ALWIN MST radar located in the Sub-Artic site ($16°N, 16°E$).

Furthermore, other numerical simulations with reference signals at different fre-

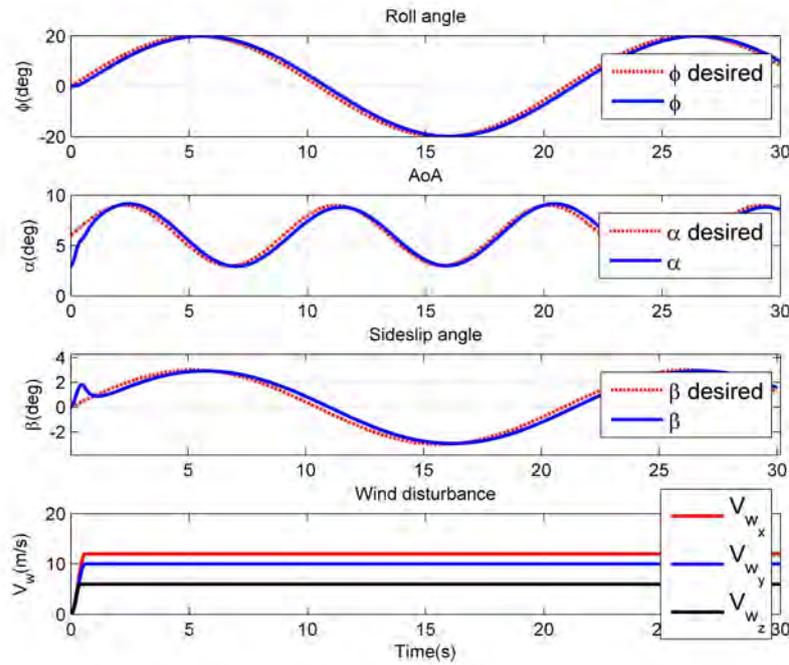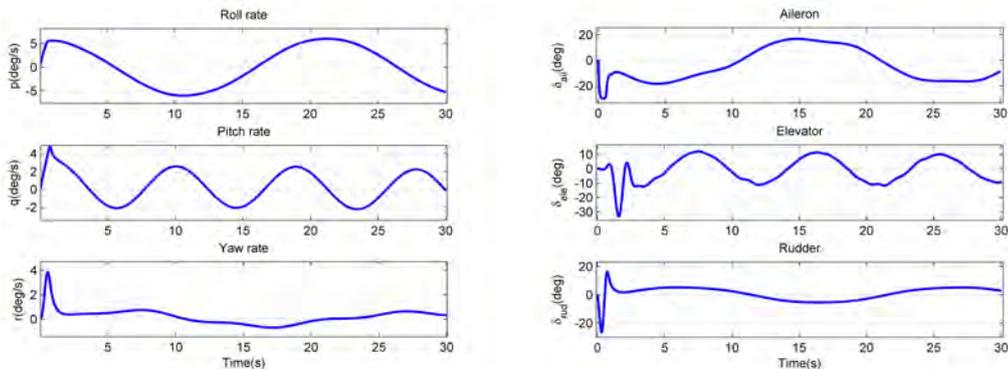FIGURE 8.2: ϕ, α and β response.

(a) Angular velocities response.   (b) Control Effort.

FIGURE 8.3: Attitude control behaviour.

quencies are shown in Figure 8.4 and Figure 8.5, to be sure that the attitude control

behaves as desired. This approach is feasible thanks to the invertibility and full
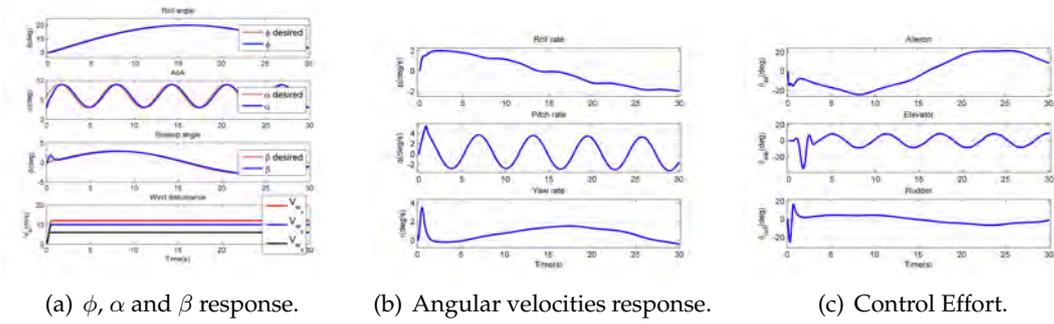

(a) ϕ, α and β response. (b) Angular velocities response. (c) Control Effort.

FIGURE 8.4: Attitude control behaviour at different frequencies.

(a) ϕ, α and β response. (b) Angular velocities response. (c) Control Effort.
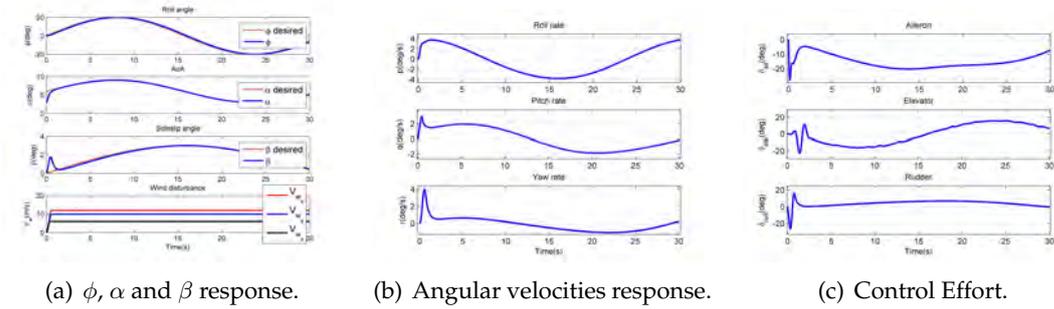
FIGURE 8.5: Attitude control behaviour at different frequencies.

knowledge of $f_2(x_1)$ and $f_4(\cdot)$ for regular operation limits of transport aircraft. For $f_2(x_1)$ to be invertible, its determinant must be different from zero, thus

$$H_{12}H_{23} - H_{13}H_{22} - tg_\theta s_\phi \left(H_{11}H_{23} - H_{21}H_{13} \right) + tg_\theta c_\phi \left(H_{11}H_{22} - H_{21}H_{12} \right) \neq 0 \quad (8.23)$$

If the wind components are neglected, the condition is reduced to

$$- c_\alpha - tg_\theta \left(tg_\beta s_\phi + c_\phi s_\alpha \right) \neq 0 \quad (8.24)$$

such that the matrix is invertible as long as $\phi \neq \pm 90$, $\gamma \neq \pm 90$. It is straightforward to infer that these conditions are never reached.

In the case of $f_4(\cdot)$, it is invertible if C_δ is invertible, such that the condition to satisfy is

$$b^2 \bar{c} C_{m_{\delta ele}} \left(C_{l_{\delta ail}} C_{n_{\delta rud}} - C_{l_{\delta rud}} C_{n_{\delta ail}} \right) \neq 0 \quad (8.25)$$

Thus, the matrix is invertible as long as $C_{m_{\delta ele}} \neq 0$ and $C_{l_{\delta ail}} C_{n_{\delta rud}} - C_{l_{\delta rud}} C_{n_{\delta ail}} \neq 0$, which is manageable.

Regarding the gain matrices k_{e_1} and k_{e_2}, since the analytical method to probe stability of the system (8.20) is based on Lyapunov, the values of the matrix gains were proposed via simulation, such that:

$$k_{e_1} = \begin{bmatrix} 9 & 0 & 0 \\ 0 & 9 & 0 \\ 0 & 0 & 9 \end{bmatrix} 0 \qquad k_{e_2} = \begin{bmatrix} 3 & 0 & 0 \\ 0 & 5 & 0 \\ 0 & 0 & 3 \end{bmatrix}$$

At this point, the task to control the attitude of the aircraft could be considered completed, even if the control surface dynamics are not included yet. However, after

considering the computing requirements needed to obtain the Jacobian of $\varphi(x_1)$ with respect to x_1 at each iteration (that make possible the computation of the control u), and the feasibility of the approach depending on the inversion of the matrix C_δ, a more intuitive controller with less computational effort is explored.

8.1.2   Non Linear Inversion

The approach consists in transform algebraically a nonlinear system into a system with linear dynamics (Slotin and Li, 1991), (Khalil, 2002). Separation of slow and fast dynamics are common practice (Snell, Enns, and Garrard, July 1992), (Lombaerts et al., August 2010). Moreover, some machine learning algorithms and/or variations of the classical NLI approach have been tested in order to improve the performance of the method and provide robustness to uncertainties like modeling and/or measuring errors, showing good simulation results (Rysdyk and Calise, November 2005),(Hameduddin and Bajodah, June 2012).
Recalling the expression in matrix form given in Chapter 3 for the AoA, sideslip angle and airspeed, rearranged for Ω denoted by:

$$
\begin{bmatrix} \dot{\alpha} \\ \dot{\beta} \\ \dot{V}_a \end{bmatrix} = \begin{bmatrix} H_{11} & H_{12} & H_{13} \\ H_{21} & H_{22} & H_{23} \\ H_{31} & H_{32} & H_{33} \end{bmatrix} \begin{bmatrix} p \\ q \\ r \end{bmatrix} + \begin{bmatrix} Q_1 \\ Q_2 \\ Q_3 \end{bmatrix} \tag{8.26}
$$

where

$$
H_{11} = -\left(tan_\beta c_\alpha + \frac{V_{w_y} c_\alpha}{V_a c_\beta} \right)
$$

$$
H_{12} = 1 + \frac{V_{w_x} c_\alpha + V_{w_z} s_\alpha}{V_a c_\beta}
$$

$$
H_{13} = -\left(tan_\beta s_\alpha + \frac{V_{w_y} s_\alpha}{V_a c_\beta} \right)
$$

$$
H_{21} = s_\alpha + \frac{V_{w_z} c_\beta + V_{w_y} s_\alpha s_\beta}{V_a}
$$

$$
H_{22} = \frac{V_{w_z} c_\alpha s_\beta - V_{w_x} s_\alpha s_\beta}{V_a}
$$

$$
H_{23} = -\left(c_\alpha + \frac{V_{w_y} c_\alpha s_\beta + V_{w_x} c_\beta}{V_a} \right)
$$

$$
H_{31} = V_{w_z} s_\beta - V_{w_y} s_\alpha c_\beta
$$

$$
H_{32} = V_{w_x} s_\alpha c_\beta - V_{w_z} c_\alpha c_\beta
$$

$$
H_{33} = V_{w_y} c_\alpha c_\beta - V_{w_x} s_\beta
$$

$$
Q_1 = \frac{1}{V_a c_\beta} \left(g_1 - \frac{1}{m} (L + F_{thr} s_\alpha) \right) + \frac{1}{V_a c_\beta} \left(\dot{V}_{w_x} s_\alpha - \dot{V}_{w_z} c_\alpha \right)
$$

$$
Q_2 = \frac{1}{V_a} \left(g_2 + \frac{1}{m} (Y - F_{thr} c_\alpha s_\beta) \right) + \frac{1}{V_a} \left(\dot{V}_{w_x} c_\alpha s_\beta - \dot{V}_{w_y} c_\beta + \dot{V}_{w_z} s_\alpha s_\beta \right)
$$

$$
Q_3 = g_3 + \frac{1}{m} (F_{thr} c_\alpha c_\beta - D) - \dot{V}_{w_x} c_\alpha c_\beta - \dot{V}_{w_y} s_\beta - \dot{V}_{w_z} s_\alpha c_\beta
$$

which can be written as:

$$\dot{R} = H(R)\Omega + Q(R) \tag{8.27}$$

Also, recalling the first-order model of the actuators, assuming δ_i^d ($i = ail, ele, rud$) as the desired positions of the control surfaces, and δ_i as the current positions of the control surfaces,

$$\dot{\delta}_i = \frac{1}{\xi_i}\left(\delta_i^d - \delta_i\right) \tag{8.28}$$

where ξ_i are the time-constants.

Taking the angular velocities as intermediary control variables, the necessary position of the actuators (deflection of aileron, elevator and rudder) as functions of the desired angular velocities must be determined, so the jerk vector of the angular velocities is obtained by differentiating one more time equation (8.1), and including (8.28), leading to

$$
\begin{bmatrix} \ddot{p} \\ \ddot{q} \\ \ddot{r} \end{bmatrix} = \frac{1}{2}\rho S I^{-1} \left\{ V_a^2 \left(\begin{bmatrix} b\dot{C}_l \\ \bar{c}\dot{C}_m \\ b\dot{C}_n \end{bmatrix} + C_\delta \xi \begin{bmatrix} \delta_{ail}^d - \delta_{ail} \\ \delta_{ele}^d - \delta_{ele} \\ \delta_{rud}^d - \delta_{rud} \end{bmatrix} \right) \right.
$$
$$
\left. + 2V_a\dot{V}_a \left(\begin{bmatrix} bC_l \\ \bar{c}C_m \\ bC_n \end{bmatrix} + C_\delta \begin{bmatrix} \delta_{ail} \\ \delta_{ele} \\ \delta_{rud} \end{bmatrix} \right) \right\} - I^{-1} I_n \begin{bmatrix} \dot{p} \\ \dot{q} \\ \dot{r} \end{bmatrix} \tag{8.29}
$$

with

$$
I_n = \begin{bmatrix} -Eq & (C-B)r - Ep & (C-B)q \\ (A-C)r + 2Ep & 0 & (A-C)p - 2Er \\ (B-A)q & (B-A)p + Er & Eq \end{bmatrix}
$$

and

$$
\xi = \begin{bmatrix} \frac{1}{\xi_{ail}} & 0 & 0 \\ 0 & \frac{1}{\xi_{ele}} & 0 \\ 0 & 0 & \frac{1}{\xi_{rud}} \end{bmatrix}
$$

where the aerodynamic moment coefficients dynamics are taken into account due to their close relation with R. On the other hand, control surfaces moment coefficients dynamics are neglected. Hence, differentiating (8.2), equation (8.29) can be rewritten as:

$$
\begin{bmatrix} \ddot{p} \\ \ddot{q} \\ \ddot{r} \end{bmatrix} = \frac{1}{2}\rho S I^{-1} \left\{ V_a^2 C_\delta \xi \begin{bmatrix} \delta_{ail}^d - \delta_{ail} \\ \delta_{ele}^d - \delta_{ele} \\ \delta_{rud}^d - \delta_{rud} \end{bmatrix} + V_a^2 C_c \begin{bmatrix} \dot{\alpha} \\ \dot{\beta} \\ \dot{V}_a \end{bmatrix} \right.
$$
$$
\left. + 2V_a\dot{V}_a \left(\begin{bmatrix} bC_l \\ \bar{c}C_m \\ bC_n \end{bmatrix} + C_\delta \begin{bmatrix} \delta_{ail} \\ \delta_{ele} \\ \delta_{rud} \end{bmatrix} \right) \right\} + I^{-1}\left(\frac{1}{4}\rho S V_a C_k - In\right) \begin{bmatrix} \dot{p} \\ \dot{q} \\ \dot{r} \end{bmatrix} \tag{8.30}
$$

where

$$
C_c = \begin{bmatrix} 0 & bC_{l_\beta} & -\frac{b^2}{2V_a^2}(C_{l_p}p + C_{l_r}r) \\ \bar{c}C_{m_\alpha} & 0 & -\frac{\bar{c}^2}{2V_a^2}C_{m_q}q \\ 0 & bC_{n_\beta} & -\frac{b^2}{2V_a^2}(C_{n_p}p + C_{n_r}r) \end{bmatrix}
$$

$$C_k = \begin{bmatrix} b^2 C_{l_p} & 0 & b^2 C_{l_r} \\ 0 & \bar{c}^2 C_{m_q} & 0 \\ b^2 C_{n_p} & 0 & b^2 C_{n_r} \end{bmatrix}$$

The vector $\dot{R}$ can be taken from (8.27), and the vector $\dot{\Omega}$ from (8.1). Therefore, inverting the dynamics leads to an attitude control input denoted by:

$$
\begin{bmatrix} \delta^d_{ail} \\ \delta^d_{ele} \\ \delta^d_{rud} \end{bmatrix} = \frac{1}{V_a^2} \xi^{-1} C_\delta^{-1} \left\{ \frac{2I}{\rho S} \begin{bmatrix} \tau_p \\ \tau_q \\ \tau_r \end{bmatrix} - \frac{2}{\rho S} \left(\frac{1}{4} \rho S V_a C_k - In \right) \begin{bmatrix} \dot{p} \\ \dot{q} \\ \dot{r} \end{bmatrix} \right.
$$
$$
\left. - 2V_a \dot{V}_a \left(\begin{bmatrix} bC_l \\ \bar{c}C_m \\ bC_n \end{bmatrix} + C_\delta \begin{bmatrix} \delta_{ail} \\ \delta_{ele} \\ \delta_{rud} \end{bmatrix} \right) - V_a^2 C_c \begin{bmatrix} \dot{\alpha} \\ \dot{\beta} \\ \dot{V}_a \end{bmatrix} \right\} + \begin{bmatrix} \delta_{ail} \\ \delta_{ele} \\ \delta_{rud} \end{bmatrix}
$$
$$(8.31)$$

where the wind effects appear in the terms involving $\dot{\alpha}$, $\dot{\beta}$ and $\dot{V}_a$. In consequence, the desired dynamics for the angular velocities are proposed as:

$$
\begin{bmatrix} \tau_p \\ \tau_q \\ \tau_r \end{bmatrix} = \begin{bmatrix} -k_1(p - p^d) - k_2(\dot{p} - \dot{p}^d) + \ddot{p}^d \\ -k_3(q - q^d) - k_4(\dot{q} - \dot{q}^d) + \ddot{q}^d \\ -k_5(r - r^d) - k_6(\dot{r} - \dot{r}^d) + \ddot{r}^d \end{bmatrix} \qquad (8.32)
$$

with $k_i > 0$ ($i = 1, ...6$) as gains, chosen in order to assure asymptotical convergence of the variables to their desired values.

One more time, the feasibility of the approach depends on the singularity of C_δ, the matrix involving the aerodynamic coefficients (assumed to be known thanks to experimental data, airflow simulations, or any other method) due to the control surfaces, aspect that can be handled.

Moreover, knowing that the state is $x = [p, \dot{p}, q, \dot{q}, r, \dot{r}]^T$ with an output $y = [p, q, r]^T$, and a control input $u = [\delta_{ail}, \delta_{ele}, \delta_{rud}]^T$, each output needs to be differentiated twice for the output to appear explicitly. Thus, the partial relative degree for each angular velocity is two, making a total relative degree of 6, equal to the number of states. Therefore, the approach will not present internal dynamics.

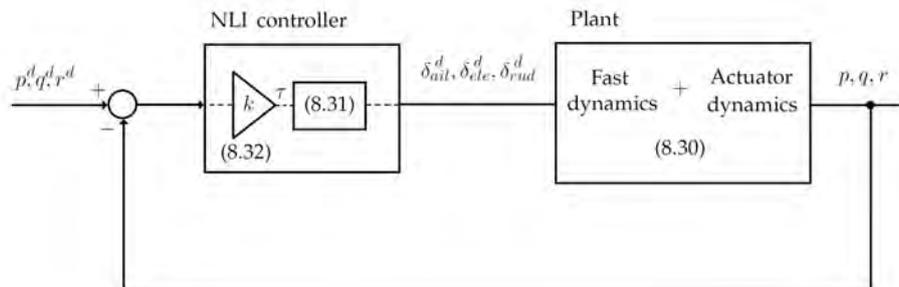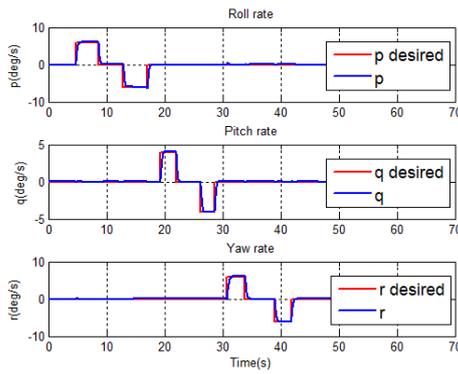A non-exhaustive block diagram of the proposed controller is shown in Figure 8.6.

FIGURE 8.6: Block diagram of the NLI controller.
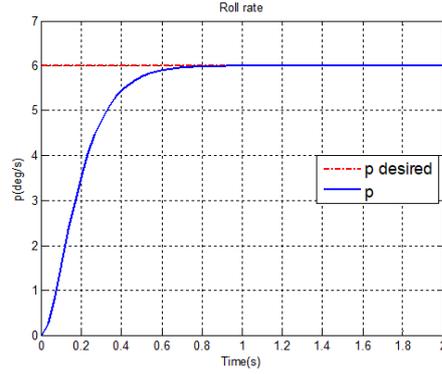
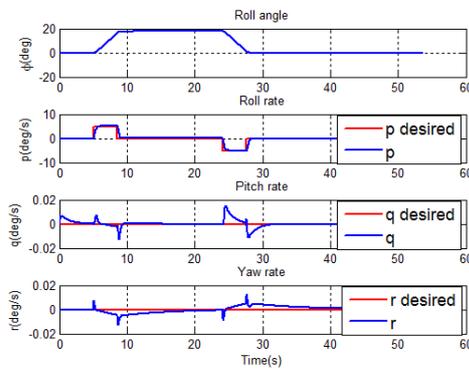(a) Attitude response to commanded angular rates.

(b) Attitude zoom to p angular rate.

FIGURE 8.7: Attitude control behaviour.
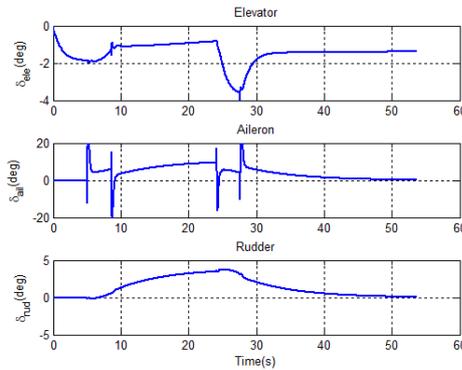

(a) Lateral displacement using roll.

(b) Deflection of control surfaces for lateral displacement (δ_{ail} has opposite sign convention).

FIGURE 8.8: Control effort.

8.1.2.1 Numerical Simulation

Regarding the attitude controller performance, in Figure 8.7(a) are shown the behaviours of the angular velocities when steps of $\pm 6°/\mathrm{s}$ are commanded to roll and yaw, while a $\pm 4°/\mathrm{s}$ rate for pitch. A zoom to the attitude response in rolling is depicted in Figure 8.7(b), and all the angular velocities are tuned to have the same performance. The response of the angular velocities is determined by the gains of the desired dynamics in (8.32), these gains were fixed such that the angular velocities behave as second order systems with a damping factor of $\zeta = 1$ (critically damped, corresponding to two equal real poles), and natural frequency of $\omega_n = 10\mathrm{rad/s}$, such that the response reaches the steady state in a time less than $1\mathrm{s}$.

This is assured because (8.32) can be seen as three scalar systems of the form

$$\ddot{e} + k_2\dot{e} + k_1 e = 0 \tag{8.33}$$

where the error e is the difference between the angular velocity and its desired value, such that after a laplace transformation and its equivalence with the 2nd order linear systems characteristic polynomial $s^2 + 2\zeta\omega_n s + \omega_n^2$, it is clear that $\omega_n = \sqrt{k_1}$ and $\zeta = \frac{k_2}{2\omega_n}$.
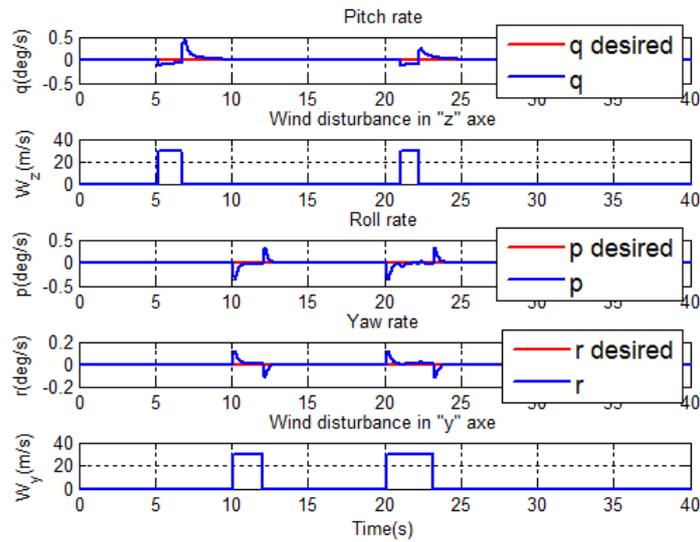
FIGURE 8.9: Attitude response to disturbances.

The influence that a yawing motion has on the roll rate and viceversa can be nullified or controlled, which plays a key roll when coordinated turns are performed.
In Figure 8.8(a), a lateral displacement using roll is simulated, holding a fixed altitude and a constant yaw angle. In order to achieve this task, the deflection of the control surfaces of the aircraft is depicted in Figure 8.8(b).
Moreover, the behaviour of the attitude under some disturbances is examined by applying wind gusts of 30m/s (58.3 knots) (see Figure 8.9).
The first disturbance is applied around the fifth second in z_B direction, which produces an asymmetric disturbance in pitch. Then, a second disturbance is applied around second 10 in the $-y_B$ direction, which affects roll and yaw rates, as expected. Finally, a disturbance with components in both mentioned directions is applied at around 21s. Note that for the moment, the error produced in position by these wind gusts is not examined and only a zero angular rate is desired to be kept under these disturbances.
Now, using the same wind disturbances like the ones used for the backstepping approach, sinusoidal functions as a reference for the pitch rate, roll rate and yaw rate are simulated to test the controller behaviour.
The pitch rate response is shown in Figure 8.10, where sinusoidal references of $1.5°/\text{s}$ magnitude at different frequencies are commanded. As expected, the control efforts and the range of motion of the pitch angle change accordingly to the pitch rate.
In the same way, even if the the rudder has indirect effects on the rolling motion, neglecting the adverse roll implies that the rudder has no *direct* effect in rolling. Thus, the rolling moment is completely controlled by the ailerons, and the behaviour of the roll rate is shown in Figure 8.11, where sinusoidal functions of $4°/\text{s}$ magnitude at different frequencies are commanded. Once again, the control efforts and the range of the involved euler angle change as expected.
 Finally, to test the yaw rate, the coupling of roll and yaw motions provoked through the ailerons (induced yaw and adverse yaw), must be taken into account as it plays a key role in heading commands, to better understand this, lets clarify what coordinated/uncoordinated turns are.
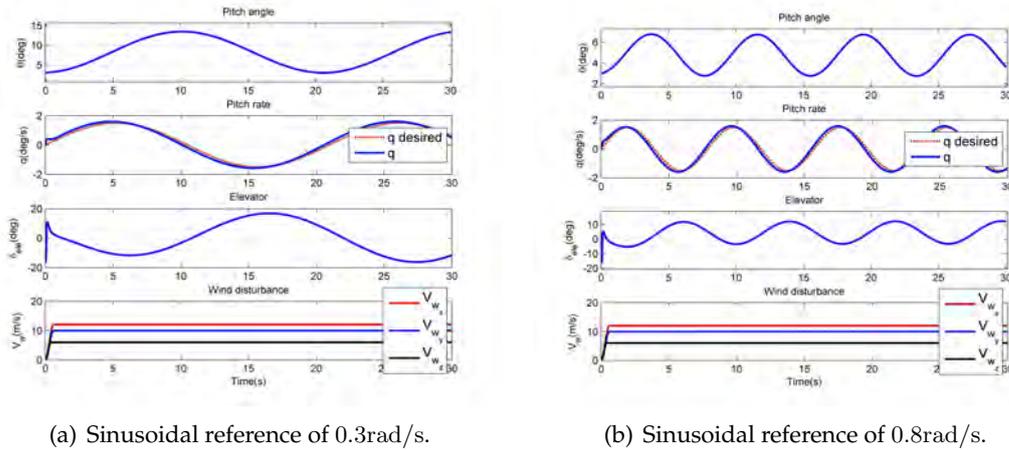
(a) Sinusoidal reference of 0.3rad/s.

(b) Sinusoidal reference of 0.8rad/s.

FIGURE 8.10: Pitch rate response.

(a) Sinusoidal reference of 0.3rad/s.

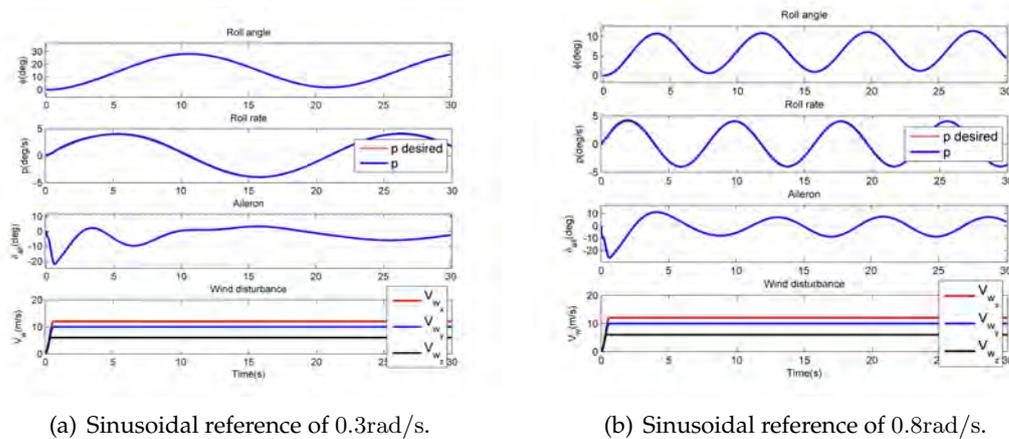(b) Sinusoidal reference of 0.8rad/s.

FIGURE 8.11: Roll rate response.

8.1.2.1.1 Coordinated and Uncoordinated turns

A coordinated turn is when the bank angle of a turning aircraft complements its turning rate. On the other hand, uncoordinated turns happen when the bank angle is too high or too low for the turning rate.

When too much aileron or not enough rudder are applied in the turning direction, the bank angle is too high and the aircraft slips, causing a slipping turn with less turning rate than expected. In this case, the nose of the airplane would be outside of the turn and the tail inside.

Similarly, when too much rudder or not enough aileron are applied in the turning direction, a bigger turning rate than the expected is experienced. This make the aircraft perform a skidding turn, with the tail of the aircraft outside the turn and the nose inside of it.

It is common to refer to a $3°/\text{s}$ turning rate ($180°/\text{min}$) as a rate one turn (*FAA December 2015*). Therefore, a rate two turn will be a $6°/\text{s}$ turning rate ($360°/\text{min}$).

The main cause of uncoordinated turns is the non-compensation or over-compensation of the adverse yaw (banking to the left due to aileron input provokes a positive yawing motion) and the induced yaw (a positive roll rate creates a positive yawing motion). In both cases, uncoordinated turns will be reflected in an increase of the

airframe drag, provoking undesired turbulence, loss of performance, and uncomfortability for passengers. Consequently, a Slip/Skid indicator (see Figure 8.12) is located in the cockpit (either electronically in the PFD or as a physical indicator) such that pilots can perform coordinated turns easily.

The roll angle to achieve a rate one turn depends on the True Air Speed of the air-

FIGURE 8.12: Slip/Skid Indicator for turn coordination. The ball to the right indicates slip and to the left indicates skid. Only gravity forces affect the ball position (CFI, 2017).

craft. As a rule of thumb, considering the TAS in kn, the operation (TAS/10)+7 gives the roll angle required to achieve a rate one turn. However, at high speed, since high roll angles are undesired, ICAO (*ICAO* 2006b) states that "All turns are to be made at a bank angle of $25°$ or at a rate of $3°/$s, whichever requires the lesser bank."

Hence, in order to analyse the yaw rate behaviour of the controller, a rate of $2°/$s at $233kn$ TAS is commanded. It is worth to mention that during flight, constant variations of the thrust are not desired, so thrust is considered constant for this simulation. The results are shown in Figure 8.13, where it can be seen how the rudder effort decreases as the roll angle increases, meaning that a skidding turn is being converted into a coordinated turn, always following the commanded $2°/$s yaw rate.

Note that the backstepping approach controls the roll angle, AoA, sideslip angle, and the angular velocities, while the direct NLI approach controls the angular velocities. This election of link variables to the guidance controller are not coincidence. Indeed, they are chosen according to current auto-guidance modes of transport aircraft, where the normal load factor (strongly related to the pitch rate) and the roll rate, are the primary variables in both Airbus and Boeing families, making possible the compatibility of the proposed approaches to today's autoguidance systems.
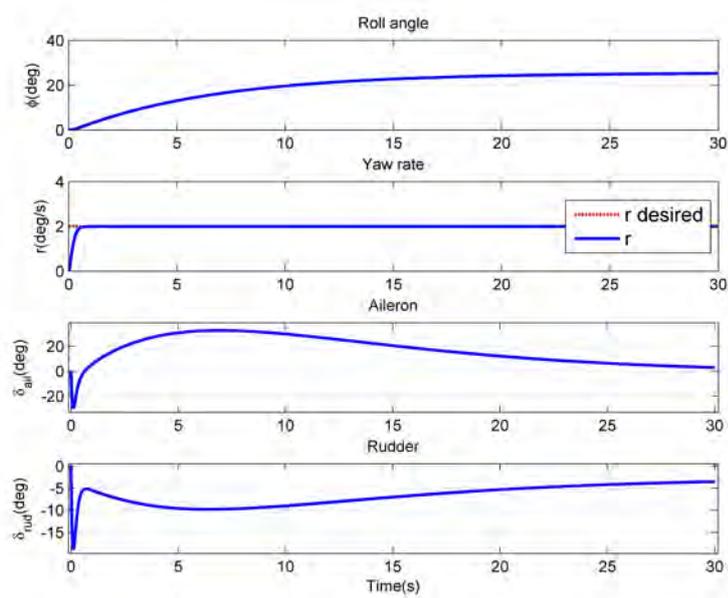
FIGURE 8.13: Yaw rate step response

8.2 Guidance Control

8.2.1 Non Linear Inversion

Since the position of an aircraft is described as an underactuated motion, once the attitude controller is defined, the control structure for guidance can be proposed. Some attempts using Non Linear Inversion have been performed recently (Wahid et al., October 2014), (Wahid et al., 2016), where space-indexed trajectory tracking is done by using the rate of the euler angles and the first derivative of the thrust as control inputs. Other authors have proposed to extend the energy-based control approach (Lambregts, 1983) to 4D guidance (Lambregts, 1996), (Chudy and Rzucidlo, August 2009). However, some limitations appear in both cases.

In the frame of direct NLI, let us first obtain the angular velocities and thrust required to follow a reference trajectory. Thus, after differentiating equation (3.15), the jerk vector of the position in F_E is obtained.

$$
\begin{bmatrix} x_E^{(3)} \\ y_E^{(3)} \\ z_E^{(3)} \end{bmatrix} = \frac{\dot{L}_{EB}}{m} \begin{bmatrix} F_{x_a} + F_{thr} \\ F_{y_a} \\ F_{z_a} \end{bmatrix} + \frac{L_{EB}}{m} \begin{bmatrix} \dot{F}_{x_a} + \dot{F}_{thr} \\ \dot{F}_{y_a} \\ \dot{F}_{z_a} \end{bmatrix} + \frac{-\dot{m}}{m^2} L_{EB} \begin{bmatrix} F_{x_a} + F_{thr} \\ F_{y_a} \\ F_{z_a} \end{bmatrix}
$$
(8.34)

Considering that the mass rate of change is very small compared to the aircraft total mass, the term containing $\frac{-\dot{m}}{m^2}$ is neglected. Also, writing the Euler property as

$$
\dot{L}_{EB} = L_{EB} \begin{bmatrix} 0 & -r & q \\ r & 0 & -p \\ -q & p & 0 \end{bmatrix}
$$

$$
= M_p p + M_q q + M_r r
$$
(8.35)

where

$$
M_p = \begin{bmatrix} 0 & c_\phi s_\theta c_\psi + s_\phi s_\psi & c_\phi s_\psi - s_\phi s_\theta c_\psi \\ 0 & c_\phi s_\theta s_\psi - s_\phi c_\psi & -s_\phi s_\theta s_\psi - c_\phi c_\psi \\ 0 & c_\phi c_\theta & -s_\phi c_\theta \end{bmatrix}
$$

$$
M_q = \begin{bmatrix} -c_\phi s_\theta c_\psi - s_\phi s_\psi & 0 & c_\theta c_\psi \\ -c_\phi s_\theta s_\psi + s_\phi c_\psi & 0 & c_\theta s_\psi \\ -c_\phi c_\theta & 0 & -s_\theta \end{bmatrix}
$$

$$
M_r = \begin{bmatrix} s_\phi s_\theta c_\psi - c_\phi s_\psi & -c_\theta c_\psi & 0 \\ s_\phi s_\theta s_\psi + c_\phi c_\psi & -c_\theta s_\psi & 0 \\ s_\phi c_\theta & s_\theta & 0 \end{bmatrix}
$$

and defining the vector $F_{ab} = [F_{x_a} + F_{thr}, F_{y_a}, F_{z_a}]^T$, equation (8.34) can be rewritten as:

$$
\begin{bmatrix} x_E^{(3)} \\ y_E^{(3)} \\ z_E^{(3)} \end{bmatrix} = \frac{1}{m} \left[M_p F_{ab} \middle| M_q F_{ab} \middle| \begin{matrix} c_\theta c_\psi \\ c_\theta s_\psi \\ -s_\theta \end{matrix} \right] \begin{bmatrix} p \\ q \\ \dot{F}_{thr} \end{bmatrix} + \frac{1}{m} M_r F_{ab} r + \frac{L_{EB}}{m} \begin{bmatrix} \dot{F}_{x_a} \\ \dot{F}_{y_a} \\ \dot{F}_{z_a} \end{bmatrix}
$$
(8.36)

with

$$
\begin{bmatrix} \dot{F}_{x_a} \\ \dot{F}_{y_a} \\ \dot{F}_{z_a} \end{bmatrix} = \begin{bmatrix} \frac{\partial F_{x_a}}{\partial \alpha} & \frac{\partial F_{x_a}}{\partial \beta} & \frac{\partial F_{x_a}}{\partial V_a} \\ 0 & \frac{\partial F_{y_a}}{\partial \beta} & \frac{\partial F_{y_a}}{\partial V_a} \\ \frac{\partial F_{z_a}}{\partial \alpha} & \frac{\partial F_{z_a}}{\partial \beta} & \frac{\partial F_{z_a}}{\partial V_a} \end{bmatrix} \dot{R} + \begin{bmatrix} \frac{\partial F_{x_a}}{\partial \rho} \\ \frac{\partial F_{y_a}}{\partial \rho} \\ \frac{\partial F_{z_a}}{\partial \rho} \end{bmatrix} \dot{\rho}
$$
(8.37)

where $\dot{R}$ is obtained from equation (8.27).

Moreover, the resultant thrust produced by the engines is supposed to behave as a first-order system, denoted by

$$\dot{F}_{thr} = \frac{1}{\xi_T} \left(F^d_{thr} - F_{thr} \right) \tag{8.38}$$

where the F^d_{thr} is the desired thrust and F_{thr} the current thrust.

In this manner, taking as guidance inputs the vector $[p, q, \dot{F}_{thr}]^T$, the inversion of the dynamics can be proposed in the form:

$$\begin{bmatrix} p \\ q \\ \dot{F}_{thr} \end{bmatrix} = m \begin{bmatrix} M_p F_{ab} & \bigg| & M_q F_{ab} & \bigg| & \begin{matrix} c_\theta c_\psi \\ c_\theta s_\psi \\ -s_\theta \end{matrix} \end{bmatrix}^{-1} \left(\begin{bmatrix} \tau_x \\ \tau_y \\ \tau_z \end{bmatrix} - \frac{1}{m} M_r F_{ab} r - \frac{L_{EB}}{m} \begin{bmatrix} \dot{F}_{x_a} \\ \dot{F}_{y_a} \\ \dot{F}_{z_a} \end{bmatrix} \right) \tag{8.39}$$

where the wind effects are involved in the vector $[\dot{F}_{x_a}, \dot{F}_{y_a}, \dot{F}_{z_a}]^T$, and the desired behaviour of the position is proposed as:

$$\begin{bmatrix} \tau_x \\ \tau_y \\ \tau_z \end{bmatrix} = \begin{bmatrix} -d_1(x - x^d) - d_2(\dot{x} - \dot{x}^d) - d_3(\ddot{x} - \ddot{x}^d) + \dddot{x}^d \\ -d_4(y - y^d) - d_5(\dot{y} - \dot{y}^d) - d_6(\ddot{y} - \ddot{y}^d) + \dddot{y}^d \\ -d_7(z - z^d) - d_8(\dot{z} - \dot{z}^d) - d_9(\ddot{z} - \ddot{z}^d) + \dddot{z}^d \end{bmatrix} \tag{8.40}$$

with $d_i > 0$ $(i = 1, ...9)$ as gains chosen in order to assure asymptotical convergence of the variables to their desired values. For the numerical choice of these gains, (8.40) can be seen as three scalar 3rd order linear systems denoted by

$$\dddot{e} + d_3\ddot{e} + d_2\dot{e} + d_1 e = 0 \tag{8.41}$$

where the error e is the difference between the position and its desired value. This 3rd order system can be seen as a second order system added with an extra real pole at $s_3 = -1$ in the Real-Imaginary plane, and its characteristic polynomial is given by: $(s^2 + 2\zeta\omega_n s + \omega_n^2)(s + 1)$. Thus, a Routh-Hurwitz stability test yields:

$$\begin{array}{c|cc} s^3 & 1 & d_2 \\ s^2 & d_3 & d_1 \\ s^1 & \frac{d_3 d_2 - d_1}{d_3} & \\ s^0 & d_1 & \end{array} \tag{8.42}$$

such that the system will be stable if $d_3 > 0$, $d_1 > 0$, and $d_3 d_2 - d_1 > 0$. Moreover, considering the characteristic polynomial $(s^2 + 2\zeta\omega_n s + \omega_n^2)(s + 1)$, it is straightforward to obtain

$$2\zeta\omega_n + 1 = d_3 \tag{8.43}$$

$$\omega_n^2 + 2\zeta\omega_n = d_2 \tag{8.44}$$

$$\omega_n^2 = d_1 \tag{8.45}$$

In order to have a smooth response of the aircraft position, a damping factor $\zeta = 1$ is forced, such that $s_{1,2} = -\omega_n$, and $s_3 = -1$. Also, since a slow and stable behaviour of the systems is needed, the poles $s_{1,2}$ will be made the dominant poles of the system by defining a $\omega_n > 0$ that satisfies the following statement:

The real part of the closest poles to the imaginary axis ($s_{1,2} = -\omega_n$) has to be from 5

to 10 times less than the real part of the closest pole to this poles ($s_3 = -1$). Therefore, with no zeros nearby, the poles $s_{1,2}$ will be called the dominant closed loop poles, and will dominate the transient response before decay slowly.

In this manner, the aircraft position response is denoted by a critically damped 2nd order system with two equal real poles close to the imaginary axis.

Values of $0.09 \leq \omega_n \leq 0.16$ will make the dominant poles to be located between $-0.16 \leq s_{1,2} \leq 0.09$ in the Real-Imaginary plane, provoking a slow and stable behaviour of the aircraft position response thanks to the small value of the natural frequency. These values of ω_n satisfy the conditions obtained by the Routh-Hurwitz stability test.

Moving forward, note that to develop a control law using NLI or any other model-based-approach relying on equation (8.36), the invertibility of the matrix:

$$M_{pqT} = \left[\begin{array}{c|c|c} M_p F_{ab} & M_q F_{ab} & \begin{matrix} c_\theta c_\psi \\ c_\theta s_\psi \\ -s_\theta \end{matrix} \end{array} \right] \tag{8.46}$$

needs to be computed, which in the case in where $\phi \approx \psi \approx 0$, the determinant of this matrix is given by:

$$\mid M_{pqT} \mid = s_\theta F_{y_a} + (s_\theta (F_{x_a} + F_{thr}) - c_\theta F_{z_a})(s_\theta F_{z_a}) + c_\theta (c_\theta (F_{x_a} + F_{thr}) + s_\theta F_{z_a}) F_{z_a} \tag{8.47}$$

and, when considered $\theta \approx 0$, a singularity appears for $F_{x_a} + F_{thr} = 0$.

This is the case when the plane is cruising at constant speed. Therefore, taking into account that the cruise phase of a flight is essential, and that the airplane will go through this condition very often, any algorithm using this control approach should be carefully analyzed. This result is not surprising, realizing that when a cruise flight with the Euler angles near zero is performed, the matrix L_{EB} will remain constant, so its derivative is expected to tend to zero. Furthermore, even if the first derivative of the Euler angles along with the thrust are considered as the control inputs, $\left[\dot{\phi}, \dot{\theta}, \dot{F}_{thr} \right]^T$ for instance, as in (Wahid et al., 2016), the corresponding matrix (similar to (8.46)) will be described by (8.48) and will also present singularities during the cruise phase.

$$M_{\phi\theta} = \left[\begin{array}{c|c|c} M_\phi F_{ab} & M_\theta F_{ab} & \begin{matrix} c_\theta c_\psi \\ c_\theta s_\psi \\ -s_\theta \end{matrix} \end{array} \right] \tag{8.48}$$

where

$$M_\phi = M_p$$

$$M_\theta = \begin{bmatrix} -s_\theta c_\psi & c_\theta s_\phi c_\psi & c_\theta c_\phi c_\psi \\ -s_\theta s_\psi & c_\theta s_\phi s_\psi & c_\theta c_\phi s_\psi \\ -c_\theta & -s_\theta s_\phi & -s_\theta c_\phi \end{bmatrix}$$

A non-exhaustive block diagram of the proposed controller is shown in Figure 8.14. Furthermore, a stability proof of the proposed approach using Lyapunov theory is provided
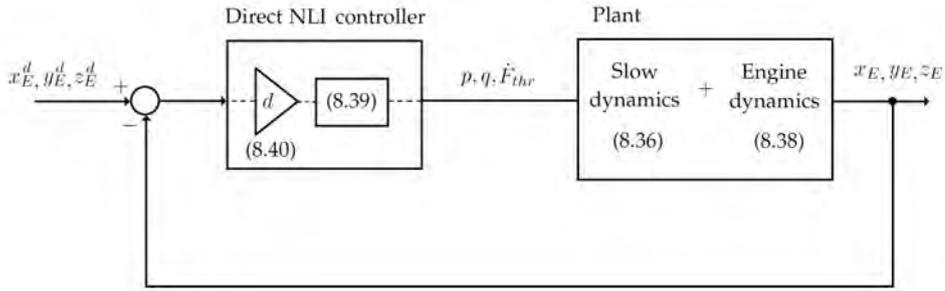
FIGURE 8.14: Block diagram of the direct NLI controller.

8.2.1.1 Stability of direct NLI Guidance Control using Lyapunov theory

Lets recall equation (8.36):

$$
\begin{bmatrix} x_E^{(3)} \\ y_E^{(3)} \\ z_E^{(3)} \end{bmatrix} = \frac{1}{m} M_{pqT} \begin{bmatrix} p \\ q \\ \dot{F}_{thr} \end{bmatrix} + \frac{1}{m} M_r F_{ab} r + \frac{L_{EB}}{m} \begin{bmatrix} \dot{F}_{x_a} \\ \dot{F}_{y_a} \\ \dot{F}_{z_a} \end{bmatrix} \tag{8.50}
$$

where $\dot{R}$ is obtained from equation (8.27).
Rewriting (8.50) as

$$
X^{(3)} = \frac{M}{m}u + \frac{N}{m} \tag{8.51}
$$

where

$$
X = [x_E(t), y_E(t), z_E(t)]^T \tag{8.52a}
$$

$$
M = M_{pqT} \tag{8.52b}
$$

$$
N = M_r F_{ab} r + L_{EB} \cdot \left[\dot{F}_{x_a}, \dot{F}_{y_a}, \dot{F}_{z_a} \right]^T \tag{8.52c}
$$

$$
u = [p, q, \dot{F}_{thr}]^T \tag{8.52d}
$$

an intermediate variable s, non related in any way with the Laplace variable, can be defined as

$$
s = \ddot{\tilde{X}} + 2\lambda \dot{\tilde{X}} + \lambda^2 \tilde{X} \tag{8.53}
$$

where λ is a 3x3 matrix containing the terms ($\lambda_{1,2,3} > 0$) in the diagonal. Note that this intermediate variable s contains the input vector in its first derivative, and the convergence to zero of this variable as $t \to \infty$ would imply that the error $\tilde{X} = X - X^d$ goes to zero. This is assured by considering that when $s \to 0$, equation (8.53) can be seen as three scalar 2nd order linear systems of the form

$$
\ddot{e} + 2\lambda_i \dot{e} + \lambda^2 e = 0 \tag{8.54}
$$

where ($i = 1, 2, 3$), and the error e is the difference between the position and its desired value, such that after making the equivalence with the 2nd order linear systems characteristic polynomial $s^2 + 2\zeta\omega_n s + \omega_n^2$, it is clear that $\omega_n = \lambda_i$ and $\zeta = 1$. In this manner, each component of the error $\tilde{X}$ will converge to zero as a critically damped 2nd order linear system with a natural frequency depending on the values of the matrix λ is proposed.

Then, introducing the variable $\ddot{X}_r$ with its derivative as

$$\ddot{X}_r = \ddot{X}^d - 2\lambda\dot{\tilde{X}} - \lambda^2\tilde{X} \tag{8.55a}$$

$$X_r^{(3)} = X^{d(3)} - 2\lambda\ddot{\tilde{X}} - \lambda^2\dot{\tilde{X}} \tag{8.55b}$$

allows to rewrite equation (8.53) in the form

$$s = \ddot{X} - \ddot{X}_r \tag{8.56}$$

Therefore, if a Lyapunov candidate function is proposed as

$$V = \frac{1}{2}ms^Ts \tag{8.57}$$

its derivative, mixing (8.55b) and (8.56) is expressed as

$$\dot{V} = s^T m \left(X^{(3)} - X_r^{(3)} \right) \tag{8.58a}$$

$$= s^T \left(Mu + N - mX_r^{(3)} \right) \tag{8.58b}$$

At this point, a choice of

$$u = M^{-1} \left(-N + mX_r^{(3)} - k_1 s \right) \tag{8.59}$$

with the positive definite matrix gain k_1, would lead to $\dot{V} = -s^T k_1 s$. Implying thanks to the Barbalat's lemma that $\dot{V} \to 0$, and in consequence $s \to 0$. Hence, the following limits are true

$$\lim_{t\to\infty} \ddot{\tilde{X}} = 0 \qquad \lim_{t\to\infty} \dot{\tilde{X}} = 0 \qquad \lim_{t\to\infty} \tilde{X} = 0 \tag{8.60}$$

8.2.1.2 Numerical Simulation

In order to get an idea of the performance of the direct NLI, Figure 8.15(a) shows the trajectory of the aircraft when different desired positions are commanded.
The initial altitude and speed are 10,000m and 250m/s, respectively. Then, an increase in altitude of 100m and return to its original altitude, as well as a lateral displacement of 100 m and return to the original position are demanded. Next, a decrease of 10m in altitude and a lateral displacement of 50m in the opposite direction to the first one are commanded. Finally, the aircraft is required to return to the original altitude and original y position. The Figure 8.15(b) displays the 3D trajectory of the described flight.
 It is a key point to remark that since the control inputs for guidance are the angular velocities, if an angular velocity is commanded for a relatively long period of time, this will result in constant and maybe undesired turning of the aircraft. One solution to avoid this problem is that, when the Euler angles reach certain magnitude, the angular velocities that caused this saturation are forced to become zero until other angular velocities in the opposite direction are commanded. The saturation of the Euler angles are: $\phi\{-30°, 30°\}$; $\theta\{-15°, 25°\}$; $\psi\{-\pi, \pi\}$.
Moreover, in order to manage the singularities of the method, the desired angular

(a) Position response to commanded positions.   (b) 3D Trajectory of guidance control test.
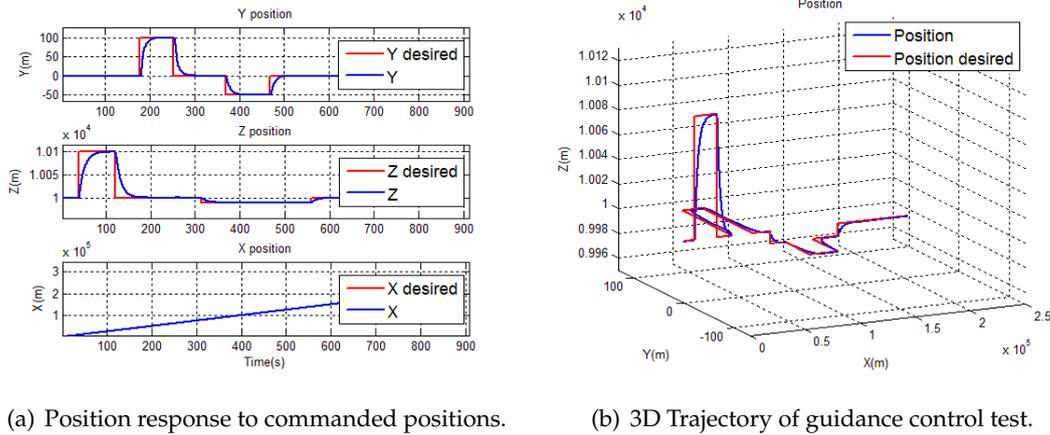
FIGURE 8.15: Guidance control test

velocities are switched to zero when the plane goes through the cruise phase at constant speed.

In order to analyze further the controller behaviour, the response to steps of 100m in the y and z axes are depicted in Figure 8.16. The initial altitude is 1,000m and the initial speed is 120m/s. Since the angular velocities serve as a link with the attitude controller, they are shown along with the corresponding euler angles. For this cases, where the thrust is kept constant, the desired values are reached in less than 50s.

On the other hand, it is a fact that the response along the z axis is affected by the

(a) Lateral response.   (b) Longitudinal response.
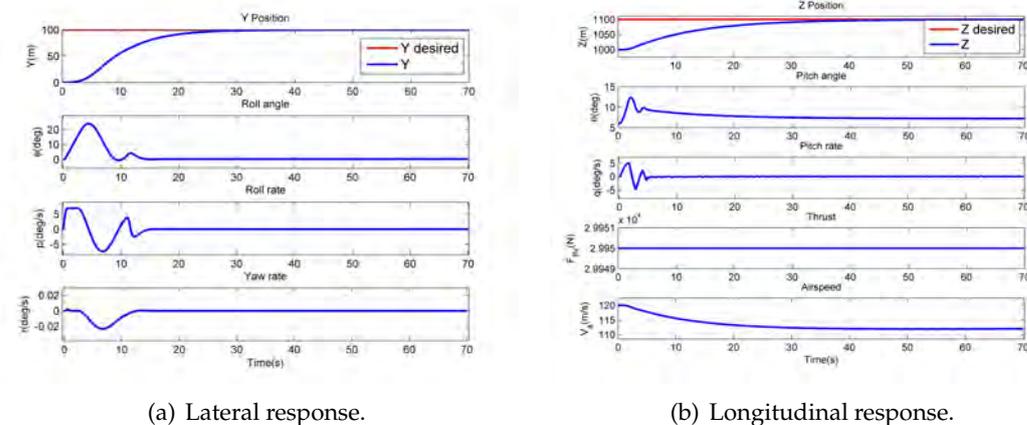
FIGURE 8.16: Guidance response to a 100m step with constant thrust.

response along the x axis. In other words, the altitude and the speed are strongly coupled. Thus, being the thrust the principal actuator in the velocity of the aircraft, the altitude is affected by the thrust variation and vice-versa (due to the exchange between potential and kinetic energy of the aircraft). This is shown in Figure 8.17, where also a 100m displacement in altitude is commanded, but this time, using the thrust as control input along with the angular velocities, the behaviour of the altitude response is modified while the convergence of the aircraft velocity to its required value to provide x position control is assured.

In this manner, even if the use of thrust decreases the performance in altitude and time for this guidance approach, Figure 8.18 shows the importance of thrust as control input when a bigger altitude step is commanded. This time, the desired altitude

can not be reached with the initial constant thrust (Figure 8.18(a)), but it is reached when the thrust is variable (Figure 8.18(b)).

Thus, the importance of the variable thrust for 4D guidance can be appreciated when comparing the time responses of the aircraft (flying at 120m/s and 1000m altitude) required to climb 100m and 300m in Figures 8.17, 8.18(b). When the thrust is part of the control variables, the altitude has the same time response disregarding the error magnitude (within reasonable error limits), which is, indeed, the designed behaviour of the system for the fixed gains $d_i > 0$ $(i = 1, ...9)$. Note the different thrust and speeds maximum values but the same altitude time response in the mentioned figures.
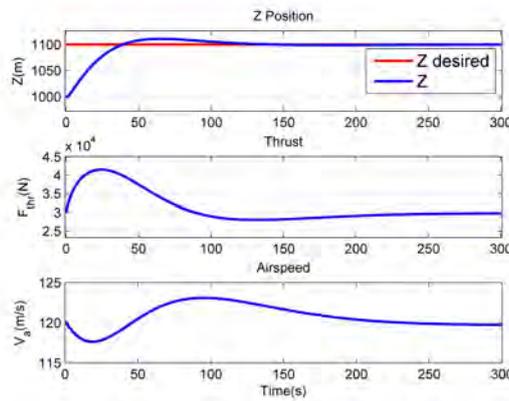

FIGURE 8.17: Longitudinal response to a 100m step with a variable thrust.

(a) Constant Thrust. (b) Variable Thrust.
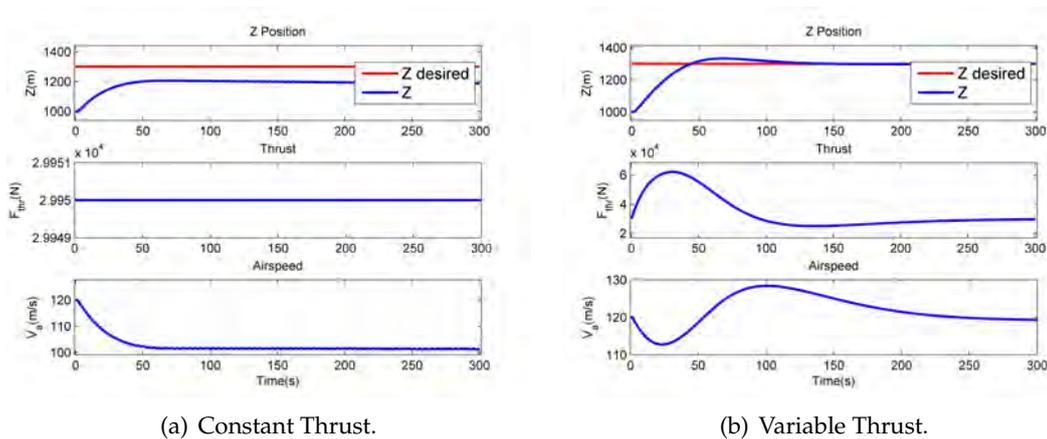
FIGURE 8.18: Longitudinal response to a 300m step with constant and variable thrust.

Let now the position errors produced by wind gusts be examined, taking into account that non-zero angular rates will allow the aircraft to reject perturbations and achieve the guidance objectives.

In figure 8.19, wind gusts in the form of an "impulse" endowed with small turbulence (using a Dryden wind turbulence model) are applied, showing the effects on y and z position errors as well as the groundspeed. In this simulation, the aircraft

is supposed to be at cruise flight at 10,000m and 250m/s velocity ($\approx$.73Mach), such that the thrust applied is considered constant. Note that a thrust compensation for wind gusts could be done. However, since the wind is assumed to be a compact perturbation in a step form, thrust and aircraft velocity are supposed to not be affected heavily. Also, the constant thrust ensures less engine fatigue in this flight phase.
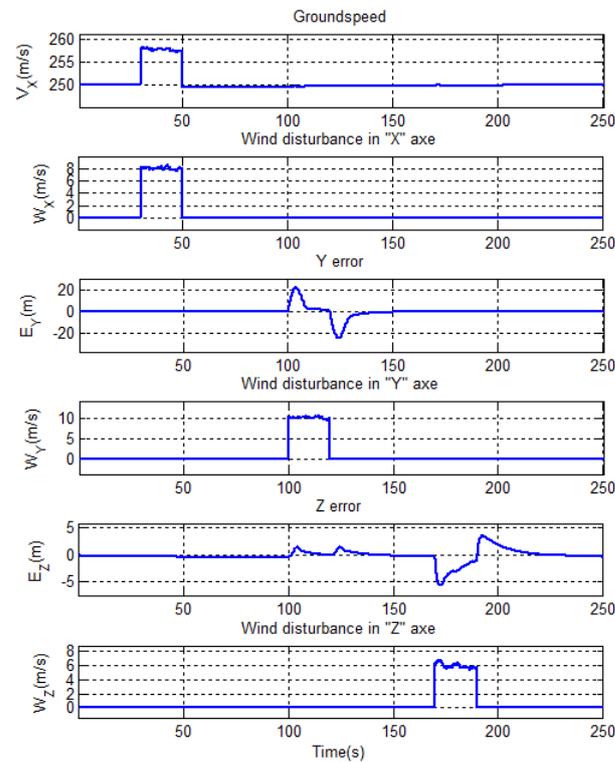

FIGURE 8.19: Position response to disturbances.

So far, the controller is assumed to have full knowledge of wind disturbances (by estimations, measures or available forecasts), but in reality, the use of corrupted measurements, approximated mathematical models, or uncertainty in parameters leave room for errors in the control, which can be studied through a sensitivity analysis.

8.2.1.3 Sensitivity analysis with respect to wind disturbances for the direct NLI approach

Full knowledge of variables and parameters cannot be acquired due to possible corrupted measures or uncertainty in parameters, leading to guidance inaccuracy. Thus, this work will provide a tool to quantify the performance of the aircraft in terms of position errors due to wind gusts "impulses" by performing a sensitivity analysis through simulation. Actuator dynamics for the control surfaces involving a time-constant are also considered.

Methods to perform sensitivity analysis such as screening are common (S. Schnelle, October 2014), where a baseline experiment is done using nominal values of parameters. Then, selecting two extreme values of these, the results of the perturbed

experiment with respect to the baseline are observed in order to decide to which parameters the model is most sensitive to. Nevertheless, interaction between parameters is neglected and the correlation between them and outputs of the system is considered linear. Variance-based approaches show how to find which are the most relevant parameters and how much they affect the system output by computing sensitivity indices such as Sobol indices, quantifying the amount of variance in the output caused by a parameter. These methods allow interaction of different parameters and nonlinear responses between them and the outputs (Janon et al., December 2014). Another technique is to compute the partial derivatives of the interesting variables to analyze the local sensitivity (Evans, June 2009), (Kanno et al., September 2010).

For our work, using an approach similar to the screening analysis, wind information is used as a changing parameter to quantify the effects it has on the aircraft position. It is assumed that wind knowledge by the controller is the main contributor to po-
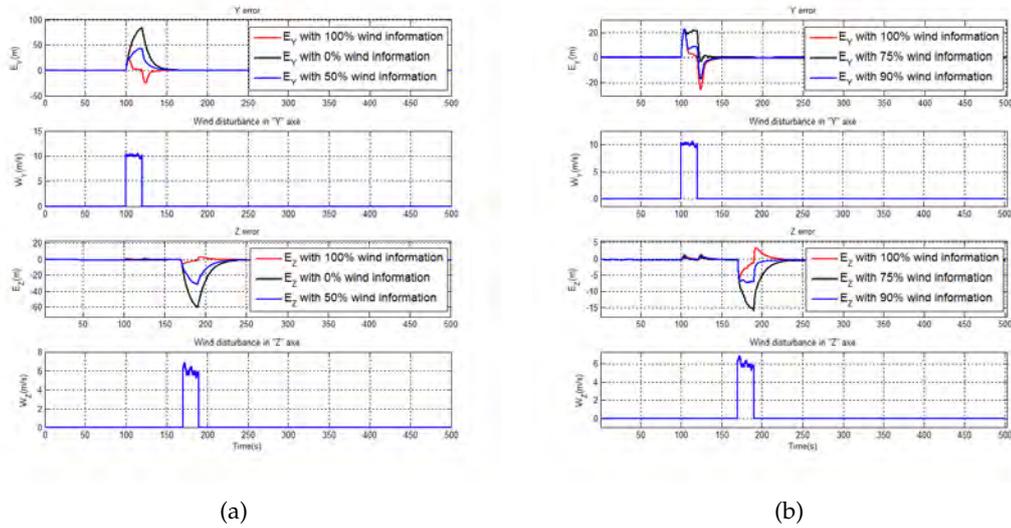

(a)   (b)

FIGURE 8.20: Wind knowledge effect on position errors.

TABLE 8.1: Error depending on Wind knowledge

	y		z	
Wind Knowledge (%)	MSE	MAE	MSE	MAE
100	10.2760	0.6731	0.7806	0.5767
90	8.4628	0.6787	2.0858	0.6993
80	13.8191	0.8001	5.8818	1.0335
70	23.0642	1.0926	11.7237	1.2839
60	35.9015	1.4416	20.3080	1.6094
50	55.9952	1.8394	31.2249	1.9199
40	78.7370	2.2092	44.1320	2.2091
30	107.6038	2.6044	59.4018	2.4883
20	140.3636	2.9848	77.5264	2.7895
10	177.5873	3.3675	97.0740	3.0764
0	220.3000	3.7540	118.4172	3.3786

sition error improvements. Note that by wind knowledge, we refer to the accuracy

of wind gust magnitude and not the direction. So, a 70% of wind knowledge when a wind gust of 10 m/s is considered, will be 7 m/s in the same direction. In this manner, a transport aircraft flying at 10,000m with a constant groundspeed of 250m/s under some wind disturbances is simulated, and endowing the controller with different wind knowledge, the position errors are examined.

The aim of this analysis is to evaluate the reactiveness of an aircraft cruising at a constant speed and a constant altitude (respecting load factor limits), when considerations of wind disturbances are included in the controller.

The position errors for y and z with 0%, 50%, 75%, 90% and 100% of wind knowledge are displayed in figure 8.20, where the error magnitude decreases when wind knowledge increases.

This means that as the components of equation (3.31) used for the control approach tend to equations (3.32a), (3.32b), and (3.32c), the controller decreases its performance drastically, corroborating that the reactiveness of the control law (and hence, the position errors), is sensitive to wind knowledge.

In Table 8.1, the Mean Squared Error (MSE) and the Mean Absolute Error (MAE) in y and z axes were computed in order to provide a clear idea of the wind sensitivity with respect to aircraft position[1]. The disturbances, simulation time (500s), and sample time (1/30s), are the same as the ones to obtain figure 8.20.

As a result, depending on each application or requirement, a maximal wind uncertainty can be allowed in order to do not exceed a desired error in position, proposed by the user. This wind uncertainty can be translated into wind sensors accuracy, wind estimations accuracy, or up-to-date forecasted wind.

The control law used in this work can be easily replaced by other control law to compare their sensitivity to wind.

In this manner, a safety envelope (or VoP) for a single aircraft or a group of aircraft can be redefined, since errors will depend on wind knowledge accuracy, allowing to create compact aircraft clusters and decrease the workload for air traffic controllers.

8.2.2 Total Energy

In this method, the concept of a potential flight path angle denoted by: $\gamma_p = \gamma + \frac{\dot{V_a}}{g}$ is considered. It indicates the potential path angle that can be achieved by bringing the acceleration to zero by applying elevator until γ becomes γ_p.

Since the total energy (E) is conformed by the kinetic (T) and potential energy (V), this yields to

$$E = mg \left(h + \frac{V_a^2}{2g} \right) \tag{8.61}$$

and the total energy rate of change, can be expressed in terms of γ_p. Hence

$$\dot{E} = V_a mg \left(\gamma + \frac{\dot{V_a}}{g} \right) \tag{8.62a}$$

$$\frac{\dot{E}}{V_a mg} = \gamma_p \tag{8.62b}$$

---

[1] The reader may notice that in Table 8.1, the MSE in y is bigger for 100% than 90% of wind knowledge. Even if this looks contradictory, it is explained due to the penalization of the squared error for high values. For example, consider the set of errors w.r.t. a reference: $S_{100} = [1, 1, 1, 2, 10]$ and $S_{90} = [1, 3, 2, 2, 9]$, clearly, S_{90} differs more from the reference than S_{100}. However, even if $MAE_{S_{100}} = 3$ is less than $MAE_{S_{90}} = 3.4$, as expected, the MSE is affected due to the square of the last value of the errors, being $MSE_{S_{100}} = 21.4$ greater than $MSE_{S_{90}} = 19.8$.

This potential flight path angle is found to be related with the specific total energy rate of the aircraft. Therefore, the approach consists in controlling the behaviour of the energy rate by controlling γ_p, using the thrust and elevator. However, the control of this variable is performed with non available plant dynamics while introducing empirically an energy rate distribution variable to distribute the energy rate between the flight path angle and acceleration. This variable is given by the first derivative of the Langrangean ($\dot{L} = \gamma - \frac{\dot{V}_a}{g}$), assuming a constant mass, and that $\gamma = \frac{\dot{h}}{V_a}$. Moreover, the distribution variable is controlled directly by the elevator, bypassing the fast dynamics and arising difficulties to integrate other autopilot functions.

Furthermore, the speed and altitude dynamics in this approach are expected to be identical, bringing to light a problem for some 4D trajectories where this is not true. Finally, no integral term has been proposed to force online position error to zero.

Note that this brief analysis is only for the longitudinal motion of the plane. However, the full total energy control, manages both lateral and longitudinal dynamics as decoupled motions. Further information is available in (Lambregts, 2013), (Lambregts, 1983), (Lambregts, 1996), (Chudy and Rzucidlo, August 2009), (Akmeliawati and Mareels, December 2001), and (Akmeliawati and Mareels, July 2010).

8.2.3 Guidance Control based on indirect NLI

The main objective for this 4D trajectory tracking control strategy is to avoid singularity issues while inverting the flight dynamics. This will be made possible by considering the equations in the wind frame from Section 3.3, where the longitudinal motion was given by:

$$\dot{V}_a = \frac{1}{m} \left(F_{thr} c_\alpha - D - mgs_\gamma \right) \tag{8.63}$$

and using the Flight Path Angle ($\gamma = \theta - \alpha$), the vertical motion was given by:

$$\dot{\gamma} = \frac{1}{mV_a} \left(F_{thr} s_\alpha + L - mgc_\gamma \right) \tag{8.64}$$

Also, considering that transport aircraft perform equilibrated turns, the heading rate is given by:

$$\dot{\psi} = \frac{g}{V_a} tg_\phi \tag{8.65}$$

Consequently, three phases to perform the guidance control are proposed:

1. Control of the longitudinal and lateral motions, θ and ϕ, with stabilisation in yaw ψ.
   It will be considered that thanks to the relation $\alpha = \theta - \gamma$, to command θ when γ is known, is equal to command the AoA. The control of θ and ϕ while stabilizing yaw motion can be performed using classical control techniques (see Section 8.1).

2. Control of Speed and the Flight Path Angle as functions of AoA and thrust using the guidance equations (8.63),(8.64).

3. Adjustment of the heading angle given by (8.65), targeted speed, and desired flight path angle as functions of the positions errors generated by a 4D reference trajectory.

Proposing desired dynamics for the speed $\left(V_a^d\right)$, heading $\left(\psi^d\right)$, and the flight path angle $\left(\gamma^d\right)$ as first order linear responses, they are such as:

$$\dot{V}_a = \frac{1}{\tau_V}\left(V_a^d - V_a\right) \tag{8.66a}$$

$$\dot{\gamma} = \frac{1}{\tau_\gamma}\left(\gamma^d - \gamma\right) \tag{8.66b}$$

$$\dot{\psi} = \frac{1}{\tau_\psi}\left(\psi^d - \psi\right) \tag{8.66c}$$

where $\tau_V, \tau_\gamma, \tau_\psi$ are time-constants.
Equations (8.63), (8.64), and (8.65) can be rewritten as

$$\frac{m}{\tau_V}\left(V_a^d - V_a\right) + mgs_\gamma = F_{thr}c_\alpha - D(\rho, \alpha, V_a) \tag{8.67a}$$

$$\frac{mV_a}{\tau_\gamma}\left(\gamma^d - \gamma\right) + mgc\gamma = F_{thr}s_\alpha + L(\rho, \alpha, V_a) \tag{8.67b}$$

$$tg^{-1}\left(\frac{V_a}{g\tau_\psi}\left(\psi^d - \psi\right)\right) = \phi \tag{8.67c}$$

Therefore, in order to obtain the values of the thrust and AoA required to follow their proposed dynamics, the nonlinear set of equations (8.67a), (8.67b) is solved for F_{thr} and α. Then, saturations are applied if the results are out of the thrust $\left[F_{thr}^{min}, F_{thr}^{max}\right]$ and angle of attack $\left[\alpha^{min}, \alpha^{max}\right]$ limits. Note that the Jacobian of the right hand side of equations (8.67a), (8.67b), w.r.t. $[F_{thr}, \alpha]^T$ is denoted by

$$J = \begin{bmatrix} c_\alpha & -\left(F_{thr}s_\alpha + \frac{\partial D(\rho,\alpha,V_a)}{\partial \alpha}\right) \\ s_\alpha & F_{thr}c_\alpha + \frac{\partial L(\rho,\alpha,V_a)}{\partial \alpha} \end{bmatrix} \tag{8.68}$$

and its determinant is

$$\mid J \mid = F_{thr} + \frac{\partial L(\rho, \alpha, V_a)}{\partial \alpha}c_\alpha + \frac{\partial D(\rho, \alpha, V_a)}{\partial \alpha}s_\alpha > 0 \tag{8.69}$$

In order to corroborate this, note that above the minimum flight speed:

- Thrust sign is positive during all flight.

- The derivative of Lift w.r.t. AoA is only negative in stall (never reached), and the term $c_\alpha \geq 0$ for $[-\pi/2, \pi/2]$, ensuring a positive sign of the term.

- The derivative of Drag w.r.t. AoA is positive when $\alpha \geq 0$ and the term $s_\alpha \geq 0$ for $[0, \pi/2]$, ensuring a positive sign of the term.

- The derivative of Drag w.r.t. AoA is negative when $\alpha < 0$ but the term $s_\alpha < 0$ for $[-\pi/2, 0)$, ensuring a positive sign of the term.

Thus, it can be assured that the inversion is possible at all times.
In addition to this, the ϕ value required to follow the lateral dynamics, it is obtained directly from (8.67c), and is also saturated within the limits $\left[\phi^{min}, \phi^{max}\right]$.
Therefore, in order to assure that the 4D trajectory error tends to zero after some perturbation, the reference values for V_a, γ, and ψ must be adapted. The proposed

adaptive scheme is the following:

$$V_a^d = V_a + \delta V_a \tag{8.70a}$$

$$\gamma^d = \gamma + \delta\gamma \tag{8.70b}$$

$$\psi^d = \psi + \delta\psi \tag{8.70c}$$

where

$$\delta V_a = \frac{1}{\tau_x}\left(x_R - x_E\right) \tag{8.71a}$$

$$\delta\gamma = \frac{1}{\tau_z}\left(z_R - z_E\right) \tag{8.71b}$$

$$\delta\psi = \frac{1}{\tau_y}\left(y_R - y_E\right) \tag{8.71c}$$

and τ_x, τ_y, τ_z are time-constants such that: $\tau_x >> \tau_V$; $\tau_y >> \tau_\psi$; $\tau_z >> \tau_\gamma$.
The term $\delta\psi$ is depicted in Figure 8.21. A non-exhaustive block diagram of the
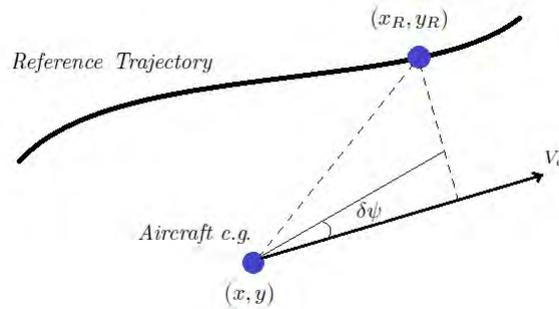

FIGURE 8.21: Change in ψ required to follow the reference trajectory

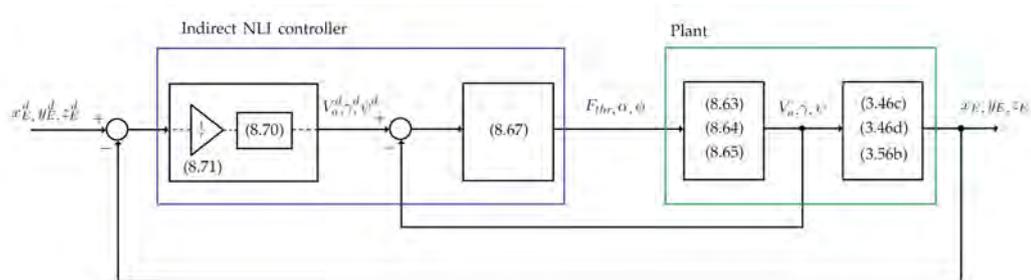proposed controller is shown in Figure 8.22.

FIGURE 8.22: Block diagram of the indirect NLI controller.

8.2.3.1 Numerical Simulation

In order to test the proposed 4D trajectory tracking approach for the longitudinal motion, a 100m amplitude sinusoidal reference trajectory for $z_R(t)$ is depicted in figure 8.23(a). The commanded trajectory is followed with a small delay. Note that

the numerical values of the simulation correspond to the ones predicted in Section 4.2. Furthermore, a step response of a 100m error for the lateral motion is shown in figure 8.23(b).
 Moreover, to further analysis of the lateral motion, a 100m sinusoidal reference tra-
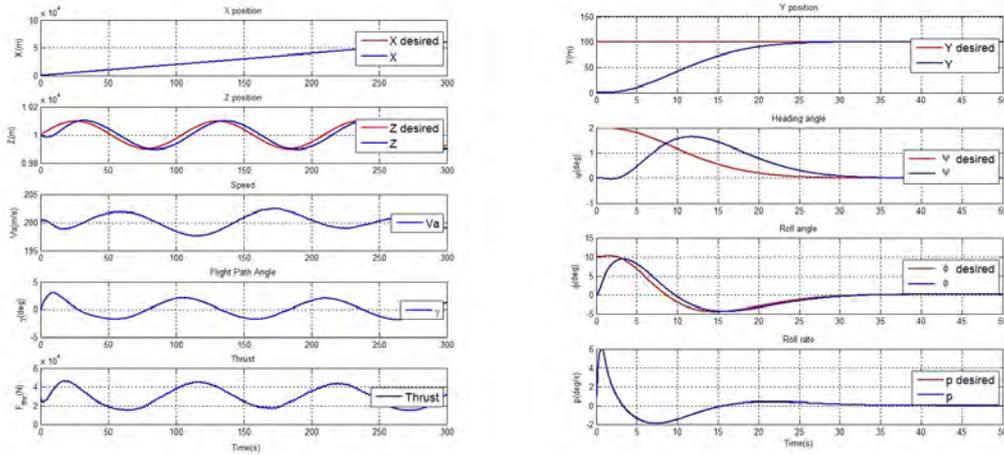
(a) F_{thr}, V_a and γ required to follow a sinusoidal reference trajectory.

(b) Lateral step response for a 100m error.

FIGURE 8.23: Trajectory tracking control law simulation.

jectory of .13rad/s frequency for $y_R(t)$ is proposed, the response of the controller is depicted in figure 8.24 along with all the variables related to the motion. For practical purposes, the initial heading of the airplane is zero degrees. Besides, the delay observed in the lateral response is due to the execution of banked turns as an underactuated motion, where yawing is provoked after a rolling through the ailerons only, instead of a yawing result of a coordination of aileron-rudder.
 The main disadvantage of this guidance approach is that wind disturbances are not
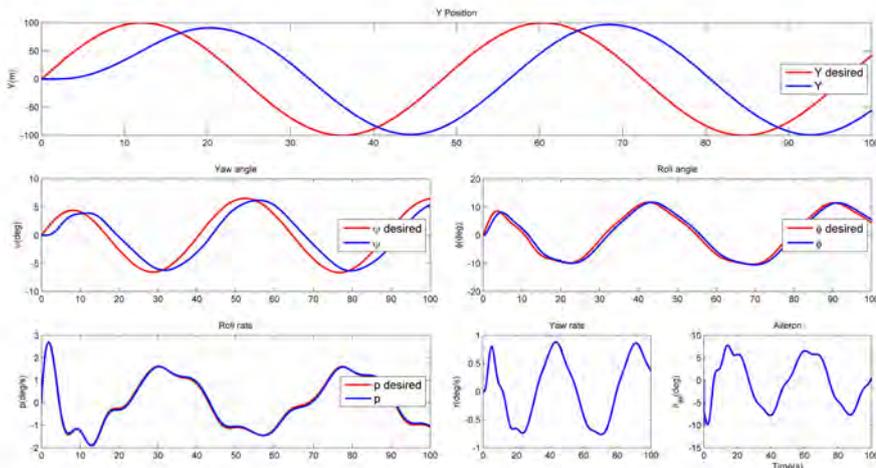

FIGURE 8.24: Y desired stands for y_R. Y stands for y_E. Heading and roll angles are also shown.

considered in the model. Thus, in contrast with the direct NLI algorithm, the invertibility guaranteed at all times comes with the lack of wind explicit considerations.

Therefore, if wind disturbances were considered, equations (8.67a), (8.67b) should be substituted for:

$$\frac{1}{\tau_\gamma}\left(\gamma^d - \gamma\right) = \frac{1}{mV_a}\left(L + F_{thr}s_\alpha - mgc_\gamma\right) - q\left(\frac{V_{w_x}c_\alpha + V_{w_z}s_\alpha}{V_a}\right) + \frac{1}{V_a}\left(\dot{V}_{w_z}c_\alpha - \dot{V}_{w_x}s_\alpha\right)$$

$$(8.72a)$$

$$\frac{1}{\tau_V}\left(V_a^d - V_a\right) = \frac{1}{m}\left(F_{thr}c_\alpha - D - mgs_\gamma\right) + q\left(V_{w_x}s_\alpha - V_{w_z}c_\alpha\right) - \dot{V}_{w_x}c_\alpha - \dot{V}_{w_z}s_\alpha \qquad (8.72b)$$

such that the solution of the system of nonlinear differential equations for α and F_{thr}, in spite of the complexity, would be of high interest.

8.3 Conclusion

Two different autopilots have been provided in this chapter, both depending on the link variables to be used with the guidance control.

The backstepping approach controls the roll angle, AoA and sideslip angle. This autopilot is ideal in terms of compatibility with modern aircraft using the AoA and roll angle as link variables for the guidance controller. However, the computation of the control law is complex, and the first order dynamics of actuators are not considered. On the other hand, the autopilot based on direct NLI assures full control of the angular velocities. This autopilot is ideal when the load factors are the link variables with the guidance controller. Moreover, the method includes the first order dynamics of actuators, and the control law computation is less complex than the backstepping approach. Nevertheless, a control loop for the Euler angles is not addressed directly. Both autopilot proposals were tested in 6DOF Matlab simulations.

In addition to this, two autoguidance approaches have been proposed, both depending on the control input variables to be used to control the aircraft position.

The first method, based on direct NLI, uses the angular velocities and the thrust rate of change as control inputs. Moreover, it provides a framework for wind sensitivity analysis, where different wind uncertainties and their effects in guidance errors are considered. In this manner, the performance of the guidance approach has been quantified at different wind uncertainties by computing the mean squared error and mean absolute error of the aircraft position with respect to the desired position.

This guidance method considers wind disturbances in the AoA and sideslip angle, as well as in airspeed. However, numerical singularities for the control law computation are present at important flight phases.

In the same tenor, an indirect NLI guidance control has been proposed as a second method. This approach was developed such that the numerical difficulties encountered by the direct NLI guidance approach are avoided. Besides, contrarily to the energy-based methods, the independence in altitude and speed dynamics is preserved, and the bypassing of attitude dynamics is avoided. The proposed approach uses the thrust, AoA, and bank angle as control inputs. However, the strategy does not include wind disturbances explicit compensation.

Both guidance methods were tested in a six degrees of freedom Matlab simulation, providing satisfying results.

In Table 8.2, a summary of all controllers is performed.

In this manner, given a desired time-parameterized trajectory to be followed, the implementation of any of these guidance algorithms along with any of the autopilots proposed, allows full 4D trajectory tracking.

 Future studies should consider the effects of introducing wind estimates accuracy and the establishment of 4D trajectory tracking performance as parameters in order to improve air traffic management.

TABLE 8.2: Controllers summary

Controller	Wind considered by controller	Invertibility at important phases	Sensitivity analysis	Actuator dynamics considered by the controller
Backstepping (Attitude)	✓	✓	X	X
NLI (Attitude)	✓	✓	X	✓
Direct NLI (Position)	✓	X	✓	✓
Indirect NLI (Position)	X	✓	X	✓

Chapter 9

Conclusions and Perspectives

With the current increase on the air traffic demand, not only efficiency and safety of air transport systems is threatened, but also the environmental and socio-economic consequences linked to a failure in providing sound solutions to this arising problem. In this manner, on-going research programs are allowing to tackle the enhancement of air traffic frameworks at different levels.

This thesis is related to the transition from rigid ATC routes to flexible trajectories under a 4D guidance framework, which is deeply related with the extension of the flexibility in separation between aircraft, and hence, with the increase of air traffic capacity under the Trajectory-Based Operations paradigm. The presented work encompassed two main contribution areas:

- Trajectory Generation.

- Flight Control Systems.

Thus, the conclusions and perspectives are also split, presenting the major actions taken to fulfill the primary objectives of the manuscript.

9.1 General Conclusions

9.1.1 Trajectory Generation

Regarding the trajectory generation, airspace users are focused on being able to plan their preferred routes (Business Trajectories) without being constraint by airspace configurations, using published or unpublished waypoints with no relation to ATS route networks. Thus, an approach based on Bezier curves was proposed to generate 4D smooth trajectories from pre-defined control points. These trajectories were endowed with:

- Curvature Continuity, meaning that the generated trajectory is smooth, helping to ease air traffic management in congested areas and improve on-board guidance systems performance.

- Time-stamps and defined speeds for every point of the trajectory, ensuring the compatibility with 4D guidance approaches.

- Load factor surveillance and control, thanks to considerations of the curvature of the path and intended speed, as well as the possibility of controlling the Euclidian distance between the control points and the proposed trajectory.

- Multiplicity, meaning that parallel trajectories to a reference one are easily generated.

- Optimized Fly-by turns, as a direct consequence of the control of the distance between control points and the proposed trajectory.

Within these advantages, a special remark was provided concerning the load factor surveillance. In general, the load factor that an aircraft experiences is computed using its own orientation, angular velocities and linear velocity, while the trajectory provoking this aircraft states is disregarded.

In the approach presented in this work, the trajectory generation algorithm was designed such that the load factor that an aircraft would experience following the generated trajectory, can be obtained using the intended aircraft speed and the curvature of the generated path. In this manner, no other aircraft state variables were required to obtain useful information about how the generated trajectory would impact an aircraft that intended to follow it. This not only simplified the computation time, but also avoided nominal assumption of aircraft state variables, while providing critical information of the generated trajectory.

However, the existent relation of the path curvature with the load factor that an aircraft flying the generated trajectory would experience was only given for decoupled motions. In other words, even if the proposed approach can generate 4D trajectories, only decoupled maneuvers in either lateral or vertical motions have an explicit analytical relation of the computed curvature with the load factor. This is because for non-decoupled maneuvers, the expression relating the radius of the path (the inverse of the curvature) and the load factor of an aircraft is not trivial.

In this manner, the trajectory generation approach was able to generate any 4D smooth trajectory, but it could only analyze the load factor of those segments with independent lateral or vertical components.

Furthermore, the mathematical relation of the curvature and load factor in the vertical motion needed to be endowed with an external negative sign for pitch down motions. This was because the curvature is always positive, and the differentiation between pitch up and down motions relies on it. In this way, the load factor was correctly affected. This remark concerns more to the practical implementation of the algorithm.

9.1.1.1 Numerical Simulation of an Aircraft

Another important challenge encountered during the development of this work, was the numerical simulation of the proposed approaches using a full 6DOF aircraft model.

Considering the fact that certified simulators are not free, and they do not allow the modification of their guidance laws, the remaining option was the use of free flight simulators. However, since many public flight simulators generally contain linearized aircraft models, they become useless for the testing of nonlinear control laws. Hence, a full nonlinear 6DOF Matlab model was developed, similar to a B737-200 / A320-200 aircraft. No aeroelasticity, nor high lift devices were considered.

A differentiation factor of the developed model, besides the full non-decoupled equations, is that the non-dimensional stability derivatives of the aircraft, instead of being a constant value during the whole flight, they depend on multiple variables such as the AOA and airspeed. This was possible through the use of Neural Networks.

Moreover, the Neural Networks used to estimate the non-dimensional stability derivatives could allow the improvement of the aircraft model with new airborne information that could modify these derivatives, such as abnormal situations of icing,

disfigurations in profile, major inertial matrix changes, etc. Also, the multi-input / multi-output data handling is efficient and intuitive, contrary to lookup tables.

9.1.2 Flight Control Systems

Regarding flight control systems, with the objective of diminishing the workload associated to a single flight, and therefore to diminish the probability of near mid-air collisions, two autopilots and two 4D guidance methods were developed.

Regarding the autopilots, two techniques were employed, backstepping and Nonlinear inversion. These autopilots were based on a complete non-decoupled aircraft modelling, and both methods considered wind disturbances. The backstepping approach controls the bank angle, AoA, and sideslip angle, while the Nonlinear inversion approach controls the angular velocities.

In addition to this, another differentiation factor between the proposed autopilots was that in the Nonlinear inversion approach, an explicit consideration of first order dynamics for the deflection of the control surfaces was made, contrary to the backstepping approach.

Concerning the guidance strategies, direct Nonlinear inversion and indirect Nonlinear inversion techniques were used.

The direct Nonlinear inversion approach considered a full 6DOF model under wind disturbances, and used the angular velocities and the thrust rate of change as control inputs. However, this approach presented feasibility issues when the plane was cruising at constant speed.

On the other hand, the indirect Nonlinear inversion approach used the Thrust, AoA, and bank angle as control inputs. This approach did not present feasibility issues, contrary to the direct Nonlinear inversion method, but it relied on a simplified decoupled aircraft modelling with no wind disturbances considered.

It is clear that the backstepping autopilot fits better with the guidance based on indirect Nonlinear inversion, and that the Nonlinear inversion autopilot fits with the direct Nonlinear inversion guidance strategy. This was due to the link variables used for each strategy.

In summary, two different approaches for the full aircraft control were provided, each one using different link variables (See Figure 9.1).

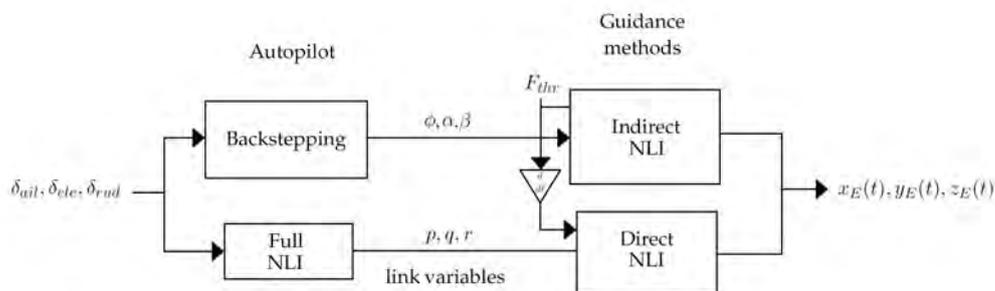Furthermore, since the guidance approach based on direct NLI considered wind

FIGURE 9.1: Panoramic view of the proposed control approaches.

disturbances in the control law, a sensitivity analysis of the position error w.r.t. wind gusts was provided. This was performed to evaluate the reactiveness of an aircraft cruising at a constant speed and a constant altitude (respecting load factor limits).

The analysis corroborated that the more accurate the aircraft model was considered for the NLI, the better cancellation of nonlinearities was performed, and consequently, this led to a better control of the aircraft position. Thus, a controller accounting for wind disturbances would perform better than a controller with no wind considerations.

Therefore, it seems clear why the wind data available to the FMS is a determinant factor for a substantial impact on the implementation of TBO. In this manner, a safety envelope (or VoP) for a single aircraft or a group of aircrafts could be redefined in terms of the wind known to the FMS, and this wind uncertainty could be translated into wind sensors accuracy, wind estimations accuracy, or up-to-date forecasted wind. Thus, aircraft position errors would depend on wind knowledge accuracy, allowing to create compact aircraft clusters and decrease the workload for air traffic controllers.

Note that a method to perform wind estimations was out of the scope of this work. The quality of data to feed the attitude and guidance control algorithms was assumed to be reliable (accurate, integral, continuous and available), thanks to the use of up-to-date navaids, GNSS and ADIRS systems.

9.1.2.1   Aircraft Mass Estimation

Moreover, it was assumed that an inaccurate aircraft mass has significant consequences in trajectory optimization, fuel consumption, and aircraft performance, such that two mass estimation methods were proposed.

- The first method relies on the knowledge of the Drag and Lift forces and measures of some longitudinal variables. This approach uses a reduced and decoupled longitudinal aircraft model to compute the aircraft mass.

- The second method uses the vector of mass estimations of the first method to compute the initial mass of the aircraft by solving a least squares problem, and then recalculates the aircraft mass estimation. This approach relies completely on the knowledge of a fuel consumption model.

These mass estimation algorithms, even if they are tested just for the climb phase, could be easily extended to full flights, such that the benefits of better trajectory prediction and ease of guidance efforts to follow a desired trajectory, could also be spread to a complete flight. Moreover, since the control approaches rely on the inversion of dynamics, the knowledge of an accurate mass helped to a more exact numerical inversion.

In general terms, these mass estimation methods were conceived to complete the simulation of a transport aircraft, seeking to ease the guidance efforts to follow a desired trajectory. This was expected since the Nonlinear inversion guidance approaches rely on a numerical inversion of the aircraft model. Therefore, a better knowledge of the aircraft parameters (like the aircraft mass), helps to improve the numerical inversion accuracy of the approach, leading to a better guidance performance.

9.2 Future Work

9.2.1 Trajectory Generation

Many improvements could be performed to the presented work. Concerning trajectory generation, the proposed approach was endowed with the capacity to generate a full flight profile without being decoupled in lateral and vertical profiles. In this manner, a conflict analysis between different trajectories could be further analyzed. Considering that the Bezier curves are polynomials, a conflict identification method could be implemented by solving a system of equations formed by the polynomials of different trajectories for different aircraft. Thus, if two polynomials have a solution, an intersection of the polynomials is inherent. Therefore, the time-stamp of each trajectory at the intersection moment could be used to analyze the possibility of a conflict, and address it if present.

9.2.1.1 Numerical Simulation of an Aircraft

Moreover, the neural networks trained for the numerical computation of the non-dimensional stability derivatives of the aircraft could be retrained periodically during flight, such that abnormal conditions modifying the aircraft model dynamics could be taken into account. This online training would allow to spread the use of these approach for more than transport aircraft. For example, a fighter aircraft after taking damage in its structure will present significant changes in its stability derivatives, impossible to predict. Thus, the neural networks could be retrained to take into account such modifications and not only ease the performance of the flight guidance system, but also to identify the remaining handling capabilities, and advert the pilot for critical aircraft performance. Note that this periodical training of the neural networks would be directly related to the evolution from supervised to unsupervised learning.

9.2.2 Flight Control Systems

Regarding the control approaches, since aircraft are expected to fly in compact flow corridors, a confidence area to assure safety in operations could be defined using the sensitivity analysis with respect to wind disturbances. This protection area could be dynamic and asymmetric depending on wind knowledge and direction. An example of this protection area for different wind directions is shown in Figure 9.2.
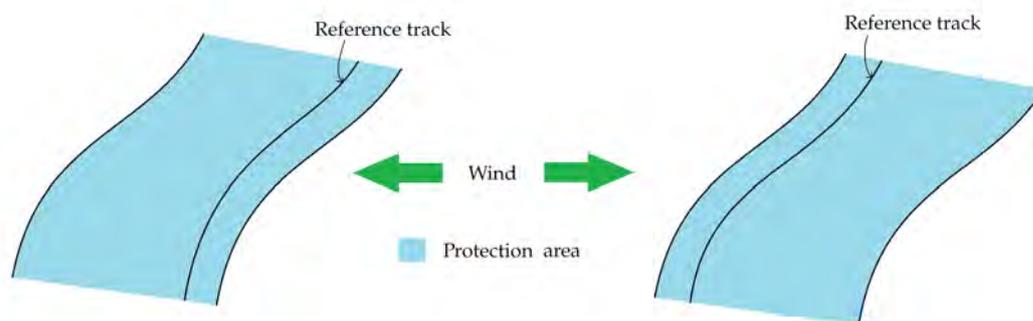

FIGURE 9.2: Dynamic protection area depending on wind direction.

9.2.2.1   Aircraft Mass Estimation

In terms of the mass estimation methods, a better assessment of the proposed algorithms could be performed with data obtained from real flights and not only simulations. However, in spite of the fact that the proposed simulated data is unlikely to be observed in real traffic, it served perfectly to show the methodology of the approach proposed, which was the ultimate goal.

Appendix A

Coordinate Transformations

This appendix is based on (Etkin and Reid, 1996).

A.1 Transformation of a Vector

Let a vector v be a vector with components $v_a = [v_{a1}, v_{a2}, v_{a3}]^T$ and $v_b = [v_{b1}, v_{b2}, v_{b3}]^T$ expressed in the reference frames $F_a = [x_{a1}, x_{a2}, x_{a3}]^T$ and $F_b = [x_{b1}, x_{b2}, x_{b3}]^T$, respectively. Both reference frames share the location of its origin.

The component v_{a1} in the direction of x_{bi} is denoted by $v_{a1}c_{\theta_{i1}}$, where θ_{i1} denotes the angle between the axes x_{bi} and x_{a1}. Therefore, taking into account the other components of v_a in the direction of x_{bi}, it is obtained that

$$v_{bi} = \sum_{j=1}^{3} l_{ij} v_{aj} \qquad i = 1, 2, 3 \tag{A.1}$$

with

$$l_{ij} = c_{\theta_{ij}} \tag{A.2}$$

as the nine director cosinus, such that

$$v_{b1} = c_{\theta_{11}} v_{a1} + c_{\theta_{12}} v_{a2} + c_{\theta_{13}} v_{a3} \tag{A.3a}$$
$$v_{b2} = c_{\theta_{21}} v_{a1} + c_{\theta_{22}} v_{a2} + c_{\theta_{23}} v_{a3} \tag{A.3b}$$
$$v_{b3} = c_{\theta_{31}} v_{a1} + c_{\theta_{32}} v_{a2} + c_{\theta_{33}} v_{a3} \tag{A.3c}$$

Thus, a vector v_a is expressed in the frame F_b by using the director cosinus. In other words, each component of v_a is related with the three axes x_{bi}.

Consequently, the matrix form of (A.3) is given by

$$v_b = L_{ba} v_a = \begin{bmatrix} l_{11} & l_{12} & l_{13} \\ l_{21} & l_{22} & l_{23} \\ l_{31} & l_{32} & l_{33} \end{bmatrix} v_a \tag{A.4}$$

The matrix L_{ba} belongs to the SO_3 group, so the transpose of the matrix equals to its inverse $\left(L_{ba}^{-1} = L_{ba}^T = L_{ab} \right)$, yielding

$$v_b = L_{ba} v_a \tag{A.5}$$
$$v_a = L_{ab} v_b \tag{A.6}$$

Since v_a and v_b represent physically the same vector v, but just seen from different reference frames, the magnitude should be the invariant, such that

$$v^2 = v_b^T v_b = v_a^T L_{ba}^T L_{ba} v_a = v_a^T v_a \tag{A.7}$$

For this equation to be satisfied, it must be true that $L_{ba}^T L_{ba} = I$.

Moreover, if several transformations through several frames of reference are performed, for example from F_a to F_c passing through F_b, the consecutive rotations are

$$v_b = L_{ba} v_a \tag{A.8}$$

$$v_c = L_{cb} v_b = L_{cb} L_{ba} v_a \tag{A.9}$$

such that

$$v_c = L_{ca} v_a \tag{A.10}$$

with

$$L_{ca} = L_{cb} L_{ba} \tag{A.11}$$

A.2   The Rotation Matrix

The transformations associated with single rotations about the three coordinate axes are given. In each case, let F_a be the original frame and F_b the frame after one single rotation. Hence, in each case, $v_b = L_i(X_i)v_a$, so different cosinus director L matrices are obtained. Using the mnemonic to obtain the angle θ_{ij} that the subindex i is the axe after the rotation (the one belonging to F_b), and j is the original axe (the one belonging to F_a), a rotation around the axe x_{a1} (see Figure A.1), leads to a matrix
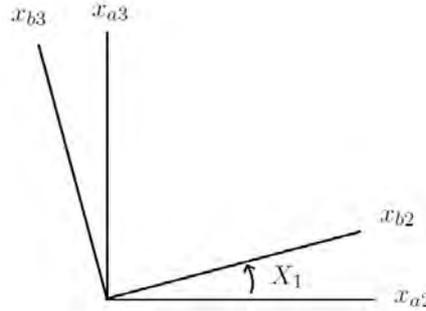

FIGURE A.1: Basic rotation about x_{a1}.

$$L_1(X_1) = \begin{bmatrix} c_0 & c_{90} & c_{90} \\ c_{90} & c_{X_1} & c_{(90-X_1)} \\ c_{90} & c_{(X_1+90)} & c_{X_1} \end{bmatrix} = \begin{bmatrix} 1 & 0 & 0 \\ 0 & c_{X_1} & s_{X_1} \\ 0 & -s_{X_1} & c_{X_1} \end{bmatrix} \tag{A.12}$$

Analogously, the rotations around the axes x_{a2} and x_{a3}, described by the angles X_2 and X_3, respectively, provide the matrices

$$L_2(X_2) = \begin{bmatrix} c_{X_2} & 0 & -s_{X_2} \\ 0 & 1 & 0 \\ s_{X_2} & 0 & c_{X_2} \end{bmatrix} \tag{A.13}$$

$$L_3(X_3) = \begin{bmatrix} c_{X_3} & s_{X_3} & 0 \\ -s_{X_3} & c_{X_3} & 0 \\ 0 & 0 & 1 \end{bmatrix} \tag{A.14}$$

Finally, the rotation matrix for any sequence of rotations can be constructed from the above basic formulas. For the case of the Euler angles, which rotate from the frame F_E into the frame F_B, the matrix corresponding to the sequence $(X_3, X_2, X_1) = (\psi, \theta, \phi)$, is given by

$$L_{BE} = L_1(\phi)L_2(\theta)L_3(\psi) \tag{A.15}$$

which results in the rotation matrix from the Earth to Body frame:

$$L_{BE} = \begin{bmatrix} c_\theta c_\psi & c_\theta s_\psi & -s_\theta \\ s_\phi s_\theta c_\psi - c_\phi s_\psi & s_\phi s_\theta s_\psi + c_\phi c_\psi & s_\phi c_\theta \\ c_\phi s_\theta c_\psi + s_\phi s_\psi & c_\phi s_\theta s_\psi - s_\phi c_\psi & c_\phi c_\theta \end{bmatrix} \tag{A.16}$$

A.3 Transformation of the Derivative of a vector

First, it is useful to consider the cross product by minors of two vectors $a = [a_1, a_2, a_3]^T$ and $b = [b_1, b_2, b_3]^T$, such that

$$c = a \times b = \begin{bmatrix} i & j & k \\ a_1 & a_2 & a_3 \\ b_1 & b_2 & b_3 \end{bmatrix} = \begin{bmatrix} a_2 b_3 - a_3 b_2 \\ a_3 b_1 - a_1 b_3 \\ a_1 b_2 - a_2 b_1 \end{bmatrix} = \tilde{a}b \tag{A.17}$$

where

$$\tilde{a} = \begin{bmatrix} 0 & -a_3 & a_2 \\ a_3 & 0 & -a_1 \\ -a_2 & a_1 & 0 \end{bmatrix} \tag{A.18}$$

is an *skew symmetric matrix*. This matrix has all its entries of the main diagonal as zero, such that the trace is also zero, and it holds the property of $\tilde{a}^T = -\tilde{a}$.

Stated this, the transformation of coordinates of the derivative of a vector using a rotation matrix is given as follows.

Assume that a vector v is observed simultaneously in two reference frames F_a and F_b, and consider that the frame F_b rotates with angular velocity ω relative to F_a, which may be regarded as fixed, then

$$v_b = L_{ba} v_a \tag{A.19}$$

or analogously

$$v_a = L_{ab} v_b \tag{A.20}$$

The derivatives of v_a and v_b are $\dot{v}_a = [\dot{v}_{a1}, \dot{v}_{a2}, \dot{v}_{a3}]^T$ and $\dot{v}_b = [\dot{v}_{b1}, \dot{v}_{b2}, \dot{v}_{b3}]^T$, respectively. Therefore, the derivative of (A.19) is

$$\dot{v}_b = L_{ba}\dot{v}_a + \dot{L}_{ba}v_a \tag{A.21}$$

or analogously

$$\dot{v}_a = L_{ab}\dot{v}_b + \dot{L}_{ab}v_b \tag{A.22}$$

Since $\dot{L}$ must be independent of v, the matrix $\dot{L}_{ab}$ can be obtained from (A.22) by considering the case when v_b constant, leading to

$$\dot{v}_a = \dot{L}_{ab}v_b \tag{A.23}$$

Moreover, the derivative of v seen from the frame F_a is denoted by

$$\dot{v}_a = \tilde{\omega}_a v_a \tag{A.24}$$

such that from (A.23), (A.24), and (A.20), it is obtained

$$\dot{L}_{ab} = \tilde{\omega}_a L_{ab} \tag{A.25}$$

If this argument is repeated with F_b considered fixed and F_a moving with an angular velocity $-\omega$, the reciprocal result is reached

$$\dot{L}_{ba} = -\tilde{\omega}_b L_{ba} \tag{A.26}$$

Thus, from the transpose of (A.25) and (A.26) it is obtained

$$\tilde{\omega}_a = L_{ab} \tilde{\omega}_b L_{ba} \tag{A.27}$$

Finally, if (A.25) and (A.27) are used in (A.22), the following expression is found

$$L_{ba} \dot{v}_a = \dot{v}_b + \tilde{\omega}_b v_b \tag{A.28}$$

Appendix B

Gaussian Distribution

B.1 Mathematical Representation

B.1.1 Univariate Gaussian Distribution

One of the most important probability distribution is the *Gaussian* or *Normal* distribution. For a single real-valued variable x, is defined by

$$\mathcal{N}(x|\mu, \sigma^2) = \frac{1}{(2\pi\sigma^2)^{1/2}} \exp\left\{-\frac{1}{2\sigma^2}(x-\mu)^2\right\} \tag{B.1}$$

where μ is the *mean*, and σ^2 is the *variance*. The square root of the variance, given by σ, is called the *standard deviation*, and the reciprocal of the variance, given by $\beta = 1/\sigma^2$, the *precision*. The Gaussian distribution satisfies

$$\mathcal{N}(x|\mu, \sigma^2) > 0 \tag{B.2}$$

$$\int_{-\infty}^{\infty} \mathcal{N}(x|\mu, \sigma^2)dx = 1 \tag{B.3}$$

So it is said to be a valid probability density. The average value of x under a Gaussian distribution is denoted by

$$\mathbb{E}[x] = \int_{-\infty}^{\infty} \mathcal{N}(x|\mu, \sigma^2)x\,dx = \mu \tag{B.4}$$

Since the parameter μ represents the average value, it is referred to as the mean. Similarly

$$\mathbb{E}[x^2] = \int_{-\infty}^{\infty} \mathcal{N}(x|\mu, \sigma^2)x^2\,dx = \mu^2 + \sigma^2 \tag{B.5}$$

and hence, from (B.4), (B.5), it is obtained

$$\text{var}[x] = \mathbb{E}[x^2] - \mathbb{E}[x]^2 = \sigma^2 \tag{B.6}$$

therefore, σ^2 is referred to as the variance parameter. For a Gaussian distribution, the mode coincides with the mean.

B.1.2 Multivariate Gaussian Distribution

A Gaussian distribution defined over a $D-$dimensional vector x of continuous variables is denoted by

$$\mathcal{N}(\text{x}|\mu, \Sigma) = \frac{1}{(2\pi)^{D/2}} \frac{1}{|\Sigma|^{1/2}} \exp\left\{-\frac{1}{2}(\text{x}-\mu)^T \Sigma^{-1}(\text{x}-\mu)\right\} \tag{B.7}$$

where the $D-$dimensional vector μ is the mean, and the $D \times D$ matrix Σ is the covariance. The determinant of Σ is denoted by $|\Sigma|$.

B.2 Regression applied to a Gaussian distribution using the Maximum Likelihood approach

Let assume a data set of observations $\mathfrak{X} = (x_1, \ldots, x_N)^T$, representing N observations of a scalar variable x. It can be supposed that the observations are taken independently from a Gaussian distribution whose mean μ and variance σ^2 are unknown, and the goal is to determine these parameters from the data set.

Knowing that the joint probability of two independent events is given by the product of the marginal probabilities for each event separately, the probability of the data set, given μ and σ^2, can be written in the form

$$p(\mathfrak{X}|\mu, \sigma^2) = \prod_{n=1}^{N} \mathcal{N}(x_n|\mu, \sigma^2) \tag{B.8}$$

Note that when it is viewed as a function of μ and σ, this is the likelihood function for the Gaussian distribution.

To determinate the parameters of the probability distribution using an observed data set, the parameters to be found will be the ones that maximize the likelihood function. This is using the frequentist criterion of maximize the probability of the data given the parameters and not the Bayesian criterion of maximize the probability of the parameters given the data.

From (B.1) and (B.8), the logarithmic function is denoted by

$$\ln p(\mathfrak{X}|\mu, \sigma^2) = -\frac{1}{2\sigma^2} \sum_{n=1}^{N} (x_n - \mu)^2 - \frac{N}{2} \ln \sigma^2 - \frac{N}{2} \ln(2\pi) \tag{B.9}$$

Maximizing (B.9) w.r.t. μ, it is obtained the maximum likelihood solution given by

$$\mu_{ML} = \frac{1}{N} \sum_{n=1}^{N} x_n \tag{B.10}$$

which is the *sample mean*. Similarly, maximizing (B.9) w.r.t. σ^2, it is obtained the maximum likelihood for the variance

$$\sigma_{ML}^2 = \frac{1}{N} \sum_{n=1}^{N} (x_n - \mu_{ML})^2 \tag{B.11}$$

which is the *sample variance* measured w.r.t. the sample mean μ_{ML}. Since the maximum likelihood solutions are functions of the data set values $x_1, \ldots, x_N$, the expectations of these solutions are

$$\mathbb{E}[\mu_{ML}] = \mu \tag{B.12}$$

$$\mathbb{E}[\sigma^2] = \left(\frac{N-1}{N}\right)\sigma^2 \tag{B.13}$$

showing that the maximum likelihood estimate will underestimate the true variance by a factor $(N-1)/N$, so the unbiased estimate for the variance is given by

$$\tilde{\sigma}^2 = \frac{N}{N-1}\sigma_{ML}^2 = \frac{1}{N-1} \sum_{n=1}^{N} (x_n - \mu_{ML})^2 \tag{B.14}$$

Note that the bias of the maximum likelihood solution becomes less significant as N grows.

Appendix C

Neural Networks Performance

In this Appendix, the performance of the neural networks developed to fit the nondimensional stability derivatives databases from the DATCOM software are presented. This performance is given in terms of the Mean Squared Error of the proposed curve with respect to the training and testing data sets.
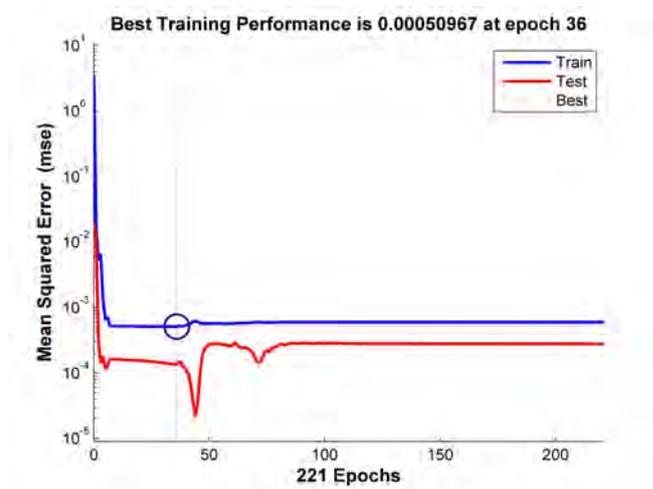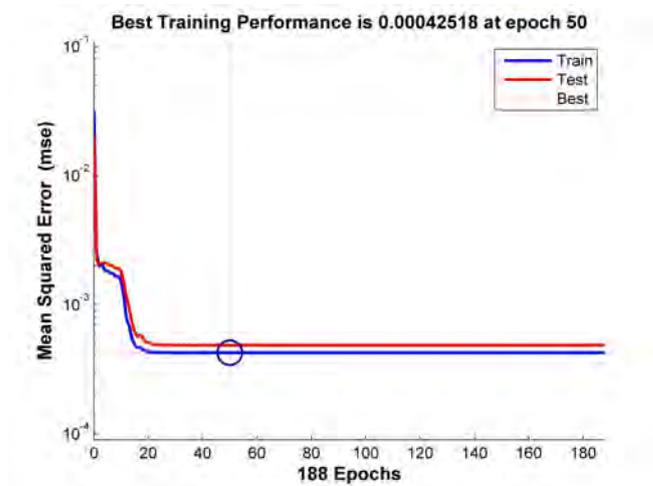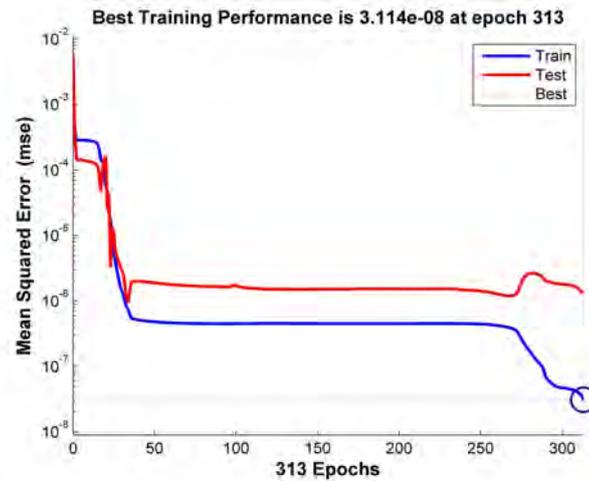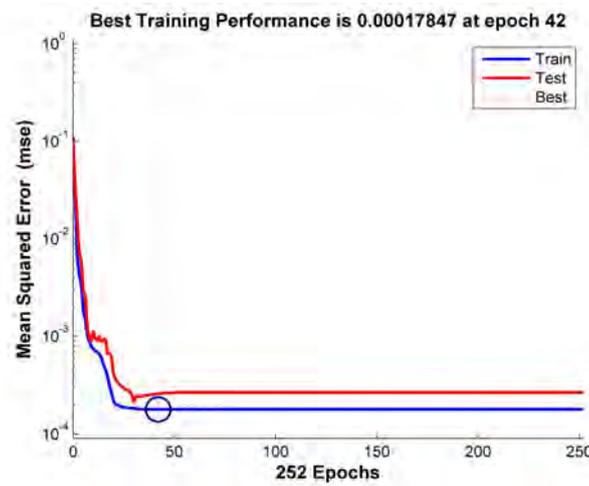

FIGURE C.1: Performance of the proposed C_L coefficient.

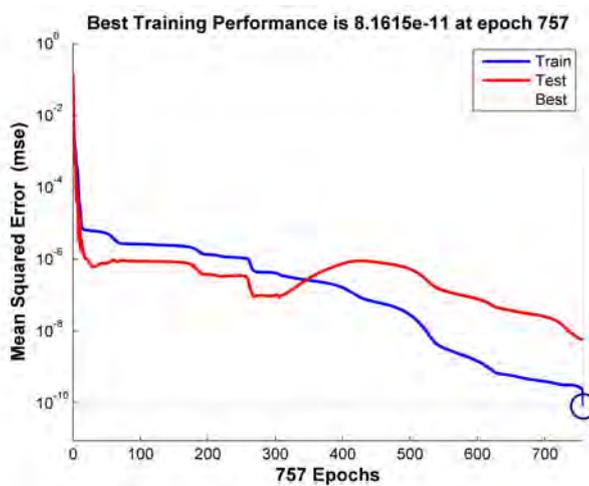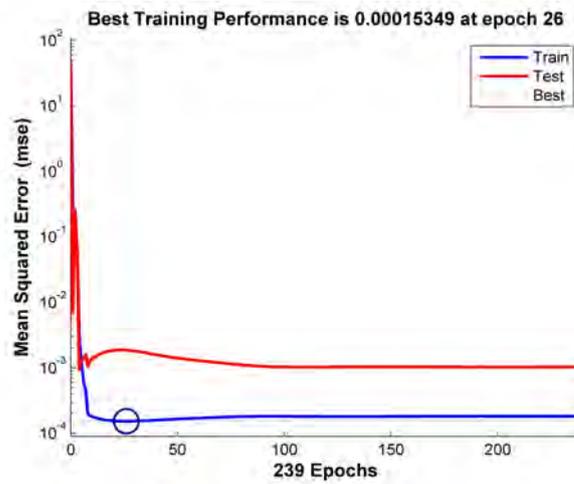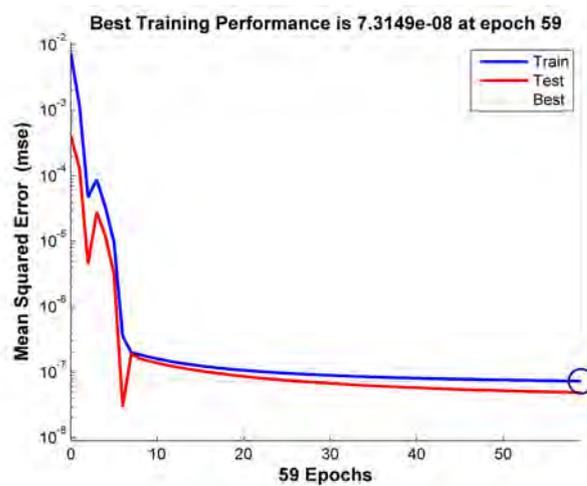FIGURE C.2: Performance of the proposed C_{Y_β} coefficient.

FIGURE C.3: Performance of the proposed C_{l_β} coefficient.

FIGURE C.4: Performance of the proposed C_{l_p} coefficient.

FIGURE C.5: Performance of the proposed C_{l_r} coefficient.
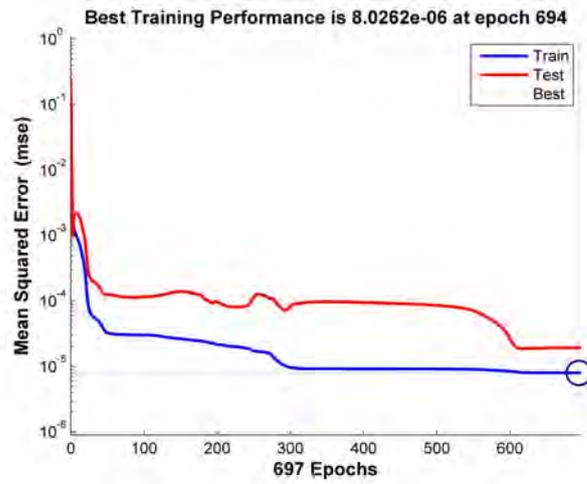
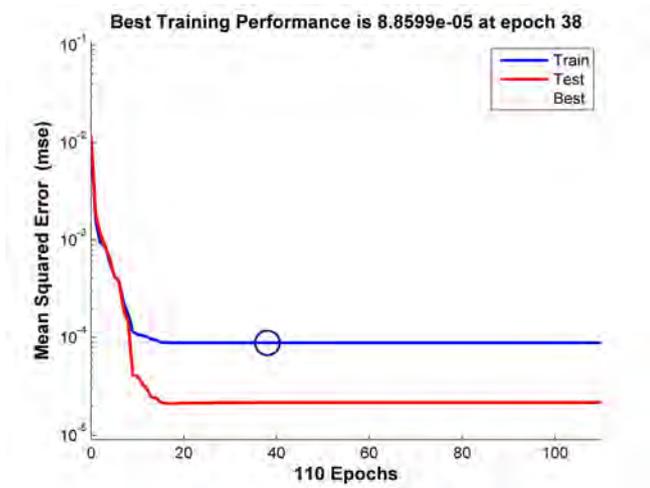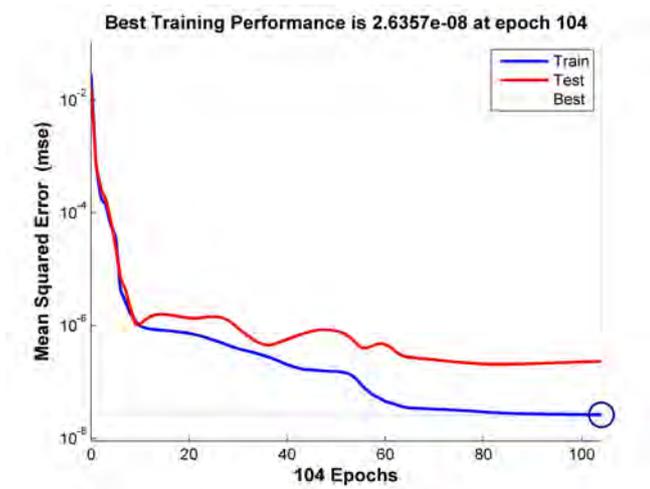FIGURE C.6: Performance of the proposed C_{m_α} coefficient.

FIGURE C.7: Performance of the proposed C_{m_q} coefficient.

FIGURE C.8: Performance of the proposed C_{n_β} coefficient.

FIGURE C.9: Performance of the proposed C_{n_p} coefficient.

FIGURE C.10: Performance of the proposed C_{n_r} coefficient.

List of Publications

- H. Escamilla Núñez, F. Mora Camino, H. Bouadi. "Towards 4D Trajectory Tracking for Transport Aircraft". *20th International Federation of Automatic Control World Congress (IFAC WC)*. Toulouse, France. 9-14 July 2017.
  DOI: https://doi.org/10.1016/j.ifacol.2017.08.1268.

- H. Escamilla Núñez, H. Bouadi, F. Mora Camino. "A Framework for Wind Sensitivity Analysis for Trajectory Tracking". *American Institute of Aeronautics and Astronautics Guidance, Navigation, and Control Conference (AIAA GNC)*. Gaylord Texan Convention Center, Grapevine, Texas, USA. 9-13 January 2017.
  DOI: http://dx.doi.org/10.2514/6.2017-1726.

- H. Escamilla Núñez, F. Mora Camino. "Generation of Curvature Continuous Trajectories for Transport Aircraft using Bezier Curves". *19th International Conference New Trends in Civil Aviation 2017 (NTCA)*. Prague, Czech Republic. 7-8 December 2017.
  ISBN: 978-0-8153-7602-6.

- H. Escamilla Núñez, F. Mora Camino. "Generation of Smooth Reference Trajectories for Transport Aircraft". *16th Simpósio de Transporte Aéreo (SITRAER)*. Rio de Janeiro, Brazil. 25-27 October 2017.

Bibliography

Akmeliawati, Rini and Iven M. Y. Mareels (December 2001). "Nonlinear Energy-Based Control Method for Aircraft Dynamics". In: *Proceedings of the 40th IEEE Conference on Decision and Control (CDC)*. DOI: 10.1109/CDC.2001.980179.

— (July 2010). "Nonlinear Energy-Based Control Method for Aircraft Automatic Landing Systems". In: *IEEE Transactions on Control Systems Technology* 18.4, pp. 871–884.

Alligier, R., D. Gianazza, and N. Durand (December 2015). "Machine learning and mass estimation methods for ground-based aircraft climb prediction". In: *IEEE Transactions on Intelligent Transportation Systems* 16.6, pp. 3138–3148.

— (June 2013). "Ground-based estimation of the aircraft mass, adaptive vs. least squares method". In: *10th USA/Europe Air Traffic Management Research and Development Seminar*, pp. 1–10.

— (May 2012). "Energy Rate Prediction Using an Equivalent Thrust Setting Profile". In: *5th International Conference on Research in Air Transportation (ICRAT), Berkeley, USA*.

— (November 2013). "Learning the aircraft mass and thrust to improve the ground-based trajectory prediction of climbing flights". In: *Transportation Research Part C: Emerging Technologies* 36, pp. 45–60. DOI: https://doi.org/10.1016/j.trc.2013.08.006.

Alligier, R. et al. (May 2014). "Comparison of Two Ground-based Mass Estimation Methods on Real Data". In: *6th International Conference on Research in Air Transportation (ICRAT), Istanbul, Turkey*.

Anderson, Erik P., Randal W. Beard, and Timothy W. McLain (May 2005). "Real-time dynamic trajectory smoothing for unmanned air vehicles". In: *IEEE Transactions on Control Systems Technology* 13.3. DOI: 10.1109/TCST.2004.839555.

AWC (2017). *US Department of Commerce. National Oceanic and Atmospheric Administration. Aviation Weather Center*. URL: http://www.aviationweather.gov/.

BADA (August 2014). *User Manual for the Base of Aircraft Data*. English. Version Revision 3.12, EEC Technical/Scientific Report No. 14/04/24-44. European Organisation for the Safety of Air Navigation. Eurocontrol.

Bakolas, Efstathios, Yiming Zhao, and Panagiotis Tsiotras (August 2011). "Initial Guess Generation for Aircraft Landing Trajectory Optimization". In: *AIAA Guidance, Navigation, and Control Conference, Portland, Oregon, USA*. DOI: http://dx.doi.org/10.2514/6.2011-6689.

Barsky, Brian A. and Tony D. DeRose (October 1984). "Geometric continuity of Parametric Curves. Technical Report No. UCB/CSD 84/205". In: *University of Berkeley, USA*.

Bishop, Christopher M. (2006). *Pattern Recognition and Machine Learning*. Springer.

CFI (2017). URL: http://www.cfinotebook.net/notebook/avionics-and-instruments/turn-coordinator.

Chati, Yashovardhan S. and Hamsa Balakrishnan (June 2017). "Statistical Modeling of Aircraft Takeoff Weight". In: *Twelfth USA/Europe Air Traffic Management Research and Development Seminar (2017 ATM R&D), Seattle, Washington, USA*.

Chen, Chi-Tsong (2013). *Linear System Theory and Design*. 4th edition. Madison Avenue, New York: Oxford University Press.

Chudy, P. and P. Rzucidlo (August 2009). "TECS/THCS based flight control system for general aviation". In: *AIAA Modeling and Simulation Technologies Conference*.

Delahaye, Daniel et al. (2014). *Mathematical Models for Aircraft Trajectory Design: A survey. In: Electronic Navigation Research Institute (eds) Air Traffic Management and Systems. Lecture Notes in Electrical Engineering*. Vol. 290. Springer, pp. 205–247. DOI: 10.1007/978-4-431-54475-3_12.

DGAC (March 2012). English. Plan PBN France. French plan for implementation of Performance Based Navigation. Ministry of Ecology, Sustainable Development, Transport and Housing.

Dubins, Lester Eli (July 1957). "On curves of minimal length with a constraint on average curvature, and with prescribed initial and terminal positions and tangents". In: *American Journal of Mathematics* 79.3, pp. 497–516. DOI: 10.2307/2372560.

EASA (2017). *ICAO Aircraft Engine Emissions Databank*. URL: https://www.easa.europa.eu/document-library/icao-aircraft-engine-emissions-databank.

EC (2017). *European Comission. Single European Sky*. URL: https://ec.europa.eu/transport/modes/air/single_european_sky_en.

ECMWF (2017). *European Centre for Medium-Range Weather Forecasts*. URL: https://www.ecmwf.int/.

Etkin, Bernard (1972). *Dynamics of Atmospheric Flight*. John Wiley and Sons.

Etkin, Bernard and Lloyd Duff Reid (1996). *Dynamics of Flight, Stability and Control*. 3rd edition. John Wiley and Sons.

Eurocontrol (2016). *Single European Sky ATM Research Joint Undertaking*. URL: http://www.sesarju.eu/.

— (2017a). *Air Traffic Flow and Capacity Management*. URL: http://www.eurocontrol.int/articles/air-traffic-flow-and-capacity-management.

— (2017b). *Air Traffic Flow Management Slots*. URL: http://www.eurocontrol.int/articles/atfm-slots.

— (2017c). *Aircraft Noise and Performance database*. URL: www.aircraftnoisemodel.org/home.

— (2017d). *Aircraft performance summary tables: Base of Aircraft Data*. URL: http://www.eurocontrol.int/aircraft-performance-summary-tables-base-aircraft-data.

— (2017e). *Aviation Meteorology (MET)*. URL: http://www.eurocontrol.int/met.

— (2017f). *Base of Aircraft Data*. URL: http://www.eurocontrol.int/services/bada.

Eurocontrol (2017g). English. Air Traffic Flow and Capacity Management Operations Manual-Network Operations Handbook. European Organisation for the Safety of Air Navigation.

Eurocontrol (2017h). *European Organisation for the Safety of Air Navigation*. URL: http://www.eurocontrol.int/articles/free-route-airspace.

— (2017i). *European Organisation for the Safety of Air Navigation*. URL: http://www.eurocontrol.int/publications/free-route-airspace-fra-implementation-projections.

— (2017j). *European Organisation for the Safety of Air Navigation*. URL: http://www.eurocontrol.int/dossiers/single-european-sky.

— (2017k). *European Organisation for the Safety of Air Navigation*. URL: http://www.eurocontrol.int/articles/functional-airspace-block-fab.

— (2017l). *European Organisation for the Safety of Air Navigation*. URL: http://www.eurocontrol.int/articles/continuous-climb-and-descent-operations.

Eurocontrol (January 2013). English. Introducing Performance Based Navigation (PBN) and Advanced RNP (A-RNP). European Organisation for the Safety of Air Navigation.

Eurocontrol (October 2011). English. Continuous Descent. A guide to implementing Continuous Descent. European Organisation for the Safety of Air Navigation.

Evans, Katie A. (June 2009). "Sensitivity analysis for control parameter determination for a nonlinear cable-mass system". In: *2009 American Control Conference (ACC)*, pp. 4091–4096.

FAA (2016). *US Department of Transportation. Federal Aviation Administration: Next Generation Air Transportation System*. URL: https://www.faa.gov/nextgen/.

— (2017). URL: https://www.faasafety.gov/gslac/ALC/course_content.aspx?cID=42&sID=505&preview=true.

FAA (December 2015). English. Air Traffic Plans and Publications. Aeronautical Information Manual: Pilot/Controller Glossary. US Department of Transportation. Federal Aviation Administration.

FAA (May 2017). English. Code of Federal Regulations (CFR)-Title 14 Aeronautics and Space. Subchapter C-Aircraft, Part 25 Airworthiness Standards: Transport Category Airplanes, Section 337 Limit Maneuvering Load Factors. US Department of Transportation. Federal Aviation Administration.

FAA (September 1983). English. AC 150/5060-5-Airport Capacity And Delay. US Department of Transportation. Federal Aviation Administration.

FlightGear (2017). *FlightGear Flight Simulator*. URL: http://home.flightgear.org/.

Flightradar24 (2017). *Flightradar24*. URL: https://www.flightradar24.com/.

Gerretsen, Arno and Sip Swierstra (January 2003). "Sensitivity of aircraft performance to Variability of input data". In: *Eurocontrol Report*.

Gloudemans, Thijs W. (2016). "Aircraft Performance Parameter Estimation using Global ADS-B and Open Data". MA thesis. Zuid Holland, 2629HS, Netherlands: Delft University of Technology.

GSA (2017). *European Global Navigation Satellite Systems Agency*. URL: https://www.gsa.europa.eu/european-gnss/what-gnss.

Hameduddin, I. and A. H. Bajodah (June 2012). "Generalized dynamic inversion control for aircraft constrained trajectory tracking applications". In: *American Control Conference (ACC)*, pp. 4599–4606.

ICAO (2006a). English. Doc 9863 AN/461. Airborne Collision Avoidance System (ACAS) Manual. International Civil Aviation Organization.

ICAO (2006b). English. Doc 8168 OPS/611. Procedures for Air Navigation Services-Aircraft Operations. Volume I. Flight Procedures. International Civil Aviation Organization.

ICAO (2008). English. Doc 9613 AN/937. Performance-Based Navigation (PBN) Manual. International Civil Aviation Organization.

ICAO (2009). English. Doc 9905 AN/471. Required Navigation Performance Authorization Required (RNP AR) Procedure Design Manual. International Civil Aviation Organization.

ICAO (2010). English. Doc 9931 AN/476. Continuous Descent Operations (CDO) Manual. International Civil Aviation Organization.

ICAO (2013). English. Doc 9993 AN/495. Continuous Climb Operations (CCO) Manual. International Civil Aviation Organization.

ICAO (2016). English. Doc 4444. Procedures for Air Navigation Services - Air Traffic Management. International Civil Aviation Organization.

ICAO (July 2001[a]). English. Annex 11 to the convention on International Civil Aviation: Air Traffic Services. International Civil Aviation Organization.

ICAO (July 2001[b]). English. Annex 4 to the convention on International Civil Aviation: Aeronautical Charts. International Civil Aviation Organization.

ICAO (July 2004). English. Annex 12 to the convention on International Civil Aviation: Search and Rescue. International Civil Aviation Organization.

ICAO (July 2005). English. Annex 2 to the convention on International Civil Aviation: Rules of the Air. International Civil Aviation Organization.

ICAO (July 2006). English. Annex 10 to the convention on International Civil Aviation: Aeronautical Telecommunications. International Civil Aviation Organization.

ICAO (July 2007). English. Annex 3 to the convention on International Civil Aviation: Meteorological Service for International Air Navigation. International Civil Aviation Organization.

ICAO (July 2010). English. Annex 15 to the convention on International Civil Aviation: Aeronautical Information Services. International Civil Aviation Organization.

ICAO (July 2014). *Trajectory Based Operations (TBO). SESAR comments on TBO*. English. International Civil Aviation Organization. Air Traffic Management Requirements and Performance Panel (ATMRPP) 26th Working Group Meeting. Tokyo, Japan.

ICAO (July 2016). English. Doc 4444. Procedures for Air Navigation Services-Air Traffic Management (PANS-ATM). International Civil Aviation Organization.

ICAO (March 2014). *Proposal for the development of TBO concept. Managing unpredictable evolution in trajectory based operations*. English. International Civil Aviation Organization. Air Traffic Management Requirements and Performance Panel (ATM-RPP) 25th Working Group Meeting. Toulouse, France.

— (October 2014[a]). *Trajectory Based Operations (TBO). Sharing Trajectory Predictions in TBO*. English. International Civil Aviation Organization. Air Traffic Management Requirements and Performance Panel (ATMRPP) 27th Working Group Meeting. Montreal, Canada.

— (October 2014[b]). *Trajectory Based Operations (TBO). Time adherence in TBO*. English. International Civil Aviation Organization. Air Traffic Management Requirements and Performance Panel (ATMRPP) 27th Working Group Meeting. Montreal, Canada.

Imran, A., R. Gianmarco, and K. Jongrae (February 2010). "Backstepping control design with actuator torque bound for spacecraft attitude maneuver". In: *AIAA Journal of Guidance, Control and Dynamics* 33.1, pp. 254–259.

Janon, A. et al. (December 2014). "Global sensitivity analysis for the boundary control of an open channel". In: *IEEE Conference on Decision and Control*, pp. 589–594.

JSBsim (2016). *JSBsim*. URL: http://jsbsim.sourceforge.net/.

Judd, Kevin B. and Timothy W. McLain (August 2001). "Spline based path planning for unmanned air vehicles". In: *AIAA Guidance, Navigation, and Control Conference and Exhibit, Montreal,Canada*. DOI: http://dx.doi.org/10.2514/6.2001-4238.

Kanno, M. et al. (September 2010). "Algebraic approach to sensitivity analysis in optimal feedback control system design". In: *IEEE International Symposium on Computer-Aided Control System Design*, pp. 1696–1701.

Khalil, Hassan K. (2002). *Nonlinear Systems*. 3rd edition. Upper Saddle River, NJ: Prentice Hall.

Kim, K. and Y. Kim (November 2003). "Robust backstepping control for slew maneuver using nonlinear tracking function". In: *IEEE Transactions on Control Systems Technology* 11.6, pp. 822–829.

KLM (2017). URL: https://blog.klm.com/tag/air-traffic-control/.

Klooster, Joel K., Ana Del Amo, and Patrick Manzi (2009). "Controlled Time-of-Arrival Flight Trials". In: *Eighth USA/Europe Air Traffic Management Research and Development Seminar (ATM2009)*.

Lambregts, A. A. (1983). "Vertical Flight Path and speed Control Autopilot design Using Total Energy principles". In: *AIAA 83-2239CP*.

— (1996). "Automatic Flight Control Concepts and Methods". In: *Koninklijke Nederlandse Vereniging voor Luchtvaar, Jaarverslag*.

— (2013). *TECS Generalized Airplane Control System Design- An Update*. Advances in Aerospace Guidance, Navigation and Control. Selected Papers of the Second CEAS Specialist Conference on Guidance, Navigation and Control. Springer.

Lee, Hak tae and Gano Chatterji (September 2010). "Closed-Form Takeoff Weight Estimation Model for Air Transportation Simulation". In: *10th AIAA Aviation Technology, Integration, and Operations (ATIO) Conference, Fort Worth, Texas, USA*. DOI: https://doi.org/10.2514/6.2010-9156.

Lee, Hyeonbeom, Hyoin Kim, and H. Jin Kim (October 2016). "Planning and Control for collision-free cooperative aerial transportation". In: *IEEE Transactions on Automation Science and Engineering* PP.99, pp. 1–13. DOI: 10.1109/TASE.2016.2605707.

Leege, A. M. P. de, M. M. van Paassen, and M. Mulder (2013). "Using Automatic Dependent Surveillance-Broadcast for Meteorological Monitoring". In: *Journal of Aircraft* 50.1, pp. 249–261. DOI: https://doi.org/10.2514/1.C031901.

Leege, A.M.P. De, M. Mulder, and M.M. Van Paassen (2012). "Novel Method for Wind Estimation Using Automatic Dependent Surveillance-Broadcast". In: *Journal of Guidance, Control, and Dynamics* 35.2, pp. 648–653. DOI: https://doi.org/10.2514/1.55833.

Lombaerts, T. et al. (August 2010). "Pseudo control hedging and its application for safe flight envelope protection". In: *AIAA Guidance, Navigation, and Control Conference*.

Lombaerts, T. et al. (May-June 2009). "Nonlinear reconfiguring flight control based on on-line physical model identification". In: *AIAA Journal of Guidance, Control and Dynamics* 32.3, pp. 727–748.

Matlab (2017). *MATLAB*. URL: https://www.mathworks.com/products/matlab.html.

Mattei, G. and S. Monaco (2014). "Nonlinear autopilot design for an asymmetric missile using robust backstepping control". In: *AIAA Journal of Guidance, Control and Dynamics* 37.5, pp. 1462–1476.

MIT (2017). *OpenCourseWare. Modelling Dynamics and Control*. English. Massachusetts Institute of Technology Department of Mechanical Engineering. URL: https://ocw.mit.edu/courses/mechanical-engineering/2-003-modeling-dynamics-and-control-i-spring-2005/readings/.

Mora-Camino, Felix (2017). *Flight Control Systems Lecture notes*. Toulouse: MAIAA, ENAC.

Mutuel, Laurence H., Erwan Paricaud, and Pierre Neri (2013). "Initial 4D Trajectory Management Concept Evaluation". In: *Tenth USA/Europe Air Traffic Management Research and Development Seminar (ATM2013)*.

NASA (2013). "Green Aviation: A Better Way to Treat the Planet". In: *NASA Facts, Washington DC*.

NOAA (2017). *US Department of Commerce. National Oceanic and Atmospheric Administration. National Center for Environmental Prediction*. URL: http://www.ncep.noaa.gov/.

Ogata, Katsuhiko (1998). *Modern Control Engineering*. 3rd edition. Prentice Hall.

Rajput, J., Z. Weiguo, and S. Jingping (June 2015). "A backstepping based flight control design for an overactuated flying wing aircraft". In: *IEEE Asian Control Conference (ASCC)*.

Rysdyk, R. and A. J. Calise (November 2005). "Robust nonlinear adaptive flight control for consistent handling qualities". In: *IEEE Transactions on Control Systems Technology* 13.6, pp. 896–910.

S. Schnelle, J. Wang (October 2014). "Sensitivity analysis of human driving characteristics on road and driving conditions for active vehicle control systems". In: *IEEE International Conference on Systems, Man, and Cybernetics*, pp. 2482–2487.

Sahingoz, Ozgur Koray (April 2014). "Generation of Bezier curve-Based Flyable Trajectories for Multi-UAV Systems with Parallel Genetic Algorithm". In: *Journal of Intelligent and Robotic Systems* 74.1-2, pp. 499–511. DOI: 10.1007/s10846-013-9968-6.

Scheuer, A. and Th. Fraichard (September 1997). "Continuous-Curvature Path Planning for Car-Like Vehicles". In: *Proceedings of the 1997 IEEE/RSJ International Conference on Intelligent Robots and Systems (IROS)*. DOI: 10.1109/IROS.1997.655130.

Schultz, Ch. A., D. Thipphavong, and H. Erzberger (August 2012). "Adaptive trajectory prediction algorithm for climbing flights". In: *AIAA Guidance, Navigation and Control Conference*, pp. 1–16.

SESAR (2017). *Ministère de la Transition Écologique et Solidaire. République Française*. URL: https://www.ecologique-solidaire.gouv.fr/sesar-volet-technologique-du-ciel-unique-europeen.

SESAR Factsheet (2012). English. I-4D - Flying a new dimension.

SKYbrary (2017). *SKYbrary*. URL: https://www.skybrary.aero/index.php/Automatic_Dependent_Surveillance_(ADS).

SkyVector (2017). *SkyVector*. URL: https://skyvector.com/.

Slotin, J. J. E. and W. Li (1991). *Applied Nonlinear Control*. Englewood Cliffs, NJ: Prentice Hall.

Snell, S. A., D. F. Enns, and W. L Garrard (July 1992). "Nonlinear inversion flight control for a supermaneuverable aircraft". In: *AIAA Journal of Guidance, Control, and Dynamics* 15.4, pp. 976–984.

StackExchange (2017a). URL: https://aviation.stackexchange.com/questions/25169/what-is-a-tracon.

— (2017b). URL: https://aviation.stackexchange.com/questions/25169/what-is-a-tracon.

— (2017c). URL: https://aviation.stackexchange.com/questions/12956/what-are-different-types-of-weights-of-an-aircraft.

Stevens, Brian L. and Frank L. Lewis (1992). *Aircraft Control and Simulation*. 2nd edition. John Wiley and Sons.

Suchkov, A., S. Swierstra, and A. Nuic (June 2003). "Aircraft Performance Modeling for Air Traffic Management Applications". In: *5th USA/Europe Air Traffic Management Research and Development Seminar, Budapest, Hungary.*

Sun, J., J. Ellerbroek, and J.M. Hoekstra (June 2016[a]). "Large-Scale Flight Phase Identification from ADS-B Data Using Machine Learning Methods". In: *7th International Conference on Research in Air Transportation: Philadelphia, USA*. DOI: `uuid: af67a6bd-d812-474d-a304-7a594991390b`.

— (June 2016[b]). "Modeling and Inferring Aircraft Takeoff Mass from Runway ADS-B Data". In: *7th International Conference on Research in Air Transportation: Philadelphia, USA*. DOI: `uuid:234f1650-d9bd-4985-a70e-2115ac9e5c95`.

Sun, Junzi, Joost Ellerbroek, and Jacco M. Hoekstra (June 2017). "Bayesian Inference of Aircraft Initial Mass". In: *Twelfth USA/Europe Air Traffic Management Research and Development Seminar (2017 ATM R&D), Seattle, Washington, USA.*

Thipphavong, David P. et al. (January-February 2013). "Adaptive Algorithm to Improve Trajectory Prediction Accuracy of Climbing Aircraft". In: *AIAA Journal of Guidance, Control, and Dynamics* 36.1, pp. 15–24. DOI: `https://doi.org/10.2514/1.58508`.

Vilardaga, Santi and Xavier Prats (October 2015). "Mass Estimation for an Adaptive Trajectory Predictor using Optimal Control". In: *Proceedings of the 5th International Conference on Application and Theory of Automation in Command and Control Systems (ATACCS '15), Toulouse, France*. DOI: `10.1145/2899361.2899369`.

Wahid, M. Ab et al. (2016). "Space-Indexed Aircraft Trajectory Tracking". In: *28th Chinese Control and Decision Conference*, pp. 5076–5081.

Wahid, M. Ab et al. (October 2014). "Design of Aircraft Space Indexed Guidance Along an Airstream". In: *33rd Digital Avionics Systems Conference.*

Walter, Randy (2014). *Digital Avionics Handbook. Chapter 24. Flight Management Systems*. Ed. by Cary R. Spitzer, Uma Ferrell, and Thomas Ferrell. 3rd edition. CRC Press, pp. 381–406. DOI: `https://doi.org/10.1201/b17545-27`.

Wang, S., W. Wang, and S. Xiong (August 2014). "Backstepping sliding-mode control for missile attitude using a linear extended state observer". In: *Proceedings of IEEE Chinese Guidance, Navigation and Control Conference*, pp. 486–491.

Webb, Dustin J. and Jur van den Berg (May 2013). "Kinodynamic RRT*: Asymptotically Optimal Motion Planning for Robots with Linear Dynamics". In: *2013 IEEE International Conference on Robotics and Automation (ICRA), Karlsruhe, Germany*. DOI: `10.1109/ICRA.2013.6631299`.

Wikipedia (2017). URL: `https://en.wikipedia.org/wiki/Traffic_collision_avoidance_system`.

Williams, John E. and Steven R. Vukelich (April 1979). *The USAF Stability and Control Digital DATCOM. Volume I. Users Manual*. English. McDonnell Douglas Astronautics Company. St. Louis Division. URL: `http://www.pdas.com/datcom.htm`. Updated by Public Domain Aeronautical Software, December 1999.

Yang, Kwangjin and Salah Sukkarieh (June 2010). "An analytical Continuous - Curvature Path - Smoothing Algorithm". In: *IEEE Transactions on Robotics* 26.3. DOI: `10.1109/TRO.2010.2042990`.

Yang, Liang et al. (28-2 September-October 2015). "Generation of dynamically feasible and collision free trajectory by applying six order Bezier curve and local optimal reshaping". In: *2015 IEEE/RSJ International Conference on Intelligent Robots and Systems (IROS), Hamburg, Germany*. DOI: `10.1109/IROS.2015.7353440`.